



L'affouillement au pied des digues

Anak Damarnegara

► To cite this version:

Anak Damarnegara. L'affouillement au pied des digues. Other. Université de Lyon, 2019. English.
NNT : 2019LYSEC008 . tel-02490935

HAL Id: tel-02490935

<https://theses.hal.science/tel-02490935>

Submitted on 25 Feb 2020

HAL is a multi-disciplinary open access archive for the deposit and dissemination of scientific research documents, whether they are published or not. The documents may come from teaching and research institutions in France or abroad, or from public or private research centers.

L'archive ouverte pluridisciplinaire **HAL**, est destinée au dépôt et à la diffusion de documents scientifiques de niveau recherche, publiés ou non, émanant des établissements d'enseignement et de recherche français ou étrangers, des laboratoires publics ou privés.



ÉCOLE
CENTRALE LYON

N°d'ordre:2019LYSEC008

THESE de DOCTORAT DE L'UNIVERSITE DE LYON
opérée au sein de l'Ecole centrale de Lyon

Ecole Doctorale N°162
Mécanique, Energétique, Génie civil, Acoustique

Spécialité de doctorat:
Mécanique des fluides

Soutenue publiquement le 29 Mars 2019, par:
DAMARNEGARA Anak Agung Ngurah Satria

SCOUR AT THE FOOT OF SEAWALLS

Jury

| | | | |
|-----------------|---------------------|-------------------------------------|--------------------|
| LI Ming | Senior Lecturer | University of Liverpool | Rapporteur |
| CONLEY Daniel | Associate Professor | Plymouth University | Rapporteur |
| RIVIERE Nicolas | Professor | INSA Lyon, LMFA | Examineur |
| SOEMITRO Ria | Associate Professor | Institut Teknologi Sepuluh Nopember | Examinatrice |
| VINCENS Eric | Professor | Ecole Centrale de Lyon, LTDS | Directeur de thèse |
| PERKINS Richard | Professor | Ecole Centrale de Lyon, LMFA | Directeur de thèse |

Abstract

Scour at the foot of the seawalls (toe-scour) is one of the major causes of structural damage to sea-walls, involved in 12% of directly-observed damages. For engineering purposes, simple empirical approaches are often used to predict toe-scour but these are often limited. And whilst data from field observations and experimental studies are both very valuable, they both suffer from practical limitations. Experimental work for example is limited by similarity constraints and full scale experiments are expensive, without allowing detailed control of individual parameters. Numerical simulations therefore offer an interesting alternative but they are not without challenges. The first problem is the correct modelling of free surface dynamics including wave breaking processes. The second is modelling the scour development process and its feedback on the flow pattern. Finally, to be practically useful, the method should be robust and use reasonably affordable computational resources for full-scale simulation.

This thesis describes the development of an integrated numerical model based on OpenFOAM – an open source CFD platform, which includes free surface dynamics, sediment transport and bed deformation processes. The free surface dynamics are modeled using the Volume of Fluid (VOF) method with wave generation and absorption capabilities, based on the use of relaxation zones. The sediment transport process is calculated based on the bed load and suspended load approach and solved for the bed boundary using the Finite Area Method. The bed deformation is calculated using the sediment continuity equation, and the mesh is updated to take account of the bed change.

Several calibration tests have been performed to determine the model capabilities. Firstly, a sensitivity analysis was performed to characterize the influence of mesh size and numerical schemes on wave propagation. Secondly, several methods were compared for eliminating unwanted wave reflection. The model was then used to compute the wave-induced mass transport velocity in a closed flume, and the results compared with the theoretical solution and experimental data. It is shown that the failure to model correctly the pressure condition at the free surface leads to an overestimate of the drift close to the surface, which has to be compensated by an excessive negative drift in the body of the fluid. Fourth, the bed shear stress calculation is tested by studying the case of an oscillatory flow boundary layer. Two methods for computing the bed shear stress have been devised and tested with different mesh sizes. Finally, a simulation is carried out using all of these developments, to simulate the problem of erosion induced by the unsteady flow resulting from a dam-break, and the results are compared with an experimental test case. The sediment transport occurs mainly in the form of sheet flow, and a new method of simulating sheet flow has been devised, based on an analogy with dispersion in a fluidized bed. This approach has the advantage over previous models that it does not require any

ad-hoc modification of existing sediment transport models. Finally, the complete model is applied to the case of waves impacting on a sea wall, first for flat bed case and second for the case of a sloped beach. The hydrodynamic properties of the flow are analyzed for both cases without using the bed deformation module. In flat bed, partial standing wave occurs and the model captured streaming pattern well in boundary layer region. The scour pattern also found agreed well with experimental measurement. However, instability occurs as ripple formed at the bed. The sloped beach case show the model captured the incident wave interaction with reflected wave well. On the other hand, the scour pattern is different with the experiment despite follow the bed shear stress pattern produced by the model.

Keywords: seawalls, waves, scour, free-surface flow, sediment transport

Abstract in French

L'affouillement au pied des digues est l'un des principaux facteurs de l'endommagement structurel des digues, impliqué dans 12% des cas documentés. Pour les applications pratiques, l'affouillement au pied des digues est souvent modélisé avec une approche empirique simple qui a ses limites. Bien que des observations sur le terrain et des travaux expérimentaux soient utiles, il existe des limites dans l'approche. La pertinence des expériences en laboratoire est limitée par des problèmes de similitude et les expériences en vraie grandeur coûtent cher, et ne permettent pas une maîtrise des conditions expérimentales. Les simulations numériques nous offrent une alternative intéressante mais posent aussi quelques défis. La première difficulté est la modélisation correcte de la dynamique de la surface libre, y compris le processus de déferlement de la vague. Le deuxième problème est la modélisation de l'érosion des sédiments du lit, et l'influence de l'évolution du profil du lit sur l'écoulement. Enfin, pour être utile, la méthode doit être robuste, ne nécessitant que des ressources de calcul raisonnables de calcul pour effectuer la simulation d'un domaine d'une taille pertinente.

Cette thèse décrit le développement d'un modèle numérique intégré basé sur OpenFOAM – une plate-forme CFD open source – qui comprend la dynamique de surface libre, le transport des sédiments et le processus de déformation du lit. La dynamique de surface libre est modélisée à l'aide de la méthode Volume of Fluid (VOF) avec des zones de relaxation pour la génération et l'absorption de la houle. Le processus de transport des sédiments est modélisé avec un transport par charriage et un transport des sédiments en suspension et l'échange avec le lit est calculé avec la méthode des Surfaces Finies. La déformation du lit est calculée avec l'équation de continuité des sédiments, et le maillage est déformé pour tenir compte du changement de lit.

Plusieurs essais d'étalonnage ont été effectués pour caractériser les capacités du modèle. Premièrement, l'influence de la résolution spatiale et des schémas numériques sur la propagation de la houle ont été étudiés. Puis, plusieurs méthodes pour éliminer la réflexion de la houle ont été implémentées et comparées. La dérive de Stokes dans un canal fermé a été calculée et comparée avec les résultats théoriques et expérimentaux. Il est montré que le modèle surestime la dérive de Stokes près de la surface, parce que la pression à la surface libre n'est pas calculée correctement, et ceci induit une vitesse négative trop importante à l'intérieur du fluide. Quatrièmement, le calcul de la contrainte de cisaillement du lit a été testé avec le cas d'une couche limite oscillatoire. Deux méthodes pour le calcul de la contrainte de cisaillement au lit ont été testées avec différentes résolutions spatiales. Enfin, tous ces éléments ont été testés ensemble, dans la simulation d'une rupture de barrage sur fond mobile, avec comparaison des résultats avec une expérience en laboratoire. Le transport solide est créé principalement par un écoulement de type 'sheet flow',

et un nouveau modèle est proposé pour la prise en compte de ce phénomène, basé sur la modélisation des lits fluidisés. Cette approche est une adaptation du modèle standard pour le transport des sédiments en suspension, avec l'avantage de ne pas nécessiter un modèle propre au phénomène. Enfin, le modèle est utilisé pour simuler l'impact de la houle sur une digue, avec un lit horizontal et une plage inclinée, sans déformation du lit. Puis l'affouillement et la déformation du lit sont inclus pour les deux cas.

Mots-clés: digues, vagues, affouillement, écoulement à surface libre, transport de sédiments

Acknowledgement

I would like to express my wholehearted gratitude to those who helped me finish this thesis. First and foremost, I would like to thank my supervisors, Prof. Richard PERKINS and Prof. Eric VINCENS. Thank you for making this research possible with your fruitful guidance and discussion over the last four years. I hope that our collaboration will continue long after the end of this PhD


I would also like to thank Associate Professor Daniel CONLEY and Associate Professor Dr. Ming LI for reviewing the manuscript of this thesis and for participating in my soutenance in Lyon. The discussion was really interesting and gave me further insight into this research topic.

I am very grateful to Dr. Ria Asih SOEMITRO for her assistance during this PhD and for accepting to participate in the jury of my soutenance. I would never have been able to go to Lyon without her help with all the scholarship issues.

I am very grateful to Professor Nicolas RIVIERE for accepting to act as the president of the jury that made my defense possible. Thank you for all your feedback on the manuscript of this thesis.

Many people and organisations in Indonesia helped to make this PhD possible; from the Biro Perencanaan dan Kerja Sama Luar Negeri (BPKLN) Kementerian Pendidikan dan Kebudayaan (Kemendikbud) Republik Indonesia, I would particularly like to thank Dr. Ananto Kusuma Seta, Dr. Suharti, Dr. Abe Susanto and Mrs. Sari Damayanti Sitompul. From the Indonesian Embassy in Paris I would like to mention the Education Attaché, Prof. Surya Rosa Putra and Mrs. Saraswati Pradhany. Thank you all for the scholarship that made it possible to pursue my PhD in Lyon. I hope this thesis will contribute to the development of business and society in Indonesia.

I also received invaluable aid and financial support from the French Embassy in Indonesia and Campus France Indonesia; I would particularly like to thank Prof. Nicolas GASCOIN, Prof. Antoine Devoucoux du BUYSSON and Mrs. Annisa Fauziah, for the Bourse Du Gouvernement Français for this PhD thesis.

This work will not possible without the help from PMCS2I (Pôle de Modélisation et Calcul en Science de l'Ingénieur et de l'Information) École Centrale de Lyon.  pecially to Dr. Dan CALUGARU and Dr. Laurent POUILLOUX for helping me working with the computation cluster.

Throughout my studies I have been supported and encouraged by the staff at the Institut Teknologi Sepuluh Nopember (ITS), so I would like to express my gratitude

to the Rector, Prof. Mochamad ASHARI, the former Rector of ITS, Prof. Joni HERMANA, the former Rector of ITS Prof. Triyogi YUWONO and the former Vice Rector of ITS Dr. Herman SASONGKO; the former Director of the Postgraduate Program of ITS, Prof. Adi SOEPRIJANTO, the Dean of the Faculty of Civil, Environment and Geo Engineering of ITS, Dr. WARMADEWANTHI, the Vice Dean of the Faculty of Civil, Environment and Geo Engineering of ITS, Dr. Budi SUSWANTO, the Head of the Civil Engineering Departement of ITS, Dr. Trijoko WAHYU ; thank you all for encouraging and supporting me to undertake this PhD research project in Lyon.

Whilst finishing this PhD I received much support and guidance from the members of the Laboratory of Hydraulic and Coastal Engineering of ITS; I hope this research will make a useful contribution to the work of the laboratory in the field of coastal engineering.

Many of my fellow students in the Laboratory of Fluid Mechanics and Acoustics (LMFA) have helped during my stay, both with practical suggestions and by creating a pleasant working environment, so I would like to thank particularly Ming, Lu, Lei, Haining, Jianzhao and Jerome; I hope that we can continue to collaborate. I have enjoyed many friendly discussions in the restaurant with members of the non-linear group from the Nanotechnology Institute – Milan, Alberto, Jimmy and Raphael. I must thank Dr. Adi RIYONO and family for their hospitality in Lyon; I am looking forward to visiting you in Bandung. And last, but not least, the water bender family: Mahendra, Ratri, Dana, Nastasia and Bagus ; thank you for your support before my departure, I hope we will all succeed together.

Finally, I would like to express my gratitude towards my family – My father Ngu-rah AGUNG, my mother Ayu EKAWANTI, my brother Andika DAMARNEGARA and my sister Laksmi DAMARNEGARI – for their support and patience during my PhD studies. I am immensely grateful to my father and mother for raising me as an independent person and for supporting me in all the decisions that I have made in my life.

Contents

| | |
|--|------------|
| Abstract | i |
| Abstract in French | iii |
| Acknowledgement | v |
| 1 Introduction | 1 |
| 1.1 Motivation | 1 |
| 1.2 Outline of the Thesis | 3 |
| 2 Wave Modeling | 7 |
| 2.1 Coastal Process | 7 |
| 2.2 Wave hydrodynamics | 12 |
| 2.3 Wave numerical modelling | 27 |
| 2.4 Volume of Fluid Method | 29 |
| 2.5 Conclusion | 39 |
| 3 Sediment Transport Modeling | 41 |
| 3.1 Effects of scour on marine structures | 41 |
| 3.2 Numerical modelling of sediment transport | 45 |
| 3.3 Sediment Transport Formulation | 50 |
| 3.4 Conclusion | 55 |
| 4 Calibration of the Numerical Model in OpenFOAM® | 57 |
| 4.1 Sensitivity analysis | 57 |
| 4.2 Wave reflection absorption | 75 |
| 4.3 Mass transport simulation | 75 |
| 4.4 Oscillatory flow boundary layer | 81 |
| 4.5 Mobile dam break case | 88 |
| 5 Scour At Seawall | 99 |
| 5.1 Seawall On Flat Bed | 99 |
| 5.2 Seawall On Sloped Beach | 111 |
| 6 Conclusions and Perspectives | 129 |
| 6.1 Conclusions | 129 |
| 6.2 Perspectives | 131 |
| Appendices | 133 |

| | | |
|----------|--|------------|
| A | OpenFOAM® An Open Source CFD Toolbox | 135 |
| A.1 | Introduction | 135 |
| A.2 | Finite volume discretization | 135 |
| A.3 | Finite area method | 140 |
| A.4 | Pressure-velocity coupled equation | 141 |
| A.5 | Boundary conditions | 142 |
| B | Ghost Fluid Method Discretization | 145 |
| B.1 | Pressure jump implementation in discretized governing equation . . . | 147 |
| C | Suspended Load Entrainment Limiter | 149 |

List of Figures

| | | |
|------|---|----|
| 1.1 | A storm hit the Dawlish seawall, (Dawlishnewspapers, 2014) | 2 |
| 1.2 | Segmental seawall failure at Dawlish, (BBC, 2014) | 3 |
| 1.3 | Forces acting on a seawall | 4 |
| 2.1 | Wind-generated waves | 7 |
| 2.2 | Coastal terminology (Sorensen, 2005) | 8 |
| 2.3 | Scheme of wave refraction approaching the shore (Sorensen, 2005) . . | 9 |
| 2.4 | Cross-shore sediment transport pattern and breaker bar development (Fredsøe and Deigaard, 1992) | 10 |
| 2.5 | Wave induced long-shore current mechanism (Sorensen, 2005) | 10 |
| 2.6 | Beach protection using groynes, showing the resulting long-shore trans- port modification at Nusa Dua, Bali (Google Earth) | 12 |
| 2.7 | Coordinate system for propagating waves adapted from Sorensen (2005) | 13 |
| 2.8 | Stokes second-order waves as a combination of first and second order components from equation 2.17 | 16 |
| 2.9 | Typical profiles for several wave theories | 18 |
| 2.10 | Wave theory regimes (Méhauté, 1976) | 19 |
| 2.11 | Comparison between the Pierson-Moskowitz and the JONSWAP spec- trum | 21 |
| 2.12 | Standing wave description with particle trajectories (a): full standing wave ; (b): partial standing wave | 23 |
| 2.13 | Wave breaker types; (a) spilling breaker, (b) plunging breaker, (c) surging breaker | 24 |
| 2.14 | Particles trajectory under progressive wave (Van Dyke, 1982) | 25 |
| 2.15 | Mass Transport Velocity with $kh = 0.79$ and $a^2\omega k = 0.378$ ($H = 2.0$, $T = 1.01$) (Mei and Liu, 1972) | 26 |
| 2.16 | Time variation of the bed shear stress for turbulent flow over relatively small roughness element (Jonsson and Carlsen, 1976) | 28 |
| 2.17 | Relaxation zone weight across the wave tank | 34 |
| 2.18 | Velocity profile according the wall function | 37 |
| 3.1 | Critical shear stress according to Shields (top), van Rijn and Soulsby equation (Soulsby, 1997) (bottom) (Schierack, 2003) | 42 |
| 3.2 | Maximum scour depth at the breakwater for regular waves in live bed. (a) Vertical-wall breakwater (b) Rubble-mound breakwater Sumer and Fredsøe, 2000 | 44 |
| 3.3 | Typical toe protection for sea walls | 46 |
| 3.4 | Detailed bottom profile of scour with toe protection for protection length of $\frac{\lambda}{4}$ and $\frac{\lambda}{8}$ (Xie, 1981). L is the protection length and λ is the wave length. | 46 |

| | | |
|------|---|----|
| 3.5 | Scour depth as a function of the width of the toe protection apron. l is the toe protection length (Sumer and Fredsøe, 2000) | 46 |
| 3.6 | Influence of the number of layers of stone on the performance of the toe protection apron. N is the toe protection layer (Sumer and Fredsøe, 2000) | 47 |
| 3.7 | Application of numerical model for investigation of scour under pipe line based on: a. dynamic mesh method (Liang et al., 2005) and b. particle based method (Li et al., 2014) | 50 |
| 3.8 | Application of numerical model for investigation of scour under jet flow on: a. dynamic mesh method (Zhou, 2016) and b. phase resolving method (Chauchat et al., 2017) | 51 |
| 3.9 | Sediment transport model scheme | 52 |
| 3.10 | Bed slope correction using the sand slide mechanism: (a) bed slope before correction, (b) bed slope after correction | 55 |
| 4.1 | Numerical domain configuration for the sensitivity analysis. | 58 |
| 4.2 | Water surface elevation for the mesh sensitivity study with interFoam solver for $t = 30T$ | 60 |
| 4.3 | Water surface elevation for the mesh sensitivity study with gfmFoam solver | 60 |
| 4.4 | Instantaneous horizontal velocity profile in the midsection of the computational domain for interFoam solver depending on the mesh size: (a) $t = 10T$; (b) $t = 30T$; (c) Instantaneous horizontal velocity minus the mass transport velocity averaged over T at $t = 30T$; left side is at wave trough and right side is at wave crest | 61 |
| 4.5 | Instantaneous horizontal velocity profile in the middle of computational domain for gfmFoam solver depending on the mesh size: (a) $t = 10T$; (b) $t = 30T$; (c) Instantaneous horizontal velocity minus the mass transport velocity averaged over T at $t = 30T$; left side are at wave trough and right side are at wave crest | 62 |
| 4.6 | Mesh configuration for the numerical scheme sensitivity study | 63 |
| 4.7 | Water surface elevation for numerical scheme sensitivity study with interFoam solver for $t = 60T$ for test cases 1.7-1.12 | 65 |
| 4.8 | Water surface elevation for numerical scheme sensitivity study with gfmFoam solver for $t = 60T$ for test cases 1.7-1.12 | 65 |
| 4.9 | Instantaneous horizontal velocity profile in the mid section of the computational domain for the numerical scheme sensitivity study with interFoam solver: (a) $t = 10T$; (b) $t = 60T$; (c) Instantaneous horizontal velocity minus the mass transport velocity averaged over T at $t = 60T$ | 67 |
| 4.10 | Instantaneous horizontal velocity profile in the mid section of the computational domain for the numerical scheme sensitivity study with gfmFoam: (a) $t = 10T$; (b) $t = 60T$; (c) Instantaneous horizontal velocity minus the mass transport velocity averaged over T at $t = 60T$ | 68 |
| 4.11 | Water surface elevation for the gradient limiter study with interFoam solver for $t = 60T$ for test cases 1.11,1.13,1.14,1.15 | 69 |
| 4.12 | Water surface elevation for the gradient limiter study with gfmFoam solver for $t = 60T$ for test cases 1.11,1.13,1.14,1.15 | 69 |

| | | |
|------|---|----|
| 4.13 | Instantaneous horizontal velocity profile in the mid section of the computational domain for the gradient limiter sensitivity study with interFoam solver: (a) $t = 10T$; (b) $t = 30T$; (c) Instantaneous horizontal velocity minus the mass transport velocity averaged over T at $t = 30T$ | 70 |
| 4.14 | Instantaneous horizontal velocity profile in the mid section of the computational domain for the gradient limiter sensitivity study with gfmFoam: (a) $t = 10T$; (b) $t = 30T$; (c) Instantaneous horizontal velocity minus the mass transport velocity averaged over T at $t = 30T$ | 71 |
| 4.15 | Water surface elevation for time derivative scheme test with interFoam solver for $t = 60T$ for test case 1.9,1.10,1.16 | 72 |
| 4.16 | Water surface elevation for time derivative scheme test with gfmFoam solver for $t = 60T$ for test case 1.9,1.10,1.16 | 72 |
| 4.17 | Instantaneous horizontal velocity profile in the mid section of the computational domain for the time derivative scheme study with interFoam solver: (a) $t = 10T$; (b) $t = 30T$; (c) Instantaneous horizontal velocity minus the mass transport velocity averaged over T at $t = 30T$ | 73 |
| 4.18 | Instantaneous horizontal velocity profile in the mid section of the computational domain for the time derivative scheme study with gfmFoam: (a) $t = 10T$; (b) $t = 30T$; (c) Instantaneous horizontal velocity minus the mass transport velocity averaged over T at $t = 30T$ | 74 |
| 4.19 | Water surface elevation for the study of wave reflexion absorption with interFoam solver | 76 |
| 4.20 | Numerical domain for the mass transport analysis with the physical beach as a wave absorber | 77 |
| 4.21 | Numerical domain for the mass transport analysis with relaxation zone | 78 |
| 4.22 | Mesh for the simulation of the mass transport with a physical beach absorber | 78 |
| 4.23 | Water surface elevation in the study related to the mass transport for $t = 600T$ | 80 |
| 4.24 | Mass transport velocity comparison for different wave absorber types | 80 |
| 4.25 | Mass transport velocity integrated over the depth for different wave absorber types | 81 |
| 4.26 | U-shaped tunnel set up in experiment by Mujal-Colilles et al. (2014), the simulation domain is marked in red dash line | 82 |
| 4.27 | Velocity profile for an oscillatory flow with $Re = 3800$ with a smooth wall | 84 |
| 4.28 | Bed shear stress for an oscillatory flow with $Re = 3800$ with a smooth wall | 84 |
| 4.29 | Velocity profile for an oscillatory flow with $Re = 12700$ for $d_{50} = 1.50$ mm | 86 |
| 4.30 | Bed shear stress for an oscillatory flow with $Re = 12700$ for $d_{50} = 1.50$ mm | 87 |
| 4.31 | Bed shear stress for an oscillatory flow with $Re = 12700$ for $d_{50} = 1.50$ mm | 87 |
| 4.32 | Numerical domain configuration for the simulation of a mobile dam break flow | 88 |
| 4.33 | Experiment snapshot from Spinewine et al. (2005) for $t = 0.25$ s, 0.50 s, $t = 0.75$ s; x position is measured from the gate | 91 |

| | | |
|------|---|-----|
| 4.34 | Suspended load concentration at 4 different axial locations ($x/L = 0, 0.167, 0.333 \& 0.5$) and three different instants in time ($t = 0.25s, 0.50s \& 0.75s$). | 92 |
| 4.35 | Simulation results for a mobile dam break simulation for $t = 0.25s, 0.50s, 0.75s$; More detailed view near the gate opening (3 last figures) | 93 |
| 4.36 | Simulation results of sheet flow model for $t = 0.25, 0.50$ and $0.75s$ using different mesh configuration | 95 |
| 4.37 | Simulation results of sheet flow model for $t = 0.25, 0.50$ and $0.75s$ using different value of k_p ; k_p values from thinnest to thickest line: 1, 2, 5, 10, 100 | 97 |
| 5.1 | Numerical domain including a vertical seawall on a flat bed | 100 |
| 5.2 | Vertical velocity profile at anti node for standing wave case | 101 |
| 5.3 | Water surface elevation for standing wave case, analytical solution calculated based on second order partial standing wave with $C_R = 86.85\%$ | 102 |
| 5.4 | (a) Horizontal velocity profile at node for the standing wave case;(b) Near bed maximum horizontal velocity normalize with boundary layer thickness, δ_1 | 104 |
| 5.5 | Vertical velocity profile at anti node for the standing wave case | 105 |
| 5.6 | Horizontal streaming velocity profile at $x = 0.125\lambda$ and $x = 0.375\lambda$ | 105 |
| 5.7 | Horizontal streaming velocity for coarse mesh configuration | 106 |
| 5.8 | Horizontal streaming velocity for fine mesh configuration | 106 |
| 5.9 | Bed shear stress (a,b) and transport stage number (c,d) for the standing wave case; solid line is for the fine mesh; dot is for the coarse mesh; thin red line is the envelope over 20 periods; thick blue line is the value integrated over 5 period | 107 |
| 5.10 | Bed deformation for standing wave case with coarse mesh configuration | 109 |
| 5.11 | Bed deformation for standing wave case with fine mesh configuration | 110 |
| 5.12 | Experimental setup for seawall on sloped beach case (Sutherland et al., 2006) | 112 |
| 5.13 | Numerical domain of a seawall on a sloped beach | 112 |
| 5.14 | Time variation of the surface elevation, for the regular wave case at 0.5 m after relaxation zone | 113 |
| 5.15 | Computed Power Spectral Density for the irregular wave case measured 0.5m downwave of the relaxation zone | 114 |
| 5.16 | Wave breaking snapshot and horizontal velocity pattern for regular wave | 115 |
| 5.17 | Wave breaking snapshot and horizontal velocity pattern for irregular wave | 116 |
| 5.18 | Water surface elevation and bed shear stress for regular wave condition; gray dot is the instantaneous value for $10T$ | 117 |
| 5.19 | Wavelength of the surface wave, the envelope of the partial standing wave and the envelope of the bed shear stress, as functions of the distance from the wall. | 118 |
| 5.20 | Wavelengths of the envelopes normalised by the surface wavelength, as functions of the distance from the wall. | 119 |
| 5.21 | Water surface elevation and bed shear stress for irregular wave condition; gray dot is the instantaneous value for $10T$ | 120 |
| 5.22 | Integrated bed shear stress over $5T$ for regular and irregular wave conditions | 120 |

| | | |
|------|--|-----|
| 5.23 | Bed profile at $t = 0$ and $t = 300T$ for the experimental study of Sutherland et al. (2006) compared with the theoretical bed profile. . . | 121 |
| 5.24 | Scouring pattern for simulated irregular and regular waves and experiment measurements after 300 wave cycles | 122 |
| 5.25 | Erosion (negative) and deposition (positive) after 300 wave periods, as a function of distance from the sea wall, for the experiments of Sutherland et al (2006) and the simulation with OpenFOAM® | 123 |
| 5.26 | Power Spectral Density of bed level change, as a function of spatial frequency | 124 |
| 5.27 | Normalised Power Spectral Density of bed level change, as a function of spatial frequency. | 125 |
| 5.28 | The experimental change in bed elevation and the model function . . | 126 |
| 5.29 | Normalised Power Spectral Density of bed level change, as a function of spatial frequency. | 127 |
| A.1 | Arbitrary polyhedral control volume in OpenFOAM®(Jasak, 1996) . | 136 |
| A.2 | Control area in finite area mesh (Tukovic and Jasak, 2008) | 141 |
| A.3 | Implementation of inlet-outlet boundary condition at OpenFOAM® . | 143 |
| B.1 | Wet and dry cells in discretization domain for ghost fluid method (Vukčević et al., 2017) | 146 |
| B.2 | Free surface distance \mathbf{x}_Γ for one interface face (Vukčević et al., 2017) | 146 |
| C.1 | Concentration as a function of stage discharge number | 150 |
| C.2 | Quadratic Bézier curve | 150 |

List of Tables

| | | |
|-----|--|-----|
| 2.1 | Default value for $k - \omega$ SST model coefficient | 36 |
| 2.2 | k_s estimation based on sediment grain diameter (Sleath, 1984) | 38 |
| 4.1 | Mesh sensitivity configuration | 59 |
| 4.2 | Numerical scheme sensitivity case configuration | 64 |
| 4.3 | Reflection coefficient for different absorption methods | 77 |
| 4.4 | Test case parameters for the oscillatory boundary layer | 82 |
| 4.5 | Sediment mass conservation using source term bed boundary for suspended load | 90 |
| 5.1 | Mesh configuration for standing wave over flat bed case | 101 |
| 5.2 | Coefficient for the model function, for the experimental and numerical data | 126 |

Chapter 1

Introduction

1.1 Motivation

Seawalls are one of the earliest types of coastal protection. These marine structures are built to protect inland areas from erosion, flood or combination of both while facilitating disembarkation of goods from ships. The earliest known seawalls can be traced back to the first century BC, built by the Romans in Sebastos Harbor, Israel. Although relatively little information about the subsequent development of seawall structures is available, the concept of shoreline protection is already established. As a small example, dikes were already used by the Xth century in Netherlands and usage of stone and masonry also already started early in the XIXth in Belgium (Walker, 2012). The type of structure for seawall has not changed very much, most of them found today use a protective armor made of wood, stone or concrete. According to Allsop (2014), the seawall infrastructures inherited from the past are often too far seaward, exposing them to unnecessarily high hydrodynamic forces, and thus likely to be aggravated in coming years with the projected rise in sea levels resulting from climate change. For those reason it might be necessary to consider relocating sea walls further inland, but in industrial areas, the relocation costs would be huge. For example, 80m long seawalls in Dawlish-England, failed during a storm in February and November 2014 (Figures 1.1 and Figure 1.2). The seawalls had been built to act both as foundations and as protection for railways and their failure caused the service to stop for two months.

But there are other threats than storms that can jeopardize the stability of seawalls. Toe-scour under wave action is the main one. It was involved in 12% of direct observed damage (an additional 5% indirectly) in seawall structures (Powell, 1987). Toe-scour is a local phenomenon which is part of the natural processes involved in coastal dynamics. Indeed, natural sandy beaches are known to have periodic cyclic behavior under wave action. In the high wave season, the coastline retreats and replenishes during the low wave season. Seawalls which are located in this dynamic area interfere with this hydrodynamic process mainly inducing higher wave reflections and higher wave breaking patterns creating erosion of the sea bed at the toe of seawalls. The creation of a scour hole results in the degradation of the safety factor of the seawall foundation stability (Figure 1.3) and eventually may lead to seawall failure.

There exist some design codes for predicting scour in front of seawalls, based on a very simple approach or empirical formulations derived from experimental works.



Figure 1.1: A storm hit the Dawlish seawall, (Dawlishnewspapers, 2014)

The Shore Protection Manual (SPM) (1984) from the United States Army Corps of Engineers (USACE) gives a prediction of scour depth as equal as the unbroken wave heights corresponding to the possible water depth at the toe of the seawall. Dean (1987) also gives a simple approach to determine the scour profile based on an equilibrium coastal profile. Powell (1987) evaluated several empirical formulae, including: the SPM rule of thumb, Dean’s approach, Herbich’s equation, Song and Schiller’s equation. However, their ability to predict wave-induced scour is both limited in scope and compounded by serious errors in their derivation. Hence, using these approaches will imply the use of a higher safety factor that leads to an extra cost for construction. A recent manual from the United Kingdom Environment Agency (Bradbury et al., 2012) gives a new empirical approach based on extensive databases involving both published laboratory data and collected field data. This manual provides conservative formulae to predict the scour depth and can be used as a preliminary approach.

Whilst both data from field observations and experimental works are valuable, there exist limitations in the approach. Indeed, field observations are generally complex to carry out and only a limited number of parameters can be measured. Experimental works offer a more controlled environment and with the advance in measurement techniques, they can provide a new insights into the physical processes at stake during the scouring process. However, experimental works can also be limited by scaling factors; moreover, full scale experiments which gives most valuable information are quite costly to carry out. However, recent efforts have been made to build large facilities for example at Deltares, Delft, Netherlands (<https://www.deltares.nl/en/facilities/delta-flume>), where a giant wave flume 300m long, 9.5m deep and 5m wide makes it possible to generate waves up to 4.5m high, overcoming some limitation related to scaling factors.

Numerical simulations may offer an interesting alternative but the simulation of



Figure 1.2: Segmental seawall failure at Dawlish, (BBC, 2014)

the wave-induced scouring process is still challenging. Indeed, it requires correct modeling of the free surface dynamics, which in this case involves a complex breaking wave process. The model must also address a possible size evolution of the scour hole which will eventually induce changes in the flow pattern. Last, it must be based on a robust algorithms and require reasonably affordable computational resources for performing full-scale simulations.

This PhD thesis aims to develop a complete numerical solver which can address the free surface dynamics, scour calculation and that will be able to couple both processes. The model is developed in OpenFOAM (Open Field Operation And Manipulation) software which is an open source Computational Fluid Dynamics (CFD) platform. This work is an extension of a previous model developed by Jacobsen (2011) and more recently Zhou (2016).

1.2 Outline of the Thesis

The manuscript thesis is composed of six chapters.

Chapter 2 gives some theoretical background about the coastal processes, wave hydrodynamics and free surface modeling. It provides a brief explanation of the physical processes in the near shore area, theoretical wave formulae for both regular and irregular waves, wave breaking, wave reflection and mass transport. A review of existing numerical methods to simulate free surface dynamics is described. In a second part, the Volume of Fluid (VOF) method which is used for wave modeling in OpenFOAM[®] code is presented. This section discusses different limits including the sharp interface two-phase method available in OpenFOAM[®], the previous interFoam solver which is based on the weighted density averaging and the gfmFoam

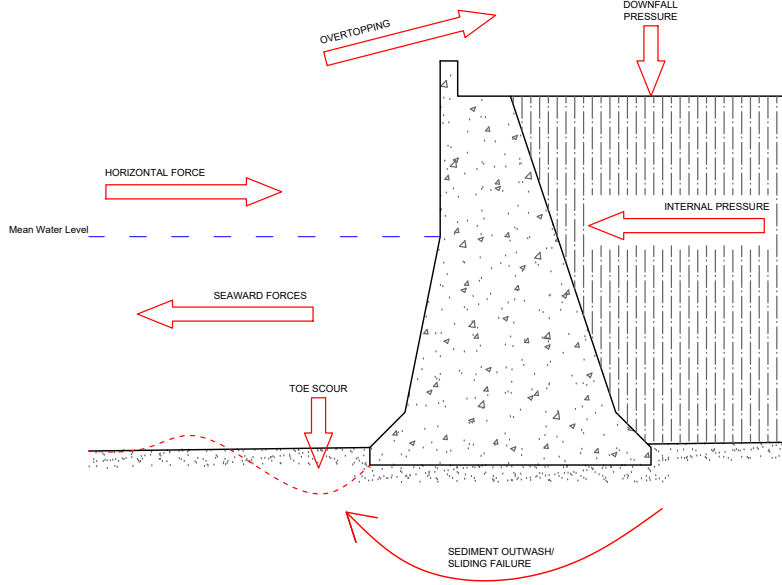


Figure 1.3: Forces acting on a seawall

which uses a sharp pressure jump condition based on the ghost fluid method. Then, a method for generating and absorbing the waves is explained. Finally, a section is dedicated to the turbulence model specifically modified for the two-phase flow solver.

Chapter 3 describes some scour implications for marine structure. Basic concepts of the sediment transport are also explained along with previous works devoted to scour at toe seawalls. The sediment transport model is based on bed-load and suspended-load calculation. The bed deformation is calculated based on the sediment continuity equation. The dynamic mesh in OpenFOAM[®] is used to update the mesh based on bed deformation calculation.

Chapter 4 is dedicated to the calibration of a numerical model that will be used to study scour at the toe of a seawall. Firstly, a sensitivity analysis is performed to analyze the influence of mesh size and numerical schemes. Secondly, different method for modeling wave reflection and absorption are compared. Then, mass transport velocities are compared to verify the mean drift in a closed domain. Fourth, the bed shear stress calculation is tested by studying the case of an oscillatory flow boundary layer. Two methods for the bed shear stress calculation is tested with different mesh sizes. Finally, a simulation is carried out where all of the aforementioned components are involved, including the free surface dynamics, the sediment transport calculation and the bed deformation module. This numerical simulation is based on the test case of the mobile bed dam break.

Chapter 5 applies the method to a wave impacting on a seawall with both flat and sloped bed. A fixed bed simulation is performed at the beginning without the bed deformation model. The hydrodynamic properties of the flow are analyzed in this test. Later the scour simulation is performed for both of the cases.

Chapter 6 provides some general conclusions and a discussion of perspectives for future work.

Chapter 2

Wave Modeling

Wave action is known as the main cause of damage to seawalls and it is important for the numerical model to reproduce the wave hydrodynamics correctly. This chapter defines the phenomena involved in coastal areas including physical properties of waves and how to model the free surface dynamics in a numerical framework. At the end of the chapter, the Volume of Fluid (VOF) model for resolving free surface dynamics is briefly described.

2.1 Coastal Process

A coast is a transitional area between land and sea. Coastal areas are known historically as one of the main development center of civilizations. As a transitional area, coasts are influenced by many hydrodynamic processes which make the coastal zone a complex system. Waves are a major force in coastal process, and are generated out at sea from either wind, tidal, tectonic or volcanic activities. Wind-generated waves are the most common type of wave. They are generated by wind stress in high seas and propagate towards the shore of islands or continents (Figure2.1).

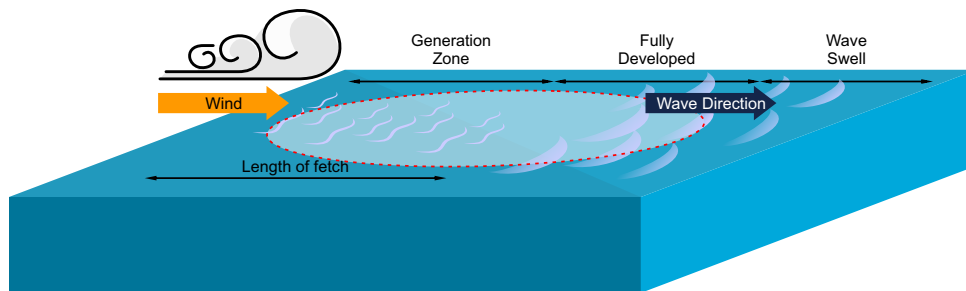


Figure 2.1: Wind-generated waves

The wind-wave characteristics depend on the wind speed, the fetch length and the wind duration. Based on these conditions, there are three type of wind-generated waves: the fetch limited, duration limited and fully developed sea wave. The fully developed sea wave is the kind where waves generated by the wind are independent

of the fetch length and of the wind duration.

Near the shore, waves interact with local bathymetry conditions. Sorensen (2005) defines, the near-shore as the area extending from deep water to mean sea water level. Then, the fore-shore is the area which is affected by wave run-up. It corresponds to the surf-zone where the complex hydrodynamical process occur and where wave breaking takes place. The main process involved in wave propagation are refraction, diffraction, shoaling and breaking.

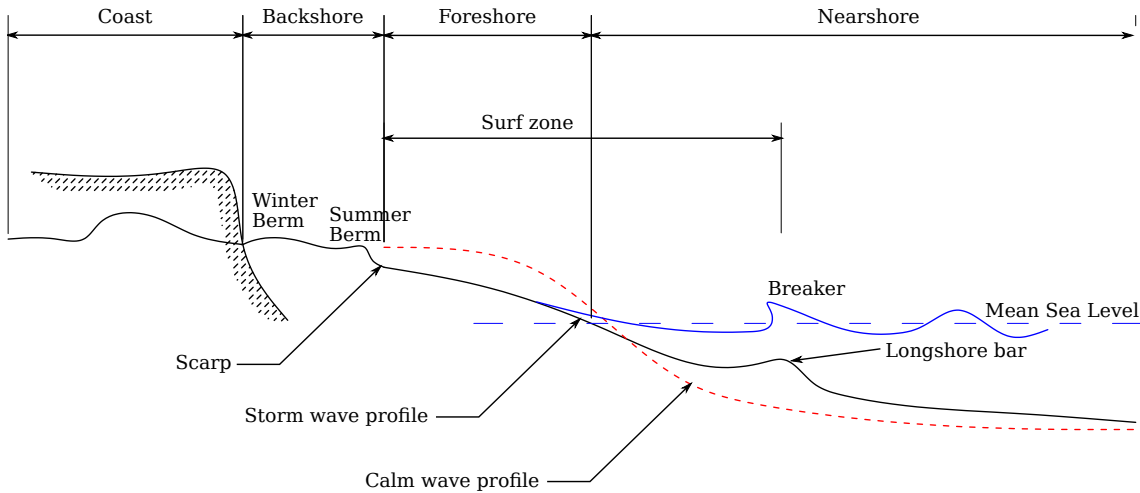


Figure 2.2: Coastal terminology (Sorensen, 2005)

Wave shoaling and refraction

Wave shoaling is the process of decreasing wave velocity and length as the depth becomes shallower. Shoaling is not associated with a change in the wave period but there is an increase in the wave height to maintain constant wave energy flux. Wave refraction induces a change in the wave direction because of the change of depth. Assuming a propagating wave, the wave celerity changes according to the water depth, being slower in shallower water. Because of refraction, the wave direction tends to approach the near shore perpendicularly. Figure 2.3 shows an idealized sea bottom contour where refraction changes the wave direction.

Wave diffraction

Waves that approach an obstacle will bend on the leeward side of the breakwater, for example when there is an island or breakwater installed. This is called the diffraction process. The diffracted wave crests behind the obstacle approximately form concentric circular arcs with a wave height decreasing exponentially with respect to the obstacle distance (Sorensen, 2005). Penney and Price (1952) modelled the diffraction of sea waves round the end of a long straight breakwater by analogy with the diffraction of light. The diffraction process is characterized by the coefficient K_d which is the ratio between the diffracted wave height and the incident wave height.

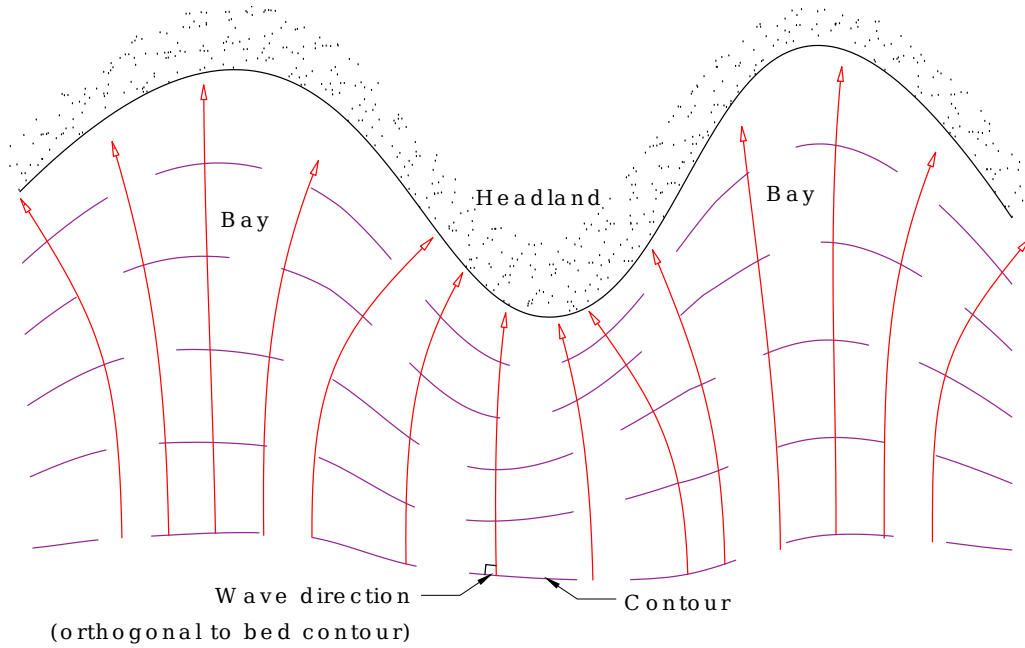


Figure 2.3: Scheme of wave refraction approaching the shore (Sorensen, 2005)

2.1.1 Coastal morphodynamics mechanism

Coastline morphodynamics is an integrated complex process involving all the hydrodynamic forces. Since the coast acts as a transitional area between land and ocean, the contributing forces may vary according to the coast morphology. For example, a coast near a river estuary has a different behaviour than a coast with plain sandy beaches. Accordingly, this feature holds true for coast with a muddy bed or which has mangrove plant along its shore. Although, all of this processes based on sediment transport occurs at the coast. The main coastal process induced by waves is generally divided into the cross-shore transport and the longshore transport (littoral drift).

Cross-shore transport

Cross-shore transport is defined as the transport of sediment with a direction normal to the coast line. It results from a complex process that occurs in the surf zone and is the main phenomenon that explains changes in the beach profile. In shallow water at the surf zone, the shoaling wave increases in height with a typical wave profile consisting of a sharp crest and a flat trough. It induces a non-linearity for the wave velocity where a higher velocity occurs under the crest and a lower one under the trough. As the wave increases its height, it eventually breaks. The breaking wave generates a bore that rushes up the coastal slope in the onshore direction, followed by a strong return offshore current called an undertow. These processes generate high levels of turbulence which maintain relatively large quantities of sediment in suspension. The cross-shore transport results from the combination of these processes.

Seasonal patterns can be observed in this process. In high wave seasons, the undertow current dominates as the result of high wave breaking. The undertow current directed offshore meets the onshore current from the non-breaking wave. A breaker bar is formed as a result of these two forces negating each other. Conversely,

in the calm wave season, the undertow is low and the onshore current moves the breaker bar to replenish the coast. These processes are described in Figure 2.4.

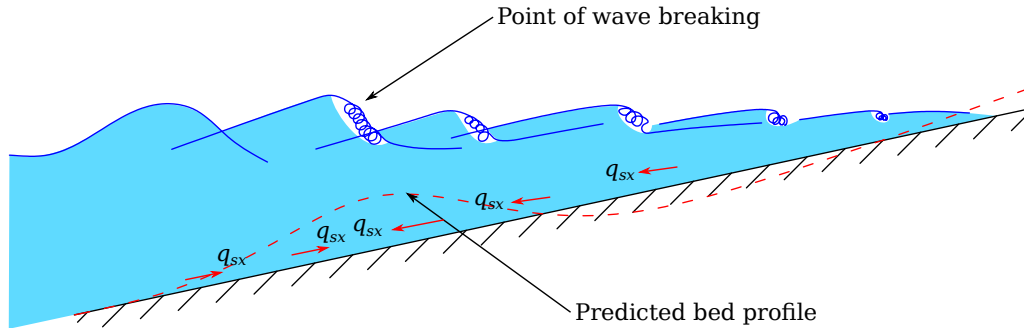


Figure 2.4: Cross-shore sediment transport pattern and breaker bar development (Fredse and Deigaard, 1992)

Long-shore transport (littoral drift)

Long-shore transport is the transport of sediment parallel to the coastline. It occurs when the wave approaches the beach at an angle. Although an oblique incoming wave from deep water will tend to bend normal to the coastline because of refraction, the wave usually breaks before it bends completely. This oblique wave induces a long-shore transport or littoral drift. The long-shore transport consists of two main motions; the saw tooth motion which is similar to the cross-shore transport, and the steady current which is parallel to the coastline, especially in the vicinity of the wave breaking, which increases sediments in suspension (Figure 2.1).

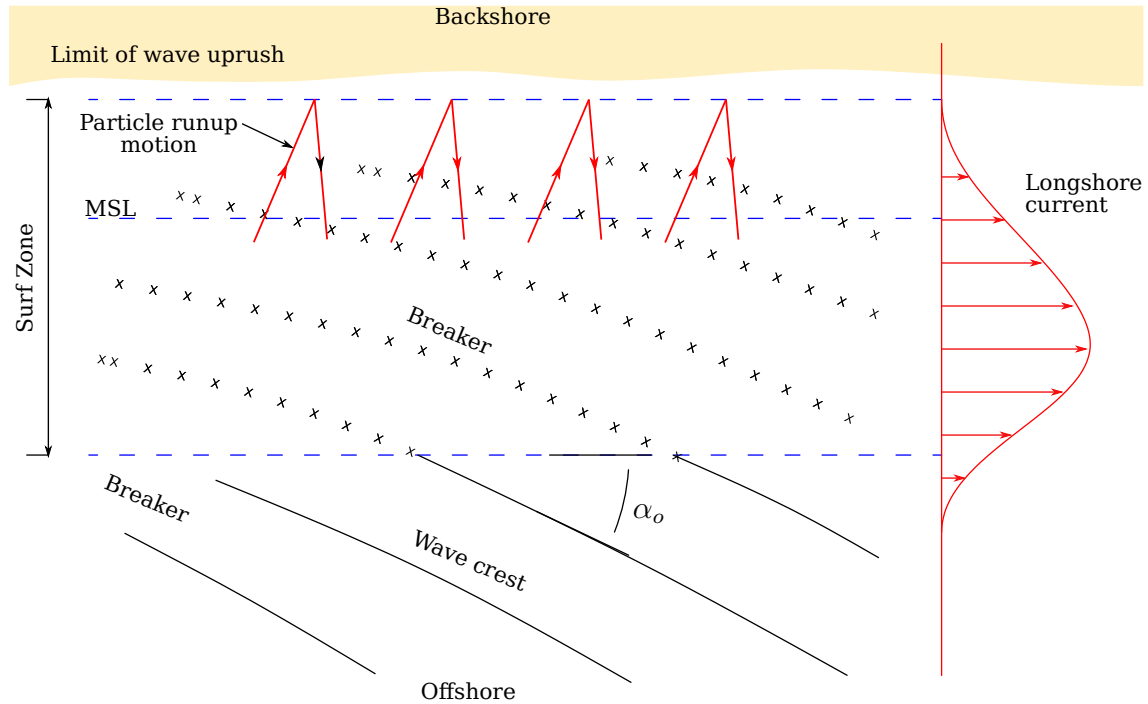


Figure 2.5: Wave induced long-shore current mechanism (Sorensen, 2005)

The long-shore transport is an important parameter that influences coastal erosion or port basin sedimentation. A well known relationship that estimates the long-shore current is given by Longuet-Higgins (1970). This equation which is included in the Shore Protection Manual (USACE, 1984) reads:

$$U_{ls} = 20.7\beta(gH_B)^{1/2} \sin(2\alpha_B) \quad (2.1)$$

where U_{ls} is the averaged long-shore current velocity, β is the coastal slope, g is gravity magnitude, H_B is the wave breaking height and α_B is the wave breaking direction. Then, the long-shore transport rate (Q_{ls}) can be estimated from the CERC (Coastal Engineering Research Center) formulae given also by US Army Coastal Engineering Research Center (USACE, 1984):

$$Q_{ls} = K \sqrt{\frac{g}{\gamma}} \frac{H_B^{5/2} \sin 2\alpha_B}{16(s-1)n} \quad (2.2)$$

where γ is the ratio of wave height to the water depth at breaking, n is the ratio of solid volume to total volume for the sediment, and s is the sediment specific gravity. K is a coefficient commonly taken as 0.32 for typical beach sands. The long-shore sediment transport greatly depends on the wave approach angle α_B , for different beach orientations the long-shore sediment transport rate can vary greatly.

Effect of man-made structures

As mentioned before, a coastline including beaches changes seasonally. However, human activities sometimes require to prevent the coastline receding, for example due to the presence of buildings or roads near the coast. Man-made protection against coastline retreat is usually composed of seawalls or revetment if not by dikes.

These structures change the pattern of the incoming waves and of the sediment transport. For example, in the presence of a seawall in the high wave season, the beach cannot deform or retreat because the seawall cuts off the sediment supply behind it. And since the wave energy is hardly dissipated, this tends to exacerbate the erosion at the toe of the seawall. The aggravation of erosion due to man-made structures is still controversial and is addressed in more detail in section 3.1.

Direct interception of the long-shore transport occurs when man-made structures are built perpendicular to the coastline. A common example is the port breakwater which stops the supply of sediments and induces erosion on the other side of the structure. However, man-made structures have also been used as protection. On an eroding beach, groyne can be built to limit the sediment movement and to prevent the coastline from erosion. However, by intercepting the long-shore sediment supply, the groyne exacerbates erosion and coastline retreat on the leeward side, so it is necessary to construct a series of groynes (figure 2.6). Other methods can also be applied including the installation of offshore (detached) breakwaters which are supposed to reduce the long-shore transport and to produce a deposit of sediments. These include more complicated process involving diffraction and refraction.



Figure 2.6: Beach protection using groynes, showing the resulting long-shore transport modification at Nusa Dua, Bali (Google Earth)

2.2 Wave hydrodynamics

In the ocean, the creation of waves and their characteristics constitute a random process. As a first approximation giving birth to the regular wave theory, the wave shape can be stated to hold a sinusoidal form. In general, two dimensionless parameters are used in the description of the wave theories, namely:

- the wave number, $k = 2\pi/\lambda$
- the wave angular frequency, $\omega = 2\pi/T$

where λ is the wave length and T is the wave period. In this section, several wave theories will be described.

2.2.1 Linear wave theory

The linear wave theory is derived from the potential flow theory, assuming a constant 2-D wave with amplitude that is small compared with the water depth and the wave length, propagating over a horizontal bed, as shown in Figure 2.7.

Following the assumption of the potential flow theory, the fluid is incompressible and irrotational:

$$\frac{\partial u}{\partial x} + \frac{\partial w}{\partial z} = 0 \quad (2.3)$$

$$\frac{\partial u}{\partial z} - \frac{\partial w}{\partial x} = 0 \quad (2.4)$$

where u and w are respectively the velocity components in the x and z direction. Based on Equation (2.3) and Equation (2.4), the velocities satisfy Laplace's equation:

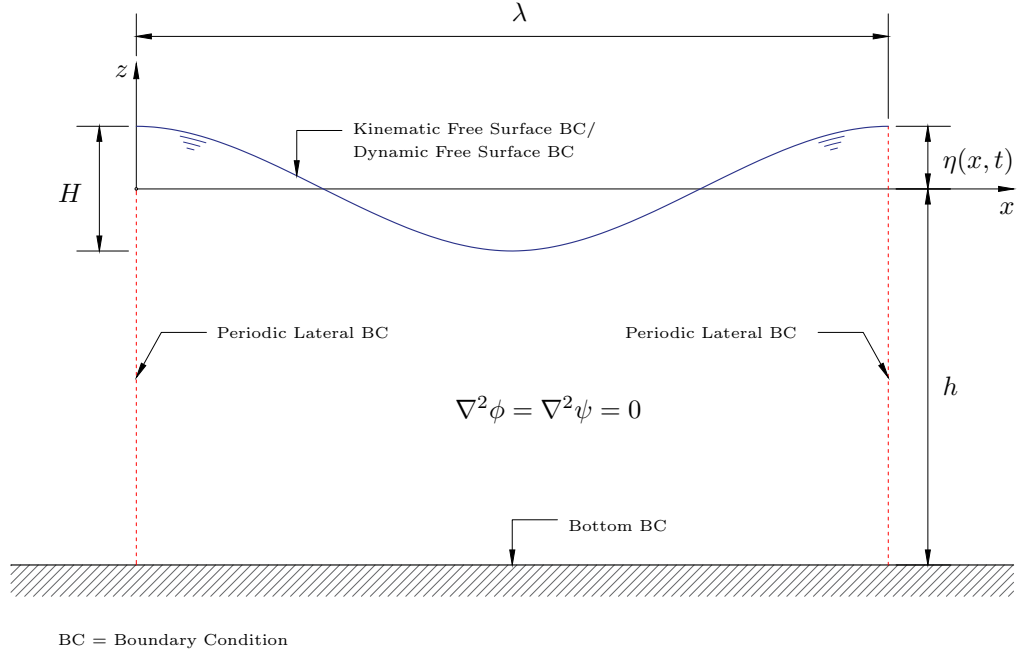


Figure 2.7: Coordinate system for propagating waves adapted from Sorensen (2005)

$$\frac{\partial^2 \phi}{\partial x^2} - \frac{\partial^2 \phi}{\partial z^2} = 0 \quad (2.5)$$

Where ϕ is velocity potential. At the bed, with the assumption of impermeable bottom, the fluid has no vertical velocity ($w = 0$). At the free surface, the free surface velocity equal the water particle velocity at the free surface, which called the kinematic boundary condition. Evaluating the boundary condition for the unknown elevation using the linear term of Taylor series gives:

$$\frac{\partial \eta}{\partial t} = u \frac{\partial \eta}{\partial x} - w \quad (2.6)$$

The Bernoulli equation for unsteady flow is given as:

$$\frac{1}{2}(u^2 + w^2) + \frac{p}{\rho} + gz + \frac{\partial \phi}{\partial t} = 0 \quad (2.7)$$

where p is the pressure, ρ the fluid density and g the acceleration due to gravity. At the free surface, the pressure is zero, then Equation (2.7) becomes:

$$\frac{1}{2}(u^2 + w^2) + gz + \frac{\partial \phi}{\partial t} = 0 \quad (2.8)$$

The boundary condition at the free surface is linearized according to the assumption of $H \ll \lambda$. $H\lambda^2/d^3$ is called the Ursell parameter. Equation (2.6) and Equation (2.8) can be rewritten:

$$\frac{\partial \eta}{\partial t} + w = 0 \quad (2.9)$$

$$g\eta + \frac{\partial\phi}{\partial t} = 0 \quad (2.10)$$

Solving the Laplace equation with the boundary condition gives the velocity potential for the small-amplitude wave theory, or Airy waves, or Stokes first order waves, which is:

$$\phi = \frac{gH}{2\omega} \frac{\cosh(k(d+z))}{\cosh kd} \sin(kx - \omega t) \quad (2.11)$$

Inserting the velocity potential into Equation (2.10), the water surface profile is consequently defines by:

$$\eta = \frac{H}{2} \cos(kx - \omega t) \quad (2.12)$$

Eliminating the water surface elevation from Equation (2.9) and Equation (2.7), the dispersion relationship reads:

$$\omega^2 = gk \tanh kd \quad (2.13)$$

The velocities within the flow are given by:

$$u = \frac{\pi H}{T} \left[\frac{\cosh k(d+z)}{\sinh kd} \right] \cos(kx - \omega t) \quad (2.14)$$

and

$$w = \frac{\pi H}{T} \left[\frac{\sinh k(d+z)}{\sinh kd} \right] \sin(kx - \omega t) \quad (2.15)$$

2.2.2 Non-linear wave theories

Due to its assumptions, linear wave theory is restricted to cases where the wave height is small compared with the water depth. In the near shore area, as the water depth decreases, the small parameter assumption for the water surface elevation is not valid anymore. Hence, a higher order solution is required to model wave properties. Other wave theories have been developed including the Stokes second order wave and the stream function theory. In fact the first order solution is just the leading term in the Stokes perturbation expansion. Higher order wave theories involve retaining higher order terms in the perturbation expansion.

Stokes second order wave

Stokes applied a perturbation approach to solve the Laplace's equation for wave propagation. Using the similar assumption as for the linear wave theory, Stokes expanded the nonlinear free surface boundary condition up to the second order using Taylor series. In fact, the Stokes method is valid for arbitrary order; it just gets very complicated to develop it at higher orders. By this approach, if the higher term is neglected, the solution will be identical to the linear wave equation given in section 2.2.1. The velocity potential is given by:

$$\phi = -\frac{Hg}{2\omega} \frac{\cosh k(h+z)}{\cosh kh} \sin(kx - \omega t) - \frac{3}{32} H^2 \omega \frac{\cosh 2k(h+z)}{\sin^4 kh} \sin 2(kx - \omega t) \quad (2.16)$$

The water surface elevation (η) is given by:

$$\eta = \frac{H}{2} \cos(kx - \omega t) + \frac{H^2 k \cosh kh}{16 \sinh^3 kh} (2 + \cosh 2kh) \cos 2(kx - \omega t) \quad (2.17)$$

The dispersion relationship is still the same as for linear wave theory (Equation 2.13). The kinematic properties for Stokes second order wave for u and w are:

$$u = \frac{H}{2} \frac{gk}{\omega} \frac{\cosh k(h+z)}{\cosh kh} \cos(kx - \omega t) + \frac{3}{16} \frac{H^2 \omega k \cosh 2k(h+z)}{\sinh^4 kh} \cos 2(kx - \omega t) \quad (2.18)$$

$$w = \frac{H}{2} \frac{gk}{\omega} \frac{\sinh k(h+z)}{\cosh kh} \sin(kx - \omega t) + \frac{3}{16} \frac{H^2 \omega k \sinh 2k(h+z)}{\sinh^4 kh} \sin 2(kx - \omega t) \quad (2.19)$$

The validity of Stokes second order wave can be described using the Ursell parameter, which is given for deep water waves by:

$$\frac{\lambda^2 H}{h^3} \ll \frac{64\pi^2}{3} \quad (2.20)$$

The Ursell parameter for shallow water waves must satisfy Equation (2.20), because in shallow water a high second order term creates a bump at the wave trough. Hence, the Ursell parameter used to ensure that the generated wave has only one crest must satisfy:

$$\frac{\lambda^2 H}{h^3} < \frac{8\pi^2}{3} \quad (2.21)$$

Figure 2.8 shows how the Stokes second order wave results from a combination of the first order component and the second order component.

Stream function wave

Stokes perturbation method can be extended to higher orders (for example 3rd and 5th order waves are used in some application), but the effort required to derive the higher order solution increases rapidly. Also, at higher order it is necessary to make assumption about the definition of parameters such as the mean water level. The stream function wave theory was developed to overcome this problem by providing a general algorithm for the N^{th} -order wave. The stream function, ψ , is defined by:

$$u = -\frac{\partial \psi}{\partial z}, w = \frac{\partial \psi}{\partial x} \quad (2.22)$$

By substituting Equation 2.22 into the irrotational flow equation (Equation 2.4), we obtain:

$$\frac{\partial^2 \psi}{\partial x^2} + \frac{\partial^2 \psi}{\partial z^2} = 0 \quad (2.23)$$

Equation (2.23) is the Laplace equation for the stream function. The stream function for progressive waves with a coordinate system moving with the wave celerity C reads:

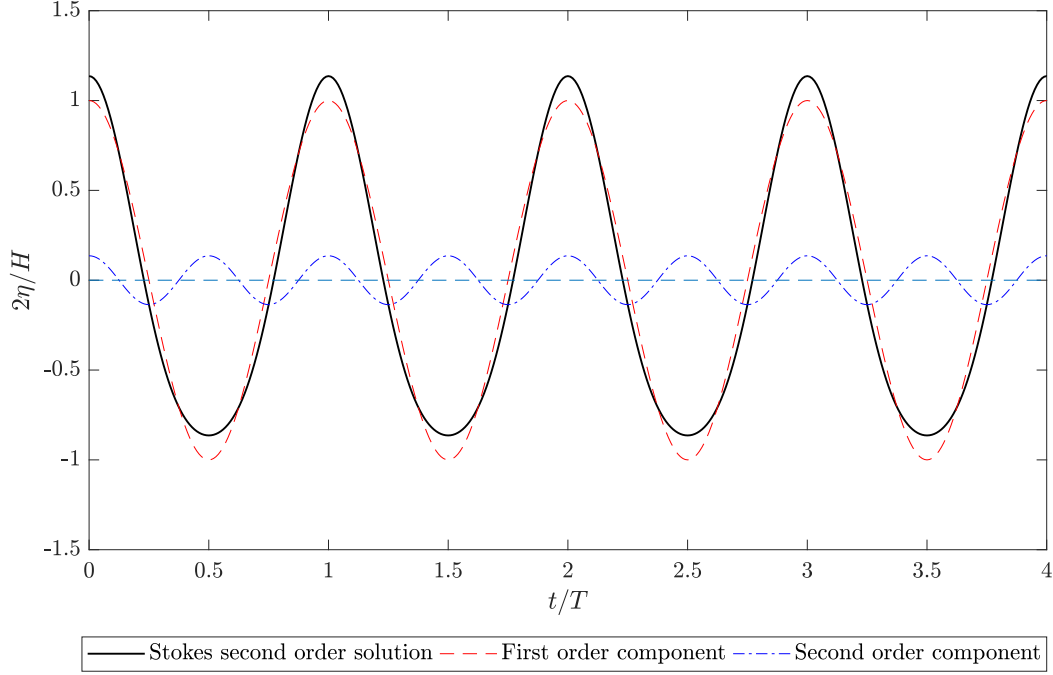


Figure 2.8: Stokes second-order waves as a combination of first and second order components from equation 2.17

$$\psi(x, z) = Cz - \frac{Hg \sinh k(h + z)}{2\omega \cosh kh} \cos kx \quad (2.24)$$

The boundary value problem for a dynamic free surface in the stream function form must satisfy:

$$\frac{1}{2} \left[\left(\frac{\partial \psi}{\partial z} \right)^2 + \left(\frac{\partial \psi}{\partial x} \right)^2 \right] + g\eta = Q \quad (2.25)$$

And the kinematic free surface boundary value is written:

$$\frac{\partial \psi}{\partial x} = -\frac{\partial \psi}{\partial z} \frac{\partial \eta}{\partial x} \quad (2.26)$$

The free surface is assumed to be a streamline and this is also the boundary condition at the bed:

$$\frac{\partial \psi}{\partial x} = 0 \quad (2.27)$$

The lateral boundary condition is written:

$$\psi(x, z) = \psi(x + L, z) \quad (2.28)$$

The N^{th} -order stream function is approximated by:

$$\psi(x, z) = Cz + \sum_{n=1}^N X(n) \sinh nk(h + z) \cos nkx \quad (2.29)$$

This equation can be solved numerically to satisfy the dynamic free surface condition. The procedure is usually solved in a discrete domain, composed of i points. The dynamic free surface boundary condition is then evaluated at every point, giving the flux Q_i which must keep constant. However, Q_i is dependent on $X(n)$, since Q_i requires the computation of $\partial\psi/\partial z$, $\partial\psi/\partial x$ and of η . Hence, an iterative procedure is used to satisfy:

$$Q_i = \frac{\left(\frac{\partial\psi}{\partial z}\right)_i^2 + \left(\frac{\partial\psi}{\partial x}\right)_i^2}{2} + g\eta_i = Q \quad (2.30)$$

Once the condition is satisfied, the values of u , w , and η can be obtained.

Validity of the wave theories

The assumptions required for the development of the wave theories show that they are not valid in all cases. As the water depth reduces, many of the assumptions are violated. The Cnoidal wave theory (Korteweg and De Vries, 1895) was developed in terms of the Jacobian elliptic integral and is more suitable for shallow water waves. Figure 2.9 shows typical shapes for several wave theories, where it can be seen that Cnoidal wave shows a flat trough. This is physically relevant since, as the wave approaches the shore, the shoaling effect causes the particle orbital motion to become rather elliptic, resulting in a flat trough. Cnoidal waves are also not irrotational. Le Méhauté (1976) provided a graphical chart to delimit the validity of the different wave theories based on the height H and the depth h (Figure 2.10). This indicates that as the wave enters the shallow water region, it tends to become steeper and at some point it will break because of the wave instability, and no wave theory will be valid to explain this process. The process of wave breaking will be explained in the next section. Investigations by Dean (1970) showed that the fifth order Stokes waves give a better representation for deep water waves, while Cnoidal wave theory works better for shallow water waves. Linear wave theory works surprisingly well for the intermediate waves. The stream function wave theory is found to work well in all conditions, even in shallow water. However, one may need to use a higher order of solution to derive the stream function wave for shallow water.

2.2.3 Solitary waves

Solitary waves are infinitely long waves which have no trough. Solitary waves can be generated in wave flume by moving the wave maker forward without return. With such a technique the transported mass of water is equal to the water volume displaced by the paddle.

The first model of this type of waves were provided by Boussinesq (1871) and Rayleigh (1876). The water elevation, η is given by:

$$\eta = a \operatorname{sech}^2 \sqrt{\frac{3}{4} \frac{a}{h^3}} x \quad (2.31)$$

The wave celerity is given by:

$$c = \sqrt{\frac{gh}{1-A}} \quad (2.32)$$

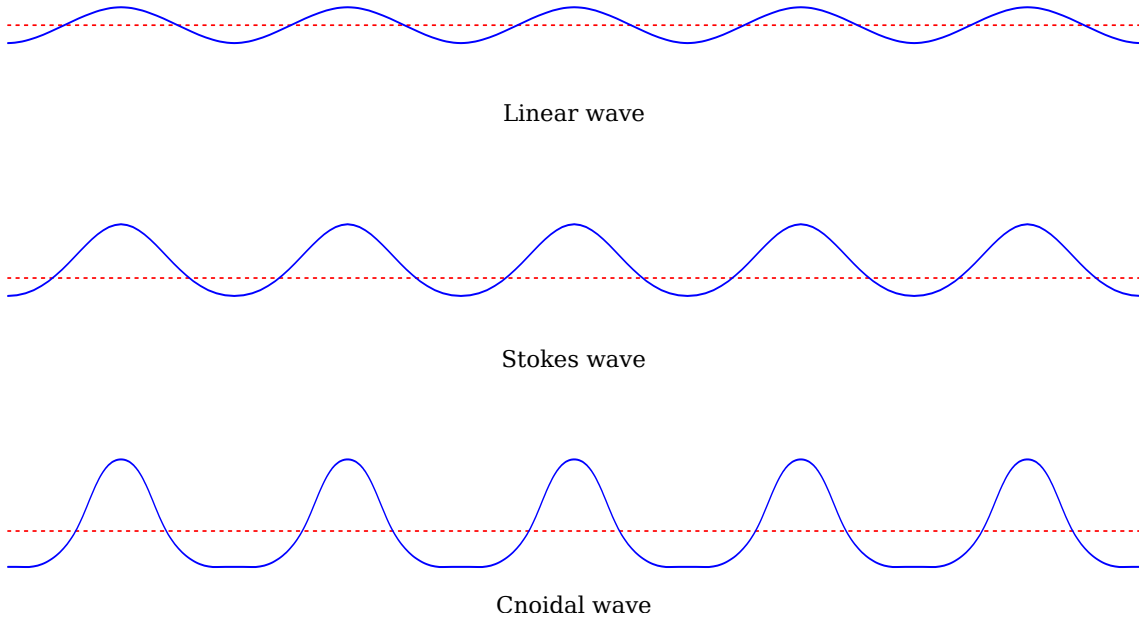


Figure 2.9: Typical profiles for several wave theories

with $A = a/h$ which is a dimensionless amplitude. The water volume transported for an infinitely long solitary wave is given by:

$$V_{\infty} = 4d\sqrt{\frac{ah}{3}} \quad (2.33)$$

For engineering application, the statement of an infinite length for the solitary wave is reduced to a length equal to 95% of the wave crest volume and is used as an equivalent wave length λ . Then, λ reads:

$$\lambda = \frac{2.12h}{\sqrt{a/h}} \quad (2.34)$$

The Boussinesq solitary wave is considered as a lower order solution, which is valid for small A . A higher order approximation is described by Chappellear (1962) and Grimshaw (1971). Grimshaw expanded the solution up to third order, which was also proposed by Wu (2014):

$$\eta = h \left(AS^2 - \frac{3}{4}A^2S^2T^2 + A^3 \left(\frac{5}{8}S^2T^2 - \frac{101}{80}S^4T^4 \right) \right) \quad (2.35)$$

with $S = \cosh -1Kx$ and $T = \tanh -1Kx$. K is the boundary outskirts decay coefficient equal to:

$$K = \sqrt{\frac{3H}{4h^3}} \left(1 - \frac{5}{8}A + \frac{71}{128}A^2 \right) \quad (2.36)$$

The wave celerity is then given by:

$$c = \sqrt{gh} \left(1 + \frac{1}{2}A - \frac{3}{20}A^2 + \frac{3}{56}A^3 \right) \quad (2.37)$$

2.2.4 Irregular waves

All the previous wave theories consider the motion of regular periodic waves. However, in practice, regular waves occur relatively infrequently. Indeed regular waves

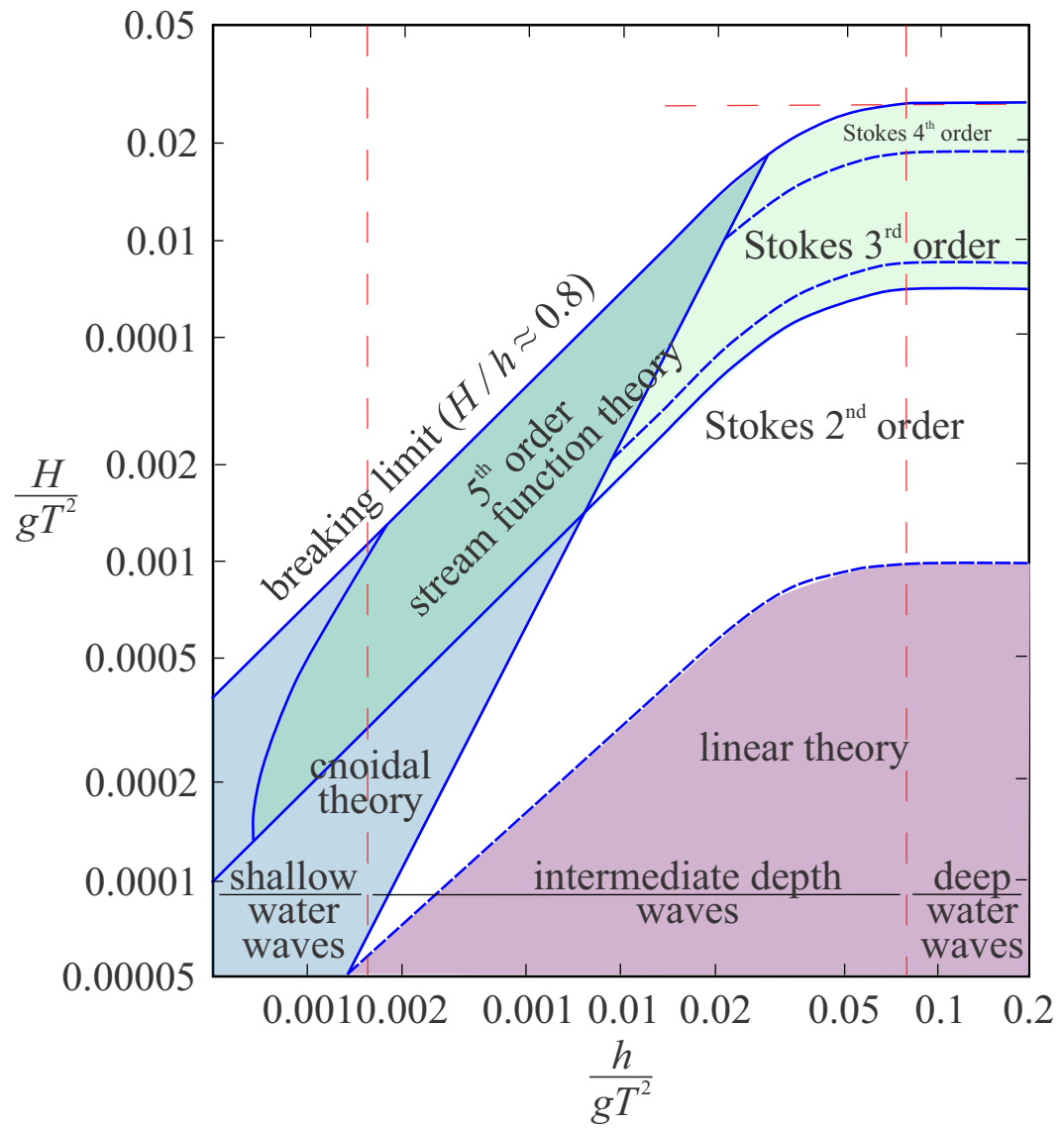


Figure 2.10: Wave theory regimes (Méhauté, 1976)

often only occur in coastal regions because of filtering by refraction of irregular deep ocean waves. The idea for the irregular wave theory is to represent the real condition as a combination of regular waves. The simplest combination could be seen in bichromatic waves where two waves with different parameters combine to form a single entity. Real waves are composed of waves of many frequencies and a decomposition is required to obtain a representative wave condition.

To model the wave components in real field, a statistical approach is often used. The wave is assumed to be composed of a set of periodic waves, each with a different frequency and amplitude. A spectral representation of the wave is then made possible. The probability density function for the wave heights agrees well with a Rayleigh distribution (Longuet-Higgins, 1952):

$$p_r(H) = \frac{2H}{H_{rms}^2} \exp^{-(H/H_{rms})^2} \quad (2.38)$$

where H_{rms} is the root mean square wave height written:

$$H_{rms} = \sqrt{\sum_{i=1}^N \frac{H_i^2}{N}} \quad (2.39)$$

where N is the number of waves occurring in a single event. Another common approach is to construct a wave spectral density model based on many wave components. The wave energy density depends on the wave height:

$$S = \frac{1}{8} \rho g H^2 \quad (2.40)$$

The general form of the spectral model equation is:

$$S(f) = \frac{\alpha}{f^5} \exp^{-\beta/f^4} \quad (2.41)$$

where α and β are the shape and the scale coefficients and $f = 1/T$ is the wave frequency.

Pierson-Moskowitz spectrum

The Pierson-Moskowitz spectrum was created from recorded data collected in the north Atlantic ocean. The power spectral density is given by:

$$S(f) = \frac{\alpha g^2}{(2\pi)^4 f^5} \exp^{-0.74(g/2\pi W f)^4} \quad (2.42)$$

where W is the wind speed measured at an elevation of 19.5 m and α is a shape coefficient equal to 8.1×10^{-3} . The Pierson-Moskowitz spectrum assumes that the sea condition corresponds to a fully-developed sea.

JONSWAP Spectrum

The Jonswap spectrum (Hasselmann et al., 1973) was derived to model wave climate in the North Sea with fetch and duration limited seas; this correspond to the majority of conditions world wide. It is derived from the Pierson-Moskowitz spectrum:

$$S(f) = \frac{\alpha g^2}{(2\pi)^4 f^5} \exp^{-1.25(f_p/f)^4} \gamma^a \quad (2.43)$$

with

$$\begin{aligned} a &= \exp^{-(f-f_p)^2/2\omega^2 f_p^2} \\ \omega &= 0.07 \text{ for } f < f_p \\ \omega &= 0.09 \text{ for } f \geq f_p \end{aligned}$$

The recommended value for coefficient γ in the JONSWAP spectrum is equal to 3.3. The coefficient α and the peak frequency f_p are given by:

$$\alpha = 0.076 \frac{gF}{W^2}^{-0.22} \quad (2.44)$$

$$f_p = \frac{3.5g}{W} \frac{gF}{W^2}^{-0.33} \quad (2.45)$$

Figure 2.11 shows a comparison between the Pierson-Moskowitz and the JONSWAP spectrum. The JONSWAP spectrum peak is higher than the peak in the Pierson-Moskowitz spectrum.

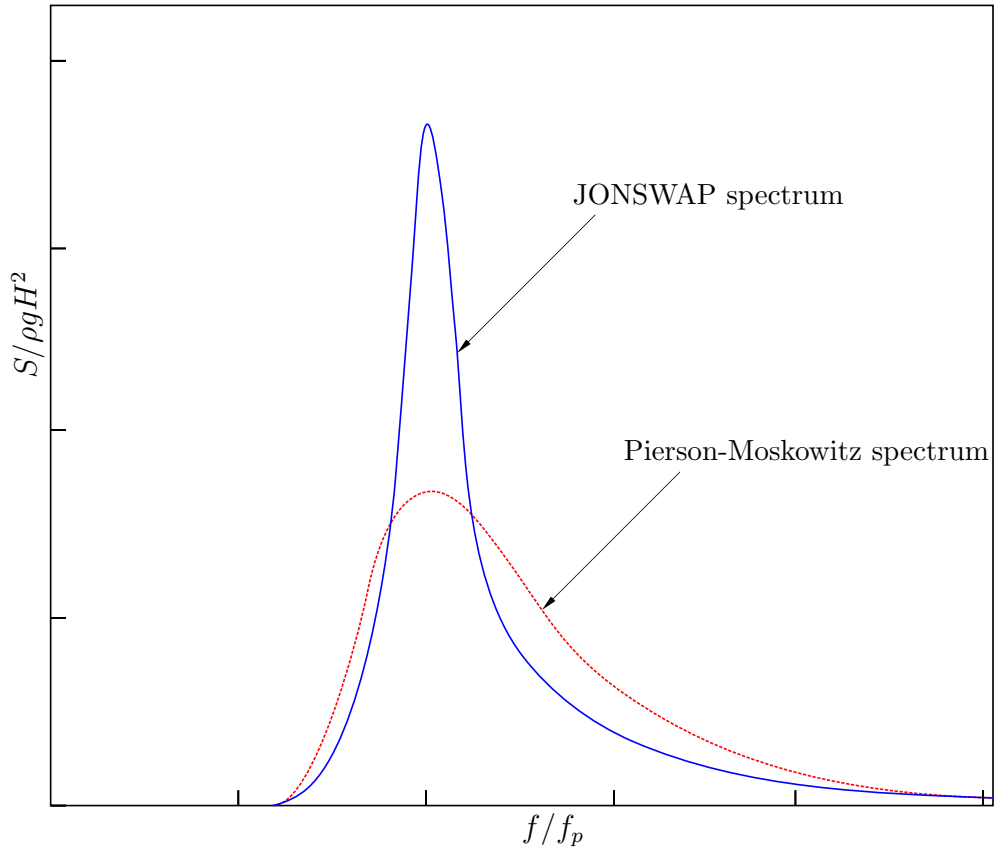


Figure 2.11: Comparison between the Pierson-Moskowitz and the JONSWAP spectrum

2.2.5 Wave reflection and standing wave

When a wave hits an obstacle, the wave reflection occurs because of the need to satisfy the impermeability condition on the obstacle boundary. The two waves propagating in opposite directions will superimpose. If the wave crest from the incident wave meets a trough of the reflected wave, the contributions from the two component cancel each other, and as a consequence the water surface elevation will be equal to the still water level. The location where this occurs is called the node. Conversely, if two wave crests or two troughs coincide, the water surface displacement will be doubled. This location is denoted anti-node. The velocity potential for a standing wave is given by:

$$\phi = \frac{gH}{\omega} \left[\frac{\cosh k(h+z)}{\cosh kh} \right] \cos kx \sin \omega t \quad (2.46)$$

Solving equation 2.46 the same way as for the progressive wave shows that the water surface elevation η is equal to:

$$\eta = H \cos kx \sin \omega t \quad (2.47)$$

with x the distance from the reflecting obstacle. The water particle in a standing wave moves constantly with the same manner ($c = 0$), which is why the term standing wave is used, to distinguish from progressive waves. As shown in figure 2.12, a water particle at the anti-node moves vertically while the particle at the node moves horizontally.

The reflection rate of the wave is described by the reflection coefficient $C_r = \frac{H_r}{H_i}$, where H_r is the reflected wave height. A partially reflected wave creates a partial standing wave and this occurs quite often for waves reflected from a seawall. In the partial standing wave, the node is not at the still water level. The incident and reflected wave heights, H_i and H_r , can be determined from the surface elevation of the standing wave:

$$H_i = \eta_{env,max} + \eta_{env,min} \quad (2.48)$$

$$H_r = \eta_{env,max} - \eta_{env,min} \quad (2.49)$$

where the *env* indicates the envelope of water surface elevation. Hence, the reflection coefficient, C_r , can be defined by:

$$C_r = \frac{\eta_{env,max} + \eta_{env,min}}{\eta_{env,max} - \eta_{env,min}} \quad (2.50)$$

In the experiments, the envelope is found by using a wave gauge which moves slowly along the tank in front of the reflecting obstacle.

2.2.6 Breaking waves

A wave approaching shallow water shows a decrease in its celerity and a reduction in its wave length. The wave height then increases to compensate for the wave deceleration to maintain the energy flux. As the water becomes shallower, the wave height continues to increase until the wave becomes unstable, leading to wave breaking. Wave breaking can be predicted from the ratio between the wave height and its depth, denoted as the breaking parameter, γ_B . The value of γ_B is between 0.78 to

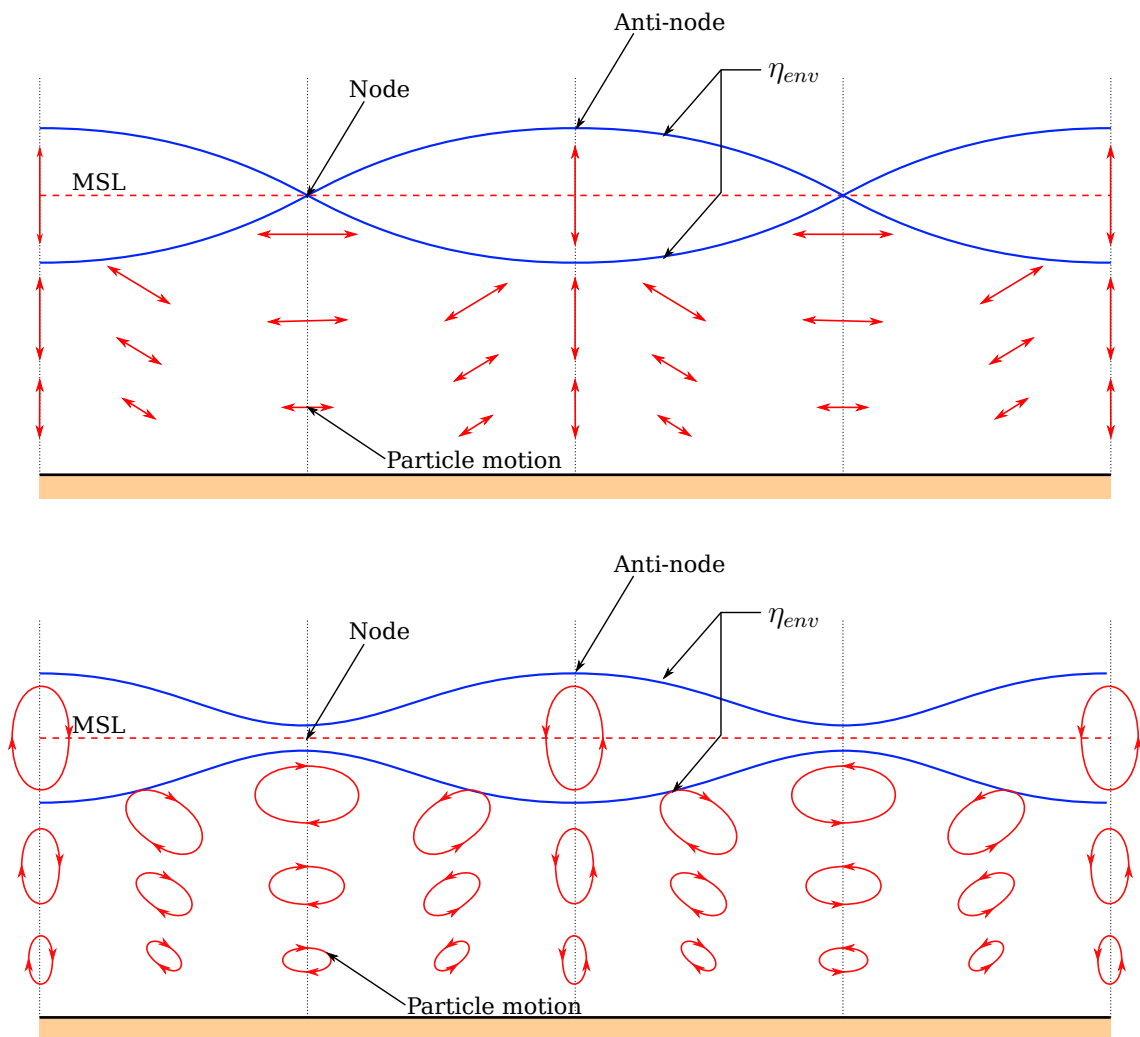


Figure 2.12: Standing wave description with particle trajectories (a): full standing wave ; (b): partial standing wave

0.8, and is the limiting value for using wave theories in figure 2.10. Observations on site shows that there exist three typical wave breaking regimes:

- Spilling breakers
Spilling breakers are characterized by the forward slope of the wave top that becomes unstable. A plume of water and air bubbles slide down the slope from the crest. Spilling breakers occur on very mild slope.
- Plunging breakers
Plunging breakers occur when the crest of the wave moves forward and falls down into the trough in front, as a single structured mass of water or a jet. The impact of the jet generates a splash-up of water which continues the breaking process and creates large coherent vortices. The jet can reach the sea bed and stir up considerable amounts of sediment.
- Surging breakers
In surging breakers, the foot of the steep front is unstable and rushes forward the shore, making the wave crest disappear. This occurs on a steep beach slope.

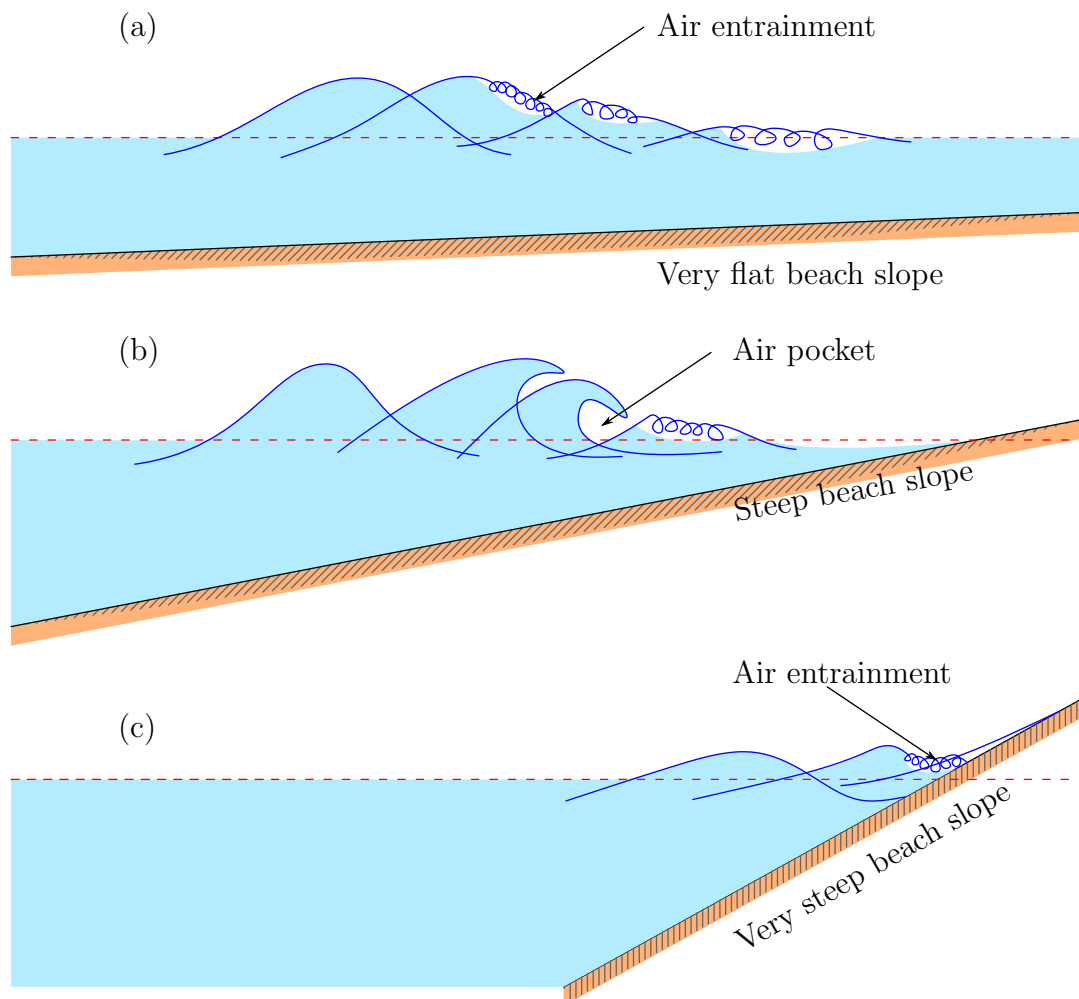


Figure 2.13: Wave breaker types; (a) spilling breaker, (b) plunging breaker, (c) surging breaker

Galvin (1968) described a fourth type of breaker called a collapsing breaker, which is a combination of plunging and surging breakers. Physically, wave breaking is a complex process and really hard to understand. The identification of the wave

breaker type however can be determined using the wave geometry as described by Galvin (1968). Using the work of Galvin, Battjes (1974) introduced the surf similarity parameter ξ , which is the ratio between the beach slope and the square root of the wave steepness. The wave steepness can be calculated for the deep water wave H_0 or for the breaking wave H_B knowing the wave length λ_0 :

$$\xi_0 = \frac{\tan \beta}{\sqrt{\frac{H_0}{\lambda_0}}} \quad , \quad \xi_B = \frac{\tan \beta}{\sqrt{\frac{H_B}{\lambda_0}}} \quad (2.51)$$

where $\tan \beta$ is the beach slope. Based on Galvin's experimental data, Battjes gave some properties for each wave breaker type:

$$\begin{aligned} \text{Spilling breakers :} & \quad \xi_0 < 0.5 \quad \text{or} \quad \xi_b < 0.4 \\ \text{Plunging breakers :} & \quad 0.5 < \xi_0 < 3.3 \quad \text{or} \quad 0.4 < \xi_b < 2.0 \\ \text{Surging breakers :} & \quad 3.3 < \xi_0 \quad \text{or} \quad 2.0 < \xi_b \end{aligned} \quad (2.52)$$

2.2.7 Mass transport in water waves

Particle trajectories under progressive waves are not closed as can be seen in Figure 2.14. This results from the difference between particle velocities at the wave crest and the wave trough. The forward displacement of particles under the wave crest exceeds the reverse displacement of particles under the wave trough, causing a net drift of water which is known as the Stokes Drift or mass transport phenomenon. This could be explained from the formulation of small amplitude waves, where in the interface of the wave crest and of the wave trough, the horizontal velocity is obtained using a Taylor series decomposition. By neglecting the second order contribution, the surface velocities can be approximated by

$$\begin{aligned} u(x, \eta) &= u(x, 0) + \eta \frac{\partial u}{\partial z} \Big|_{z=h} \\ &= \frac{g a k}{\omega} \frac{\cosh k(z)}{\cosh k h} \Big|_{z=h} \cos(\omega t - k x) + \frac{g a^2 k^2}{\omega} \tanh k h \cos^2(\omega t - k x) \\ &= \frac{g a k}{\omega} \cos(\omega t - k x) + a^2 k \omega \cos^2(\omega t - k x) \end{aligned} \quad (2.53)$$

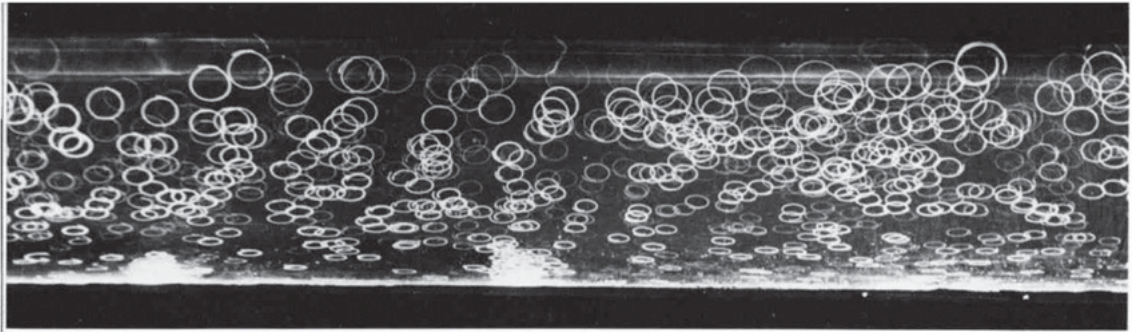


Figure 2.14: Particles trajectory under progressive wave (Van Dyke, 1982)

The Stokes drift formulation does not consider the shear stress at the sea bed since in this formulation, the sea depth is supposed to be high and the shear stress at seabed very small. In shallower water, the bed shear stress increases and its effect

become more apparent. Furthermore, in a closed system (for example for a propagating wave in a tank), the transported mass of water must be compensated by a return flow. In the work by Russell (1957), Longuet-Higgins described a formulation of mass-transport velocity in a closed channel that considers the effect of viscous force in the bottom boundary layer.

$$U_m = \frac{a^2 \omega k}{4 \sin^2 kh} \left[2 \cosh(2kh(\mu - 1)) + 3 + kh \sinh 2kh(3\mu^2 - 4\mu + 1) + 3 \left(\frac{\sinh 2kh}{2kh} + \frac{3}{2} \right) (\mu^2 - 1) \right]. \quad (2.54)$$

where μ is the relative depth described as $(z/h - 1)$. Thanks to experiments, Russell (Russell and Osorio, 1957) showed that the theoretical solution is in a good agreement with the experiment data. Carter (Mei and Liu, 1972) also performed experiments in a closed channel. Figure 2.15 shows the results compared with the Longuet-Higgins solution. All of these experiments (Russell and Osorio, 1957; Mei and Liu, 1972; Dyke and Barstow, 1981;) show a good agreement at the bottom of channel with the experiments, while some differences were observed at the surface (Sleath, 1984).

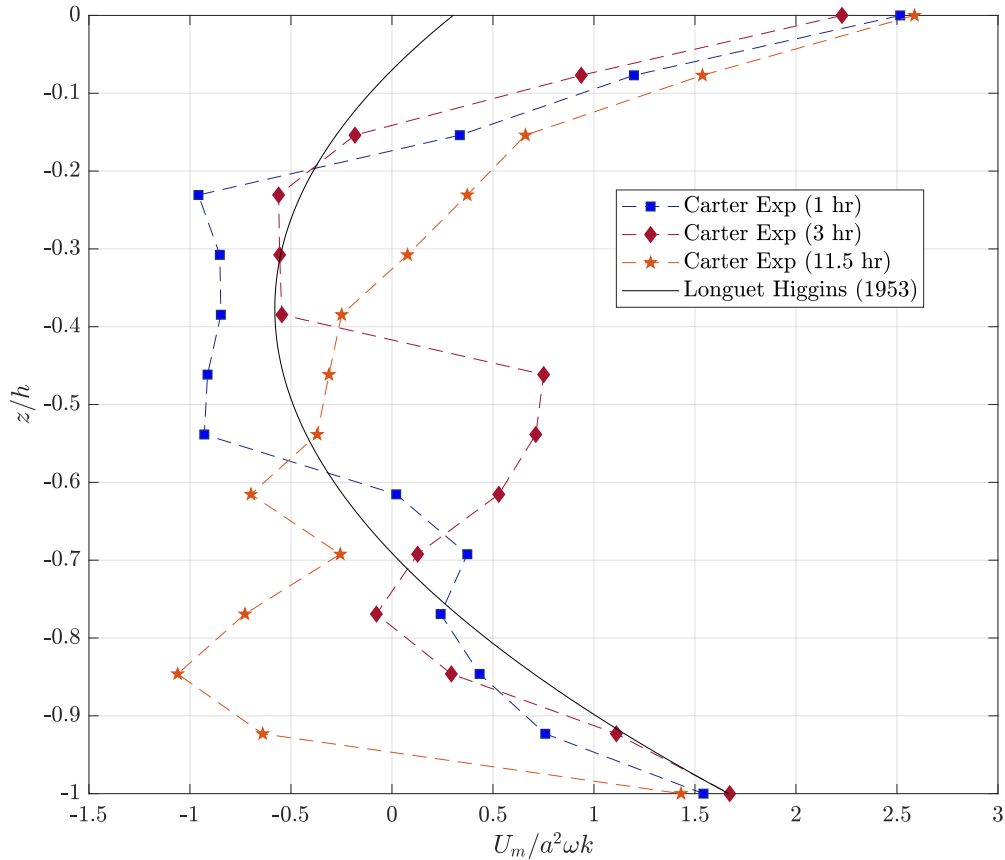


Figure 2.15: Mass Transport Velocity with $kh = 0.79$ and $a^2 \omega k = 0.378$ ($H = 2.0$, $T = 1.01$) (Mei and Liu, 1972)

2.2.8 Wave Boundary Layer

The information about wave boundary layer is important in order to determine the bed shear stress in wave induced flow. It has distinct differences if compared with the boundary layer in a steady flow. In steady flow conditions, the boundary layer growth depends greatly on downstream distance in the flow, such that, sufficiently far down stream from the the origin of the boundary layer, the flow becomes fully-developed. The wave boundary layer, however, is periodical, which mean the velocity direction changes over time. Hence, the boundary layer thickness depends on the wave period. A common approach for understanding the wave boundary layer is to assume an oscillatory flow, driven by a pure oscillatory velocity stream. This can be produced, for example, by oscillating flow in a U-shaped tube. Assuming the free stream velocity U_∞ varies with angular frequency σ as:

$$u_0 = U_\infty \sin \sigma t \quad (2.55)$$

the solution for the horizontal component of the laminar wave boundary layer velocity for $u = 0$ at $z = 0$ and $u \rightarrow u_0$ at $z \rightarrow \infty$ can be written:

$$u(z) = U_\infty \sin(\omega t) - U_\infty \exp -\frac{z}{\delta_\infty} \sin \left(\omega t - \frac{z}{\delta_\infty} \right) \quad (2.56)$$

where δ_∞ is the laminar boundary layer thickness known as Stokes length, defined as:

$$\delta_\infty = \sqrt{\frac{2\nu}{\omega}} \quad (2.57)$$

The bed shear stress for a laminar oscillatory flow is calculated as:

$$\tau_b = \rho \frac{\nu U_\infty}{\delta_\infty} [\sin(\omega t) + \cos(\omega t)] \quad (2.58)$$

The analytical solution shows a phase shift of 45° of the boundary layer velocity ahead of the free stream velocity. This analytical solution showed a good agreement with the measurements performed by Sleath (1968) and 1976 in experiments. However, in turbulent flow condition, the phase shift is smaller than 45° (figure 2.16).

In turbulent flow, no analytical solution is available and the bed shear stress calculation is usually based on the wave friction factor, f_w , which is defined as:

$$f_w = \frac{2\tau_b}{\rho U_\infty^2} \quad (2.59)$$

A range of experimental results are available for estimating f_w – see, for example, Kamphuis (1975).

2.3 Wave numerical modelling

2.3.1 Free surface modelling

The free surface dynamics is one of the main important processes in modelling waves. The most used formulation today to address this boundary value problem is based on the depth integrated version of the Navier-Stokes equation, which is known as Saint Venant equation for the 1D problems and extended to 2D problems by means

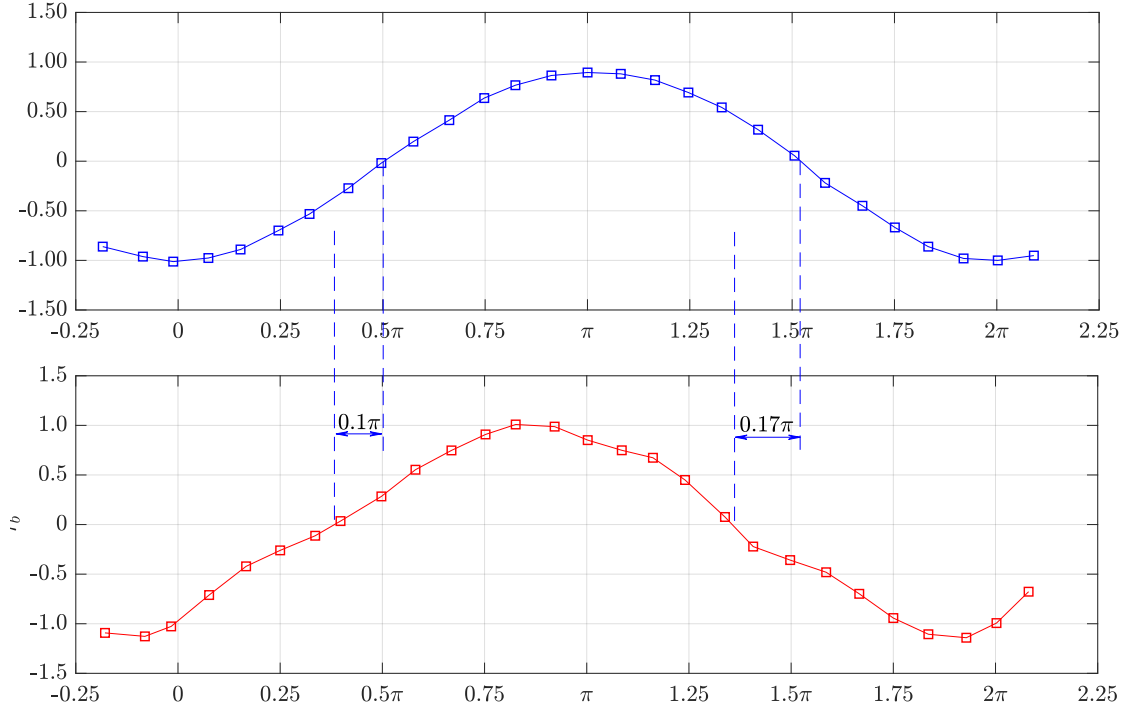


Figure 2.16: Time variation of the bed shear stress for turbulent flow over relatively small roughness element (Jonsson and Carlsen, 1976)

of the Shallow Water Equation (SWE). The free surface is calculated as the total water column height and the pressure distribution as a hydrostatic stress. However, because the fluid velocity vector is averaged over the depth, this method is not capable of solving the complex free surface dynamics. BOUSS-2D model (Nwogu and Demirbilek, 2001) is another approach for depth integrated waves modelling application. It is based on the Boussinesq equation (Boussinesq, 1871) to model the nonlinear-dispersive waves. While the SWE approach does not involve a frequency dispersion, the Boussinesq equation allows it, even though it still uses the depth integrated approach. It is capable of modelling wave transformation processes such as: shoaling, refraction, diffraction and full or partial reflection. The model also incorporates a wave breaking model, however it does not resolve the dynamic free surface due to depth averaging statements.

The use of the full Navier-Stokes equations to solve the free surface dynamic problem is possible, for example by using linear wave theory or by solving the potential flow model. In the case of problems involving ocean waves, the capability of these approaches to address wave breaking phenomena is limited. Numerical approaches for solving complex free surface dynamics have undergone much development over the last few years. In general, there are two types of model for free surface dynamics that will be investigated: the Eulerian method and the Lagrangian method.

The Eulerian methods are based on a fixed observation of the fluid movement passing through the computational grid. In these methods, the free surface is usually assumed as a scalar quantity, and is not straightforwardly defined. One of the

pioneering method related to this case is the marker and cell (MAC) approach by Harlow and Welch (1965). This method assigns a marker in the grid (cell) which is filled by the fluid. The free surface motion is then computed by moving the marker based on the fluid velocity. The MAC approach has inspired other methods, which use a scalar properties to define the free surface. However, this method needs high computational resources and does not perform well if there exists a stagnation point in the flow. The extension of the MAC method is the volume of fluid method (VOF) by Hirt and Nichols (1981). Instead of using a marker, the fluid is marked as its fractional volume in the computational cell, with 1 corresponding to a cell full of water and 0 to an empty cell. This eliminates the problem of the high number of markers used in the MAC method, and also conserves the fluid mass because the volume fraction is only advected based on fluid velocity. The level set method (LS) is the other common method for addressing free surface dynamic problems. It uses a signed distance function to determine the free surface, where the free surface corresponds to a signed function equal to zero. The signed function is not bounded unlike the VOF which need to be between 0 to 1. This is the advantage of the level set method which does not need an additional numerical scheme to bound the solution. However, the mass conservation may not be satisfied, hence some additional terms are added in the equations to improve the conservation of the fluid mass.

The Lagrangian method is based on a moving observation of the fluid, which means that the observer accompanies the fluid movement. Here, the solution of the free surface dynamics, if processed through a mesh based calculation, needs a re-meshing to follow the free surface position. The task may become quite difficult if the free surface dynamics are very complex since the mesh can be distorted and as a result the calculations may not converge. This explains why the meshless method is very popular to solve this problem. The smoothed particle hydrodynamics method (SPH) (Gingold and Monaghan, 1977) which was initially developed to solve astrophysical problems in a three-dimensional open space was later adapted for fluid dynamics simulations. The moving particle semi-implicit method (MPS) by Koshizuka and Oka (1996) which solves the governing equations using the semi-implicit prediction correction rather than the fully explicit solution in the SPH method was derived from the SPH method. The advantage of meshless or particle based methods is that the definition of the free surface is straightforward since directly represented by the position of the fluid particles. Moreover, it can handle large and complex deformations of the free surface.

Both of these methods were successfully used to simulate free surface dynamics problems. The VOF method is used in many free surface flow applications, especially wave breaking simulations (Lin and Liu, 1998; Guignard et al., 2001; Hieu et al., 2004) which have also been modelled using the SPH method (Monaghan, 1994; Rogers and Dalrymple, 2005). While both approaches give reasonable results, SPH needs higher computational resources if a high resolution is required. The detailed formulation used in free surface simulations is described in section 2.4.

2.4 Volume of Fluid Method

The hydrodynamic model used in this thesis is based on the VOF method, which is an Eulerian-mesh based approach for solving the flow of a two-phase immiscible

fluid. The model is developed based on the interFoam solver in OpenFOAM[®]. It uses the conditionally averaged momentum formulation, which is known to induce an additional acceleration of the lighter fluid phase (Vukčević et al., 2017). Another approach proposed by Vukčević et al. (2017) based on the ghost fluid method is also described.

2.4.1 Conditionally averaged volume of fluid method

The existing two-phase immiscible fluid flow solver in OpenFOAM[®] solves the incompressible continuity and Reynold-averaged Navier Stokes equations as one mixture of fluid:

$$\nabla \cdot \mathbf{U} = 0 \quad (2.60)$$

$$\frac{\partial(\rho\mathbf{U})}{\partial t} + \nabla \cdot (\rho\mathbf{U}\mathbf{U}) = -\nabla p - \rho\mathbf{g} + \nabla \cdot \boldsymbol{\tau} + \mathbf{f}_\sigma \quad (2.61)$$

where ρ is the fluid mixture density, \mathbf{U} is the velocity vector, p is the total pressure, \mathbf{g} is the gravity vector, $\boldsymbol{\tau}$ is the stress tensor and \mathbf{f}_σ is the effect of surface tension. The pressure is defined as the modified pressure, p_d , which is obtained by removing the hydrostatic pressure:

$$p_d = p - \rho\mathbf{g} \cdot \mathbf{x} \quad (2.62)$$

where \mathbf{x} is the position vector. This modified pressure is then introduced into equation 2.61 for the pressure gradient term:

$$\begin{aligned} \nabla p_d &= \nabla p - \nabla(\rho\mathbf{g} \cdot \mathbf{x}) \\ &= \nabla p - \rho\mathbf{g} - \mathbf{g} \cdot \mathbf{x} \nabla \rho \end{aligned} \quad (2.63)$$

The stress tensor $\boldsymbol{\tau}$ then reformulated for efficient numerical evaluation following Rusche (2003):

$$\begin{aligned} \nabla \cdot \boldsymbol{\tau} &= \nabla \cdot (\mu_e (\nabla \mathbf{U} + (\nabla \mathbf{U})^T)) \\ &= \nabla \cdot (\mu_e \nabla \mathbf{U}) + \nabla \cdot (\mu_e (\nabla \mathbf{U})^T) \\ &= \nabla \cdot (\mu_e \nabla \mathbf{U}) + (\nabla \mathbf{U}) \cdot \nabla \mu_e + \mu_e \nabla (\nabla \cdot \mathbf{U}) \\ &= \nabla \cdot (\mu_e \nabla \mathbf{U}) + (\nabla \mathbf{U}) \cdot \nabla \mu_e \end{aligned} \quad (2.64)$$

where μ_e is the effective viscosity with $\mu_e = \rho(\nu + \nu_T)$. Combining equation 2.63 and equation 2.64 into equation 2.61 gives:

$$\frac{\partial(\rho\mathbf{U})}{\partial t} + \nabla \cdot (\rho\mathbf{U}\mathbf{U}) = -\nabla p_d - \mathbf{g} \cdot \mathbf{x} \nabla \rho + \nabla \cdot (\mu \nabla \mathbf{U}) + (\nabla \mathbf{U}) \cdot \nabla \mu + \mathbf{f}_\sigma \quad (2.65)$$

The volume fraction α is defined as the fraction of the cell volume which is filled with water, hence it is defined as:

$$\alpha = \begin{cases} 1, & \text{if the cell is filled with water} \\ 0 < \alpha < 1, & \text{in the interface region} \\ 0, & \text{if the cell is filled with air} \end{cases} \quad (2.66)$$

Herein, any physical property Φ is given by:

$$\Phi = \alpha\Phi_1 + (1 - \alpha)\Phi_0 \quad (2.67)$$

the subscripts 1 and 0 are related to the physical properties of water and air respectively. The transport of the volume fraction is defined as a passive advection induced by the fluid velocity, \mathbf{U} :

$$\frac{\partial\alpha}{\partial t} + \alpha\nabla \cdot \mathbf{U} = 0 \quad (2.68)$$

The compression of the interface is given by adding an artificial compression term in equation 2.68 as described by Rusche (2003):

$$\frac{\partial\alpha}{\partial t} + \alpha\nabla \cdot \mathbf{U} + \nabla \cdot (\mathbf{U}_r\alpha(1 - \alpha)) = 0 \quad (2.69)$$

\mathbf{U}_r is the compressive velocity which is only active at the interface. Indeed, the multiplier $\alpha(1 - \alpha)$ is equal to zero in the non-interface region. The solution of the continuity and momentum equations are obtained using the velocity-pressure coupling (Issa, 1986), as specifically described for OpenFOAM[®] by Jasak (1996). Vukčević (2016) found that this method induces an additional acceleration in the lighter fluid also known as a spurious velocity, which is particularly significant when there is a high density ratio as in the water-air case. It comes from the imbalance between the modified pressure gradient, ∇p_d , and the density gradient, $\nabla\rho$.

2.4.2 Ghost fluid method

Vukčević et al. (2017) assumed the governing equations as those for a single phase fluid which gives:

$$\nabla \cdot \mathbf{U}_i = 0 \quad (2.70)$$

$$\frac{\partial\mathbf{U}_i}{\partial t} + \nabla \cdot (\mathbf{U}_i\mathbf{U}_i) - \nabla \cdot (\nu_{e,i}\nabla\mathbf{U}_i) = -\frac{1}{\rho_i}\nabla p_i + \mathbf{g} \quad (2.71)$$

The subscript i denotes the fluid index, $\nu_{e,i}$ is the kinematic viscosity, p_i is the pressure and \mathbf{g} is the gravity. ρ_i is assumed constant for incompressible flow. For convenience, β_i is introduced as the inverse of density, $\frac{1}{\rho_i}$ and a modified pressure $p_{d,i}$ is introduced:

$$-\beta_i\nabla p_i + \mathbf{g} = -\beta_i\nabla p_i + \nabla(\mathbf{g} \cdot \mathbf{x}) = -\beta_i\nabla \left(p_i - \frac{\mathbf{g} \cdot \mathbf{x}}{\beta_i} \right) = -\beta_i\nabla p_{d,i} \quad (2.72)$$

Substituting equation 2.72 into equation 2.71, the momentum equation for incompressible single phase flow becomes:

$$\frac{\partial\mathbf{U}_i}{\partial t} + \nabla \cdot (\mathbf{U}_i\mathbf{U}_i) - \nabla \cdot (\nu_{e,i}\nabla\mathbf{U}_i) = -\beta_i\nabla p_{d,i} \quad (2.73)$$

Assuming that equation 2.73 works for the whole system, for the two-phase flow the index i is removed, which gives the equation following Vukčević et al. (2017):

$$\frac{\partial\mathbf{U}}{\partial t} + \nabla \cdot (\mathbf{U}\mathbf{U}) - \nabla \cdot (\nu_e\nabla\mathbf{U}) = -\beta\nabla p_d \quad (2.74)$$

Equation 2.74 is valid for both of the phases, however it does not hold for the free surface.

Free surface jump condition

The existence of different phases at the free surface is addressed by introducing a jump condition. The approximation of the jump condition is summarized in Vukčević et al. (2017):

- The velocity field is continuous even between different phases;
- The surface tension is neglected considering the scale of the problem;
- The tangential stress balance assumes a continuous effective viscosity;
- There is a pressure jump in the free surface because of a jump in density.

The jump condition is introduced into the equations through the use of brackets [...]. The sign convention following the ghost fluid method is: $-$ is for small distances from the lighter phase, $+$ is for small distances for the heavier phase, Γ is at the free surface. The kinematic jump condition at the free surface is given by:

$$[\mathbf{U}] = \mathbf{U}^- - \mathbf{U}^+ = 0, \mathbf{U} \in \Gamma \quad (2.75)$$

Equation 2.75 states that the velocity field across the interface is continuous. The dynamic pressure jump condition and the pressure gradient jump condition is given by:

$$[p_d] = -\frac{1}{\beta} \mathbf{g} \cdot \mathbf{x} \quad (2.76)$$

$$[\beta \nabla p_d] = 0 \quad (2.77)$$

This jump condition is then applied in a finite volume discretization near the free surface for the dynamic pressure and density. This discretization method will be explained briefly in Appendix B, and for further details the reader can refer to Vukčević (2016) and Vukčević et al. (2017).

2.4.3 Wave generation and absorption

One main important force in coastal and ocean problems usually comes from waves. When generating waves in a confined environment, such as in a physical laboratory or in a numerical model, it is necessary to take into account waves absorption to reduce the reflections at the boundaries of the domain, boundaries which may not exist on site. In numerical approaches, there are different methods for addressing the absorption of waves. Three methods are considered here: body force method, relaxation zone and dynamic absorption. The wave generation, however is only available and described in the relaxation zone method and in the active wave absorption method.

Body force dissipation based on velocity field

The idea of this method is to introduce a damping body force with a magnitude which depends on the velocity field and the location of the grid cell within the studied domain. The damping body force, f_d is in fact a linear wave damping or a quadratic wave damping. The linear wave damping is described by:

$$f_{d,l} = \rho C_{d,l} \mathbf{U} \quad (2.78)$$

and for quadratic wave damping:

$$f_{d,q} = \rho C_{d,q} |\mathbf{U}| \mathbf{U} \quad (2.79)$$

C_{damp} is the damping coefficient which varies in space. A smooth blending function is used to avoid a sudden increase of the damping force to avoid reflection at the entrance to the damping zone. Choi and Yoon (2009) give a combination of both approaches using a blending function defined by the damping coefficient:

$$f_{d,m} = \rho (C_{d,l} + C_{d,q} |\mathbf{U}_z|) f_b(x) \mathbf{U}_z \quad (2.80)$$

where \mathbf{U}_z is the vertical component of the velocity and $f_b(x)$ is the spatial blending coefficient with $f_b(x=0) = 0$ and $f_b(x=\lambda_d) = 1$. λ_d is the damping zone length. Perić and Abdel-Maksoud (2016) give a practical approach to determine the damping coefficient.

For the linear wave damping, $C_{d,l}$ is given as:

$$C_{d,l} = \Psi_l \sigma \quad (2.81)$$

where $\Psi_l = \pi$, σ is the wave frequency and $\lambda_d = 2\lambda$.

For the quadratic wave damping, $C_{d,q}$ is given as:

$$C_{d,q} = \Psi_q \lambda^{-1} \quad (2.82)$$

where $\Psi_q = 2\pi \cdot 10^2$ and $\lambda_d = 2\lambda$.

Relaxation zone

The relaxation zone uses a blending function to impose the wave field in the computational domain. Jacobsen et al. (2012) implemented the relaxation zone method in a toolbox called waves2foam, which is available as an open source extension in OpenFOAM®. The relaxation zone acts as a sponge layer, which uses a source term to dissipate the wave, modifying the wave field into the desired target function. It is similar to the approach of Mayer et al. (1998). This application can also be used at the wave generation boundary, because the target function can be associated to the propagating wave field.

The blending function involves the weighting coefficient, β_R , and appears explicitly in \mathbf{U} and α :

$$\mathbf{U} = (1 - \beta_R) \mathbf{U}_{target} + \beta_R \mathbf{U}_{model} \quad (2.83)$$

$$\alpha = (1 - \beta_R) \alpha_{target} + \beta_R \alpha_{model} \quad (2.84)$$

The weighting coefficient of the blending function is given by:

$$\beta_R = 1 - \frac{\exp(\chi_R^{3.5}) - 1}{\exp(1) - 1} \quad (2.85)$$

where χ_R is the relative distance, defined as $(x - x_{start})/(x_{end} - x_{start})$. The value of β_R ranges between 0 at the outer boundary of the relaxation zone and 1 at the inner boundary in contact with the studied system. Figure 2.17 shows the implementation of the relaxation zone in a wave tank.

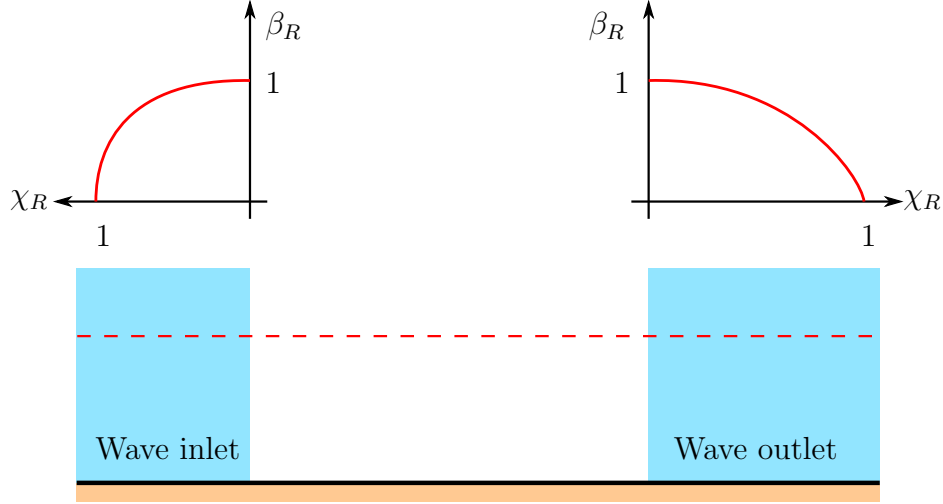


Figure 2.17: Relaxation zone weight across the wave tank

Active wave absorption

The body force method and the relaxation zone method both need an extra domain to dissipate the wave energy, which increases the required computational resources. The active wave absorption method uses a similar approach which can also be used in a physical model test. In a physical model, the wave maker movement takes into account the measured feedback to avoid the re-reflection of incoming wave. The wave absorption method is based on the work of Schäffer and Klopman (2000) and was developed for three types of problems: 2D, quasi-3D and 3D. In OpenFOAM[®], it was implemented by Higuera et al. (2013) in the IHFoam package.

The 2D active wave absorption is based on the shallow water theory, where the velocity along a water column is constant. The velocity field relationship can be derived:

$$Uh = c\eta \quad (2.86)$$

Assuming a shallow water regime, the wave celerity c is given by $c = \sqrt{gh}$. The condition at the boundary is modified in order to cancel the incoming wave field with an opposite correcting velocity, U_c :

$$U_c = -\sqrt{\frac{g}{h}}\eta_R \quad (2.87)$$

with η_R the free surface corresponding to reflected wave. The 2D active wave absorption works for waves perpendicular to the boundary, hence it allows the tangential

component of the wave to propagate. The quasi-3D approach is developed to absorb the oblique wave. The method involves a modification of equation (2.87) by projecting the calculated correcting velocity onto the wave direction. The 3D method calculates the mean horizontal velocity with its mean direction. This velocity is then decomposed according to the normal and tangential direction of the boundary. The total expected modulus, U_{calc} of the velocity is calculated from equation 2.87:

$$|U_{calc}| = \sqrt{\frac{g}{f}} \eta_R \quad (2.88)$$

The decomposition of U_{calc} gives:

$$U_{calc}^2 = U_c^2 + U_{tg}^2 \quad (2.89)$$

Hence, the correction velocity is described as:

$$U_c = \sqrt{U_{calc}^2 - U_{tg}^2} \quad (2.90)$$

The implementation of the active wave generation is similar to the relaxation zone method, by setting the velocity, \mathbf{U} , and the volume fraction, α , at the model boundary. The value of the velocity and of the volume fraction is taken from the wave theory. The wave generation boundary can include an active absorption condition by correcting the inlet velocity.

2.4.4 Turbulence modelling and bed shear stress calculation

The wave breaking usually generates high levels of turbulence and this aspect must be taken into account in the model. Resolving the turbulence in a direct numerical simulation and large eddy simulation requires a huge amount of computational resources, hence the Reynold-averaged (RANS) approach is generally used. The incompressible two-equation $k - \omega$ SST is used based on Menter (1994):

$$\frac{\partial k}{\partial t} + \nabla \mathbf{U} k = P_k - \beta^* \omega k + \nabla \cdot [(\nu + \sigma_k \nu_t) \nabla k] \quad (2.91)$$

$$\frac{\partial \omega}{\partial t} + \nabla \mathbf{U} \omega = \frac{\gamma}{\nu_t} G - \beta \omega^2 + \nabla \cdot \left[\left(\nu + \sigma_\omega \frac{k}{\omega} \right) \nabla \omega \right] + 2(1 - F_1) \frac{\sigma_{\omega,2}}{\omega} \nabla k \cdot (\nabla \omega)^T \quad (2.92)$$

$$\begin{aligned} P_k &= \min(G, 10\beta^* k \omega) \\ G &= \nu_t \nabla \mathbf{U} (\nabla \mathbf{U} + \nabla \mathbf{U}^T) \\ \nu_t &= \frac{a_1 k}{\max(a_1 \omega, S F_2)} \end{aligned} \quad (2.93)$$

here k is the turbulence kinetic energy, P_k is the production term of k , ν is the kinematic viscosity, ν_t is the turbulence kinematic viscosity, ω is the specific dissipation rate, S is the mean rate of strain tensor, β^* and a_1 are coefficients which are equal respectively to 0.09 and 0.31. The $k - \omega$ SST uses a blending function, F_1 and F_2 . The blending function is involved in σ_k , σ_ω , β and γ , for arbitrary variable ϕ such as:

Table 2.1: Default value for $k - \omega$ SST model coefficient

| ϕ | σ_k | σ_ω | β | γ |
|----------|------------|-----------------|---------|----------|
| ϕ_1 | 0.850 | 0.500 | 0.075 | 0.553 |
| ϕ_2 | 1.000 | 0.856 | 0.083 | 0.440 |

$$\phi = F_1\phi_1 + (1 - F_1)\phi_2 \quad (2.94)$$

The default value for each variable is given in table 2.1 as found in Devolder et al. (2017). The existing turbulence model implementation in OpenFOAM[®] is generic, hence no two-phase systems can be addressed. It generates high levels of turbulence at the free surface, because the phase difference leads to a high velocity gradient and the model assumes that a high shear is induced at the free surface region. The high turbulence intensity generates a high turbulence viscosity which is able to dissipate the wave. However, this does not agree with experimental observations because for a free surface flow between water and air, shear only occurs in a small layer of flow and can hardly generate a high turbulence. This problem was reported by several authors such as Mayer and Madsen (2001), Liu and Garcia (2008) and Jacobsen and Fredsøe (2011).

A different approach is used in this work. A buoyancy based correction in the free surface region is introduced as proposed by Devolder et al. (2017). The density, ρ , is included in the equation and a buoyancy term, G_b , is added into the turbulence kinetic energy equation. The resulting equation reads:

$$\frac{\partial \rho k}{\partial t} + \nabla \rho \mathbf{U} k = \rho P_k + G_b - \rho \beta^* \omega k + \nabla \cdot [\rho (\nu + \sigma_k \nu_t) \nabla k] \quad (2.95)$$

$$\begin{aligned} \frac{\partial \rho \omega}{\partial t} + \nabla \rho \mathbf{U} \omega = & \frac{\gamma}{\nu_t} \rho G - \rho \beta \omega^2 + \nabla \cdot \left[\rho \left(\nu + \sigma_\omega \frac{k}{\omega} \right) \nabla \omega \right] \\ & + 2(1 - F_1) \rho \frac{\sigma_{\omega,2}}{\omega} \nabla k \cdot (\nabla \omega)^T \end{aligned} \quad (2.96)$$

$$G_b = -\frac{\nu_t}{\sigma_t} \nabla \rho \cdot \mathbf{g} \quad (2.97)$$

$\sigma_t = 0.85$ is a scalar to weight the buoyancy influence on the equation. The buoyancy term is only active near the free surface region, where the gradient of density is not zero. Near the wall the boundary condition as described by Jacobsen and Fredsøe (2011) is used:

$$\omega_{nw} = \frac{u_f}{\sqrt{\beta^* \kappa \Delta y}} \quad (2.98)$$

and for k :

$$k_{nw} = \frac{u_f^2}{\sqrt{\beta^*}} \quad (2.99)$$

2.4.5 Bed shear stress calculation

Several methods are available to calculate the bed shear stress. The bed shear stress for a turbulent flow can be described as:

$$\tau_b = -\rho(\nu_t + \nu)\nabla\mathbf{U} \quad (2.100)$$

This method is applicable for small cell sizes, where the velocity gradient can be evaluated correctly. Another method consists in using the wall function to obtain the friction velocity. Based on the wall function, the boundary layer flow is divided into a viscous sub-layer and a logarithmic layer (figure 2.18). The wall function formulation uses several dimensionless parameters:

$$y^+ = \frac{yu_f}{\nu} \quad (2.101)$$

$$u^+ = \frac{u_{tg}}{u_f} \quad (2.102)$$

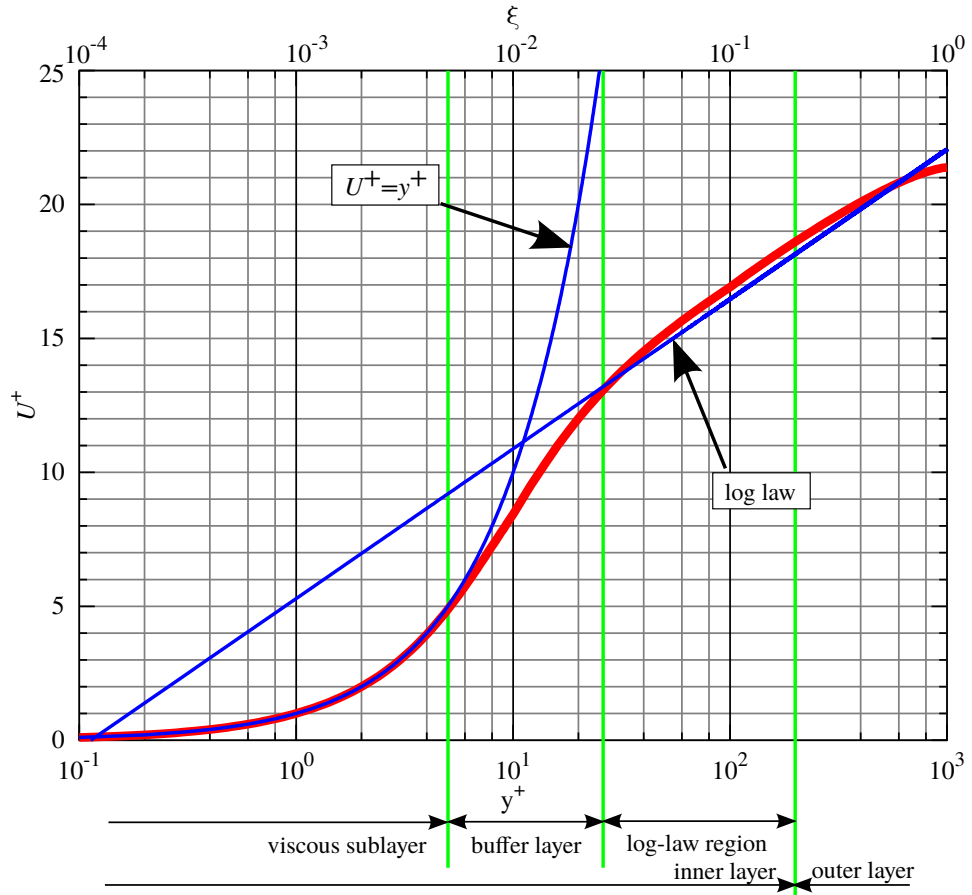


Figure 2.18: Velocity profile according the wall function

y^+ is the dimensionless wall distance, u^+ is the dimensionless velocity, y is the distance from the wall, and u_{tg} is the tangential velocity. In the viscous sub layer, the viscous force dominates the flow and a linear relationship of u^+ and y^+ is defined such as:

Table 2.2: k_s estimation based on sediment grain diameter (Sleath, 1984)

| | |
|------------------------|--------------------|
| Acker-White (1973) | $k_s = 1.25d_{35}$ |
| Einstein (1950) | $k_s = d_{65}$ |
| Engelund-Hansen (1967) | $k_s = 2d_{65}$ |
| Hey (1979) | $k_s = 3.5d_{84}$ |
| Kamphuis (1975) | $k_s = 2d_{90}$ |
| Mahmood (1971) | $k_s = 5.1d_{84}$ |

$$u^+ = y^+ \\ u_f = \sqrt{\frac{u_{tg}\nu}{y}} \quad (2.103)$$

This is approximately valid for $y^+ < 5$. The logarithmic layer starts at $y^+ > 30$ and the friction velocity for a smooth wall is defined as in a logarithmic form:

$$u^+ = \frac{1}{\kappa} \ln y^+ + 5.5 \\ \frac{u_{tg}}{u_f} = \frac{1}{\kappa} \ln \frac{yu_f}{\nu} + 5.5 \quad (2.104)$$

Equation 2.104 is non-linear, hence an iterative method is required to calculate the friction velocity. Between $5 < y^+ < 30$, there is no established relationship for the friction velocity. However, the two formulations intersect at $y^+ = 11$. In this model, $y^+ = 11$ is used as the boundary for the formulation used between $y^+ = 5$ and $y^+ = 30$. If y^+ is less than 11 equation 2.103 is used and for $y^+ > 11$ equation 2.104 is used. For rough walls, the u^+ value is calculated based on the roughness height:

$$u^+ = \frac{1}{\kappa} \ln \frac{y}{z_0} \quad (2.105)$$

Here z_0 is the roughness length defined as $k_s/30$ with k_s the Nikuradse roughness coefficient. k_s is estimated based on the sediment grain diameter. Several relationships are available for estimating k_s , as explained in table 2.2. $k_s = 2.5d_{50}$ is frequently used (Raudkivi, 1998).

As described in section 2.2.8, the calculation of the bed shear stress in an oscillatory flow is based on the wave friction factor, f_w . While there exist graphical results based on experiments by Kamphuis (1975), in numerical models this method is not practical. Hence, an generalized expression is used (Rijn, 2007):

$$f_w = e^{-6+5.2(a/k_s)^{-0.19}} \quad (2.106)$$

with a :

$$a = \frac{u_b T}{2\pi} \quad (2.107)$$

where in this case, u_b is the maximum free stream velocity near the bed.

2.5 Conclusion

In this chapter, a brief explanation of the hydrodynamic processes in coastal areas were described. Several methods to model the free surface dynamics were also mentioned. In particular, two well known methods to model systems where waves occur were reported: the smoothed particle hydrodynamic (SPH) method using the mesh-less lagrangian framework and the volume of fluid (VOF) method using a fluid volume approach in an eulerian framework. They are both capable of modelling the complex free surface dynamics and are already used in many coastal engineering applications.

In this work, the VOF model from foam-extend OpenFOAM[®]4.0 is used because of its robustness and suitability for large scale simulations. In particular, two types of VOF solvers are studied: the interFoam solver based on the conditionally averaged method and gfmFoam (Vukčević et al., 2017) based on the ghost fluid method.

Chapter 3

Sediment Transport Modeling

This chapter describes the modeling of sediment transport. First, the general process of sediment transport and its effects on marine structures and the environment are introduced. Then, the numerical solution of such a problem is developed together with its limits.

3.1 Effects of scour on marine structures

Marine structures are often exposed to extreme weather conditions which are expected to become worse due to the climate change. Scour is a major concern when designing such structures since it affects the foundations of the structures and as a consequence their stability. The scouring process in the marine environment is influenced by many factors especially the driving forces arising from waves and currents.

Scour is generally a result from a non-balanced sediment transport process. It occurs when the supply of sediments is smaller than the transport rate of sediments away from the observation area. Sediment transport is commonly characterized by three different processes:

- A bed load transport which consists in a transport of material that stays in contact with the bed during the transport process ;
- A suspended load which consists in a transport of material that moves with the flow without continuous contact with the bed, as a result of agitation by the fluid turbulence
- A wash load which consists in a transport of very fine material which is normally not represented in the bed

In calculations of sediment transport, the wash load is often neglected.

3.1.1 Sediment transport process

The lift and movement of grains on the bed is determined by a threshold value described by Shields (Shields, 1936) as the Shields parameter. This movement depends on the shear stress at the sea bed and is due to friction forces between the fluid and the grain of the seabed.

$$\theta_c = \frac{\text{force}}{\text{resistance}} = \frac{\tau_c d^2}{(\rho_s - \rho_w)gd^3} = \frac{\tau_c}{(\rho_s - \rho_w)gd} \quad (3.1)$$

θ_c is known as the critical Shields parameter, τ_c is the critical shear stress, ρ_s and ρ_w are respectively the density of the grain and of the water, and d is the grain diameter. The critical Shields number can also be described using the critical friction velocity $u_{f,c}$, given $\tau_c = \rho u_{f,c}^2$:

$$\theta_c = \frac{u_{f,c}^2}{(s-1)gd} = f(Re_*) = f\left(\frac{u_{f,c}d}{\nu}\right) \quad (3.2)$$

where Re_* is the particle Reynolds number and s is the grain specific gravity (relative to water density). Re_* indicates whether the grain protrudes into the turbulent boundary layer or stays within the viscous sub-layer. It differs from the normal Reynolds-number and gives no indication about the flow characteristics of the flow as a whole (which is usually turbulent). Van Rijn (1984) replaced the Re_* parameter by introducing a dimensionless particle diameter d^* given as:

$$d^* = d \left[(s-1) \frac{g}{\nu^2} \right]^{1/3} \quad (3.3)$$

with ν the kinematic viscosity of water. Soulsby (1997) introduced an equation for calculating the critical Shields number based on the dimensionless particle diameter:

$$\theta_c = \frac{0.3}{1 + 1.2d^*} + 0.055(1 - \exp^{-0.02d^*}) \quad (3.4)$$

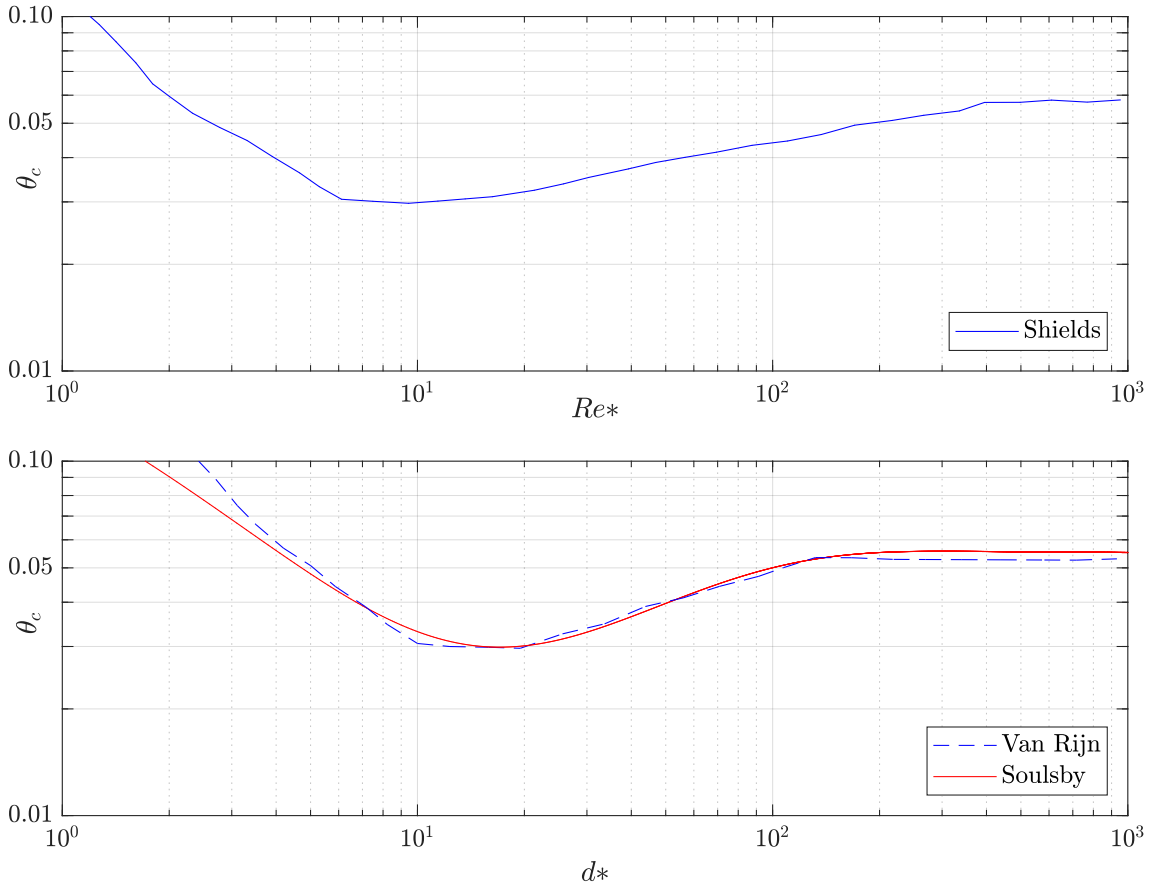


Figure 3.1: Critical shear stress according to Shields (top), van Rijn and Soulsby equation (Soulsby, 1997) (bottom) (Schierack, 2003)

Figure 3.1 shows the critical Shields number given by Shields (1936) in terms of Re_* , and the models of van Rijn (1984) and Soulsby (1997). On the other hand, Einstein (1950) developed a theoretical approach for predicting the sediment transport

rate, using probability theory to account for the statistical variation of the agitation forces on the bed particles caused by turbulence. There are also numerous empirical formulae for calculating the sediment transport rate such as the ones proposed by Meyer-Peter-Müller (1948), Engelund and Fredsøe (1976), Van Rijn (1984), and Wu (2000). More details, will be given in section 3.3.

3.1.2 Scour problems on seawalls

As described in section 2.1.1, waves generate cross-shore and long-shore transport of sediments. Introducing a structure in this environment disturbs the natural process of sediment transport. In this case, two main concerns arise: the impact of structures on the environment and the safety of the structure itself. Seawalls are often constructed as a land protection from the storm or the receding coast line. Even if the influence of seawalls on the sediment transport pattern is still debatable, seawalls placed near the surf zone influence the coastal hydrodynamics. Pilkey and Wright (1988) concluded that there are three ways in which a seawall can degrade the coastline:

1. by passive erosion due to conditions which existed before the wall was in place,
2. by active erosion due to the modification of the sediment budget due to the seawall (but subject to debate),
3. construction of the wall in the inter-tidal zone.

Kraus and McDougal (1996, 1988) investigated the effect of seawalls on the beach and found that the contribution of wave reflection to the beach profile change might be not as great as believed. Accordingly, several studies (Barnett and Wang, 1988, Griggs et al., 1991, McDougal et al., 1994, Moody, 1996) showed that the wave reflection is probably not a significant contributor to the beach profile change or scour in front of seawalls, at least during a storm. Moody (1996) also found that the erosion rate of a beach in front of a seawall was almost identical to the one without the seawalls.

To better understand how the presence of seawall affects the long-shore transport, Kamphuis (1992) conducted a set of three-dimensional tests on an infinite beach backed by a seawalls. He found that the long-shore sediment transport rate in front of seawalls decreased as the beach in front of the seawalls eroded. In their experiments, Dean and Yoo (1994) also found that the presence of seawall affects the long-shore sediment transport behaviour. The sediment material was found to move rapidly in a coherent body instead of in a diffuse way. Kraus (1996) pointed out that this might be the result of scale effects (small scale experiments) since they did not find such effects in numerical simulations (Hanson and Kraus, 1985; 1986).

From experiments, Sumer and Fredsøe (2000) found that scour in front of a rubble mound breakwater is smaller than in front of a vertical wall. The results also showed that the location of the scour is shifted (Figure 3.2) compared with scour in front of a vertical wall. The difference observed between these two types of structures is related to the reflected waves which are less intense for a rubble mound breakwater which generates partial standing waves instead. It highlights the importance of wave reflections in the scour process. Moreover, the influence of external sources of additional turbulence could enhance the bed shear stress and the

associated bed load transport rate (Sumer et al., 2001).

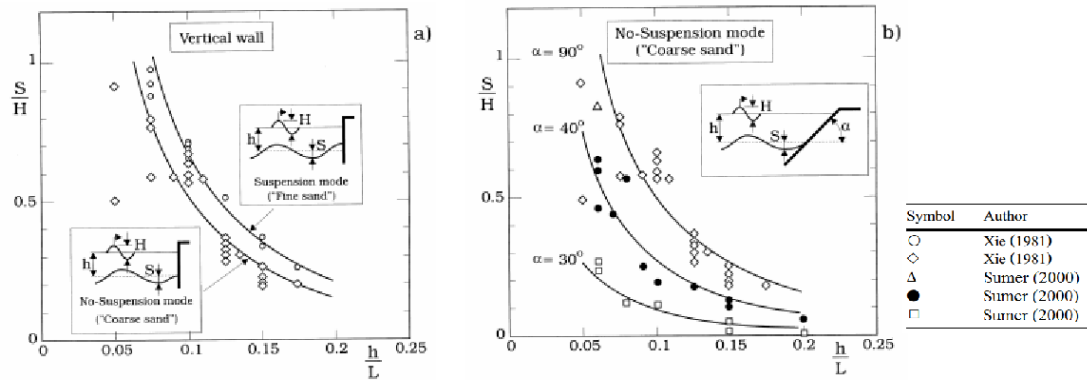


Figure 3.2: Maximum scour depth at the breakwater for regular waves in live bed. (a) Vertical-wall breakwater (b) Rubble-mound breakwater Sumer and Fredsøe, 2000

The field study by Miles et. al (2001) showed some agreement with Sumer and Fredsøe's experiments. By measuring the wave reflection in front of sea walls and comparing it to that for a natural beach, they found a higher reflection coefficient in front of sea walls (three times more than for a natural beach) which resulted in a higher sediment transport rate both in the cross-shore and along shore direction. Moreover, they found that the suspended material tends to increase in the presence of seawalls. Indeed, the cross-shore current at the measurement rig was found to be off-shore, while the value near the seawalls is found to be on-shore. The wave reflection tended to reduce the net on-shore transport slowing down the process of beach recovery. However, the observed value measured at the rig lay inside the error bar of the measurements so it was not possible to draw definite conclusions.

The along-shore sediment transport is found to increase due to the washing of suspended materials by the along-shore current or as the effect of inevitable reflection of waves on the walls. However, according to Kamphuis et al. (1992), as the beach at the front of seawalls erodes, the breaking wave decreases and less suspended material is found in the along-shore current. Then, the role of the seawalls in determining the along-shore sediment transport is still not clear.

Sutherland et al. (2006) showed that there is no obvious direct connection between the wall slope and the scour depth. Indeed, some experiments showed that a 1:2 sloped wall gave a result similar to that for a vertical wall. Sutherland et al. (2006) suggested that scour is more sensitive to water depth at the structure toe ($\frac{h}{L}$) and to the Iribaren number (surf similarity parameter, Equation 2.51). This result shows that scour depends on the wave breaking regime in the front of the structure.

Another influence comes from the ocean current, usually generated by the tide. Sutherland's experiments (Sutherland et al., 1999) for a detached breakwater showed the ability of the current to shift the scour location along the toe of breakwater. Recent experiments conducted by Cartensen and Sumer (2015) showed differences between the pattern obtained from the scour caused by the waves alone and that caused by a combination of waves and current. However, the experiments were carried out at a small scale and it is difficult to generalize the conclusions to full

scale systems. A direct comparison of the bed profile subjected to waves with and without current is therefore not meaningful according to these authors. However, a sediment regime change from a suspension regime to a no-suspension regime when the current was added was observed which is worth mentioning.

Sumer and Fredsøe (2001) carried out an extensive review of the effect of pore pressure in the seabed on scour. It is known that the pore pressure can induce a liquefaction of the sandy bed. However, it is still unclear whether wave-induced pore pressure gradients close to the critical values have an effect or not on scour and sand transport. In steady flow conditions where an upward flow can cause fluidisation of the bed, bedload transport rates may significantly increase near the threshold condition. Scour and coastal responses in the presence of seawalls proved to be a combination of complex hydrodynamic processes and definite conclusions about the relative influence of each process on scour are still uncertain.

3.1.3 Protection measure against scour

As mentioned in section 1.1, scour is a major factor contributing to seawall failure. To limit this risk, the possibility of scour occurring can be taken into account in the seawall foundation design or by protecting the seawall toe from scour. Including the scour depth in the structure design requires a correct prediction of the process since an overestimate of the erosion will increase the cost of the structure. It is also possible to limit scour by increasing the grain diameter in the potentially scoured area, because this will decrease the Shields parameter in the zone of possible erosion thereby limiting the transport of sediment. Figure 3.3 illustrates some protection measures that are commonly employed to protect seawalls against scour.

Any intervention in front of the seawall may just shift the problem without totally solving it (Figure 3.4). Nevertheless, some experiments showed that a protection layer in front of the toe wall tends to decrease the scour depth even if a new scour hole is generated in front of the protection layer (Xie, 1981). The reduced scour pattern at the toe of the wall then depends on the length of the protection layer. Finally, no essential scour was found over a distance of half a wavelength when the protection layer length is more than $\frac{3\lambda}{8}$. Sumer and Fredsøe (2000) also investigated the protection layer influence on toe scour in their experiments. The protection layer length should be at least equal to the length of the scour hole without protection layer as shown in Figure 3.5. Another test carried out with several layers of stone protection showed that the scour depth tends to be constant if the protection layer reaches a certain value, in this case after 4-5 layers (Figure 3.6). However, no study has examined the combined influence of the number of layers and the length of the protection layer, which makes the study of the influence of both factors incomplete. Furthermore, the authors used coarse sand for the sea bed, so poor sediment suspension was expected in this case which limits the generalizeability of the results.

3.2 Numerical modelling of sediment transport

The scour calculation is generally based on the sediment transport formulation. Then, scour is defined as the imbalance of sediment transport rate in a given control

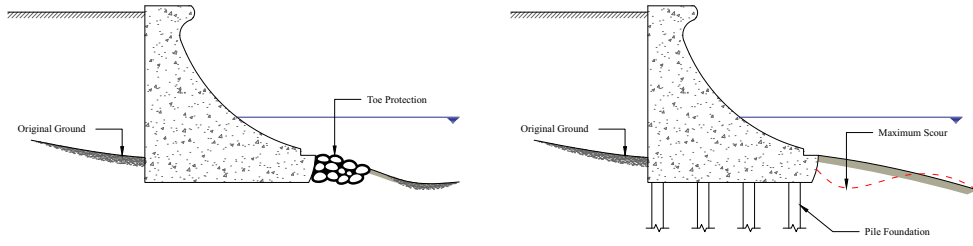


Figure 3.3: Typical toe protection for sea walls

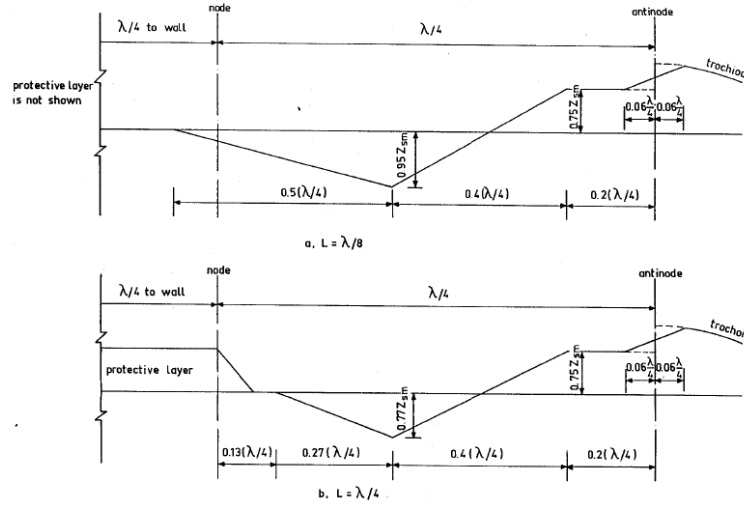


Figure 3.4: Detailed bottom profile of scour with toe protection for protection length of $\frac{\lambda}{4}$ and $\frac{\lambda}{8}$ (Xie, 1981). L is the protection length and λ is the wave length.

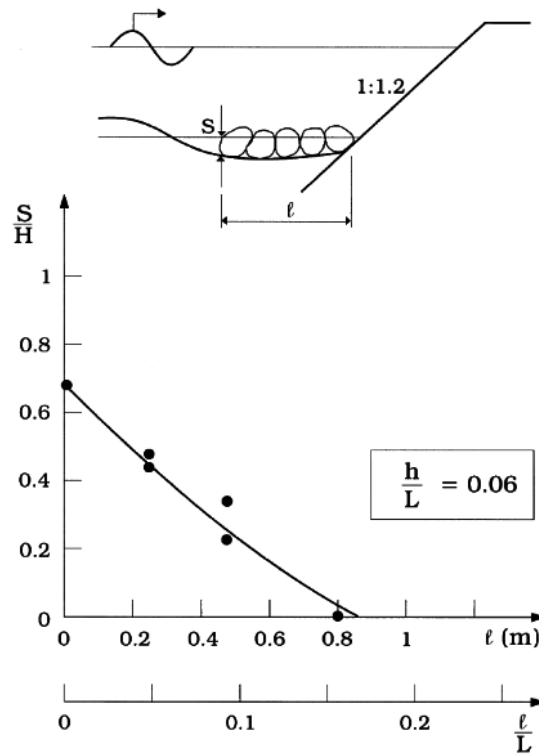


Figure 3.5: Scour depth as a function of the width of the toe protection apron. l is the toe protection length (Sumer and Fredsøe, 2000)

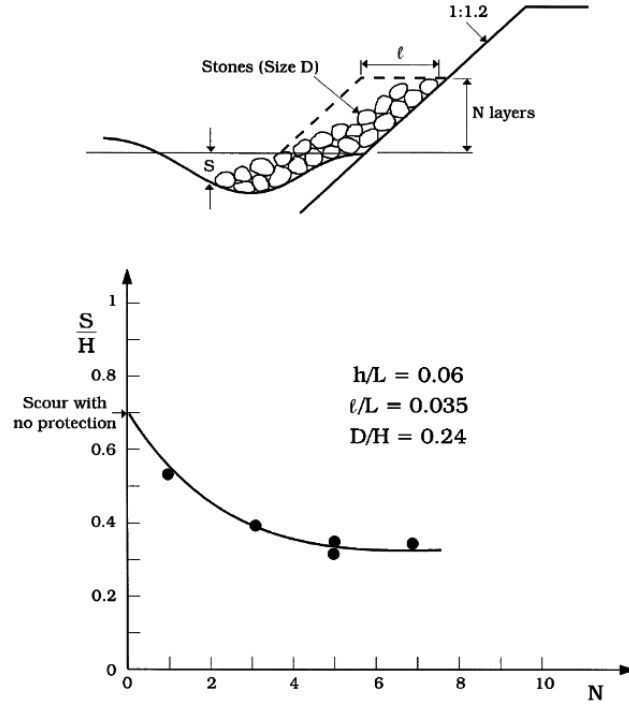


Figure 3.6: Influence of the number of layers of stone on the performance of the toe protection apron. N is the toe protection layer (Sumer and Fredsøe, 2000)

volume. To understand the scour development in front of a marine structure, one could start from the natural process of coastal dynamics. But since coastal erosion is usually addressed using a simple approach, the physical processes involved are not properly modeled in detail. Early attempts to estimate coastal erosion were based on the equilibrium profile approach developed by Bruun (1962) which is known as the Bruun rule. Bruun assumed that the sand volume in an equilibrium profile is constant, hence in response to the sea level rise, the loss of sand from coastline retreat will be deposited in the off-shore region. Kriebel and Dean (1985) developed a schematic model to estimate the coastline change in response to storms without modeling the physical processes of the erosion. Larson et al. (2004) also developed a model for dune erosion calculation based on an analytical formulation. This model combined a transport relationship for the dune based on the wave impact theory with the sediment volume conservation equation. The analytical solution was used for solving the governing equation and the model was validated using available experimental data. The model itself was defined as an approximate estimate of the erosion process in the initial project stages. Despite assumptions based on physical processes, the analytical approaches rely on many simplifications that may be violated in complex cases.

The development of computational resources makes the process based numerical model a feasible approach. In this case, it is possible to include the complete formulation of hydrodynamic effects into the model for more detailed results. There are mainly three types of models based on the sediment transport and scour calculation which are: dynamic mesh method, phase-resolving method and particle based method.

Dynamic mesh method

The dynamic mesh method is a fluid solver with mesh deformation capabilities to accommodate bed change. The fluid solver is used to calculate the flow field and the sediment transport rate. The bed deformation is calculated from a flux balance for the sediment transport and the computational mesh is then deformed to fit the new bed profile. Roulund et al. (2005) successfully applied the method to calculate the scour around a circular pile. The model is based on the 3D incompressible Navier-Stokes (N-S) equation with the bed load sediment transport formulation based on Engelund and Fredsøe (1976). Liang et al. (2005) used a similar approach to calculate the scour below a pipeline where the bed load equation is based on Van Rijn (1984a). However, both simulations did not resolve the free surface dynamics. Gislason et al. (2009) used a similar approach to study the scour and deposition caused by a standing wave in the front of a reflecting breakwater. Similarly to Roulund's calculation, the simulation did not resolve the free surface dynamics, instead a kinematic boundary condition was used. Hence they were not able to take account of wave breaking. Liu and Garcia (2008) introduced the N-S based model, including free surface dynamics by means of the VOF method. The model is based on the two phase immiscible flow solver in OpenFOAM®. The equation is solved on an unstructured mesh using finite volume discretisation and the suspended load is taken into consideration. Jacobsen et al. (2011; 2014a; 2014b) used a similar approach to simulate the development of a breaker bar offshore of a planar coastline. This simulation solves the bed load equation in the bottom patch of the finite volume mesh based on the Finite Area Method (FAM) developed by Tuković (2005). This work included the development of wave generation and absorption based on relaxation zones (Jacobsen et al., 2012). A similar approach was also used by Zhou (2016) to perform a scour simulation using the test case of Roulund et al. (2005). More recently, Sattar et al. (2017) studied the morphological development of a bend in a channel, using bed load, suspended load and mesh deformation with a modified VOF method. The free surface dynamics used the ghost fluid method to resolve the pressure discontinuity between the water and the air interface. However, this type of model becomes unstable when high deformation of the interface occurs because the mesh quality cannot be conserved.

Concerning the bed deformation, a structured grid can be used where the grid is not deformable but the properties associated to the sediment can evolve (immersed boundary method). This holds some advantages, where the grid must not necessarily follow the frontiers of the modeled objects. Various studies have been performed, based on this approach, amongst them Wei et al. (2014) and Ahmad et al. (2015). Recently, Peng et al. (2018) developed the novel partial cell technique and applied it successfully to model scour at the front of seawalls.

Phase resolving method

The bed load and suspended load approach which is used in the dynamic mesh method depends on empirical formulations based on experimental data. It also cannot resolve the bed dynamics, which also depend on the mechanical characteristics of the bed materials. The phase resolving method is based on a two-phase model where one of the phases models the bed materials. It is possible for this type of approach to incorporate the real interaction between the fluid and the sediment. The

main component of this method is the modelling of the different physical processes involved in sediment transport, including: fluid-particle interaction, turbulence effects and particle-particle interaction. Asano (1991) developed a two-phase model to investigate oscillatory sheet-flow, based on a continuum assumption for the fluid and cohesionless sediment mixture. The turbulence model uses the mixing length formulation whilst the intergranular stress is based on a relationship by Savage and Mckeown (1983). The model is capable of predicting the fluid and sediment transport velocity obtained in experiments, however some discrepancy is found for fine-grained sediments. Bakhtyar et al. (2010) used a similar approach for the sediment transport in the inner-surf and swash zone. The VOF method was used to solve the free surface dynamics. The turbulence closure was modeled using the two equation $k - \epsilon$ model. The inner particle closure was modeled as in Bagnold (1954). The governing equation was discretized based on the finite-difference method. The model provided qualitative agreement with existing experimental data. However, by solving two momentum equations, the model consumes more computational resources. More recently, Chauchat et al. (2017) introduced a two-phase model for fluid and sediment interaction based on the OpenFOAM® framework. It offered two types of sediment closure, one based on Mohr-Coloumb friction and the other on μ - I rheology. The model was shown to be able to compute sediment transport, and represent scour processes, and is available as open-source code. However, it did not resolve the free surface dynamics. Most of the models described above also assume that the bed remains permanently saturated, so sediment parameters do not change (as they might if the bed is exposed to air), and there are no groundwater effects.

Particle based method

The particle based method uses a particle based solver to model the sediment component. Hajivalie et al. (2012) combined the free surface dynamic solver based on the VOF method with a discrete granular model by Yeganeh-Bakhtiary et al. (2009). The model uses a one-way coupling approach, in which the fluid affects the particle movement but there is no influence of the particles on the flow. The model is used to simulate the scour process in front of a vertical breakwater with a horizontal bed. The model was shown to be capable of predicting the steady streaming and the scour pattern when compared with the experimental results. Li et al. (2014) also developed a model based on VOF, taking into account particles using the cell method, to investigate scour under a subsea pipe. The particle distribution is calculated using the Liouville equation based on Snider et al. (1997). The inter-particle stress is modeled as a continuum medium based on the model by Snider (2001). Other methods use particle based modeling for both the fluid and solid phase. Shakibaeinia and Jin (2011) developed a weakly compressible moving particle semi-implicit method for mobile-bed simulations of the dam break problem. Vetsch (2012) on the other hand combined the SPH method with the Discrete Element Method for the same application. Particle-based models for the solid phase give greater freedom for modelling the physical processes that occur in the sediment bed, and, in particular, the changes that occur between dry and submerged conditions (Jafari-Nodoushan et al. (2017)). However, the particle based method is known to be computationally more demanding than mesh-based methods. The solution of a large scale problem with a long simulation time requires huge computational resources, especially if one wants to use a fine particle resolution.

Conclusion

The existing methods for solving free surface dynamics and sediment transport processes to investigate the scour process, have been presented, including those that will be used in this study. These methods have shown their capacity to give reasonable results for scour related problems, for example scour under a pipeline (figure 3.7), scour due to a jet flow (figure 3.8) or wave induced scour Liu and Garcia (2008) and Jacobsen and Fredsøe (2011). The volume of fluid method with dynamic mesh deformation has been chosen for this study because it has been found to be accurate and to require less computational resources.

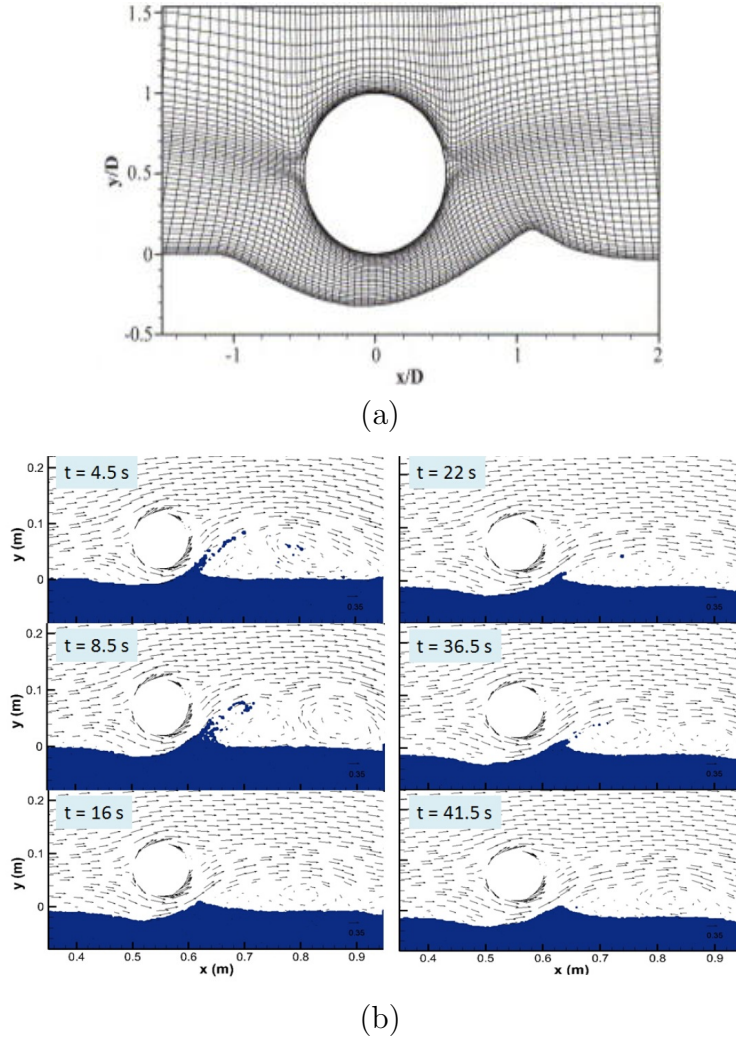


Figure 3.7: Application of numerical model for investigation of scour under pipe line based on: a. dynamic mesh method (Liang et al., 2005) and b. particle based method (Li et al., 2014)

3.3 Sediment Transport Formulation

The sediment transport is computed on the basis of information related to the bed load, the suspended load and using the sediment continuity equation from the erosion and deposition rate. The model solves the equation in three steps, also denoted

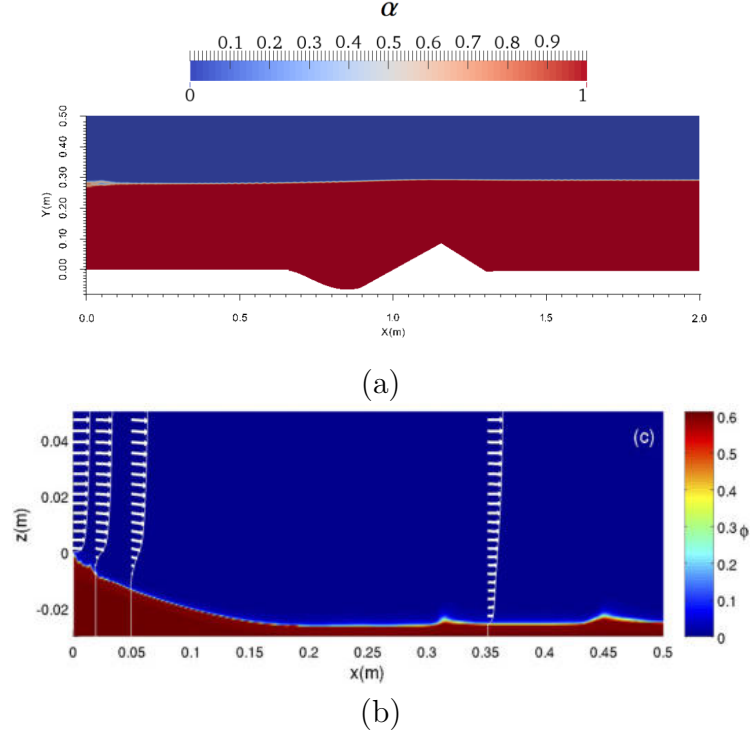


Figure 3.8: Application of numerical model for investigation of scour under jet flow on: a. dynamic mesh method (Zhou, 2016) and b. phase resolving method (Chauchat et al., 2017)

hereafter as modules: the hydrodynamic, sediment transport and morphodynamic modules. First, the hydrodynamic problem with a free surface is solved. The bed shear stress is then calculated in the hydrodynamic module. The bed load and the suspended load are calculated separately based on the bed shear stress. Then, the sediment continuity equation is solved to obtain the bed deformation in the sediment transport module. Finally, in the morphodynamic module, the bed deformation is used to modify the mesh configuration. There are two kinds of mesh used in the model, first the finite volume mesh which is used for the fluid hydrodynamics and suspended load transport calculation, and secondly the finite element mesh which is used for the bed load calculation and which must satisfy the sediment continuity equation. The brief explanation of the finite element discretization is explained in Appendix A.3. The scheme for the sediment transport module is shown in Figure 3.9.

3.3.1 Bed load transport

The bed load transport as already explained in section 3.1, is described as the transport of sediment which remains in contact with the bed. In this model, the bed load transport Φ_b is formulated using a dimensionless bed load transport rate q_b :

$$\Phi_b = \frac{q_b}{\sqrt{(s-1)gd_{50}^3}} \quad (3.5)$$

where s is the sediment grain specific gravity, g is the gravity and d_{50} is the median sediment grain size. The dimensionless bed load transport rate is then calculated from an empirical or an analytical formula based on a relation between the Shields number and the critical Shields number. The formula developed by Engelund and

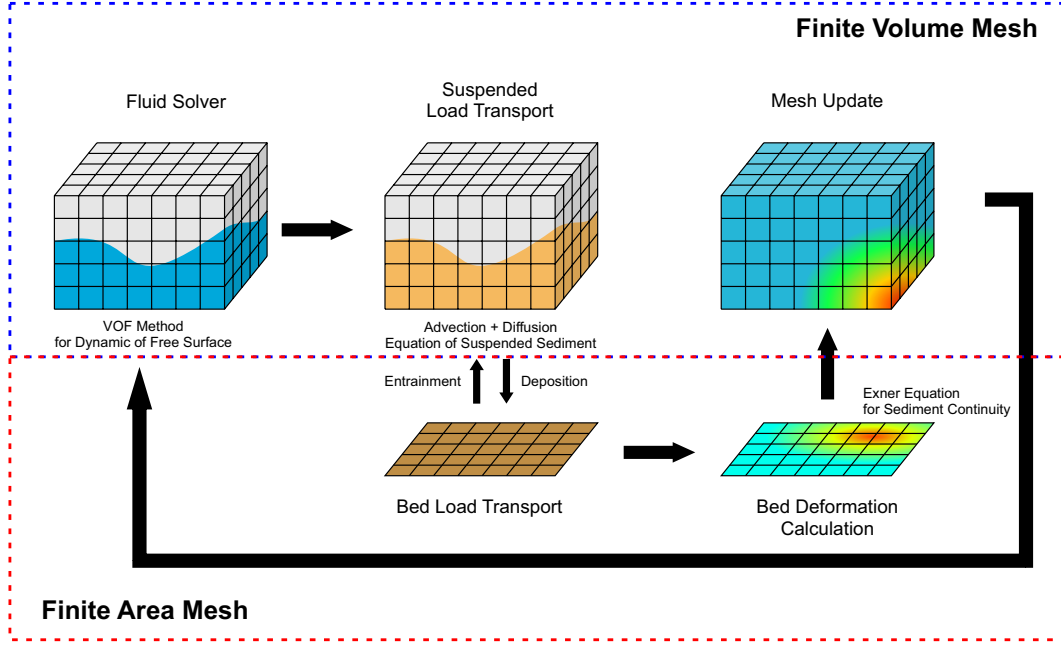


Figure 3.9: Sediment transport model scheme

Fredsøe (1976) will be used in this work. It is based on a balance between stabilizing and destabilizing forces as proposed by Bagnold (1954). The dimensionless bed load transport formula is given by:

$$\Phi_b = 5p_b \left(\sqrt{\theta} - 0.7\sqrt{\theta_c} \right) \quad (3.6)$$

where p_b is the probability that a sediment grain near the surface of the bed will move. It is derived from experimental data from Fernandez Luque and Van Beek (1976) and Guy et al. (1966). By limiting the maximum value of $p_b = 1$, p_b reads (Engelund and Fredsøe, 1976):

$$p_b = \left[1 + \left(\frac{\pi\mu_d}{6(\theta - \theta_c)} \right)^4 \right]^{-1/4} \quad (3.7)$$

where μ_d is the dynamic friction coefficient of the grains which is equal to $\tan \phi_d$. ϕ_d is the dynamic friction angle of the sediment grains.

The results presented in this report were obtained using the formulation of Engelund and Fredsøe (1976).

The dimensional form for bed load transport can be obtained from equation 3.5. However, it only gives the magnitude of the bed load transport, q_b . The bed load transport vector is assumed collinear to the bed shear stress and following Liu and Garcia (2008) is equal to:

$$\mathbf{q}_b = q_b \frac{\boldsymbol{\tau}_b}{|\boldsymbol{\tau}_b|} \quad (3.8)$$

The critical shields number calculated from Equation 3.4 was derived for a horizontal bed. For a non-horizontal bed, the critical Shields number is corrected as follows (Liu and Garcia, 2008):

$$\theta_c = \theta_{c0} \left(\cos \beta \sqrt{1 - \frac{\sin^2 \psi \tan^2 \beta}{\mu_s^2}} - \frac{\cos \psi \sin \beta}{\mu_s} \right) \quad (3.9)$$

where μ_s is the static friction coefficient, β is the angle of the bed slope and ψ is the angle between the bed shear stress vector and the bed slope vector.

3.3.2 Suspended load transport

The volumetric concentration of the suspended load transport is governed by an advection-diffusion equation for C_s :

$$\frac{\partial C_s}{\partial t} + \nabla \cdot [(\mathbf{U} + \mathbf{V}_s)C_s] = \nabla \cdot [(\nu_e + \epsilon_p) \nabla C_s] + C_{s,f} \nabla \alpha \quad (3.10)$$

\mathbf{V}_s is the sediment fall velocity. $\epsilon_p = \nu_t / \sigma_c$ is the suspended load diffusivity, where σ_c is the Schmidt number defined as the ratio of the momentum diffusivity to the mass diffusivity. The last term on the r.h.s is included in order to satisfy a zero-flux boundary condition at the free surface to prevent a sediment flux into the air phase. The sediment fall velocity, \mathbf{V}_s is calculated from:

$$\mathbf{V}_s = \frac{(s-1)d_{50}^2 \mathbf{g}}{18\nu + [0.75(s-1)d_{50}^3 g]^{0.5}} \quad (3.11)$$

Soulsby (1997) gives an alternative relationship to calculate \mathbf{V}_s :

$$\mathbf{V}_s = \frac{\nu}{d_{50}} \left[\sqrt{10.36^2 + 1.049d_*^3} - 10.36 \right] \frac{\mathbf{g}}{g} \quad (3.12)$$

where d_* is the dimensionless sediment grain size described as:

$$d_* = \left[\frac{(s-1)g}{\nu^2} \right]^{1/3} d_{50} \quad (3.13)$$

Near the bed, the sediment concentration depends on the exchange between the settling and the entrained sediment caused by the flow field. The entrainment rate, E , is obtained from C_e which stands for the equilibrium concentration of the suspended load at a reference level near the bed:

$$E = C_e |\mathbf{V}_s| \quad (3.14)$$

where C_e is calculated by means of empirical formulations such as the one proposed by Smith and McLean (1977):

$$C_e = \frac{0.65\gamma_0 T}{1 + \gamma_0 T} \quad (3.15)$$

where $T = 1 - \theta_c$ is the dimensionless transport stage parameter and γ_0 is a constant which is found to be $2.4 \cdot 10^{-3}$. The reference level, Δ_b , is given as:

$$\Delta_b = 26.3Td_{50} + k_s \quad (3.16)$$

Another proposal for C_e from Van Rijn (1984b) reads:

$$C_e = 0.015 \frac{d_{50} T^{3/2}}{\Delta_b d_*^{0.3}} \quad (3.17)$$

The reference level is taken equal to k_s which must correspond to the first cell height near the bed. Equation 3.17 can evolve to infinite values as the concentration grows in proportion to $T^{3/2}$ and is unbounded. However, this is not physical as the concentration in the water column cannot exceed the packing ratio. Hence, a limiter is applied to reduce the entrainment rate (see in more detail Appendix C). The deposition rate, D , is obtained from the sediment concentration near the bed from previous time step, C_d :

$$D = C_d |\mathbf{V}_s| \quad (3.18)$$

The exchange between entrained and deposited sediment is used as a boundary condition at the bed, so the change in the concentration of the suspended load is given by the flux into or out of the suspended load, which depends on the difference between the entrainment and deposition fluxes;:

$$\Delta C = \frac{(D - E)}{\epsilon_p} \quad (3.19)$$

3.3.3 Bed deformation

The bed deformation is calculated by solving the sediment continuity equation, also known as Exner equation (Fredsoe and Deigaard, 1992):

$$\frac{\partial z_b}{\partial t} = -\frac{1}{1-n} (\nabla \cdot \mathbf{q}_b - E + D) \quad (3.20)$$

where n is the porosity of the sediment in the bed assumed as packing ratio of sediments. Equation 3.20 is basically a 2D equation, with the bed load (q_b) flux working in bed boundary, with z_b as the unknown

Dynamic mesh deformation

The bed deformation from equation 3.20 only gives the value of the bed elevation for the finite element mesh which is coupled with the bed boundary of finite volume mesh. OpenFOAM® computes the mesh deformation by solving a Laplace equation for the mesh point velocity field, v :

$$\nabla \cdot (\gamma \nabla v) \quad (3.21)$$

The solution is controlled by the diffusion coefficient γ , which depends on dynamic conditions in the simulation. The diffusion coefficient is important to distribute the displacement for each point, to avoid mesh distortion. Further details can be found in Jasak and Tukovic (2006).

Sand-sliding mechanism

The bed deformation in this work is calculated based on the sediment continuity equation. In several cases when the sediment imbalance is important, the calculated bed deformation may become unrealistic. In reality, when the local bed slope becomes sufficiently steep, a sediment avalanche occurs. In the simulation, this implies that a sliding mechanism for the sand must be included such that, after the mechanism has been triggered, the local slope nowhere exceeds the angle of repose for the

sediment. Figure 3.10 illustrates the basic principle of the sand sliding mechanism. In this work, the sand sliding mechanism is based on the method by Marieu et al. (2008) and Jacobsen and Fredsøe (2011). Further details of the sand sliding algorithm used in this study can be found in Zhou (2016).

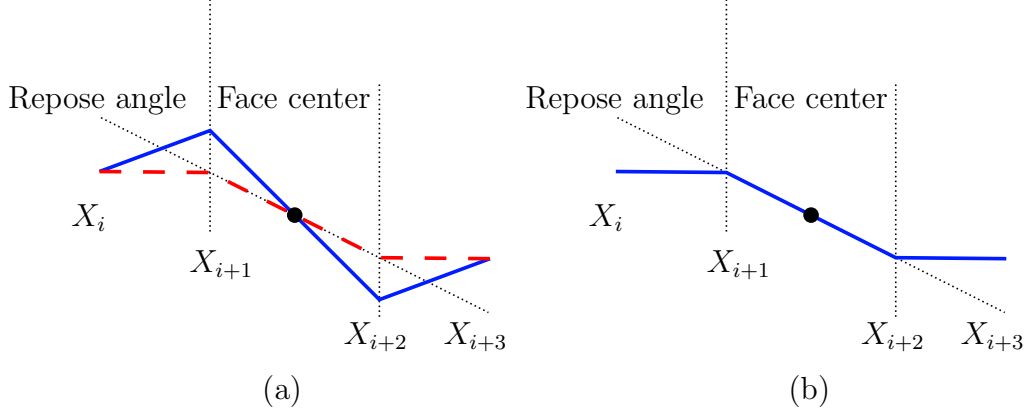


Figure 3.10: Bed slope correction using the sand slide mechanism: (a) bed slope before correction, (b) bed slope after correction

3.4 Conclusion

This section has provided a general description of the sediment transport process, together with previous results related to scour at seawall and several protection measures. Three types of numerical models for the sediment transport calculation have been described: the dynamic mesh method, the phase resolving method and the particle based method.

The dynamic mesh method coupled with the VOF method (Presented in chapter 2) will be used in this work following the work from Zhou (2016). The sediment transport is divided into the bed load and the suspended load transport. The bed deformation is calculated based on the sediment continuity equation. The mesh is then adapted using the dynamic mesh library in OpenFOAM[®].

Chapter 4

Calibration of the Numerical Model in OpenFOAM®

This chapter describes several test cases for the calibration of a model in OpenFOAM® in order to address the problem of scour at toe seawall. The test cases involve free surface dynamics for modelling the flow and the scour model applied to an unsteady flow. The following cases have been studied:

Sensitivity analysis

First, a study is carried out to establish influence of the mesh size on the results and to define optimal resolution, which is necessarily a compromise between the accuracy of the results and the computational time required. Then, several numerical schemes are tested to choose the most efficient one for simulating free surface waves correctly. Two of the VOF approaches described in chapter 2 are used.

Wave reflection and absorption

This case examines three different approaches for including wave absorption: body force damping, a relaxation zone and active wave absorption.

Mass transport simulation

This case tests the model capability to compute correctly the mass transport in a closed wave tank.

Oscillatory flow boundary layer

This case focuses on the modeling of the bottom boundary layer in an oscillatory flow to test the way in which the bed shear is calculated. The test case is carried on the basis of existing experiments using 2-D flow in a U-tube. The flow regimes are laminar and transitional.

Mobile bed dam break flow

The last case addresses the capability of the model to represent the scouring process in a dam break flow. All available modules are involved in the calculation: hydrodynamics, sediment transport and the bed deformation modules.

4.1 Sensitivity analysis

A mesh sensitivity analysis is first performed to understand the influence of the mesh size and the numerical scheme on the results of the simulation. The goal is to obtain

reasonably accurate results at a reasonable computation time cost. Two different configurations are investigated, first to establish the optimal mesh resolution and second to determine the best in relation with the numerical scheme. The tests are performed by simulating 2D wave propagation in a straight wave flume with a horizontal bed. The numerical domain configuration is described in figure 4.1, with the following boundary conditions:

- *Inlet boundary*, the inlet boundary is set with a wave condition using the relaxation zone method. The wave is generated using the Stokes 2nd order theory with $H = 0.02$ m, $T = 1.00$ s. The relaxation zone length is equal to 2λ .
- *Outlet boundary*, the outlet boundary is set as a wave absorption region using the relaxation zone method with a length of 3λ .
- *Bottom boundary*, the bottom boundary condition is a no slip condition imposing a zero normal and tangential velocities.
- *Top boundary*, the top boundary is set at atmospheric pressure which means that a free flow of air is possible.

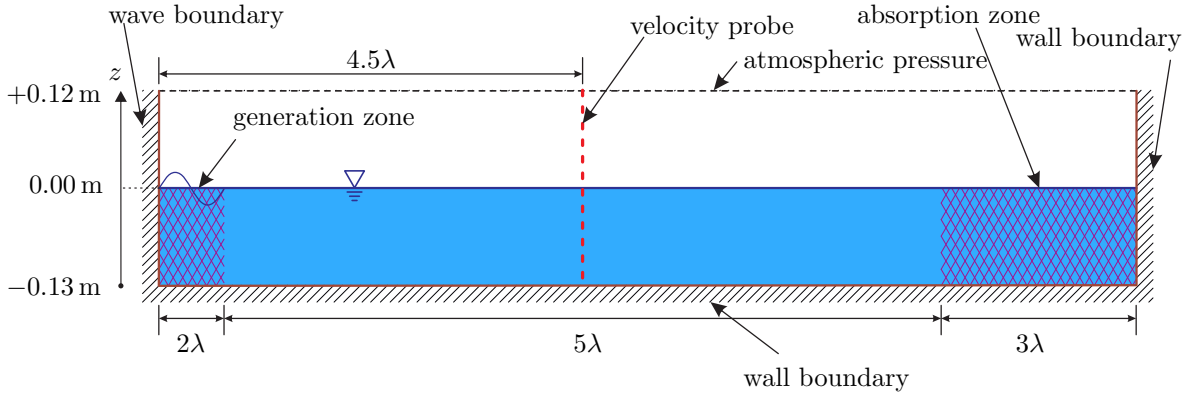


Figure 4.1: Numerical domain configuration for the sensitivity analysis.

The water surface elevation is measured along the channel using the *surfaceElevation* utility provided by waves2foam. A velocity probe is placed at 4.5λ from the inlet, or in the median section of the numerical domain. The velocity parameter is made dimensionless using $a^2\omega k$ where a is the wave amplitude equal to $0.5H$, ω is the wave angular frequency equal to $2\pi/T$ and k is the wave number equal to $2\pi/\lambda$.

Mesh sensitivity

The analysis of the mesh size influence on the numerical results is carried out by studying five different mesh configurations as described in table 4.1. Case 1.6 uses a non-uniform refinement for the free surface area and the value in the table refers to the minimum cell size. For each case, two different solvers are used: interFoam which uses the conditionally averaged approach and gfmFoam which uses the ghost fluid method approach. The simulation is run for 30s which is equal to $30T$. The simulation is carried out with a constant Courant number of 0.5 with a dynamic time step to satisfy the same stability criterion for all the studied cases. The maximum allowed time step is set to a large value in order to allow the time step to be

Table 4.1: Mesh sensitivity configuration

| Case No | Δx (mm) | Δz (mm) | $H/\Delta z$ | $\lambda/\Delta x$ | $\Delta x/\Delta z$ |
|-----------|-----------------|-----------------|--------------|--------------------|---------------------|
| Case 1.1 | 4 | 4 | 5 | 257 | 1 |
| Case 1.2 | 2 | 2 | 10 | 515 | 1 |
| Case 1.3 | 1 | 1 | 20 | 1030 | 1 |
| Case 1.4 | 2 | 1 | 20 | 515 | 2 |
| Case 1.5 | 1 | 2 | 10 | 1030 | 0.5 |
| Case 1.6* | 1 | 5 | 10 | 206 | 5 |

* Case 6 use non-uniform refined mesh

limited by the Courant number.

Figures 4.2 and 4.3 give the water surface elevation results for each case. The interFoam solver induces a wave dissipation while the wave is propagating which increases for a coarser mesh (case 1.1 to 1.3). However, the wave dissipation decreases when the mesh is refined in the horizontal direction, indeed case 1.2 dissipates more wave than case 1.5. Increasing the resolution in the horizontal direction will greatly increase the computational resources and is not feasible. On the other hand, gfmFoam seems unstable for a coarse mesh.

The horizontal velocity field is given in figure 4.4 and figure 4.5 for the interFoam and gfmFoam solvers respectively. The wave dissipation induces a decrease of the horizontal velocity, as would be expected. The results obtained using the interFoam solver are consistent since there is a correlation between the wave dissipation and the decrease in velocities. Interestingly, the results obtained by gfmFoam indicate that the instability in the free surface region does not influence the velocity field in the water column except for case 1.1.

It is known that a higher mesh resolution gives more accurate results but at the expense of computation time. The unstructured mesh configuration of OpenFOAM[®] allows to use a different resolution for specific regions as shown in case 1.6, however the results are still not satisfactory. All these simulations were run with a first order time derivative scheme and according to Toro (2013) this may lead to high numerical diffusion which induces wave dissipation. Hence, in the next section, the case 1.6 configuration is tested using different numerical schemes.

Numerical scheme sensitivity

OpenFOAM[®] allows the use of different discretization scheme options with different orders of accuracy and stability. Without being exhaustive, several schemes have been tested to understand their influence on the accuracy of the simulations. The different schemes that have been studied are:

- *Time derivative scheme*: Euler scheme which is a first-order accurate scheme and a backward scheme which is a second-order accurate scheme;
- *Gradient scheme*: Gauss gradient scheme which is a second-order accurate scheme and a least squares scheme which is also second order accurate. Based on the report by DHI (Petersen and Heilskov, 2015), the velocity field could be-

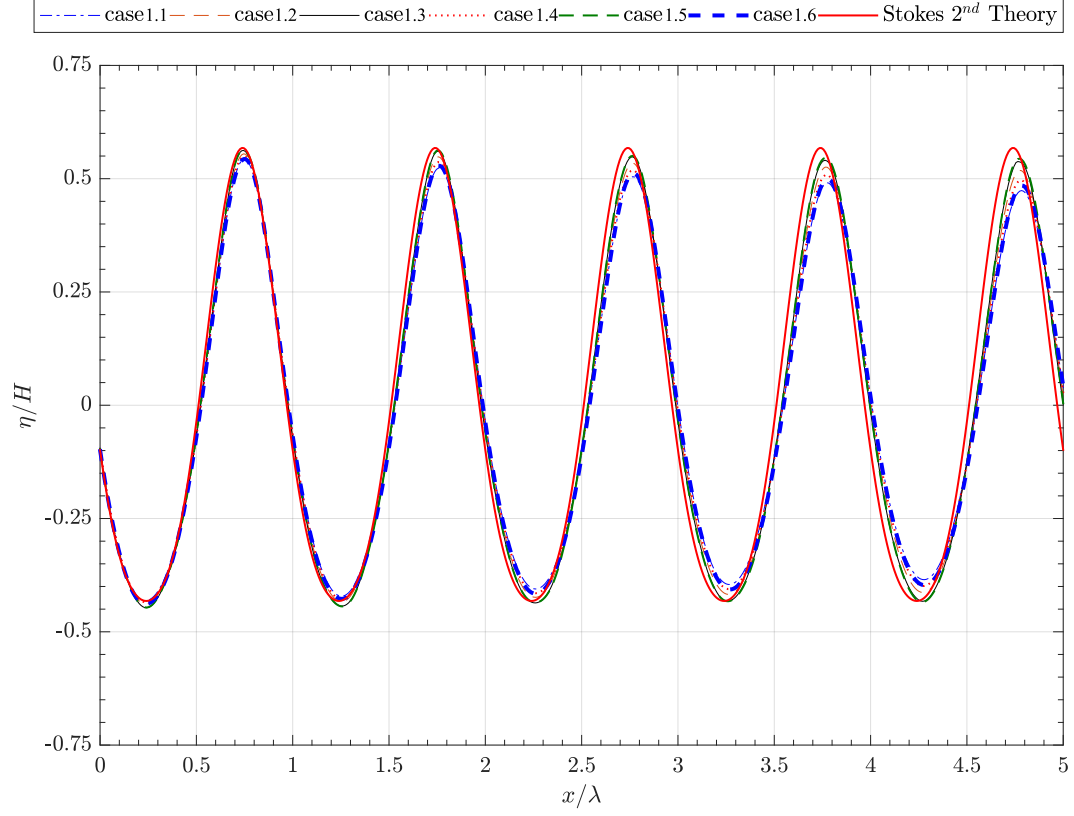


Figure 4.2: Water surface elevation for the mesh sensitivity study with interFoam solver for $t = 30T$

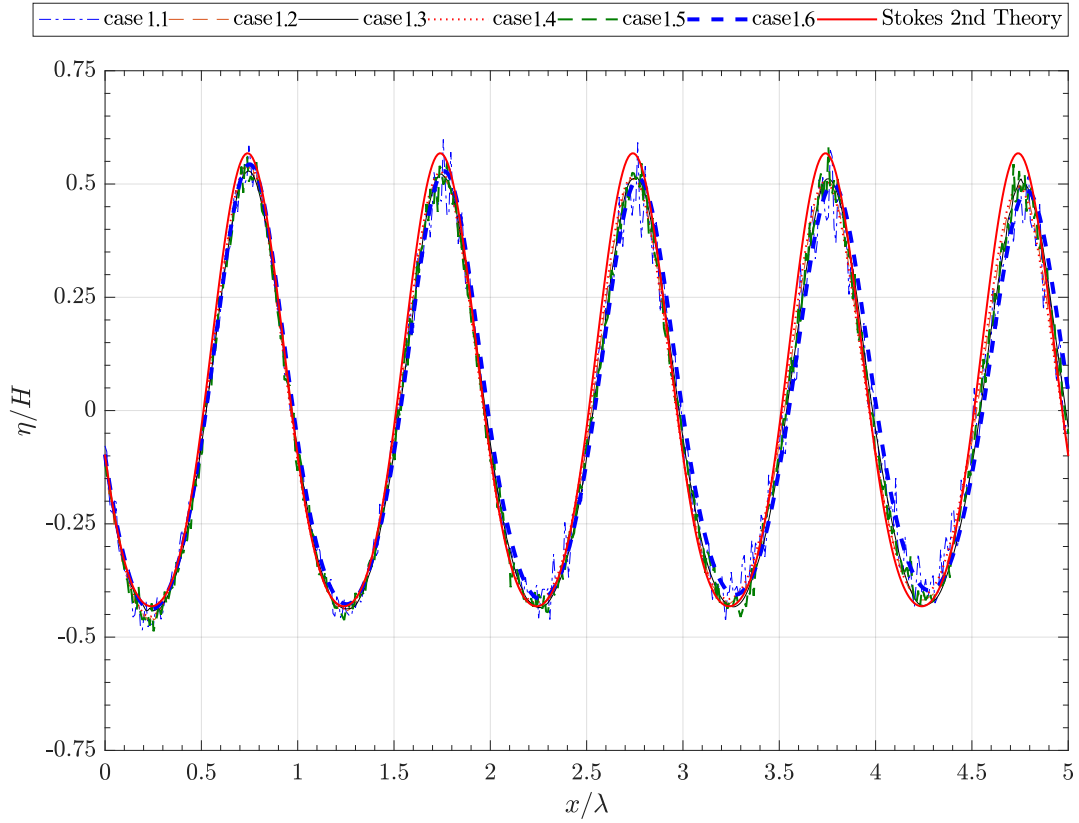


Figure 4.3: Water surface elevation for the mesh sensitivity study with gfmFoam solver

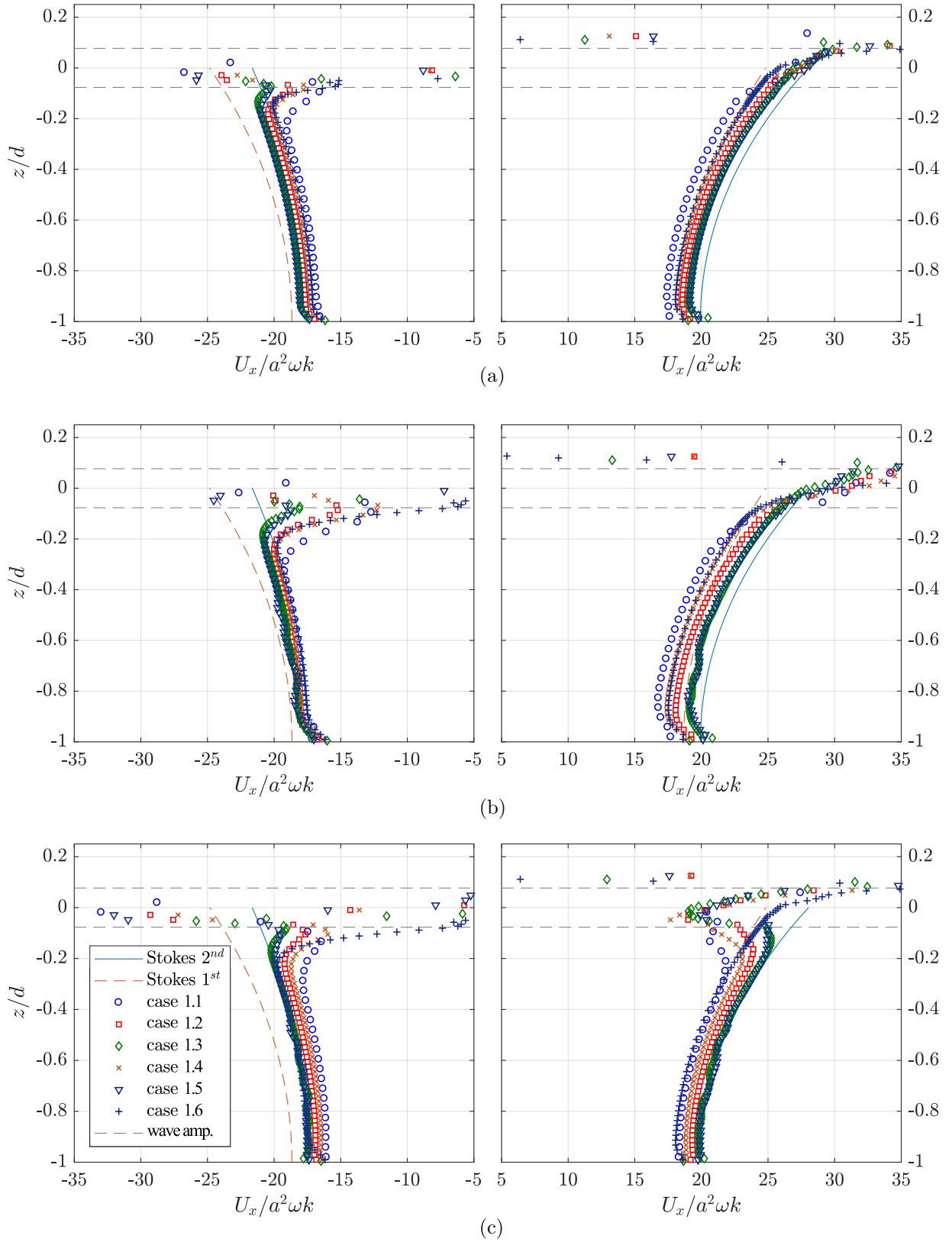


Figure 4.4: Instantaneous horizontal velocity profile in the midsection of the computational domain for interFoam solver depending on the mesh size: (a) $t = 10T$; (b) $t = 30T$; (c) Instantaneous horizontal velocity minus the mass transport velocity averaged over T at $t = 30T$; left side is at wave trough and right side is at wave crest

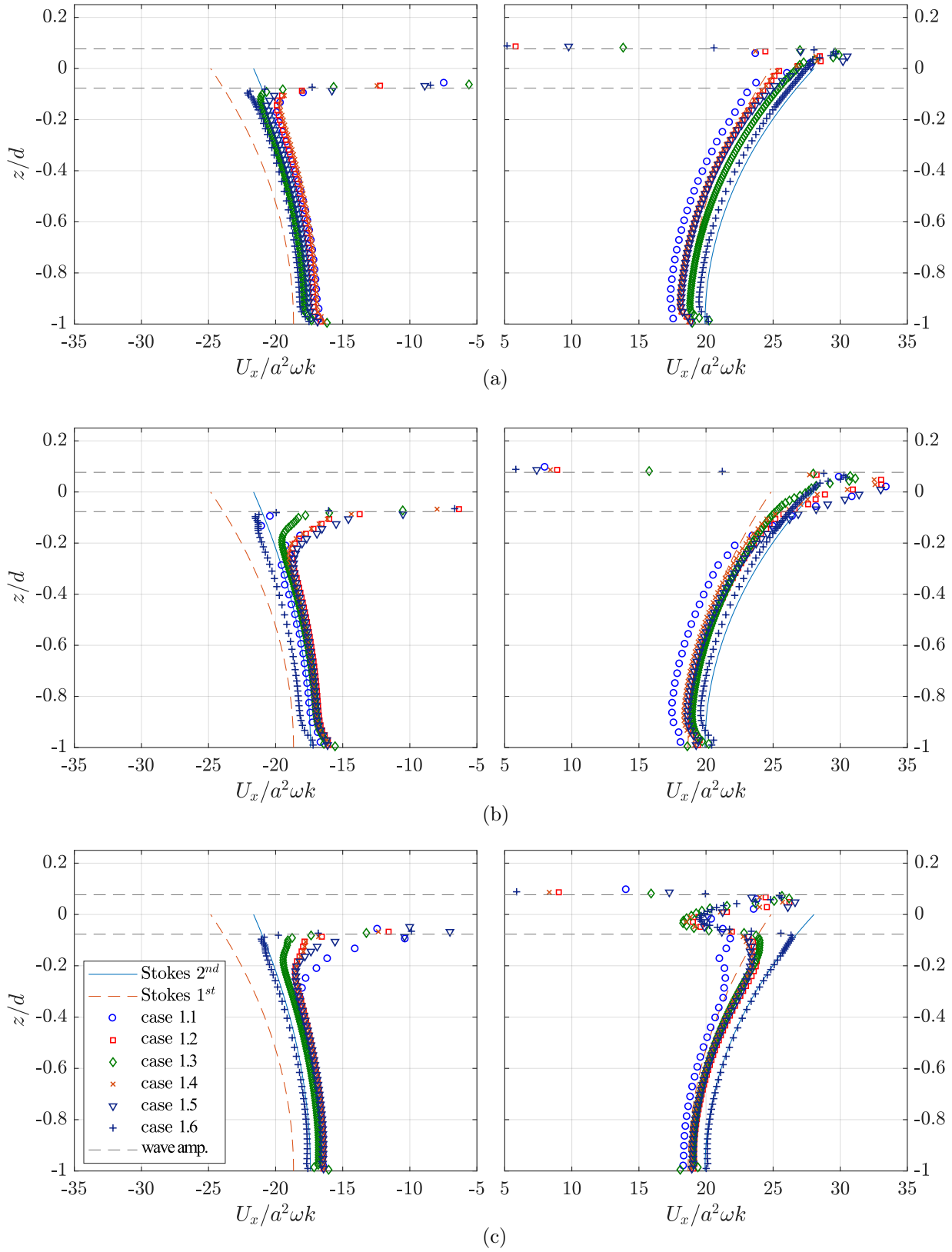


Figure 4.5: Instantaneous horizontal velocity profile in the middle of computational domain for gfmFoam solver depending on the mesh size: (a) $t = 10T$; (b) $t = 30T$; (c) Instantaneous horizontal velocity minus the mass transport velocity averaged over T at $t = 30T$; left side are at wave trough and right side are at wave crest

came unstable if no gradient limiter is applied, especially for a long simulation time. Hence, limited gradient schemes are also tested;

- *Divergent scheme*: Gauss linear which is an unbounded second order accurate scheme and a Gauss linear blended with upwind where the upwind scheme is a first order accurate bounded.

A brief explanation of the OpenFOAM[®] discretization schemes is described in Appendix A.2. Based on the schemes that will be tested, ten cases were prepared for both the interFoam and gfmFoam solver as described in table 4.2. The mesh configuration used in this simulation is optimized where $H/\Delta z = 20$ in the free surface region and $\lambda/\Delta x = 206$. The mesh configuration details are depicted in figure 4.6. All the boundary specifications are those previously described in figure 4.1.

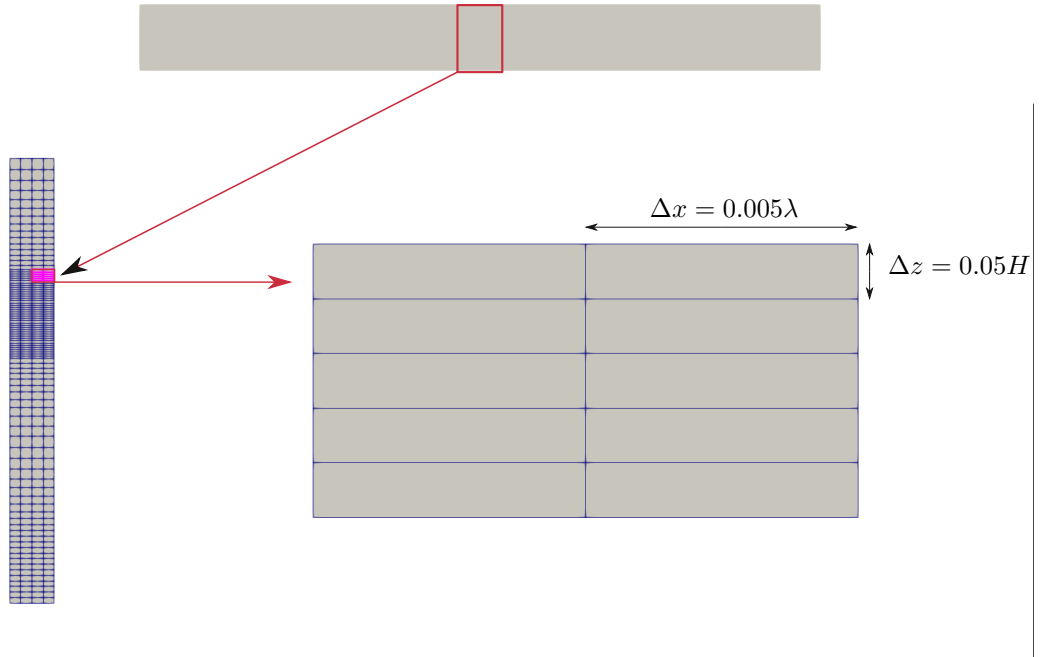


Figure 4.6: Mesh configuration for the numerical scheme sensitivity study

Numerical scheme comparison

The influence of the numerical schemes is tested in case 1.7 to case 1.12 (table 4.2).

The water surface elevation plotted in figure 4.7 and 4.8 shows that the wave dissipation is sensitive to the time derivative scheme. For both solvers, the first order time derivative gives a higher wave dissipation, which suggests that it would be better to use a second order scheme for wave simulation. The backward scheme gives a higher dissipation for the interFoam solver. Conversely, the Euler scheme gives less dissipation with the interFoam solver. This implies that the gfmFoam solver is more sensitive to the type of time derivative scheme but it also gives the least dissipation if the second order scheme is used. A phase shift is also observed irrespective of the time derivative scheme, but the phase shift is greatest with the interFoam solver. We can conclude, therefore, that the solver introduces a time shift,

Table 4.2: Numerical scheme sensitivity case configuration

| Case No | Time discretization | Gradient scheme | Divergent scheme |
|-----------------------------|---------------------|---------------------------------|---|
| Numerical scheme comparison | | | |
| Case 1.7 | Euler | No limiter + Gauss linear | Gauss linear |
| Case 1.8 | Backward | No limiter + Gauss linear | Gauss linear |
| Case 1.9 | Euler | Face limiter + least squares | Gauss linear + upwind + face limiter |
| Case 1.10 | Backward | Face limiter + Gauss linear | Gauss linear + upwind + face limiter |
| Case 1.11 | Backward | Face limiter + least squares | Gauss linear + upwind + face limiter |
| Case 1.12 | Backward | Face limiter + least squares | Gauss linear + limiter |
| Gradient limiter comparison | | | |
| Case 1.13 | Backward | Cell limiter + Least squares | Gauss linear + upwind + cell limiter |
| Case 1.14 | Backward | MD face limiter + Least squares | Gauss linear + upwind + MD face limiter |
| Case 1.15 | Backward | MD cell limiter + Least squares | Gauss linear + upwind + MD cell limiter |
| Crank Nicholson Scheme | | | |
| Case 1.16 | Crank Nicholson* | Face limiter + Gauss linear | Gauss linear + upwind + cell limiter |

MD : Multi directional limiter scheme

* : 0.5 off-centering coefficient is applied for stability

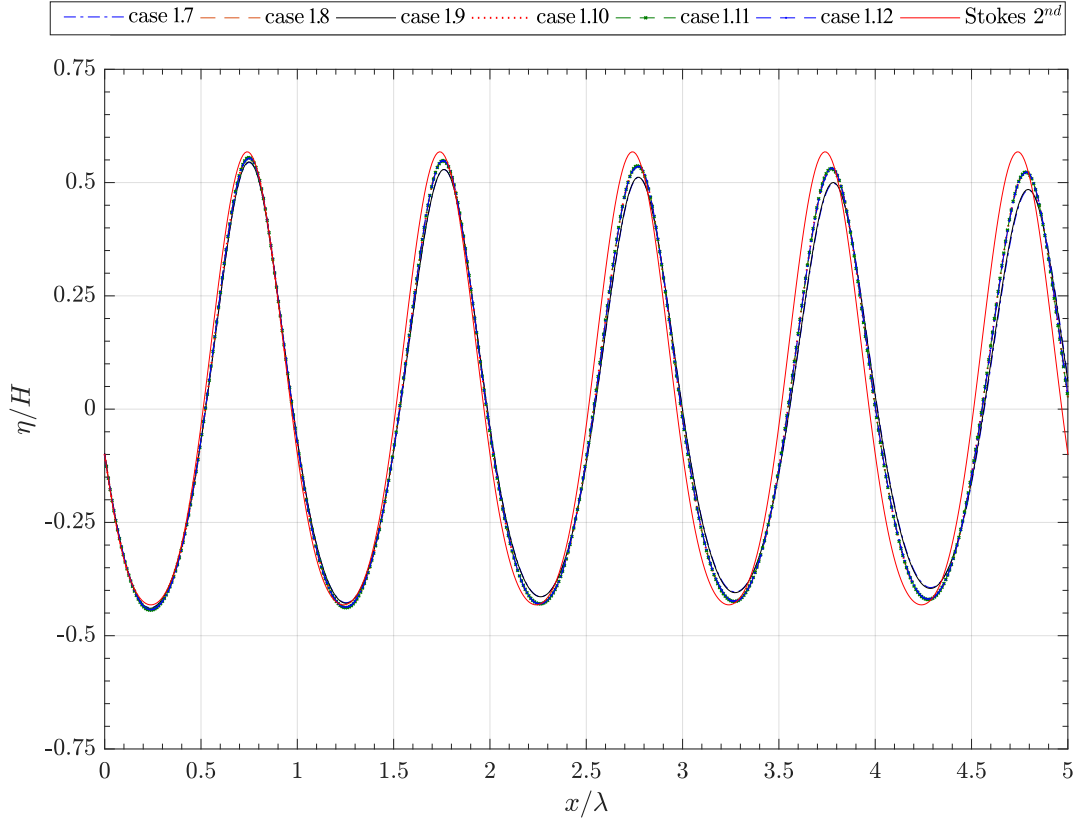


Figure 4.7: Water surface elevation for numerical scheme sensitivity study with interFoam solver for $t = 60T$ for test cases 1.7-1.12

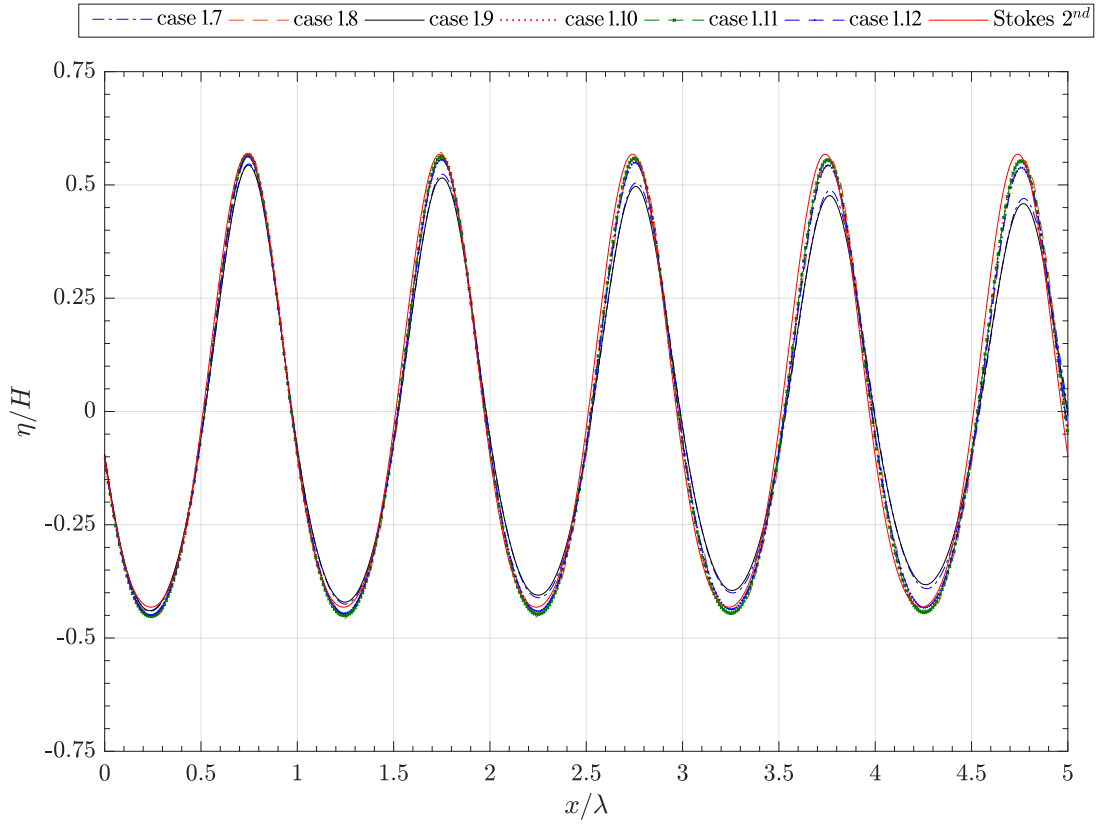


Figure 4.8: Water surface elevation for numerical scheme sensitivity study with gmFoam solver for $t = 60T$ for test cases 1.7-1.12

which depends on the numerical scheme.

The gfmFoam solver seems more accurate than interFoam solver for the near surface velocity as shown in figure 4.9 and 4.10. This is expected since the gfmFoam solver resolves the pressure discontinuity at the free surface rather than using an averaged diffusion parameter as for the interFoam solver. It is also important to note that for a long simulation, the effect of the mass transport velocity in the wave tank is also important. For the velocity field at $t = 60T$, discrepancies arise from the theoretical Stokes second order solution. If the mass transport velocity is subtracted from the instantaneous horizontal velocity, the velocity profile agrees well with the theoretical result. However, the subtracted velocity profile does not agree with the theory close to the free surface. This problem will be addressed specifically in section 4.3.

Gradient limiter sensitivity

As stated before, according to Petersen and Heilskov (2015), the velocity field can become unstable if no limiter is applied in the gradient scheme. In the free surface simulation, a high velocity gradient occurs at the interface, and applying a limiter is important in order to bound the gradient calculation. Hence, the different gradient limiters available in OpenFOAM[®] are tested in cases 1.11 - 1.15. The details of each scheme are described in Appendix A.2. From the test cases, one can note that the multi directional face limiter dissipates more than any other limiter (figures 4.11 and 4.12). Moreover, the gfmFoam solver seems to be more sensitive to the schemes as the dissipation is quite high compared with the other limiter. However, interesting results are found for the velocity profile with the use of interFoam solver, while the multi directional face limiter gives a higher dissipation (figure 4.13 and 4.14). Indeed, the free surface velocity especially in the waves trough is less affected by the spurious air velocity. Hence, for the interFoam solver, a multi directional face limiter will be used in further simulations while for the gfmFoam solver the non-multi dimensional limiter will be used.

Time derivative scheme sensitivity for dynamic mesh simulation

Previous results have shown that, it is necessary to use the second order time derivative to minimize dissipation. However, the simulations revealed that the dynamic mesh solver is not compatible with the backward time derivative scheme. Another alternative lies in the use of the Crank Nicholson scheme which is also second order accurate. In this case, a blending is used together with the implicit Euler scheme to improve the stability where a value of 0.5 is used for the off-centering coefficient. In this context, test case 1.16 is compared to test case 1.10. The results of the simulations show that the Crank Nicholson scheme is able to minimize the dissipation compared with the backward scheme for the interFoam solver as shown in figure 4.15. The gfmFoam solver is more sensitive to the numerical scheme; as can be seen in figure 4.16, the implicit Euler scheme gives the highest dissipation, followed by the Crank-Nicholson scheme, and finally the backward scheme, which gives the least dissipation. The velocity field in the mid-section gives similar results where a higher dissipation leads to a smaller velocity amplitude.

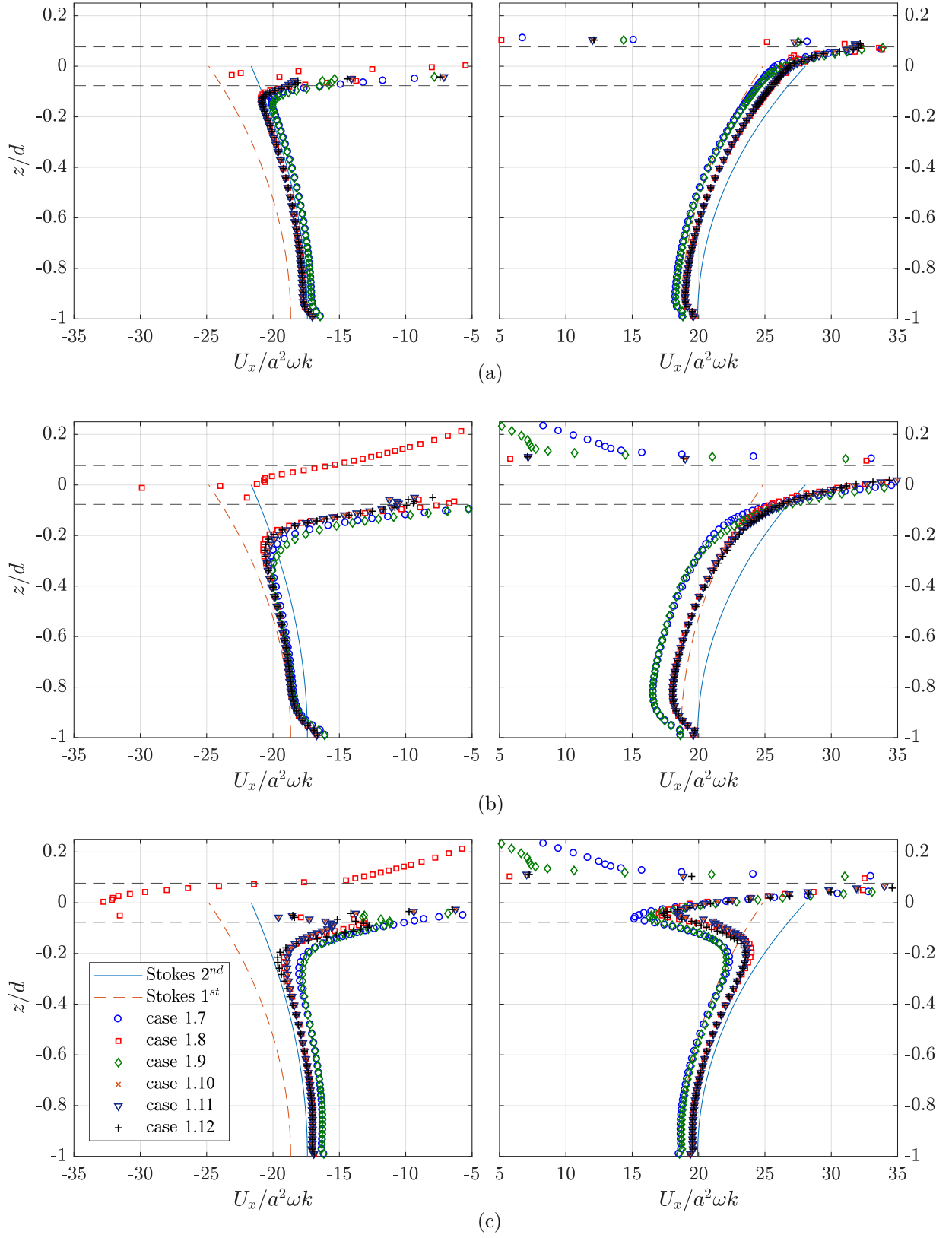


Figure 4.9: Instantaneous horizontal velocity profile in the mid section of the computational domain for the numerical scheme sensitivity study with interFoam solver: (a) $t = 10T$; (b) $t = 60T$; (c) Instantaneous horizontal velocity minus the mass transport velocity averaged over T at $t = 60T$

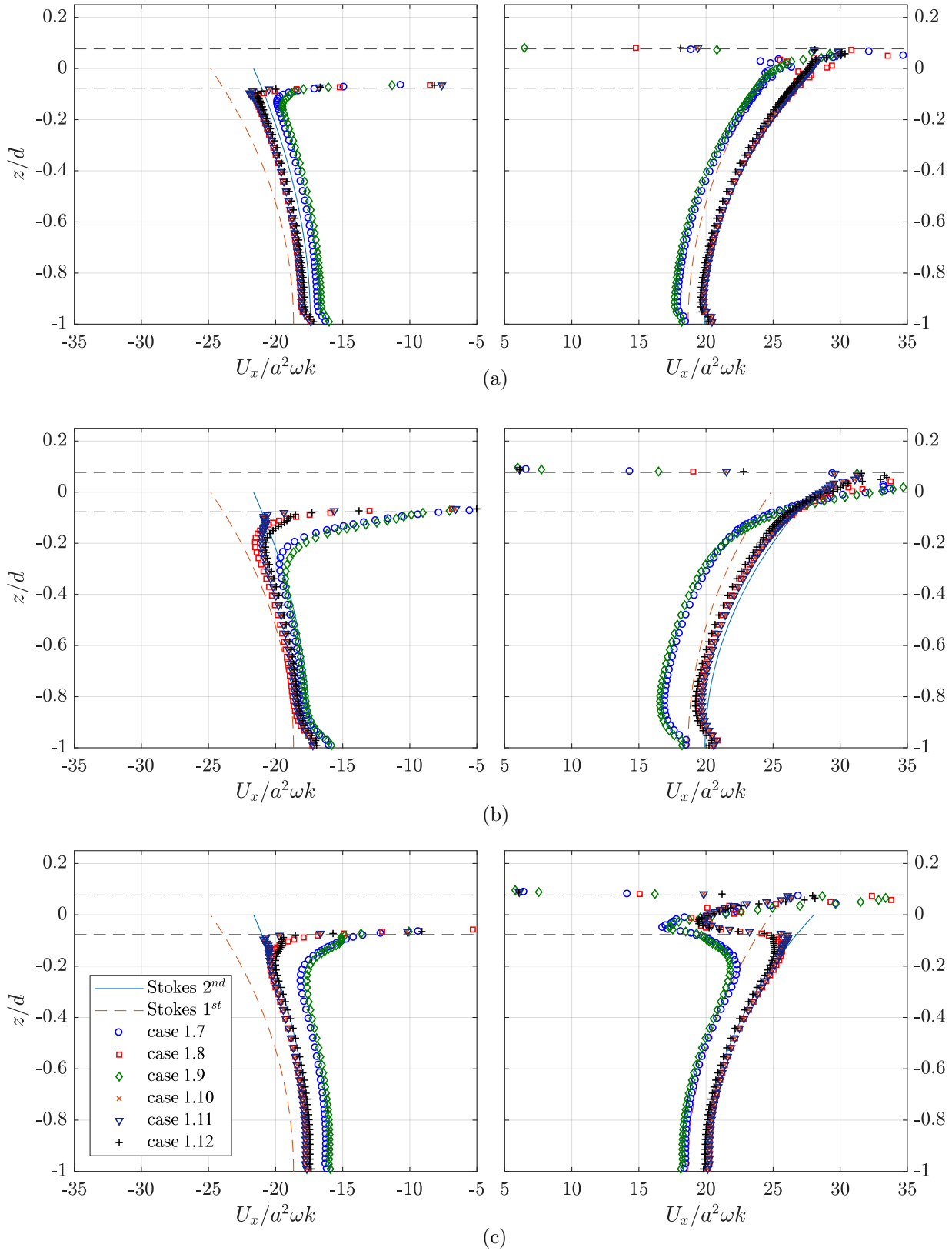


Figure 4.10: Instantaneous horizontal velocity profile in the mid section of the computational domain for the numerical scheme sensitivity study with gmFoam: (a) $t = 10T$; (b) $t = 60T$; (c) Instantaneous horizontal velocity minus the mass transport velocity averaged over T at $t = 60T$

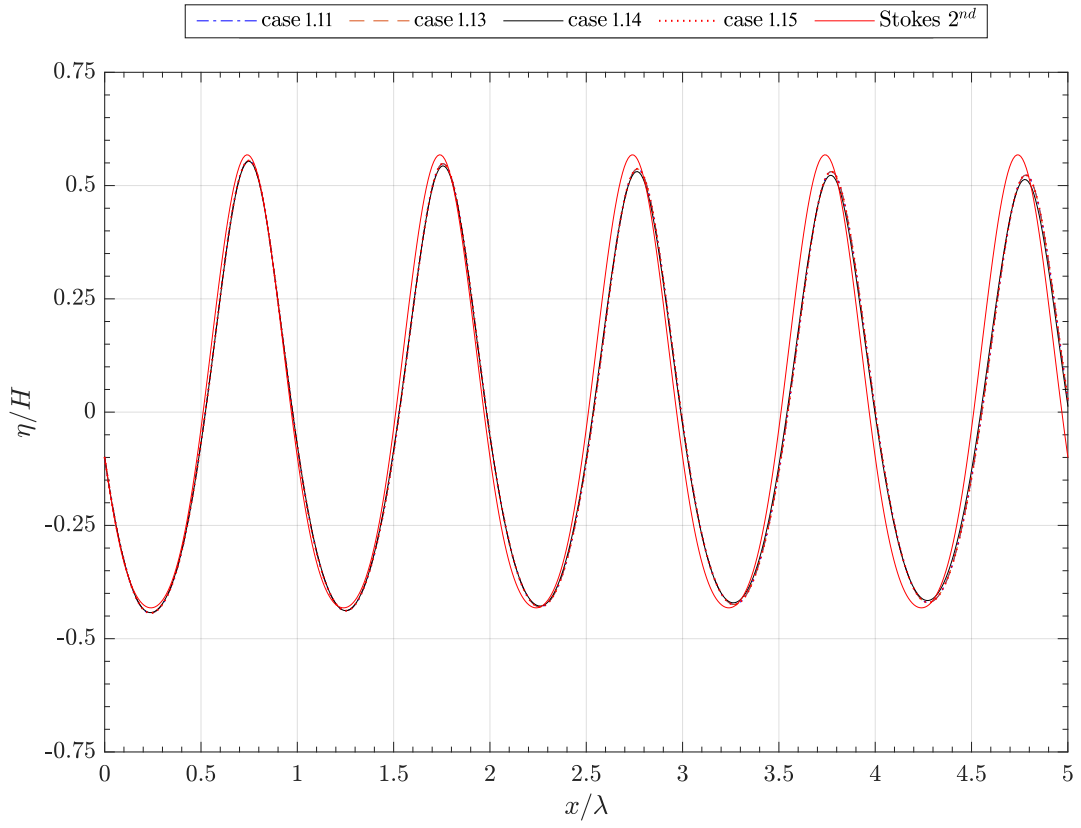


Figure 4.11: Water surface elevation for the gradient limiter study with interFoam solver for $t = 60T$ for test cases 1.11,1.13,1.14,1.15

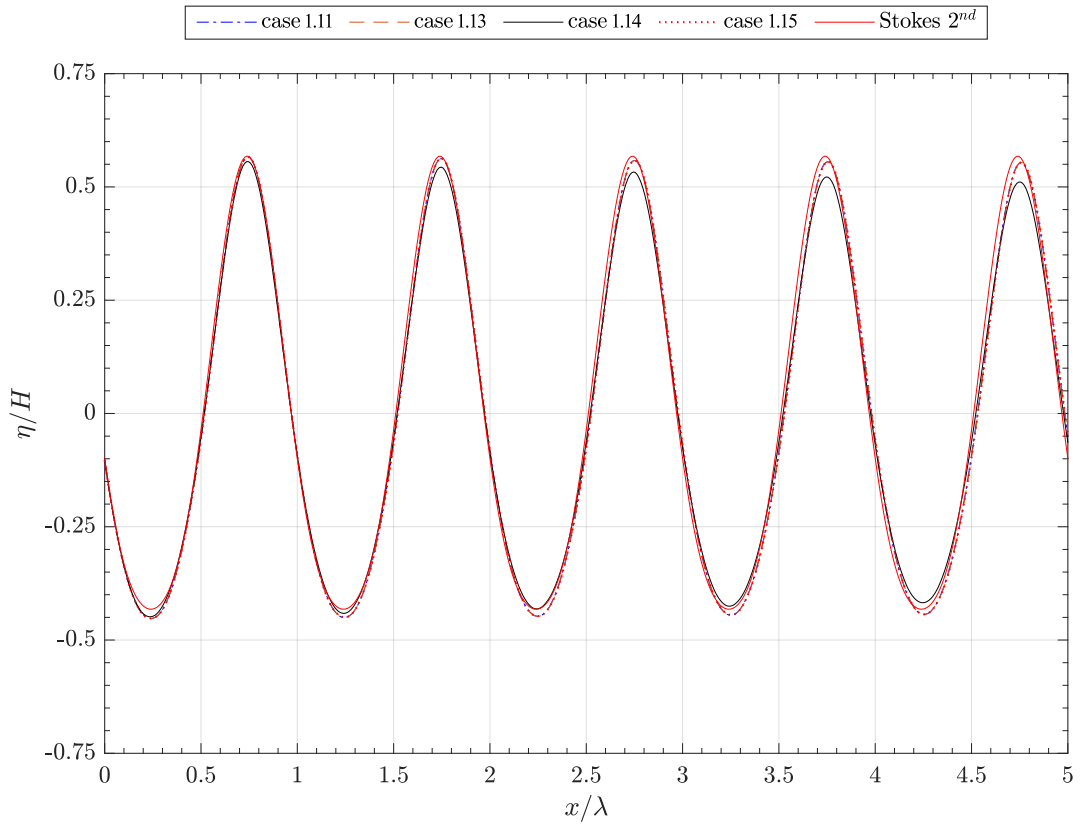


Figure 4.12: Water surface elevation for the gradient limiter study with gfmFoam solver for $t = 60T$ for test cases 1.11,1.13,1.14,1.15

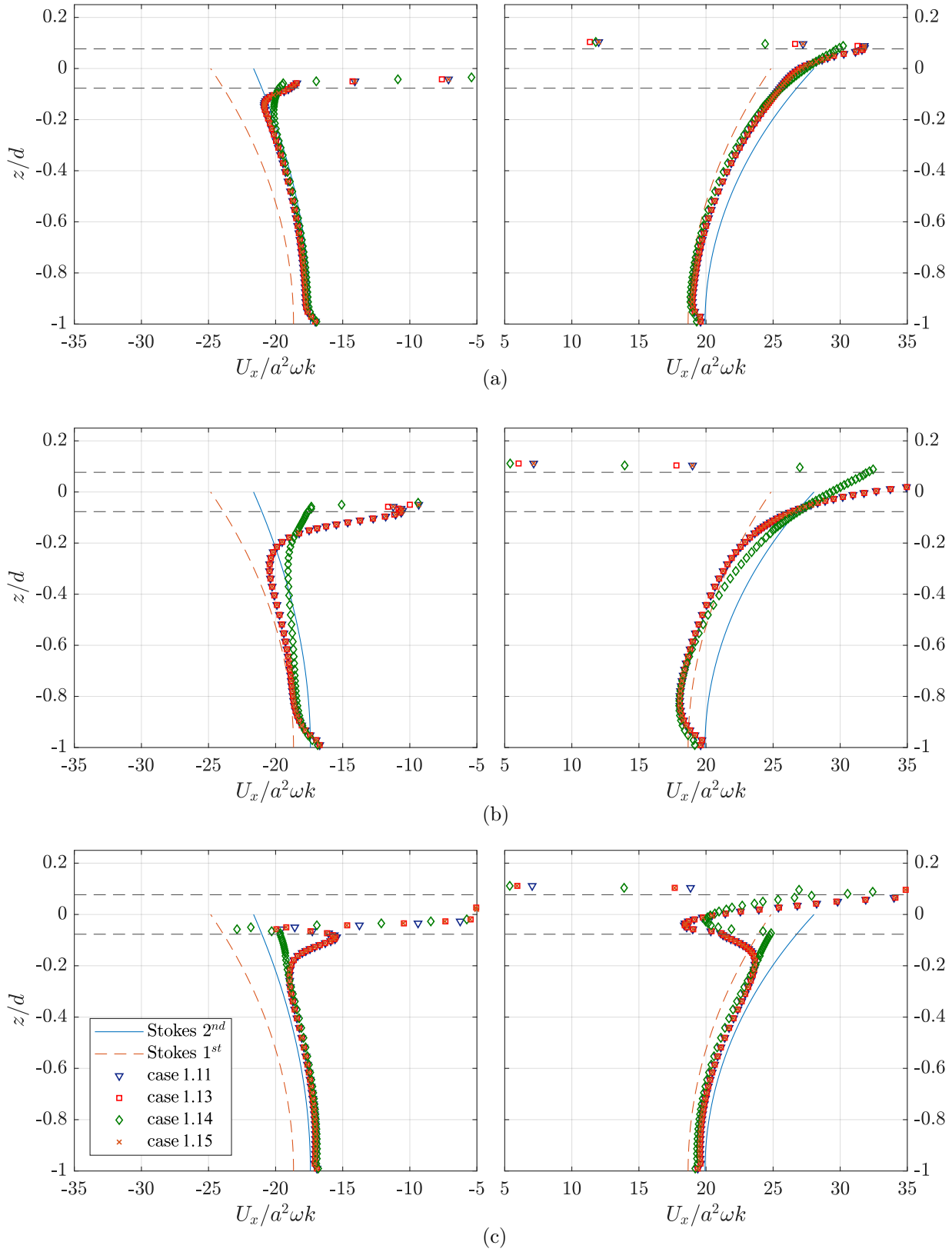


Figure 4.13: Instantaneous horizontal velocity profile in the mid section of the computational domain for the gradient limiter sensitivity study with interFoam solver: (a) $t = 10T$; (b) $t = 30T$; (c) Instantaneous horizontal velocity minus the mass transport velocity averaged over T at $t = 30T$

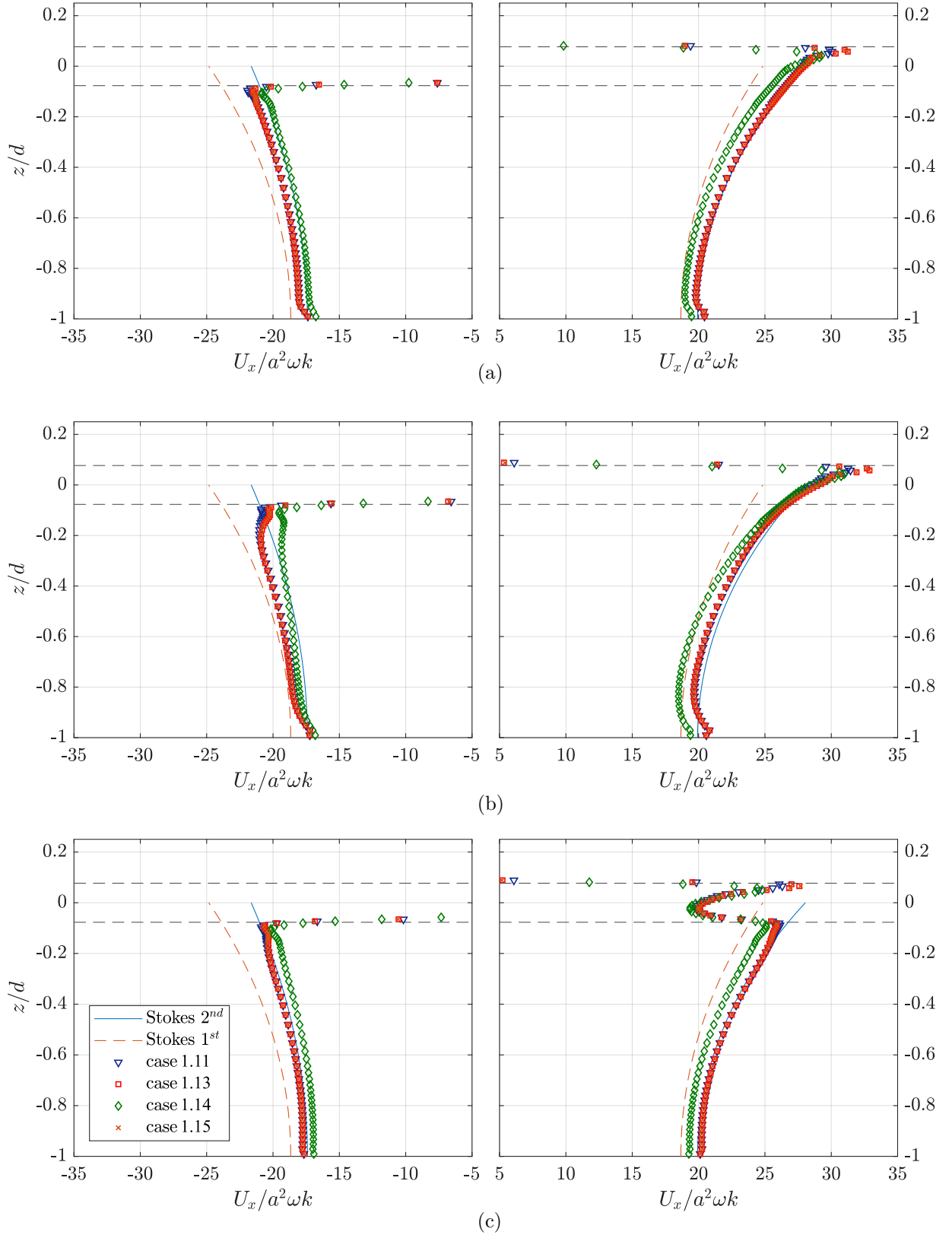


Figure 4.14: Instantaneous horizontal velocity profile in the mid section of the computational domain for the gradient limiter sensitivity study with gfmFoam: (a) $t = 10T$; (b) $t = 30T$; (c) Instantaneous horizontal velocity minus the mass transport velocity averaged over T at $t = 30T$

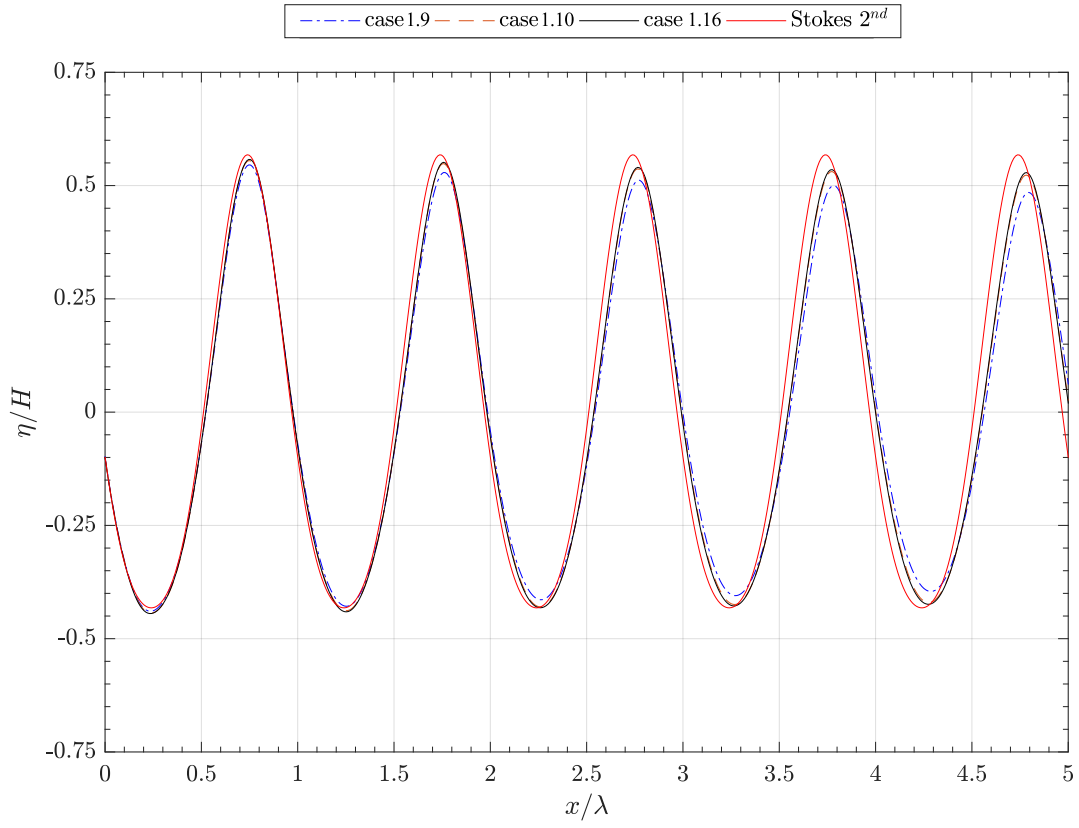


Figure 4.15: Water surface elevation for time derivative scheme test with interFoam solver for $t = 60T$ for test case 1.9,1.10,1.16

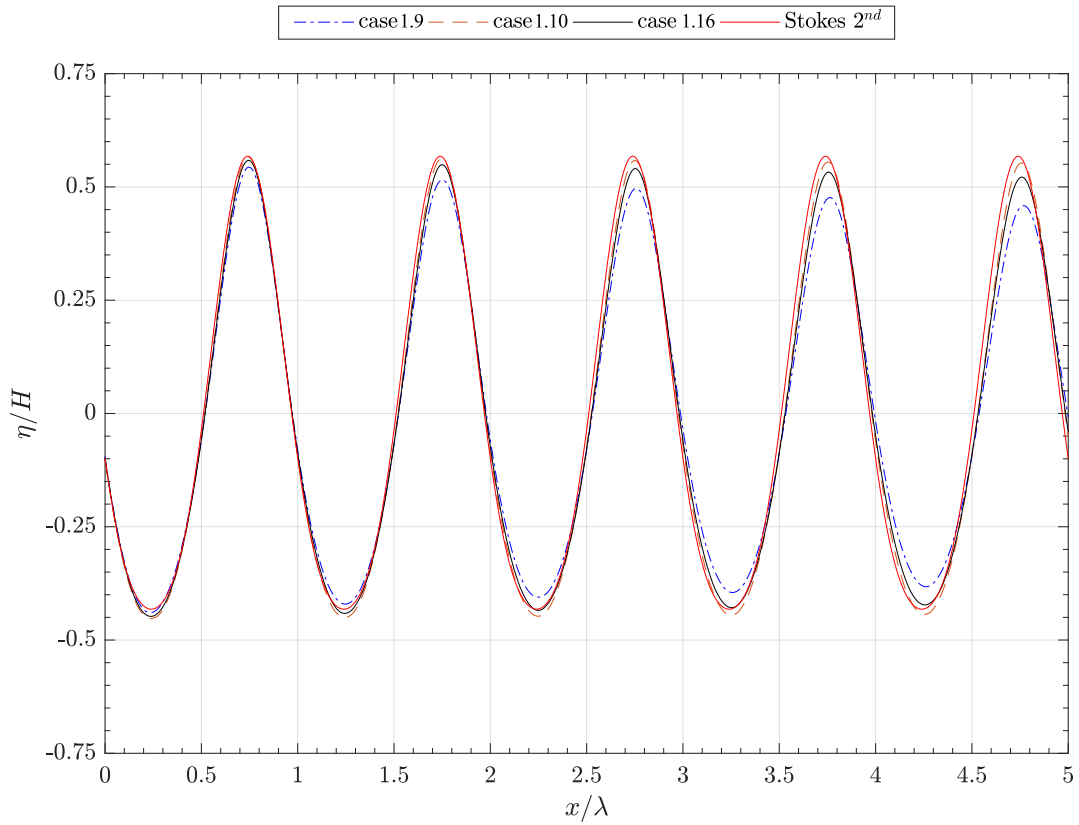


Figure 4.16: Water surface elevation for time derivative scheme test with gfmFoam solver for $t = 60T$ for test case 1.9,1.10,1.16

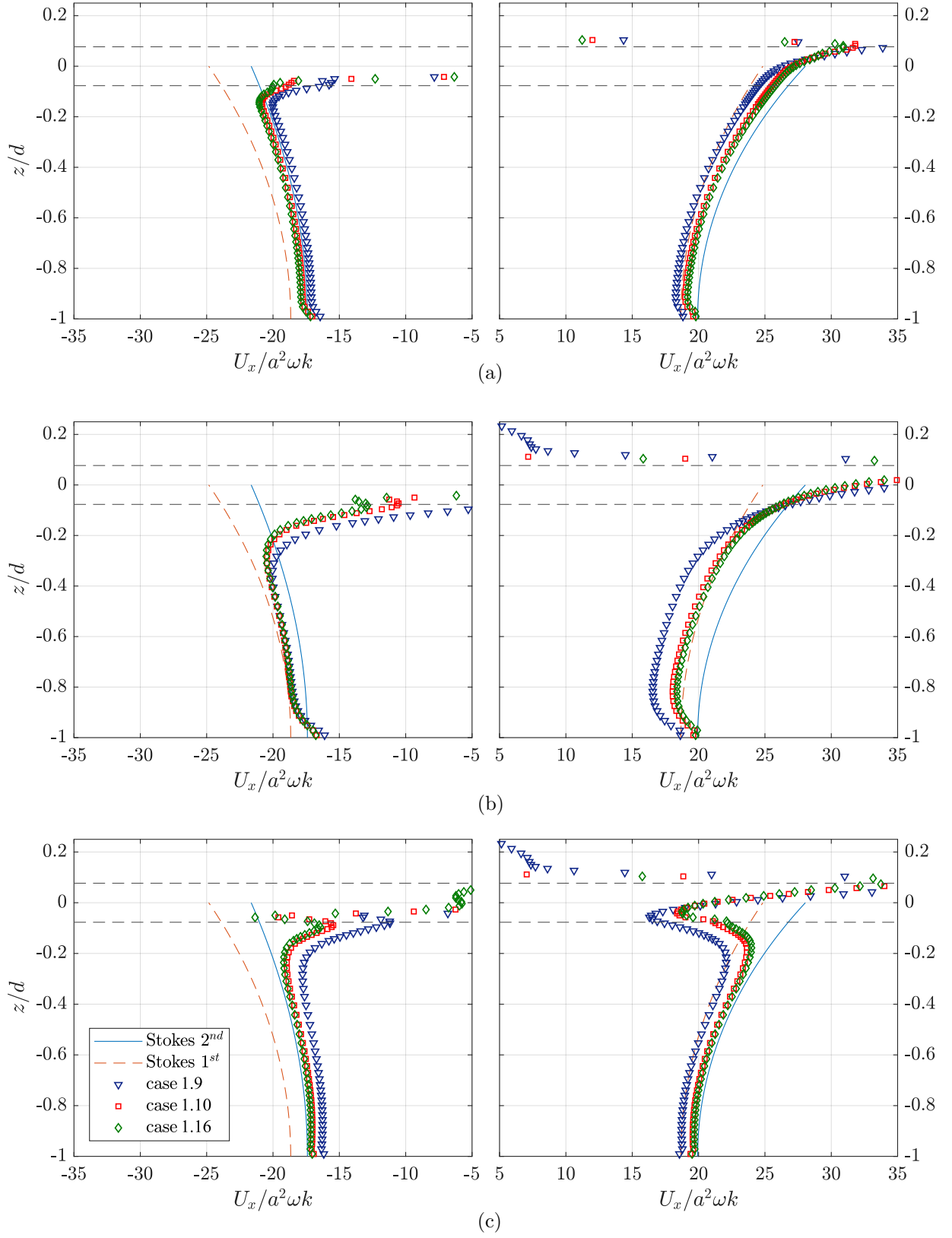


Figure 4.17: Instantaneous horizontal velocity profile in the mid section of the computational domain for the time derivative scheme study with interFoam solver: (a) $t = 10T$; (b) $t = 30T$; (c) Instantaneous horizontal velocity minus the mass transport velocity averaged over T at $t = 30T$

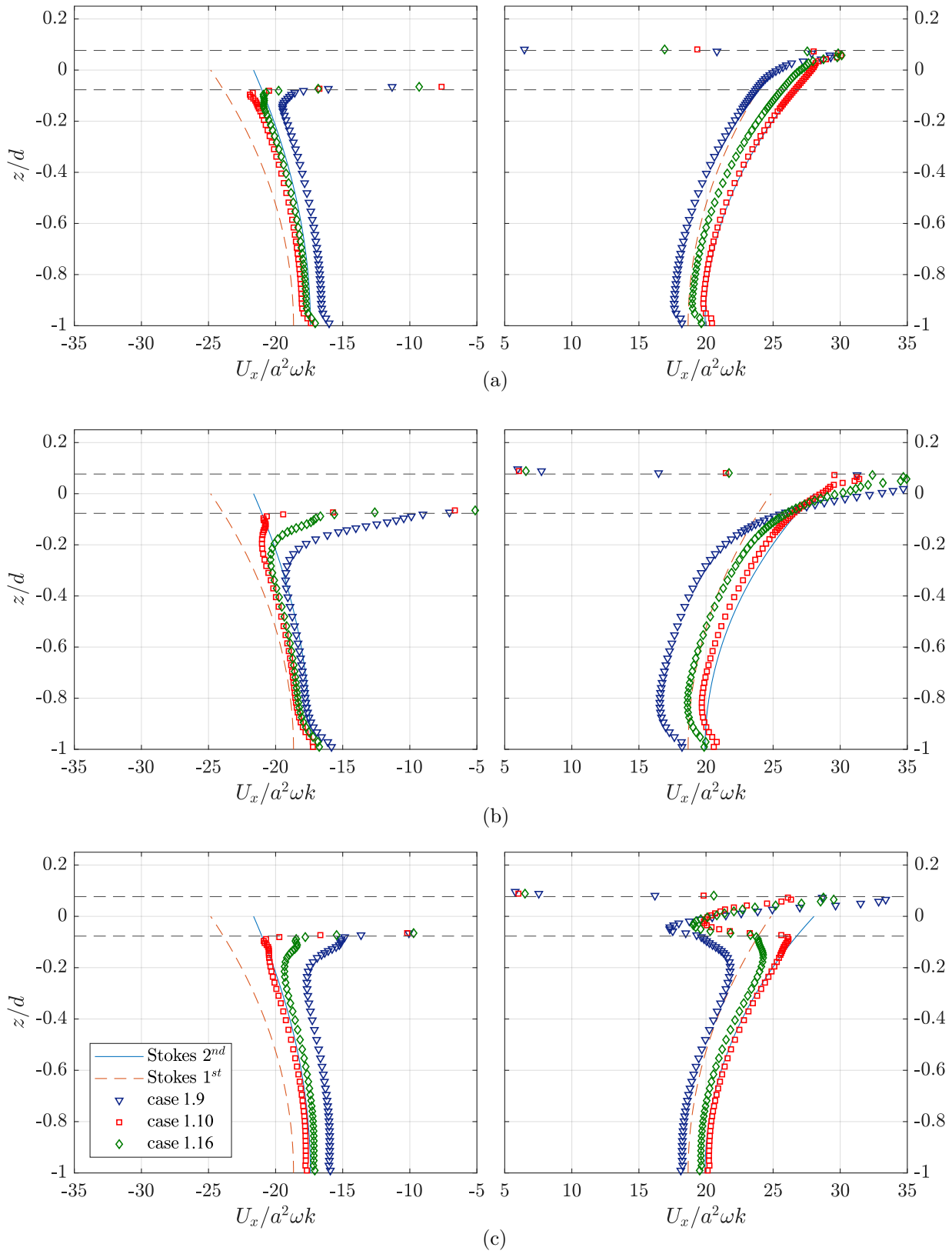


Figure 4.18: Instantaneous horizontal velocity profile in the mid section of the computational domain for the time derivative scheme study with gfmFoam: (a) $t = 10T$; (b) $t = 30T$; (c) Instantaneous horizontal velocity minus the mass transport velocity averaged over T at $t = 30T$

Conclusion

In this section, two sensitivity tests were carried out, to investigate the influence of the mesh resolution and the numerical scheme. The mesh sensitivity test showed that the coarser mesh results in higher dissipation, and instability for the gfmFoam solver. Dissipation is reduced by reducing the mesh size in the horizontal direction. However, this is not a practical solution because the domain is usually quite long in the horizontal direction. Hence, a non-uniform refined mesh is used ignoring the fact that dissipation may still be high. This problem is partly mitigated by using a second order time derivative scheme. The study related to the numerical schemes shows that:

- Time derivative schemes are second order accurate. For the static mesh problem, a backward scheme can be used. In the case of a dynamic mesh, to maintain the second order accuracy, the Crank Nicholson scheme must be used. The backward scheme was found to be incompatible with dynamic mesh algorithm.
- The gradient scheme must be used with a limiter. For the interFoam solver, the multi-directional face limiter can be used because the spurious air velocity at the free surface is found to be minimal. For the gfmFoam solver, the non-multi directional limiter should be used to minimize the wave dissipation.

4.2 Wave reflection absorption

In this study we examine the performance of different wave absorption methods. Three different methods are compared: the body force absorption with a quadratic coefficient, the relaxation zone and the active wave absorption. The body force absorption and the relaxation zone tests use a similar mesh resolution. The practical approach from Perić and Abdel-Maksoud (2016) is used, where the damping coefficient $C_{d,q}$ varied as $50k, 100k, 200k, 400k$ (see Chapter 2). The recommended value is $C_{d,q} = 100k$ (Perić and Abdel-Maksoud (2016)). The active absorption test can use a finer meshing, since the generation and absorption zones are not required in this case, which is definitely an advantage.

The wave reflection coefficient C_r is calculated based on equation 2.48 and the results are given in table 4.3. The simulations show that the relaxation zone method gives the least reflection. The body force absorption method also gives reasonable results with an optimum value of $C_{d,q} = 100k$ as recommended by Perić and Abdel-Maksoud (2016). The active absorption method gives the highest reflection coefficient.

4.3 Mass transport simulation

The sensitivity study for the numerical scheme showed that in a simulation involving a closed domain, the mass transport velocity has a significant effect on the velocity field, because the return flow affects the velocity profile inside the domain. Hence, it is important to understand how the OpenFOAM® two-phase solver generates this mass transport velocity. To investigate this, we have simulated the experiments of

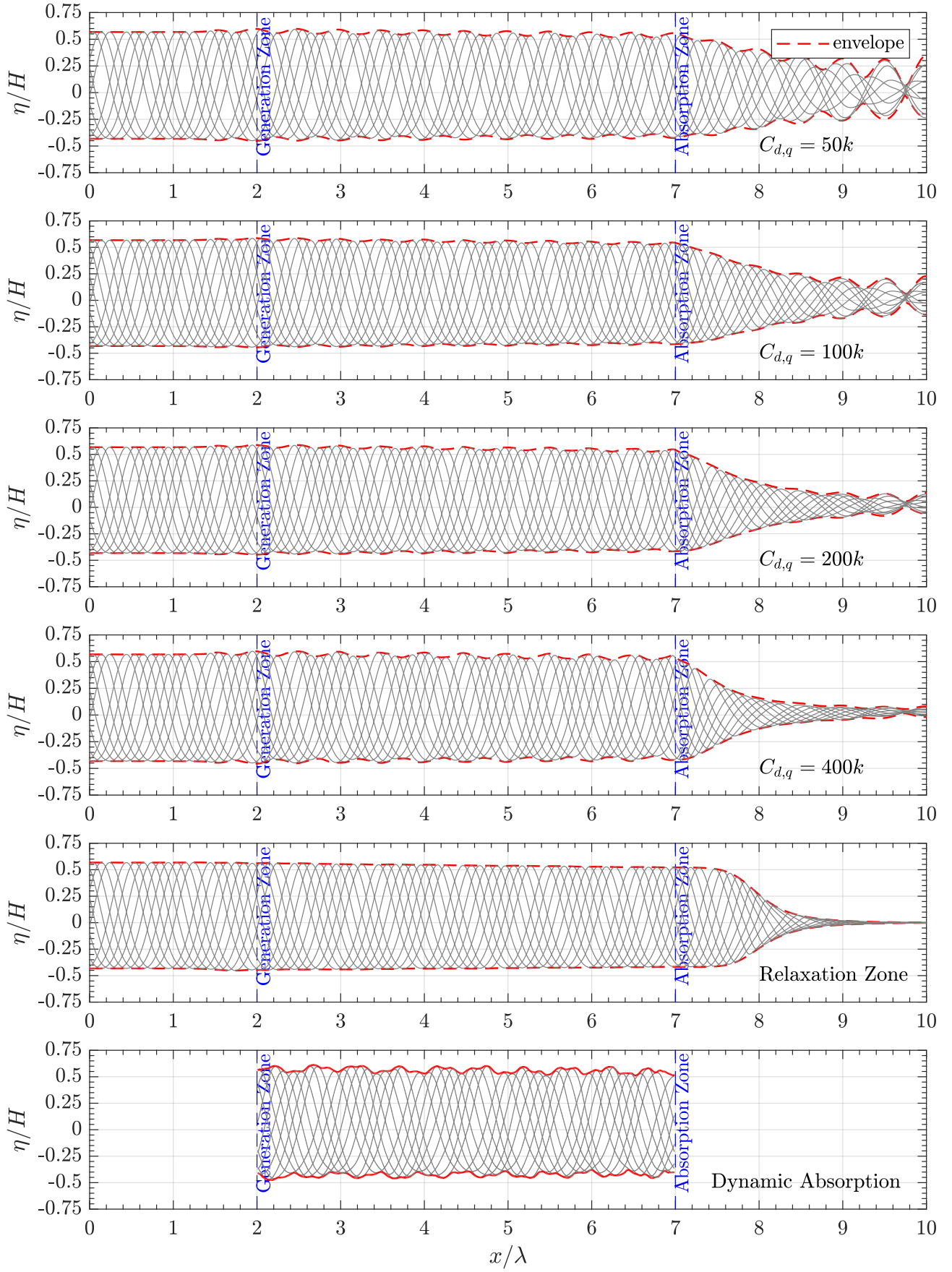


Figure 4.19: Water surface elevation for the study of wave reflexion absorption with interFoam solver

Table 4.3: Reflection coefficient for different absorption methods

| Case | Absorption Type | η_{max}/H | η_{min}/H | C_r |
|----------|------------------------------|----------------|----------------|-------|
| Case 2.1 | body force, $C_{d,q} = 50k$ | 0.5551 | 0.5182 | 3.44% |
| Case 2.2 | body force, $C_{d,q} = 100k$ | 0.5439 | 0.5277 | 1.51% |
| Case 2.3 | body force, $C_{d,q} = 200k$ | 0.5476 | 0.5260 | 2.01% |
| Case 2.4 | body force, $C_{d,q} = 400k$ | 0.5561 | 0.5178 | 3.57% |
| Case 2.5 | relaxation zone | 0.5256 | 0.5215 | 0.39% |
| Case 2.6 | active absorption | 0.5793 | 0.5109 | 6.27% |

Carter (1972).

The experiments of Carter (1972), were performed in a wave flume 12m long, 76cm wide and 20cm deep, with the water depth set to 13cm. The computations have been performed with two different solvers: interFoam and gmFoam. In each case, two different simulations were performed, the first using a physical beach to dissipate the wave similar to the experiment (Figure 4.20) and the second using the relaxation zone method (Figure 4.21). These two approaches are used to understand how the mass transport velocity is influenced by the way the relaxation zone is modeled. The relaxation method uses a damping function which progressively reduces the amplitude of the surface elevation fluctuations; unfortunately, as can be shown, this does not conserve the mass flux passing through the relaxation zone.

The wave parameters are described in Appendix II of Carter (1972), with a wave height of 2cm and a period of 1.01s; this corresponds to a 2nd order Stokes wave. Based on the previous results, the interFoam solver is employed with the face multi-directional limiter since this is supposed to give a better velocity profile.

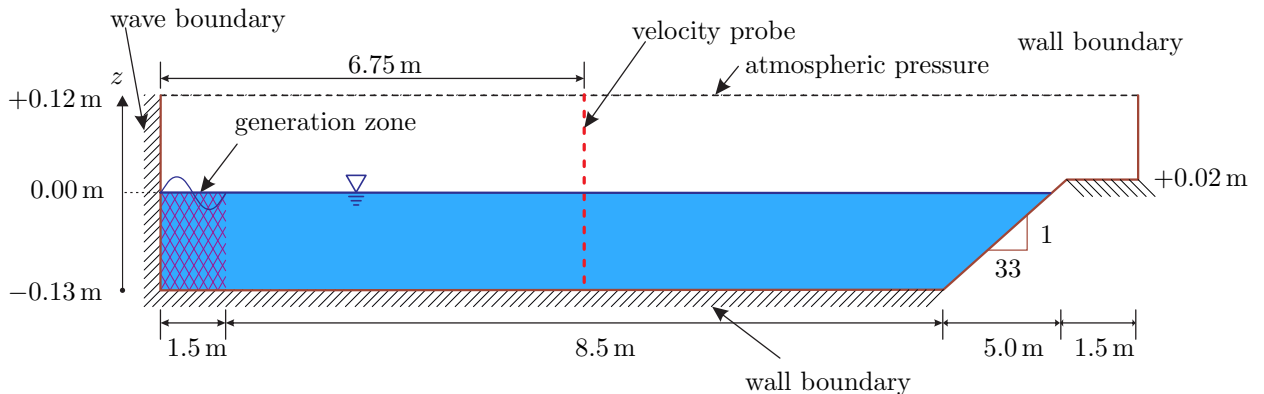


Figure 4.20: Numerical domain for the mass transport analysis with the physical beach as a wave absorber

The system involving the physical beach absorber is described in figure 4.20. The mesh is generated using the blockmesh utility and consists of hexahedral cells. Because of the existence of the physical beach, it is hard to only refine the free surface area because this would induce a distortion of the mesh and the free surface refinement would not be valid anymore. Hence, a uniform size for the mesh from the bed to an elevation of $z = 0.02$ m above the free surface is used with $\Delta x = 10$ mm and $\Delta z = 1.25$ mm. The horizontal and vertical distances above the physical beach

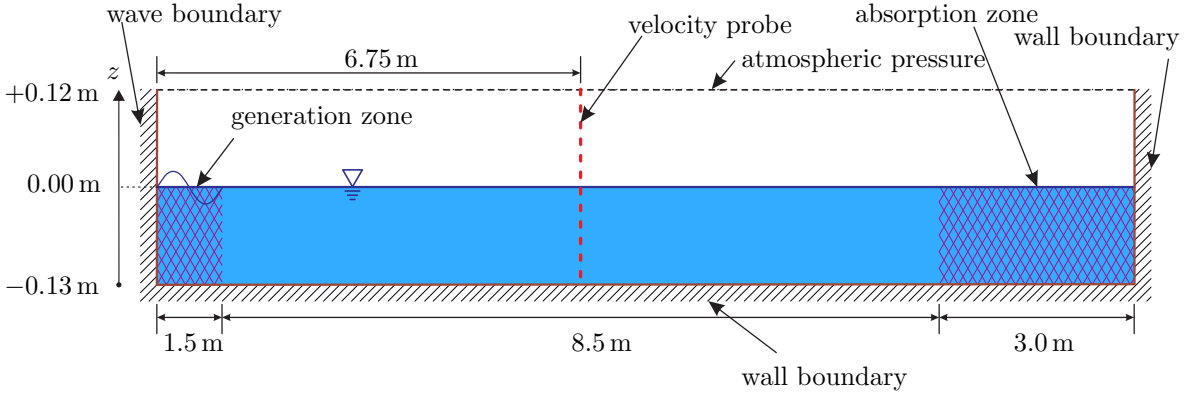


Figure 4.21: Numerical domain for the mass transport analysis with relaxation zone

reduce gradually to $\Delta x = 5$ mm and $\Delta z = 0.5$ mm as described in figure 4.22. For the simulation, the interFoam solver is used, because gfmFoam solver is unstable in the presence of wave breaking because, when the wave breaks, the air pocket is compressed by the water, and this phenomenon is not taken into account in the gfmFoam solver which consequently generates a high pressure spike. The mesh configuration and refinement for the relaxation zone absorber are identical to the ones used for the numerical sensitivity tests as described in figure 4.6.

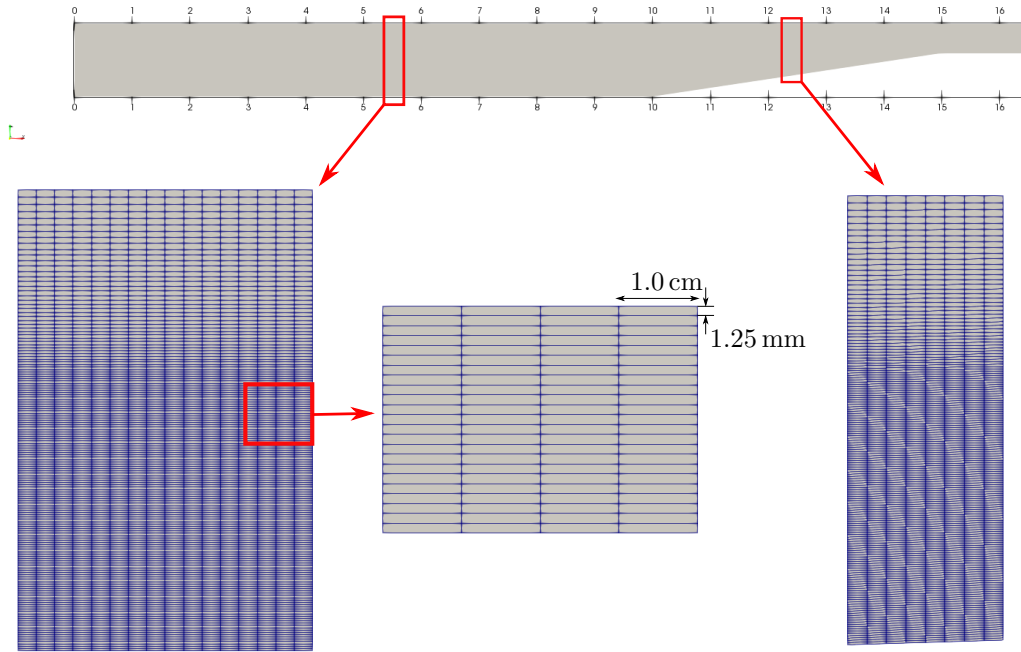


Figure 4.22: Mesh for the simulation of the mass transport with a physical beach absorber

The mass transport velocity is then calculated by integrating the velocity over NT wave periods as follows:

$$U_{m,x}(z) = \frac{1}{NT} \int_{t_0}^{t_{NT}} u_x(z) dt \quad (4.1)$$

where $U_{m,x}$ is the horizontal mass transport velocity at z , N is the number of periods used for the integration (in this case equal to 10), T is the wave period and u_x is the instantaneous horizontal velocity measured by the velocity probe. In the closed channel the conservation of mass dictates that the mass transport induced flux in the direction of wave propagation must be balanced by an equal return flow; thus, in steady state conditions the net mass transport velocity over the water depth must be equal to zero:

$$U_{net,x} = \int_{z=0}^{z=h} U_{m,x}(z) dz = 0 \quad (4.2)$$

The simulation shows that physical beach produces more wave dissipation than does the relaxation zone. The gfmFoam solver also gives less dissipation which is consistent with the preceding study of the sensitivity to numerical schemes. The water surface elevation over the simulation domain is described in Figure 4.23. The horizontal mass transport velocity for both absorber methods is shown in Figure 4.24. There are several conclusions to be drawn from these results. Firstly, as can be seen from Figure 4.25, in steady state conditions, the physical beach configuration satisfies the zero net flux conditions, as required by mass conservation. This is not true, however, for the cases with a relaxation zone, where the net mass flux is positive – in other words, not all of the mass transport induced flux is being returned, which means that mass is effectively being destroyed in the relaxation zone. (The reason that the water level in the simulation does not gradually drop over time is that the water level is maintained at a certain height in the relaxation zone.) Given this conclusion, it might be expected that the physical beach would produce the best agreement between the simulations and the experiments (and theory of Longuet Higgins) for the vertical profile of the mass transport velocity (Figure 4.24) but this is not the case. The numerical solutions overestimate the fluid velocities close to the free surface, because of a failure to model correctly the jump condition at the free surface – the water velocities in the cells containing the interface are much too high, and as a result the mass transport velocity in the direction of wave propagation is greatly overestimated, as can be seen from Figure 4.24. Consequently, the case with the physical beach must overestimate the return velocity, in order to conserve mass, and this effect is visible in the high values of negative velocity close to the bed. Paradoxically, the case with the relaxation zone, because it does not conserve the mass flux, produces a lower over estimate for the negative mass transport velocity. So an initial error in the estimation of the near surface velocities is partially corrected by an error in the conservation of mass flux. It follows from this that if the incorrect representation of the jump condition at the free surface is corrected, the relaxation zone will perform less well in representing the mass transport velocity.

Conclusion

Computations of the mass transport velocity show that the model over-estimates the velocities close to the surface and this leads to an over-estimate of the positive mass transport velocity close to the surface, and a corresponding over-estimate of the negative mass transport velocity close to the bed. The relaxation method partially corrects for the effects of the over-estimate of the mass transport velocity at the surface through its failure to conserve the mass flux. These problems need to be considered together, because of their influence on the onshore-offshore transport of sediment, but it will be necessary to correct both problems.

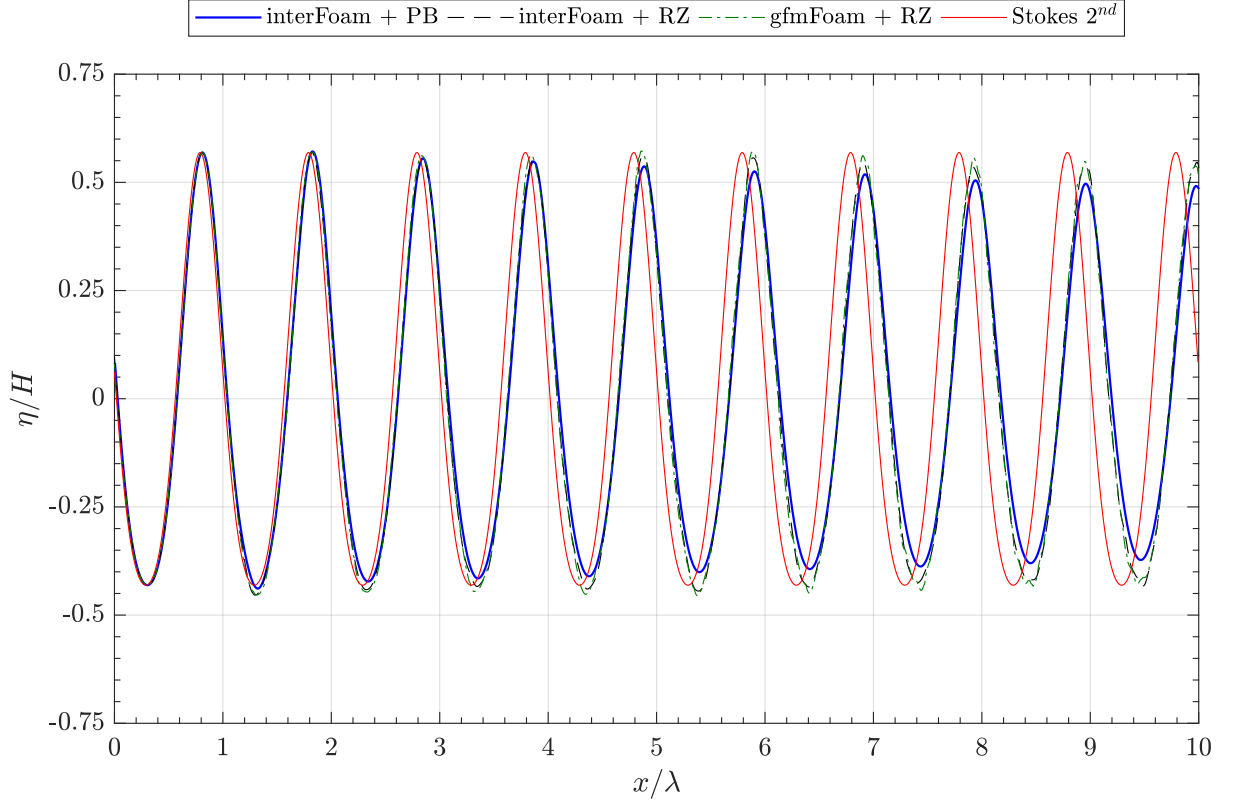


Figure 4.23: Water surface elevation in the study related to the mass transport for $t = 600T$

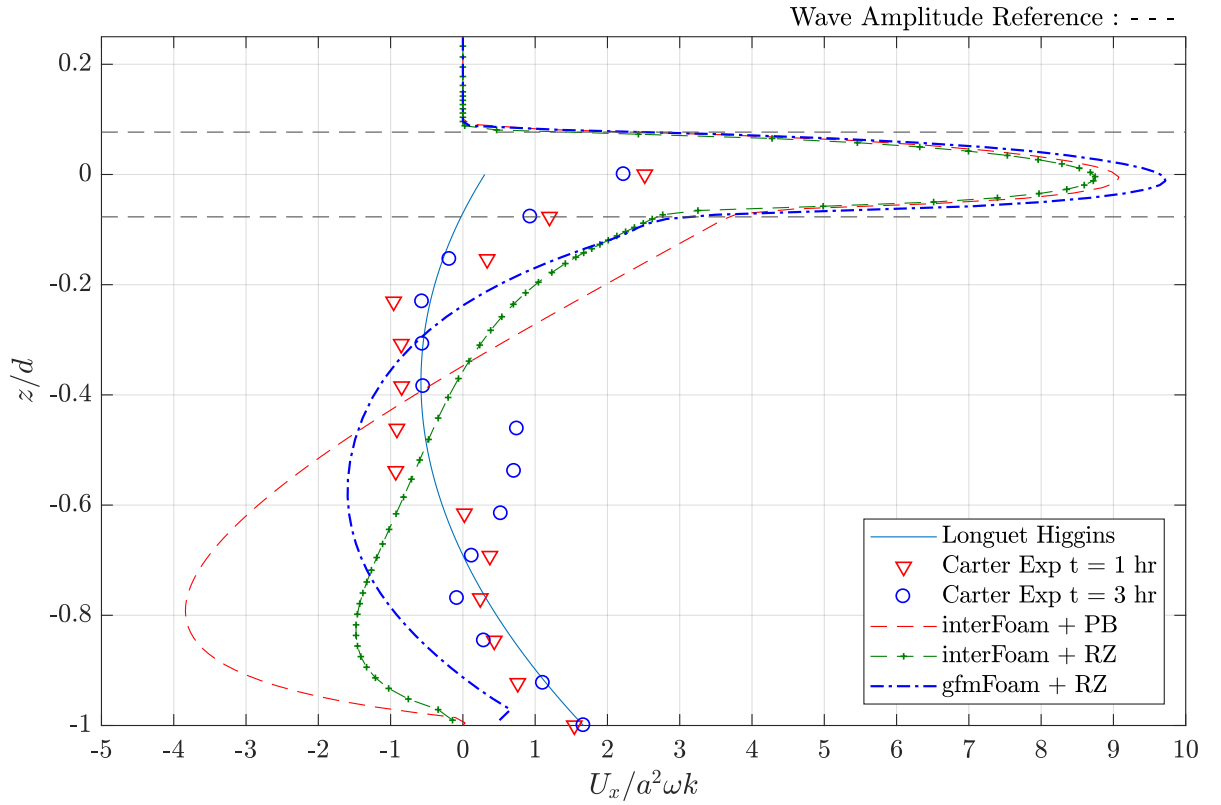


Figure 4.24: Mass transport velocity comparison for different wave absorber types

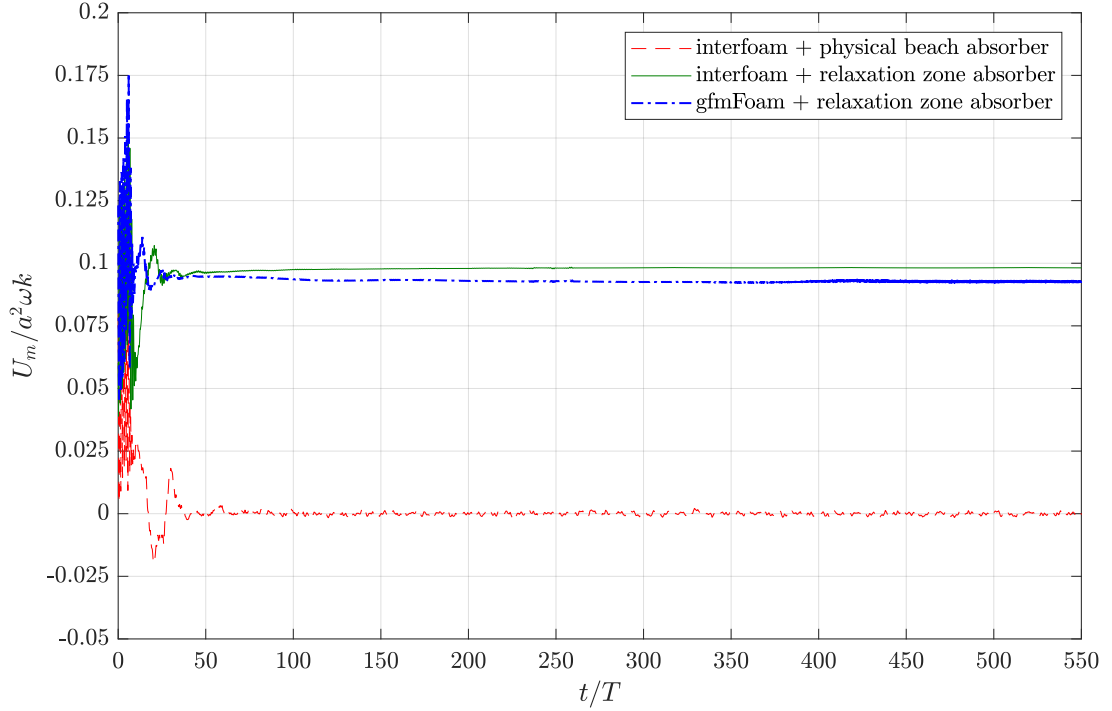


Figure 4.25: Mass transport velocity integrated over the depth for different wave absorber types

4.4 Oscillatory flow boundary layer

The sediment transport calculation depends on the accuracy of the bed shear stress estimate. From section 2.2.8, it is known that the wave boundary layer plays an important role. In the wave related problem, the boundary layer development depends on the wave period—the boundary layer grows as the flow accelerates, and reaches a maximum thickness under the wave crest and the wave trough. The viscous effect at the bottom creates a lag between the maximum velocity near the bed and the free stream velocity with the result that at certain phases and certain elevations, the shear stress is acting in the direction of the flow, rather than against it, causing overshoot in the velocity profile. The idealized case for this problem is known as the oscillatory flow boundary layer or the Stokes boundary layer problem.

The oscillatory flow boundary simulation is based on the experiment run by Mujal-Colilles et al. (2014). A U-shaped tunnel (Figure 4.26) is used to generate an oscillatory flow with a smooth or a rough wall. The section of the central part of the system is 25cm high and 20cm wide. The total flume length is equal to 3.70m with a laser sheet measurement section of length 1.50m. The flow field is measured using a particle-image velocimetry (PIV) technique. In the proposed simulation, the studied domain is restricted to half of the tunnel height with a length of 3.70m. Based on the experiments, two Reynolds numbers of Re 3800 and 12700 are considered. The data related to the test case are given in table 4.4.

The simulation boundary condition are compatible with a flow between two flat plates with an oscillation of the free stream velocity, where U_∞ is described as:

$$u_0 = U_\infty \sin \omega t \quad (4.3)$$

The Reynolds number is defined as (Jensen et al., 1989):

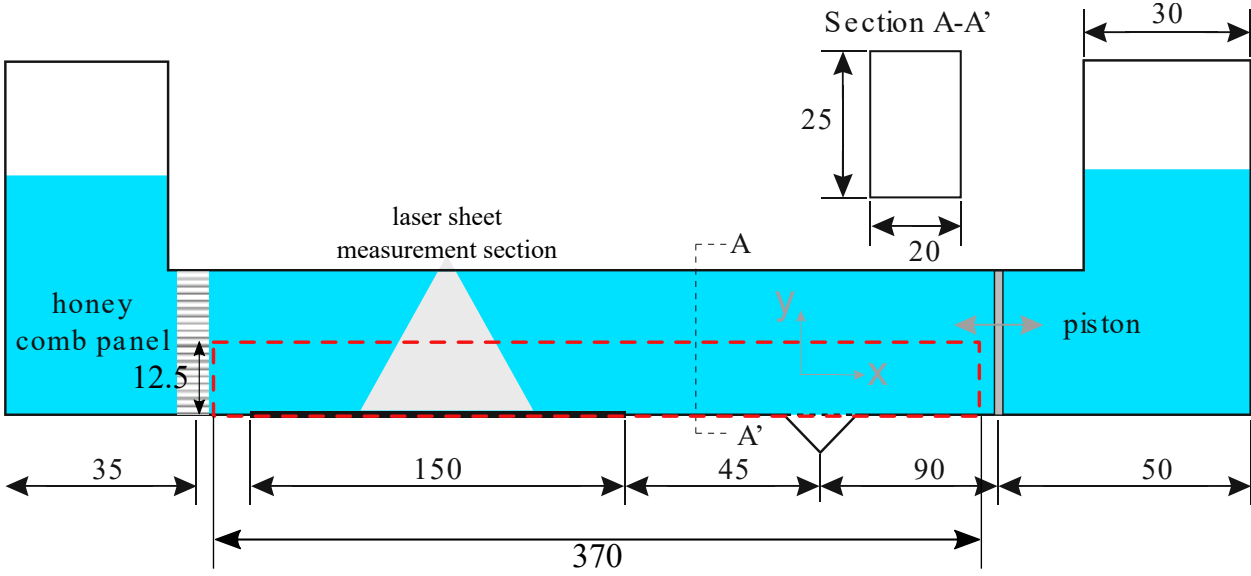


Figure 4.26: U-shaped tunnel set up in experiment by Mujal-Colilles et al. (2014), the simulation domain is marked in red dash line

Table 4.4: Test case parameters for the oscillatory boundary layer

| Case no. | $T(s)$ | $A(mm)$ | $U_{\infty}(mm\ s^{-1})$ | Re | $\delta(mm)$ | $A/2D_{50}$ | $\Delta z_b(mm)$ | $\delta/\Delta z_b$ |
|--------------------------------|--------|---------|--------------------------|-------|--------------|-------------|------------------|---------------------|
| Smooth wall | | | | | | | | |
| 4.1 | 3.3 | 45.5 | 86 | 3800 | 2.2 | - | 0.5 | 4.400 |
| 4.2 | 3.3 | 45.5 | 86 | 3800 | 2.2 | - | 5 | 0.440 |
| Rough wall | | | | | | | | |
| 4.3 | 5 | 100 | 125 | 12700 | 3.0 | 33 | 0.5 | 6.000 |
| 4.4 | 5 | 100 | 125 | 12700 | 3.0 | 33 | 1.5 | 2.000 |
| 4.5 | 5 | 100 | 125 | 12700 | 3.0 | 33 | 5 | 0.600 |
| Friction factor by Rijn (2007) | | | | | | | | |
| 4.6 | 5 | 100 | 125 | 12700 | 3.0 | 33 | 1.5 | 2.000 |
| 4.7 | 5 | 100 | 125 | 12700 | 3.0 | 33 | 5 | 0.600 |
| 4.8 | 5 | 100 | 125 | 12700 | 3.0 | 33 | 10 | 0.300 |

$$Re = \frac{aU_\infty}{\nu} \quad (4.4)$$

where A is the amplitude of the free stream motion and is defined as U_∞/ω . Two methods for the bed shear stress calculation are used: the logarithmic law and the friction factor formulation from van Rijn (2007).

Smooth wall test

The smooth wall test is carried out for $Re = 3800$ in the laminar flow regime. Two mesh configurations have been tested, with near bed cell heights Δz_b of 5mm, considered as a coarse mesh and Δz_b of 0.50mm, considered as a fine mesh. The grid cells in the coarse mesh are too large to resolve the boundary layer, because the mesh height is greater than δ . However, for the fine mesh, the boundary layer is resolved with four cells ($\delta/\Delta z_b = 4.4$). The simulation results will be compared with experimental data and with the analytical solution for a laminar oscillatory flow. The analytical solution is given on section 2.2.8 equation (2.56) and equation (2.58).

The instantaneous velocity profiles have been plotted in Figure 4.27 for 6 different phase angles, for the two simulations, the experimental data and the analytical solution for laminar flow. In general the experimental results agree well with the analytical solution, although the differences in the free stream velocities ($z/\delta_L \gtrsim 5$) suggest that the driving force in the experiment might have had some higher frequency components (the U-tube will have its own natural frequency, and although the authors don't state the water level in the legs of the U-tube, it is likely that the natural period of the system was of the order of 0.7s-1s). The numerical simulations with the fine resolution agree excellently with the analytical profiles, at all phase values, and at all vertical positions. The simulations with the coarse resolution also agree reasonably well with the analytical solution, although they do not quite capture the velocity overshoot, so the difference is greatest at the extreme values of the phase. So if the only variable of interest were the velocity, the coarse resolution could be considered acceptable. Unfortunately, the parameter that is of greatest interest is the bed shear stress, which depends on the gradient of the velocity profile, at the bed. As Figure 4.27 illustrates, a linear interpolation of the velocities close to the bed will result in a large underestimate of the bed shear stress for the simulation with a coarse resolution, because of the failure to resolve the velocity profile in the regions $0 < z/\delta_L < 2$. This point is illustrated in detail in Figure 4.28, where the bed shear stress has been plotted as a function of phase, for the two numerical simulations and the analytical solution. The results from the fine resolution simulation agree very closely with the analytical solution, with just a very slight phase shift – the amplitude of the variation in shear stress is captured perfectly. On the other hand, as already predicted, the coarse resolution underestimates the amplitude of fluctuation of the bed shear stress, and introduces a significant phase shift. (The experimental measurements of bed shear stress have not been plotted because they were found not to agree with the analytical solution. Mujal-Colilles et al. (2014) attempted to calculate the bed shear stress from their measured velocity profiles using two methods – the sum of the viscous and Reynolds stress terms, and the momentum integral approach. They found that the momentum integral approach produced bed shear stresses twice those obtained from the sum of viscous and turbulent stresses, and that both methods significantly over-estimated the values compared with the analytical solution.)

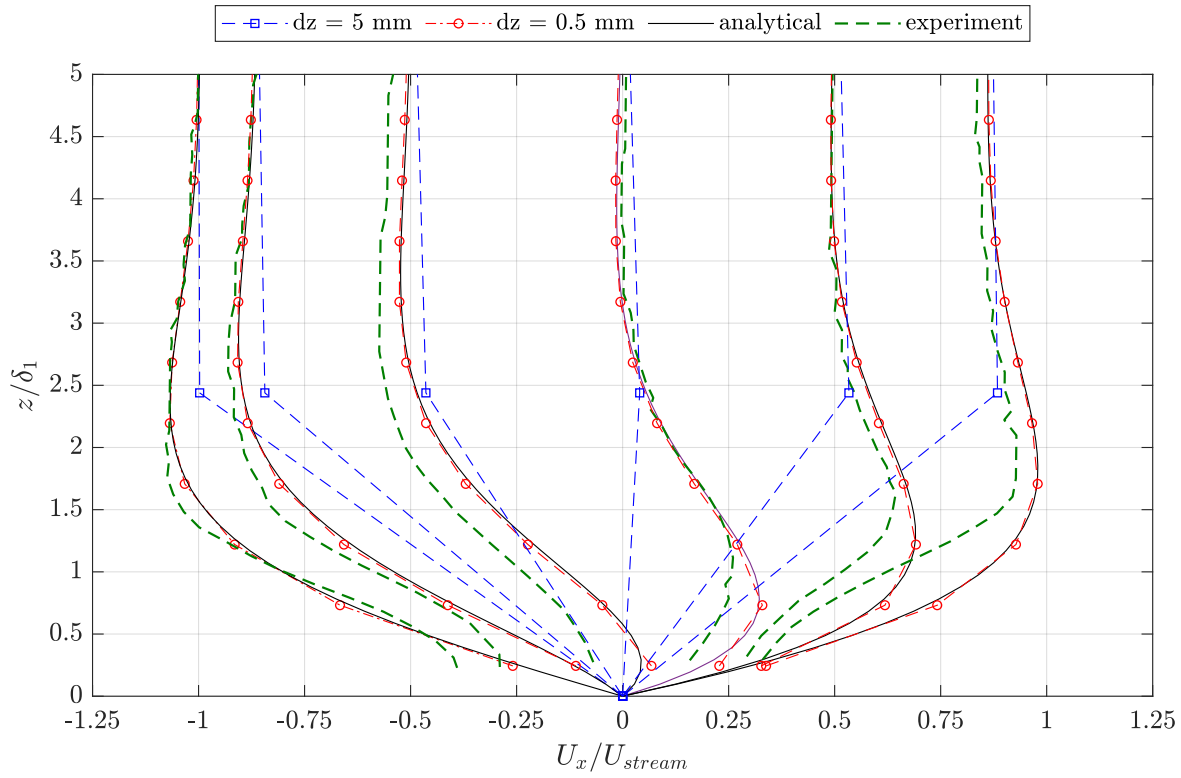


Figure 4.27: Velocity profile for an oscillatory flow with $Re = 3800$ with a smooth wall

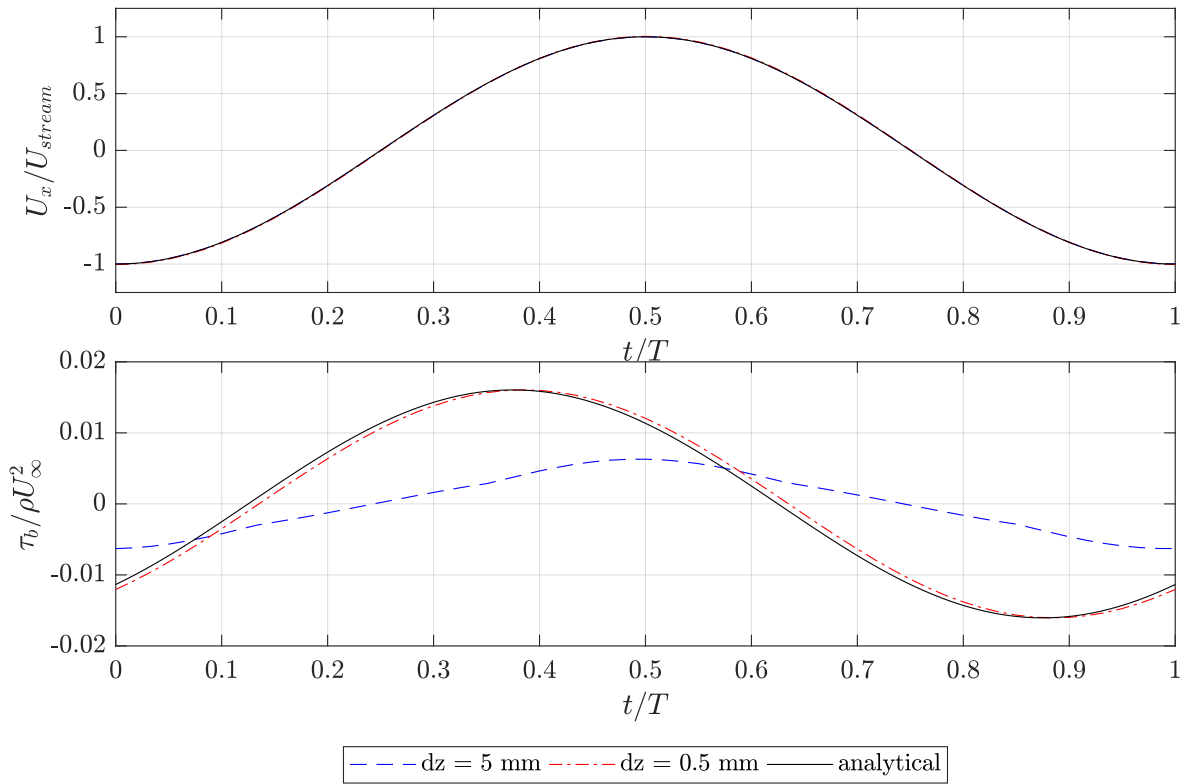


Figure 4.28: Bed shear stress for an oscillatory flow with $Re = 3800$ with a smooth wall

Rough wall test

A second set of simulations has been performed, for a rough wall boundary at a Reynolds number $Re=12700$, which corresponds to one of the experimental tests of Mujal-Colilles et al. (2014), which they considered as a transition to the rough turbulent regime. Three mesh resolutions were tested – $\Delta z_b = 5mm, 15mm$ and $0.5mm$, with the $k-\omega$ SST turbulence model. The bed shear stress in the simulations was computed using two different approaches – the rough wall law (equation 2.105) and the friction factor prediction (equation 2.106) with $f_w = 0.047$ with the time-varying bed shear stress is calculated using equation (2.59).

The instantaneous velocity profiles are plotted in Figure 4.29, for 6 different phase angles. For certain phase angles the analytical and experimental profiles coincide almost exactly, despite the fact that the analytical profiles are for laminar flow over a smooth bed. At the extreme values of phase angle the experimental profiles show much higher velocities close to the bed (and hence imply very high values of the shear stress) but this is probably partly due to the difficulty of obtaining reliable PIV data close to the boundary. However the amplitude of oscillation measured in the experiments agrees reasonably closely with that predicted by the analytical solution. It is therefore reasonable to continue to compare the numerical solutions with the analytical solution. The results for the three different resolutions show that only the finest resolution ($\Delta z_b = 0.5mm$) is capable of capturing all the details of the velocity profile; the coarsest resolution, in particular, introduces both a phase shift and a large reduction in the velocity amplitude close to the bed.

The time varying bed shear stress has been plotted in figure 4.30, for the two calculation methods and the three different grid resolutions. For both methods, the grid resolution has a significant effect on the calculated results. For the method based on eq. 2.105 the two coarser resolutions give similar results, with just a shift in the phase of the maximum value, but the finest resolution shows an increase in the amplitude of the bed shear stress, and a phase shift – the maximum shear stress leads the maximum velocity by about 7.2° . The shear stress computed from f_w is much more sensitive to grid resolution, but the effect is the opposite to that for the first method – increasing the resolution (i.e. decreasing the grid spacing) *reduces* the amplitude of oscillation of the shear stress, and the result for the finest grid resolution ($\Delta z_b = 15mm$) is much smaller than the amplitude calculated with any of the grid resolutions for the first method. If we assume, based on the preceding results for the laminar boundary layer, that the first method, with $\Delta z_b = 0.5mm$ provides the best estimate for the bed shear stress, then it follows that the best estimate for the bed shear stress using the method with f_w is provided with a resolution $\Delta z_b = 10mm$, and the only significant difference between the two methods then comes from the phase of the shear stress, since the f_w method computes a phase *lag* of 14.4° , whereas the earlier method produced a phase *lead* of 7.2° . All the profiles exhibit two ‘shoulders’ where the shear stress flattens out around zero; this is because, if the turbulent eddy viscosity depends on time (as it should) then the product of the eddy viscosity and the vertical gradient of the velocity – $\nu_t du/dz$ – must contain a term in the square of the velocity, and hence produce a plateau around zero.

The effective bed friction factor f_w can be back-calculated from the shear stress calculations, for both methods, and all three resolutions, and this has been plotted

in figure 4.31, together with the estimates of Kamphuis (1975), Rijn (2007) and Pedocchi and Garcia (2009). This confirms that the grid resolution has a strong influence on the shear stress estimate, and that the log profile method (eq. 2.105) should be used when the grid resolution is much smaller than the thickness of the boundary layer ($\delta/\Delta z_b > 5$), but that the friction factor approach should be used when the grid resolution is larger than the boundary layer thickness ($\delta/\Delta z_b < 0.5$). The results also show that the estimate from Pedocchi and Garcia (2009) is probably too low, and that the estimates from Rijn (2007) and Kamphuis (1975) might be a little high.

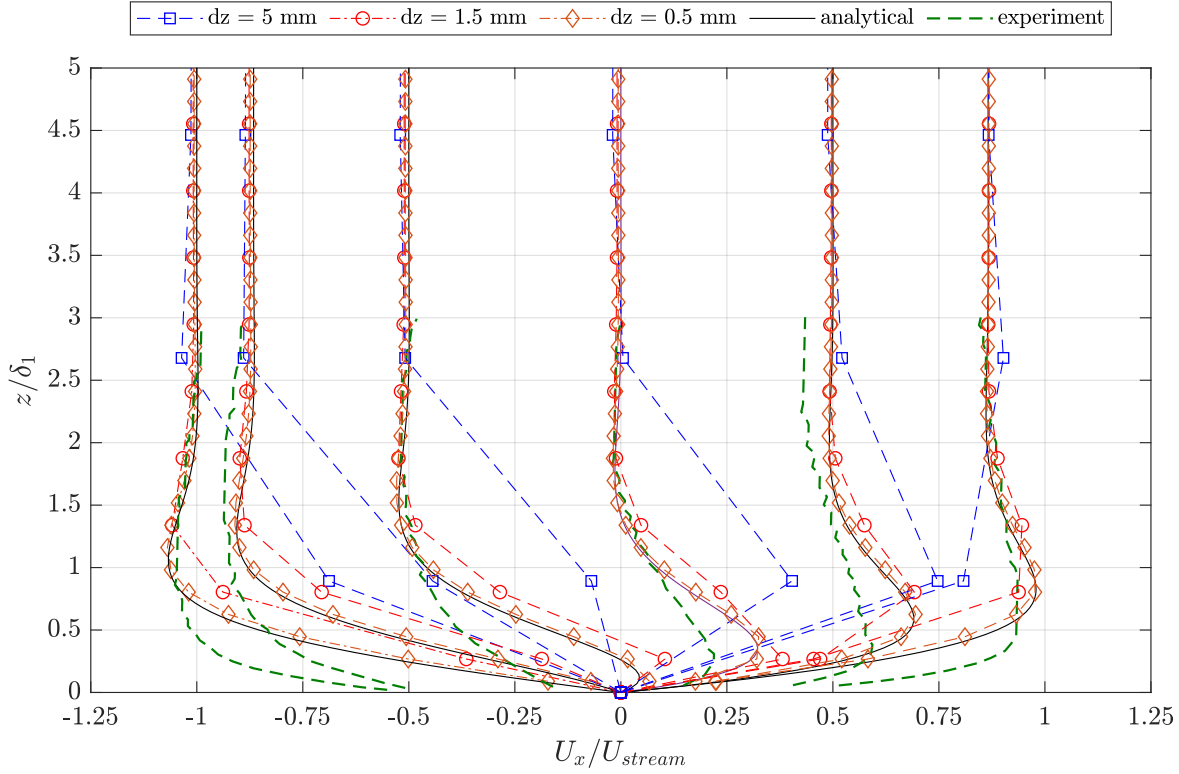


Figure 4.29: Velocity profile for an oscillatory flow with $Re = 12700$ for $d_{50} = 1.50$ mm

Conclusion

In this chapter, the oscillatory boundary layer is investigated based on the experiments by Mujal-Colilles et al. (2014). The simulation results for the laminar case showed a good agreement with the analytical solution. The rough wall case showed that the bed shear stress calculation is dependent on the near wall mesh size. The logarithmic law method needs to resolve the boundary layer and the near wall mesh height should be less than the boundary layer thickness δ . The friction factor method on the contrary must be used with the coarse near wall mesh, where the near wall velocity is not affected by the boundary layer.

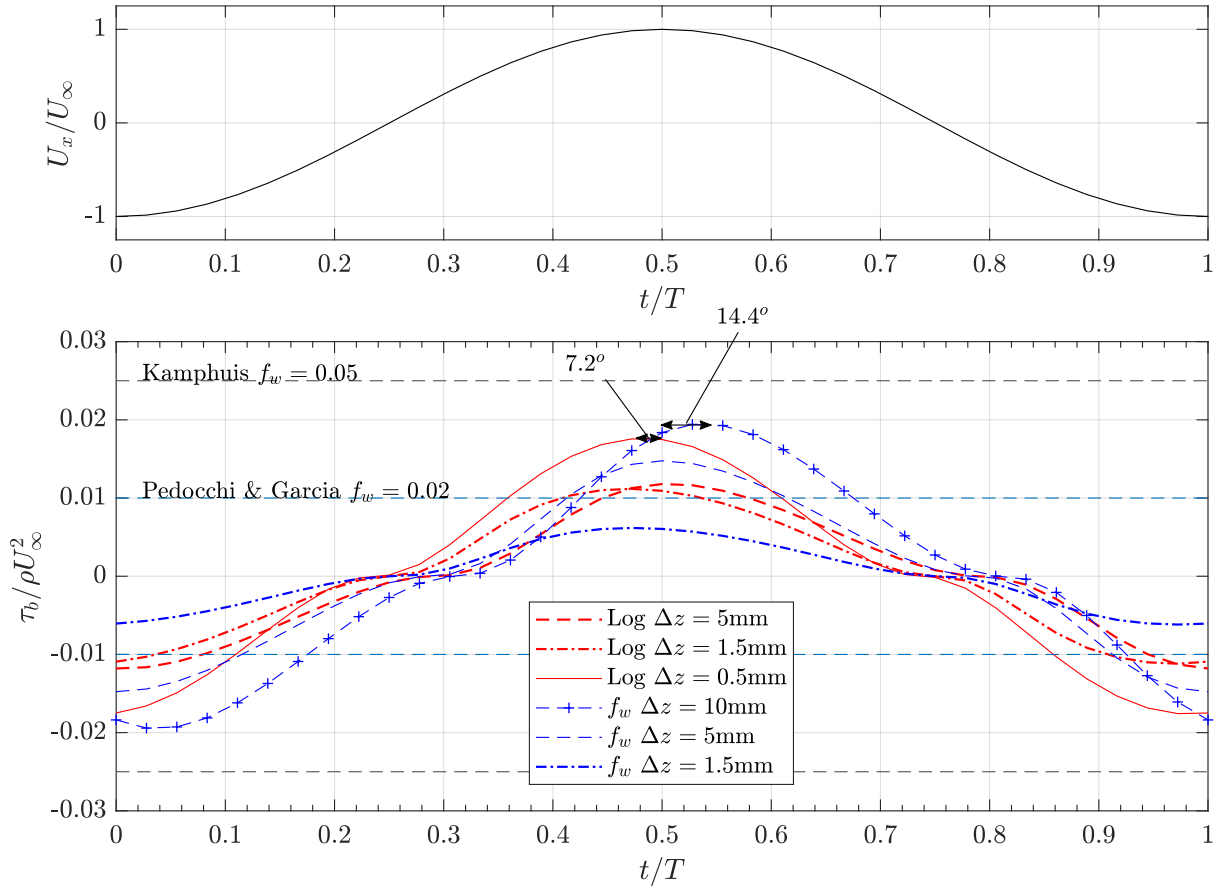


Figure 4.30: Bed shear stress for an oscillatory flow with $Re = 12700$ for $d_{50} = 1.50 \text{ mm}$

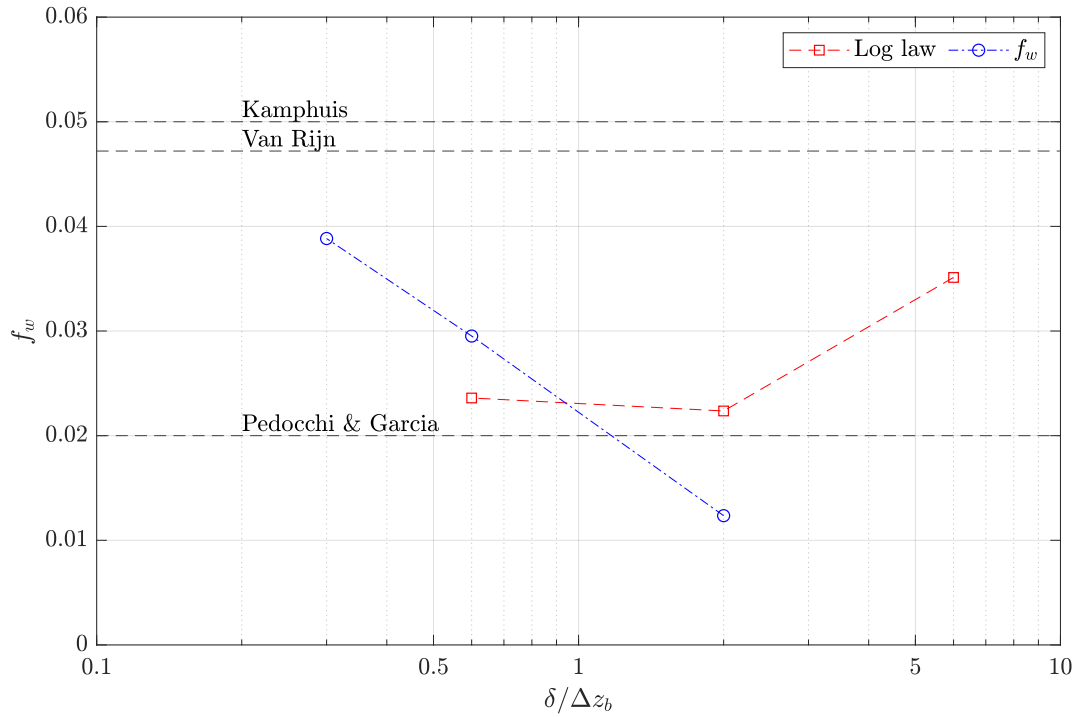


Figure 4.31: Bed shear stress for an oscillatory flow with $Re = 12700$ for $d_{50} = 1.50 \text{ mm}$

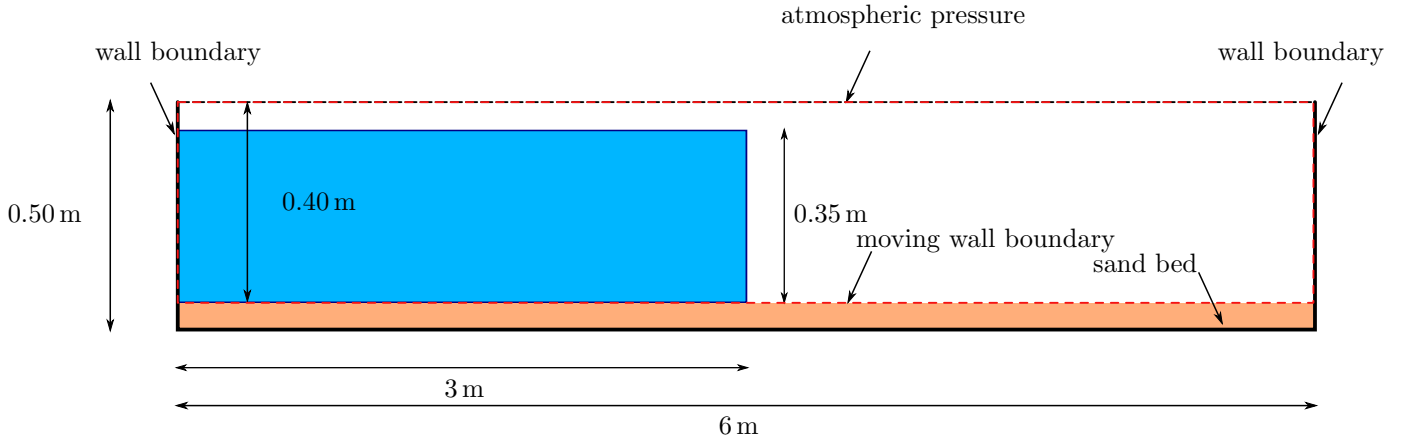


Figure 4.32: Numerical domain configuration for the simulation of a mobile dam break flow

4.5 Mobile dam break case

The sediment transport and bed deformation module is used to calculate scour underneath a dam break flow. The dam break flow case is suitable for testing the model performance because it requires the simulation of an unsteady flow with complex free surface dynamics. The model itself was already tested for steady flow conditions in Zhou (2016) and performed well. The test case here is based on the experiment of Spinewine et al. (2005). Spinewine's experiment, which was performed in a flume 6m long, 0.4m wide and 0.5m high. A vertical gate was installed half-way along the flume, impounding water on one side to a depth of 0.35m; this gate could be lifted rapidly, releasing the water, to simulate a dam-break flow. The mobile bed was composed of a 10cm thick layer of sand, with a $d_{50} = 1.82\text{mm}$, density 2683kg.m^{-3} and porosity 0.53. Although Spinewine et al. (2005) describe the sediment transport mechanism in the experiment as being essentially sheet flow, several researchers have attempted to simulate this using bed load and suspended load models (Wu and Wang, 2007; Marsooli and Wu, 2014)

The simulation is carried out in 2D with a mesh resolution of 5mm for both x and z directions. A wall boundary is applied for the surrounding flume, and atmospheric pressure is imposed at the top boundary. The suspended load model boundary condition is set using the equilibrium concentration and described in detail in the next section. The $k-\omega$ SST turbulence model with a buoyancy correction is used in the simulation. The mobile bed roughness is set equal to $2.5d_{50}$. The sediment transport simulation is performed for the case of bed and suspended load. The bed load transport is calculated using the formula of Engelund and Fredsøe (1976) whilst the suspended load entrainment rate is calculated based on van Rijn (1984). The suspended load entrainment model is found to give an unreasonably high value for high bed shear stress. A limiter is used as explained in Appendix C. The morphological time step for this simulation is the same as the hydrodynamical time step because a rapid deformation is expected at the beginning of simulation. A full description of the simulation domain is given in figure 4.32. The simulation is performed for 1.25s.

Suspended load model boundary condition

The boundary condition for the suspended load model at the mobile bed is based on the equilibrium concentration of sediment entrainment and deposition. The concentration flux $q_{c,b}$ near the bed is given as:

$$\begin{aligned} q_{c,b} &= \frac{1}{k_q} \frac{\partial C_s}{\partial z} \\ &= \frac{1}{k_q} [E - D] \end{aligned} \quad (4.5)$$

where k_q is a coefficient related to the sediment diffusivity $\nu + \nu_t/\sigma_c$. However, a preliminary study where the flux at the bed boundary was imposed showed some numerical instabilities. So another approach has been adopted, based on assuming that the sediment entrainment provides a source term in the advection-diffusion equation for the sediment concentration. Hence equation 3.10 reads:

$$\frac{\partial C_s}{\partial t} + \nabla \cdot [(\mathbf{U} + \mathbf{V}_s)C_s] = \nabla \cdot [(\nu_e + \epsilon_p) \nabla C_s] + C_{s,f} \nabla \alpha + S(E) \quad (4.6)$$

where $S(E)$ is calculated from:

$$S(E) = \frac{E}{\Delta z_b} \quad (4.7)$$

The boundary condition at the bed for the sediment concentration is set as a zero gradient. The flux at the bed is set equal to the deposition flux because of the influence of fall velocity near the bed. The bed deposition is calculated after the advection-diffusion equation has been solved with $D = C_s V_s$.

Simulation results

Figure 4.33 shows the snapshots of the experiment performed by Spinewine et al. (2005) for $t = 0.25$ s, 0.50 s and 0.75 s. Experimental measurements were made using image processing techniques to separate the flow into clear water, sheet flow and immobile grain regions. To verify the implementation of the suspended load boundary condition at the bed, the sediment mass conservation was calculated as follows:

$$(1 - n)V_{b,net} + V_C = 0 \quad (4.8)$$

where $V_{b,net}$ is the net volume of the bed deformation from the total load transport and V_C is the total suspended load volume in the water column. The simulation shows that the difference between the net volume of the bed and the total suspended load volume is about 1.6 - 2.2% (table 4.5), with the bed net deformation volume slightly larger than the suspended load concentration. This difference may arise from interpolation errors in the bed deformation algorithm as mentioned in Jacobsen (2015).

The suspended load concentration has been plotted in figure 4.34 for 4 different axial locations ($x/L = 0, 0.167, 0.333 \& 0.500$) and three different instants in time ($t = 0.25$ s, 0.50 s & 0.75 s), where $x/L = 0$ corresponds to the location of the gate,

Table 4.5: Sediment mass conservation using source term bed boundary for suspended load

| $t(s)$ | $(1 - n)V_{b,net}(m^3)$ | $V_C(m^3)$ | $ \frac{(1-n)V_{b,net}+V_C}{(1-n)V_{b,net}} $ |
|--------|-------------------------|------------------------|---|
| 0.25 | -5.197×10^{-5} | 5.112×10^{-5} | 1.64% |
| 0.50 | -1.296×10^{-4} | 1.274×10^{-4} | 1.69% |
| 0.75 | -1.610×10^{-4} | 1.574×10^{-4} | 2.19% |

and $t = 0$ to the instant at which the gate is removed. These concentration profiles show that most of the erosion takes place downstream of the gate (the suspended concentration at the gate location remains small throughout, and does not penetrate much into the fluid), with the maximum concentration reaching a value of 0.22 (percent of volume of sediment with volume of water), at the nose of the current. By comparing the profile at $x/L = 0.500, t = 0.75s$ with that at $x/L = 0.333, t = 0.50s$, it can be seen that as the current advances over the sediment bed it is continuing to pick up sediment from the bed – the suspended concentration at the bed increases – although the sediment is not mixed any higher in the water column. Behind the nose of the current the concentration decreases over time ($x/L = 0.333, t = 0.50s$ compared with $x/L = 0.333, t = 0.75s$) indicating that after the erosive power of the flow is decreasing. Since the bed concentration at $x/L = 0.333, t = 0.75s$ is less than that at $x/L = 0.167, t = 0.50s$, it is possible to conclude that some deposition is taking place from the flow behind the nose.

A more complete picture is provided by the results in figure 4.35 which compare the results from the simulation with the results obtained from image processing analysis of the film of the experiment. Three variables are plotted – the height of the water surface (in blue), the upper boundary of the suspended load region (in green) and the boundary of the immobile bed (in red). (The upper boundary of the suspended load, in the simulation, has been defined as the height at which the concentration of suspended sediment drops to 0.01.) These profiles show that the numerical simulation reproduces closely the evolution of the free surface, even in the detailed pictures of the movement of the front of the gravity current. The upper limit of the suspended load region is also reproduced acceptably: the figures show that suspension occurs following the passage of the front of the gravity current, although the model overestimates, *perhaps* a little bit, the height of this region. In fact, it is difficult to estimate exactly where to place this boundary, when comparing with the experiments, since the experimental result depends on the detection of suspended grains, and it is not evident that the optical configuration permitted the detection of the very low concentration chosen as the threshold in the analysis of the computational results. The problem of the definition of the frontier between two regimes is more critical for the definition of the bed elevation, since the experiment assumes that transport takes place as sheet flow above an immobile bed, whereas the simulation assumes that there is also some transport in the form of bed load. So whereas the experimental analysis define the bed as the region in which there is no discernible movement of the grains, the bed load formulae do not, in general, give an estimate for the thickness of the bed load layer. Consequently the estimate of the bed elevation in the simulation would be expected to be higher than that in the experiments, and this is confirmed in Figure 4.35. It can be observed that the general tendency observed in the experiments is reproduced in the simulations, in

particular with the development of an initial scour hole between $x/L_0 = -0.1$ and $x/L_0 = 0.1$. The most significant discrepancy occurs in the region $0.1 < x/L_0 < 0.3$, where the simulation fails completely to reproduce the erosion that is observed in the experiments. Again, this could be explained by the assumption of the existence of a layer of bed load transport without a defined thickness, so to test this hypothesis, we have estimated the thickness of the bed load layer as:

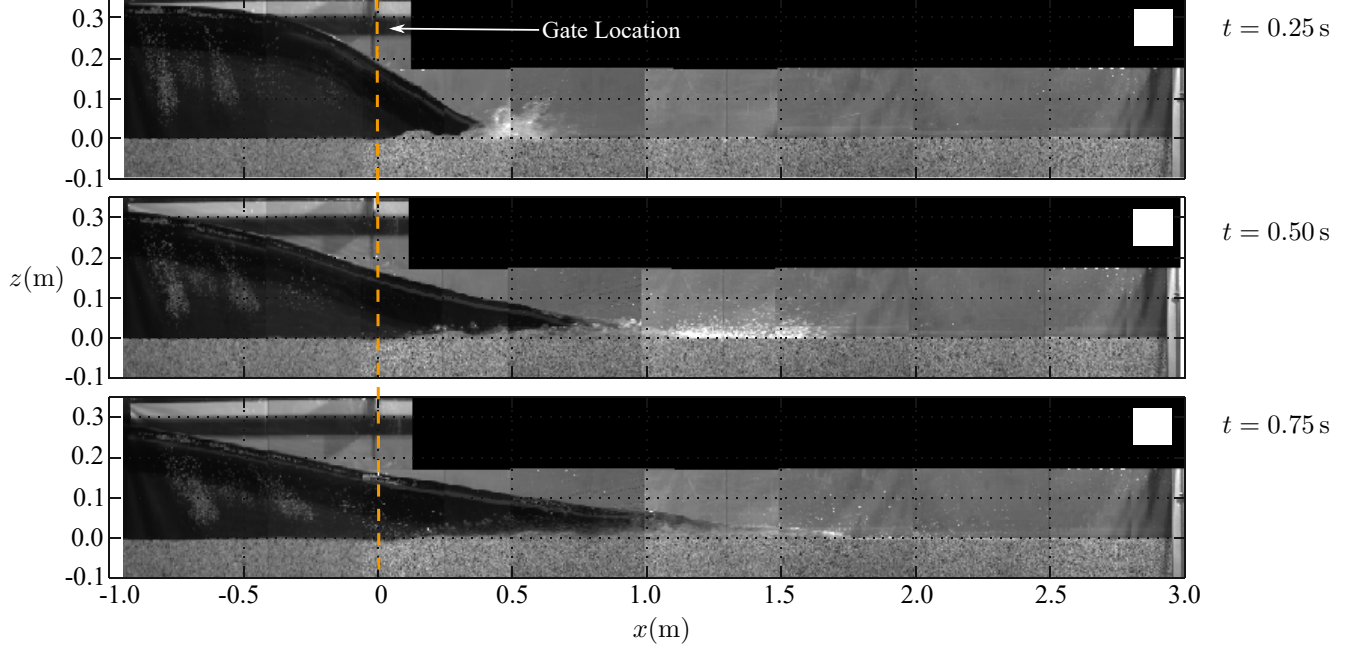


Figure 4.33: Experiment snapshot from Spinewine et al. (2005) for $t = 0.25$ s, 0.50 s, $t = 0.75$ s; x position is measured from the gate

To take account the thickness of the bed load layer, the thickness of particles moving above the bed $H_{q,b}$ is calculated as:

$$H_{q,b} = \frac{q_b}{u_b} \quad (4.9)$$

where u_b can be calculated using the modified Van Rijn formula (Wu and Wang, 2007):

$$u_b = 1.64T^{0.5} \sqrt{\left(\frac{\gamma_s}{\gamma_w} - 1\right) g d_{50}} \quad (4.10)$$

γ_s and γ_w are the specific weights of the sediment and the water respectively. However even if we subtract the estimated thickness of this layer from the bed elevation computed in the simulations, as shown in figure 4.35, the computed height of the region of immobile grains does not agree with that observed in the experiments. For this reason we have developed an alternative approach, based on the explicit modelling of a region of sheet flow.

Alternative sheet flow model using modified suspended load approach

In this section we propose a new model for representing sheet flow, as an adaptation of existing models for the suspended load. The reason for proposing this type of approach is that, in principle, sediment flow in sheet flow is no different from sediment

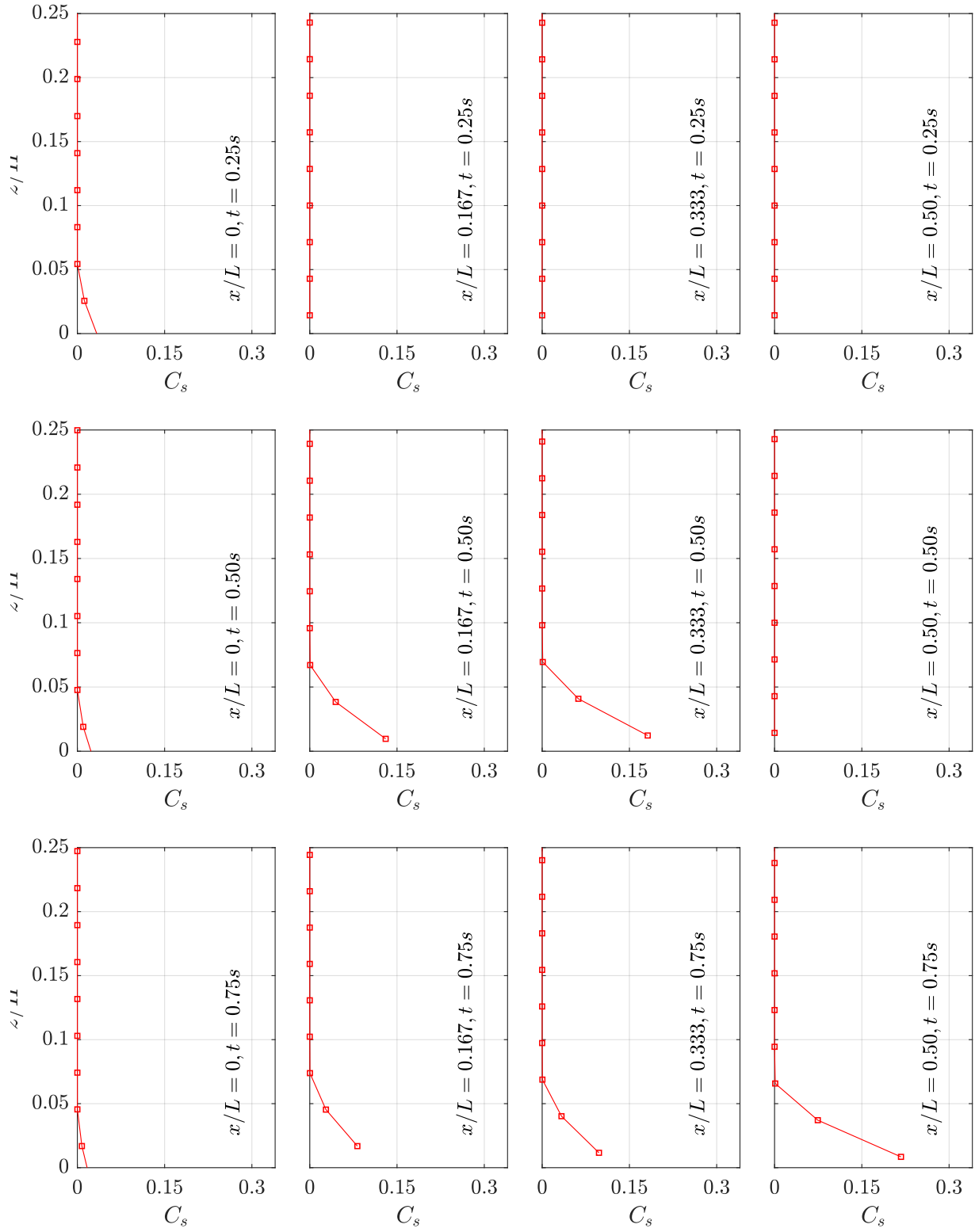


Figure 4.34: Suspended load concentration at 4 different axial locations ($x/L = 0, 0.167, 0.333, 0.50$) and three different instants in time ($t = 0.25s, 0.50s, 0.75s$).

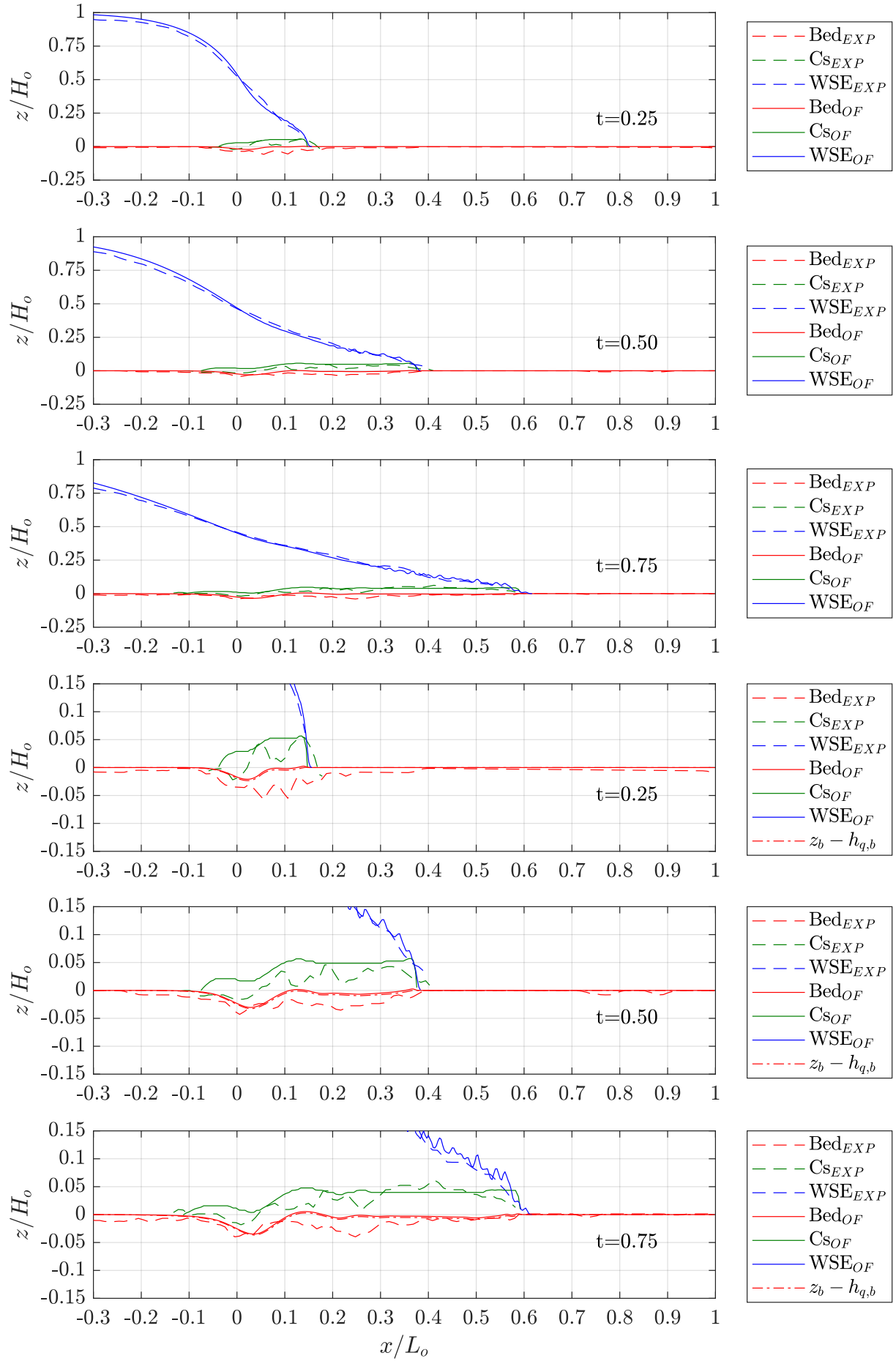


Figure 4.35: Simulation results for a mobile dam break simulation for $t = 0.25$ s, 0.50 s, 0.75 s; More detailed view near the gate opening (3 last figures)

flow in the suspended load, except that the dispersive process is provided as much (or even more so) by particle-particle collisions as by the fluid turbulence, and that, in principle, it ought to be possible to have a flow with a transition from sheet flow at the bed to suspended flow further from the bed, without requiring two explicitly different models to represent the two regimes. To model sediment transport in the sheet flow we therefore assume that the particle dispersion is provided by particle-particle collisions, and can be modelled by the kinetic theory of granular flow, based on the work of Ding and Gidaspow (1990) where the bulk viscosity, ϵ_p , is given as:

$$\epsilon_p = \frac{4}{3} C_s \rho_s d_{50} g_0 (1 + e) \sqrt{\frac{T}{\pi}} \quad (4.11)$$

where C_s is the solid fraction, ρ_s is the solid density, d_{50} is the sediment median diameter, e is the restitution coefficient for particle-particle collisions and T is a measure of the energy fluctuation. g_0 is a radial function, defined as:

$$g_0 = \left[1 - \left(\frac{C_s}{C_{max}} \right)^{1/3} \right]^{-1} \quad (4.12)$$

in this work, the energy fluctuation is represent as the vertical gradient of horizontal velocity, assuming that the particles only diffuse in the vertical direction. The particle diffusion then described as:

$$\epsilon_p = \frac{4}{3} \pi r^3 r g_0 \frac{\partial U}{\partial z} C_N^{2/3} \quad (4.13)$$

Here C_N is the number of particles per cubic meter and r is the sediment particle radius taken as $0.5d_{50}$. The suspended load transport equation is written in terms of a sediment concentration C_s which is related to C_N by:

$$C_s = \frac{4}{3} \pi r^3 C_N \quad (4.14)$$

where V_p is the sediment particle volume. Hence equation 4.13 becomes:

$$\epsilon_p = k_p \frac{4}{3} \pi r^2 g_0 \frac{\partial U}{\partial z} C_s^{2/3} \quad (4.15)$$

and k_p is a calibration coefficient. The suspension initiation is still based on the empirical formulation given by van Rijn(1984).

Simulation results

The configuration is similar to that for the dam break case without the bed load transport module. A second configuration was prepared using a finer mesh with Δ_z of 2 mm to investigate the influence of grid resolution, and, as can be seen in figure 4.36 the grid resolution plays an important role in determining the thickness of the suspended sediment layer. The results from that simulation show that it is necessary to use a fine resolution close to the bed, so the rest of the analysis will be performed on the results from that simulation. As can be seen from the plots at $t = 0.5s$ and $t = 0.75s$ the use of a sheet flow model reduces the height of the suspended layer significantly, bringing it much closer to the values measured in the experiments, and it also provides an elevation profile for the boundary with the immobile grains in the bed which is close to that measured in the experiments. The new model also avoids the deposition that was observed in the previous simulations, in the region $0.1 < x/L_0 < 0.2$, but which was not observed in the experiments.

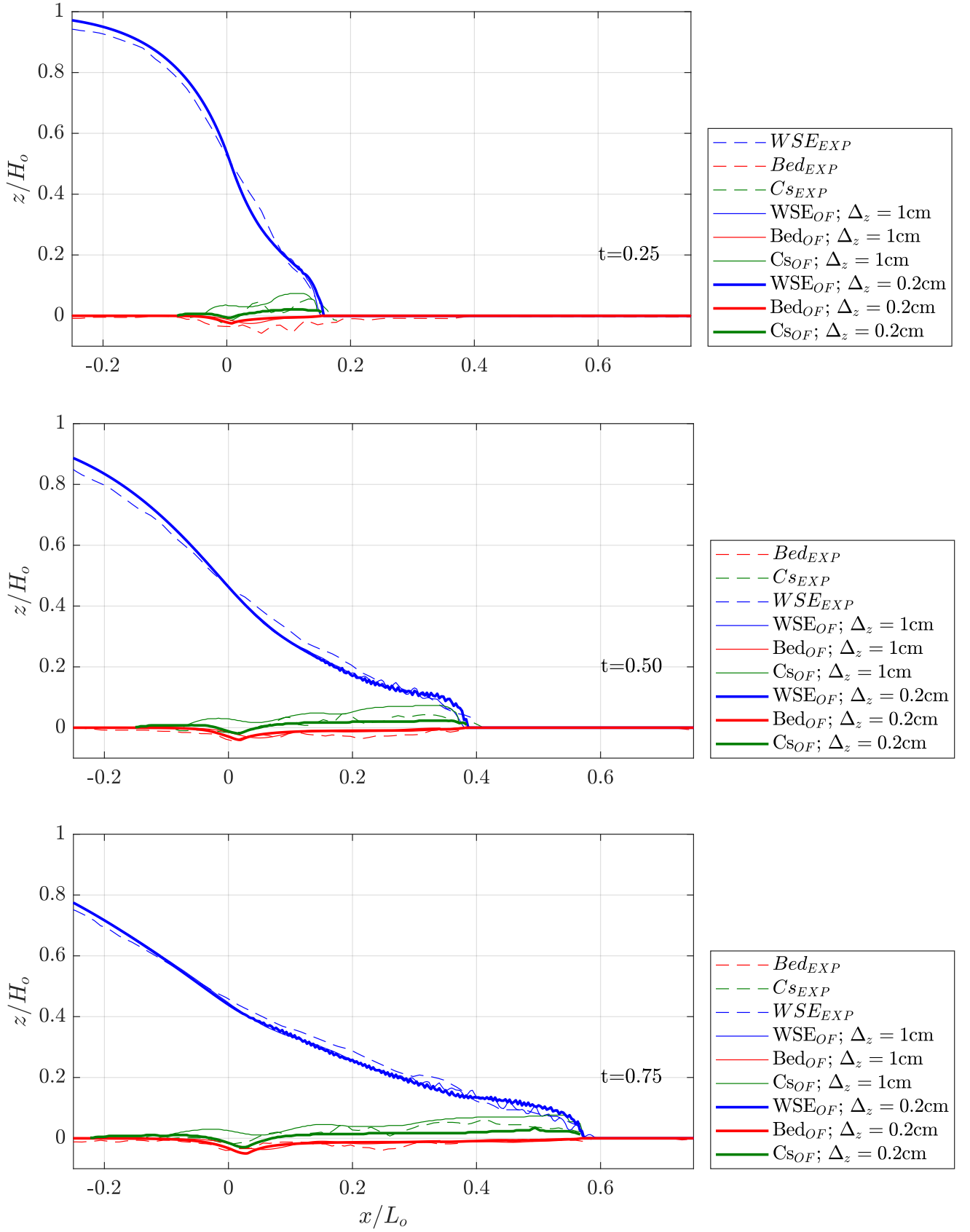


Figure 4.36: Simulation results of sheet flow model for $t = 0.25, 0.50$ and 0.75 s using different mesh configuration

Calibration of k_p

The model for the particle diffusivity (eq. 4.15) also contains an empirical coefficient k_p whose value has to be obtained by comparison with experimental results, but whose value is expected to be of order 1. To determine this value, 5 simulations were run with the fine mesh, and values of $k_p = 1, 2, 5, 10$ and 100 . The results from these simulations are plotted in figure 4.37, and these suggest that the best value for k_p lies between 5 and 10; the predicted scour depth for $k_p = 1$ agrees best with the data, whereas $k_p = 10$ gives the best estimation of the position of the scour hole, but the scour depth is over-estimated. A value of $k_p = 10$ provides the best agreement with the position of the upper boundary of the suspended load, and $k_p = 1$ gives a significant under-estimate of that thickness.

Conclusion

In this section, the complete model is used to simulate the case of a dam break flow with a mobile bed. The simulation reproduced the spatial and temporal variation in the free surface elevation very satisfactorily, and the combination of suspended and bed load modules gave a reasonable estimate of the sediment transport. However the calculation of the boundary between the undisturbed bed and the sediment in motion was less satisfactory, perhaps because the primary mechanism for sediment transport in the experiment was sheet flow, whereas the model assumes a combination of suspended load and bed load. To correct this we have developed a model for sheet flow, using the same formulation as that for suspended flow, but with a particle diffusivity based on the kinetic theory of granular flow, following Ding and Gidaspow (1990). With this model it is therefore possible to handle the transition from sheet flow to suspended load, without the need to specify the regime or the boundaries between the two. This model gave an improved agreement with all aspects of the experimental data, and a calibration procedure suggests that the best value for the empirical coefficient k_p lies somewhere between 5 and 10.

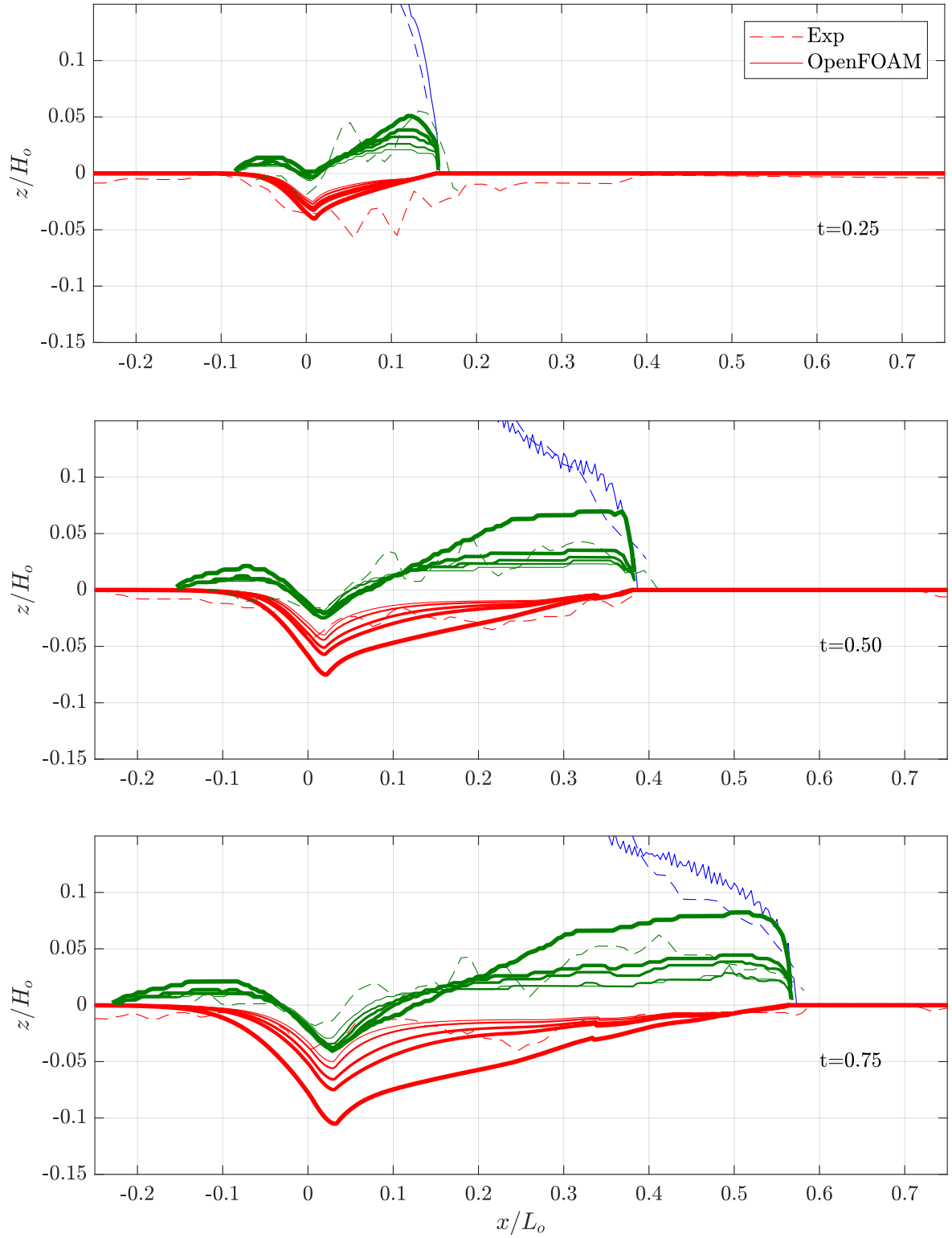


Figure 4.37: Simulation results of sheet flow model for $t = 0.25, 0.50$ and 0.75 s using different value of k_p ; k_p values from thinnest to thickest line: 1, 2, 5, 10, 100

Chapter 5

Scour At Seawall

This section describes the application of the numerical model to predict the scour pattern in front of seawalls. Two kinds of simulation were carried out: one with a fixed bed and another with a mobile bed. The simulation involving a fixed bed condition focuses on the wave hydrodynamics and their influence on the sediment transport process in front of the wall. The mobile bed case is eventually performed in order to calculate scour at seawall toe. The modeled system involves either a flat bed or a sloping beach. The results provided by the simulation are then compared with available experimental measurements from the literature.

5.1 Seawall On Flat Bed

The flat bed test case is based on an experiment by Gislason et al. (2009) where a fully reflecting vertical wall was installed at the end of the wave flume and impacted by a progressive wave. The fully reflecting wall generated a standing wave. The wave flume was 28 m long, 0.8 m deep and 0.6 m wide. The regular wave was generated by a piston wave maker which was capable of absorbing the waves reflected from the wall. The mobile bed material used in the experiments consisted of acrylic grains with a $d_{50} = 0.44$ mm and a specific density ρ_s of 1130 kg m^{-3} . The bed thickness was 2 cm extending 2.4 m in from the wall the offshore direction.

In the simulation, the wave height is set to $H = 2$ cm with a period of $T = 2$ s. The water depth h is equal to 29 cm with the corresponding wave length $\lambda = 3.3$ m.

The 2D simulation is carried out for a domain 9.9 m long and 0.4 m high as illustrated in figure 5.1. The mesh is refined close to the free surface and close to the bed to improve the resolution of the bottom boundary layer. The boundary conditions are defined as follows:

- The *inlet boundary* is defined based on Stokes 2nd order wave for the velocity and the fluid volume fraction. A 2λ wide relaxation zone is defined at the inlet;
- The *bed boundary* is defined as a no-slip condition. However, the bed boundary is divided into a fixed bed and a mobile bed. The bed roughness is set to $2.5d_{50}$ ($=1.1$ mm);
- The *end wall boundary* is defined as a no-slip condition with a smooth surface;

- The *top* boundary is defined as an atmospheric boundary condition.

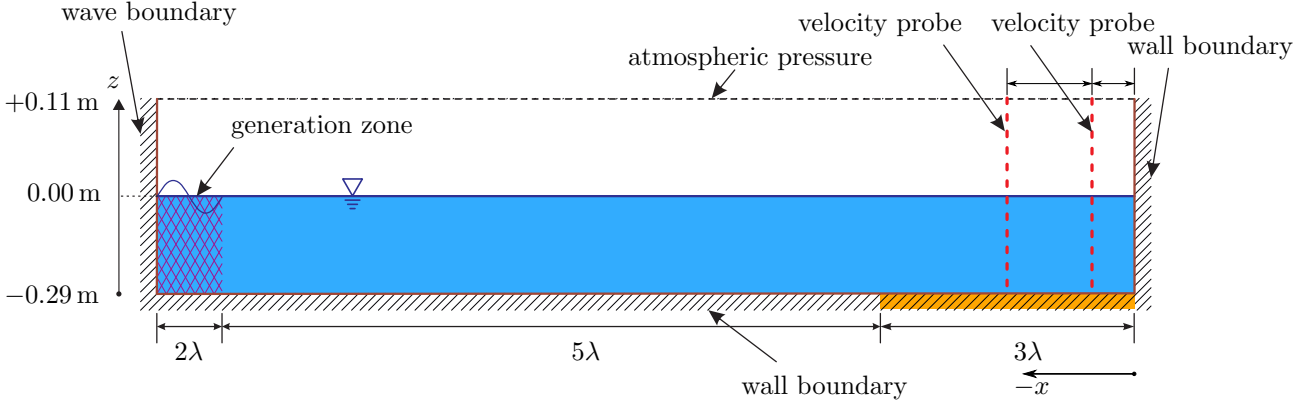


Figure 5.1: Numerical domain including a vertical seawall on a flat bed

5.1.1 Fixed bed case

The fixed bed case is studied without employing the bed deformation module. For the standing wave case, two modes for scour are observed as explained by Xie (1981) according to the sediment grain type: the coarse bed mode and the fine bed mode. In the coarse bed mode case, scour occurs between the node and the anti-node. Conversely, in the fine bed mode case, scour occurs at the node. Xie (1981) and Gislason et al. (2009) attributed this difference to the steady streaming motion which occurs near the bed in the standing wave case.

This is illustrated schematically in figure 5.2; two recirculating cells are created between each node and antinode, with flow at the bed and the surface towards the nodes, and flow at the horizontal interface between the two cells away from the node, towards the anti-node. The cells are not the same size – the lower cell is much smaller (‘squashed’) than the upper cell, and this size difference has an influence on the way the sediments are moved. Xie (1981) and Gislason et al (2009) argue that if the bed is composed of coarse grains, sediment movement will be restricted to a fairly thin layer close to the bed, and as a result sediment transport should follow the flow pattern in the lower cell, with transport towards the nodes, and hence an accumulation of sediment at those points. Conversely, fine sediments will be suspended more easily, and might be expected to move with the flow in the upper cell, with scour occurring at the nodes, driven by the downward flow in the upper cells.

The analysis of Xie(1981) and Gislason et al (2009) suggests that these flow structures will be important in determining scour, deposition and sediment transport in front of a sea wall, and it is likely that the ability of the simulation to reproduce them correctly will depend, at least partially, on the spatial resolution of the computational grid, particularly in the near-bed region. To test this, therefore, four simulations were conducted with different spatial resolution close to the bed, but the same resolution at the free surface. The parameters for these four simulations are given in table 5.1. Velocities were measured using velocity probes located at distances of 0.125λ , 0.250λ , 0.375λ and 0.500λ from the wall. The simulation was performed for 20 wave periods.

The envelope of the water surface elevation is plotted in figure 5.3 for the four different cases, together with the analytical solution for the partial standing wave

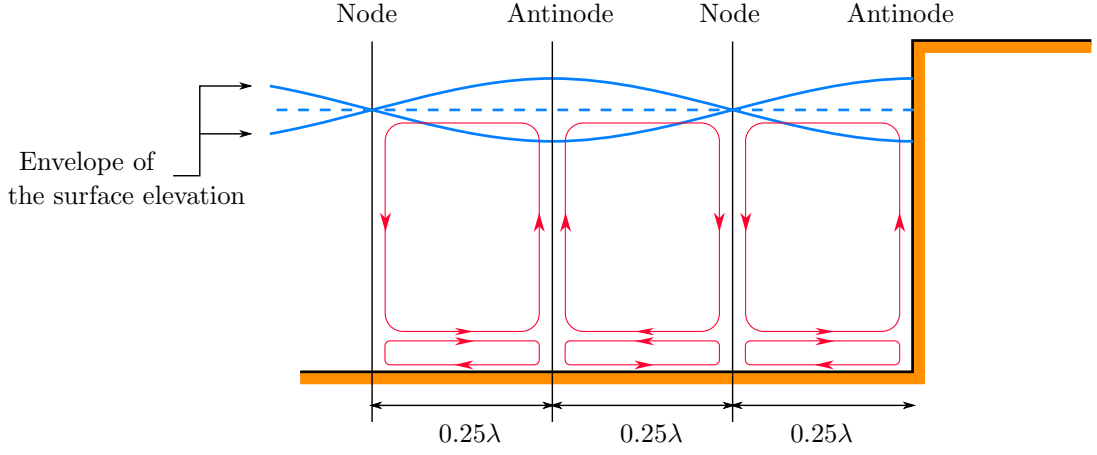


Figure 5.2: Vertical velocity profile at anti node for standing wave case

Table 5.1: Mesh configuration for standing wave over flat bed case

| Case No | Near Bed Mesh Size | | Free Surface Mesh Size | |
|----------|--------------------|-----------------|------------------------|-----------------|
| | Δx (mm) | Δz (mm) | Δx (mm) | Δz (mm) |
| Case 5.1 | 10 | 0.5 | 10 | 2 |
| Case 5.2 | 10 | 2 | 10 | 2 |
| Case 5.3 | 10 | 4 | 10 | 2 |
| Case 5.4 | 10 | 10 | 10 | 2 |

created by reflection of second order Stokes wave, with a reflection coefficient $C_R = 86.85\%$; this value was obtained from an analysis of the envelope of the partial standing wave, as described in eq. 2.50. There are three conclusions to be drawn from these results. The first is that even for the idealised case of a plane vertical wall, the reflection coefficient is not equal to 1, and this is probably because the reflection at the wall dissipates some additional wave energy. The second is that envelope of the partial standing wave is not sensitive to the grid resolution in the near-bed region. (the resolution at the free surface was kept the same in all the tests). And finally, the maximum amplitude of oscillation for the analytical solution is consistently greater than computed in the simulations, although the computed troughs match the analytical solution exactly. The second order wave is not symmetric about the still water line – the crests are more peaked than in the first order solution, and the troughs are flatter, so this reduction in the peak values (which can be observed even at the antinode at the wall) might be due to additional dissipation.

The amplitude of the velocity oscillations has been plotted as a function of depth for the node (the horizontal velocity – figure 5.4a) and the antinode (the vertical velocity – figure 5.5). The figures also show the expected amplitude, from the analytical solution, computed using a reflection coefficient $C_R = 86.85\%$. As might be expected from the previous results, the velocity amplitudes do not show any dependence on the grid resolution close to the bed. The measured velocity amplitudes are noticeably less than the analytical values, for both the positive and the negative values, although the difference is slightly greater for the positive velocities than for the negative velocities. This reduction in velocity amplitude is partially consistent with the observed wave envelope, which showed a reduction in the height of the crests of the partial standing wave, compared with the theoretical solution. But those results also showed that the troughs were very close to the analytical solution,

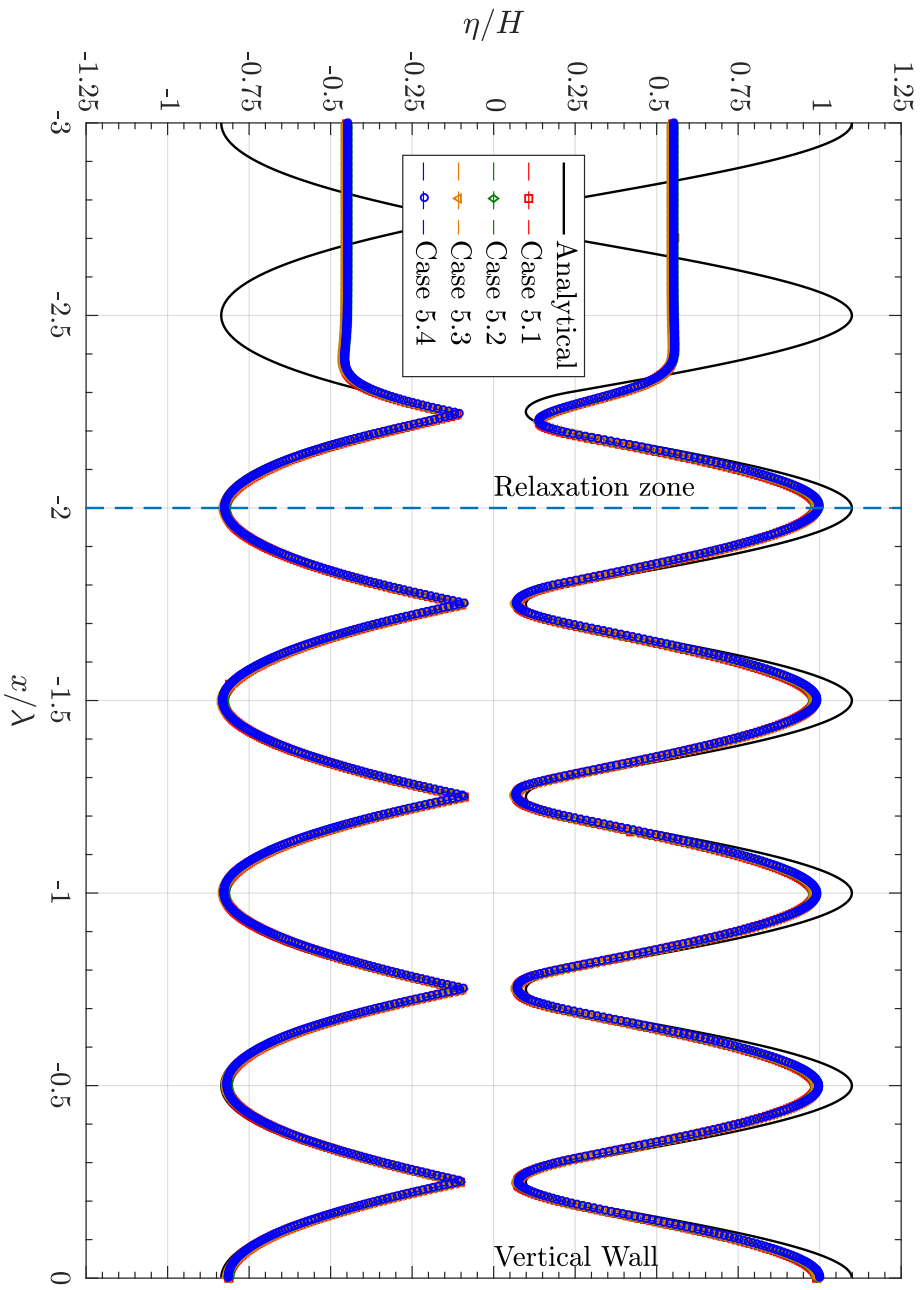


Figure 5.3: Water surface elevation for standing wave case, analytical solution calculated based on second order partial standing wave with $C_R = 86.85\%$

whereas the velocity amplitude in the trough is much less than the analytical value. The amplitude of the velocity oscillations very close to the bed has been plotted in figure 5.4b, with greater resolution, and this shows that only the finest of the four test resolutions is capable of reproducing the characteristic velocity overshoot in the near-bed region.

Streaming velocity is obtained by integrating the velocity over ten wave periods. Only two cases are considered in this test, the fine mesh case for Case 5.1 and the coarse mesh case for Case 5.4. In figure 5.6, the double cell circulation streaming near bed is well captured by the fine mesh, while the coarse mesh could only retrieve a single circulation pattern. Figure 5.7 and figure 5.8 also provide the streaming velocity plot close to the bed for both the coarse and the fine mesh. The bed streaming magnitude for the coarse mesh case is found to be less than for the fine mesh case. However, the bed streaming for both cases are in the same direction. If one assumes the streaming velocity affects the sediment transport, both cases will give a same pattern even though the simulation involving the coarse mesh was not able to model the second circulation cell.

The bed shear stress is calculated using the logarithmic rough wall law for the fine mesh case and the wave friction factor f_w for the coarse mesh case. Using equation 2.106, f_w is found equal to 0.0278.

Figure 5.9(a,b) gives the value of the bed shear stress and Figure 5.9(c,d) the transport stage number ψ multiplied with bed shear stress direction. The coarse mesh configuration gives a higher bed shear stress magnitude. The fine mesh configuration gives lower f_w of 0.0168 than 0.0278 compared to what calculated by equation 2.106. Next, a net bed shear stress is calculated by integrating the bed shear stress over 5 wave periods. The fine mesh case induces a higher net bed shear stress and what is more with a completely opposite direction than the one obtained with the coarse mesh. This is because the bed shear stress is not symmetrical for the direction away to the wall and the direction into the wall. The transport stage number shows a similar trend. The mesh size is then a concern since the modeled scour pattern will be different.

5.1.2 Mobile bed case

In this part, the scour process is modeled using the sediment transport and bed deformation module from chapter 3. The suspended load transport is not included in the calculation since no suspended sediment was found in the experiment Gislason et al. (2009). Two mesh configurations are used, based on Case 5.1 for the fine mesh and case 5.4 for the coarse mesh. To evaluate the best time step for the morphological model, a set of preliminary simulations were performed for a duration of 200s, using three different timesteps: $\Delta t_m = 0.125T$, $0.25T$ and $0.5T$. The bed shear stress for the coarse mesh calculations was computed using the $f_w = 0.168$, obtained from calculations with the fine mesh.

The bed deformation pattern is shown Figure 5.10 for the simulation with the coarse resolution and in Figure 5.11 for the simulation with the fine resolution. In both cases the results have been plotted for different morphological time steps, $\Delta t_m = 0.125T$, $0.25T$ and $0.5T$. The simulations were run for a duration of 200s,

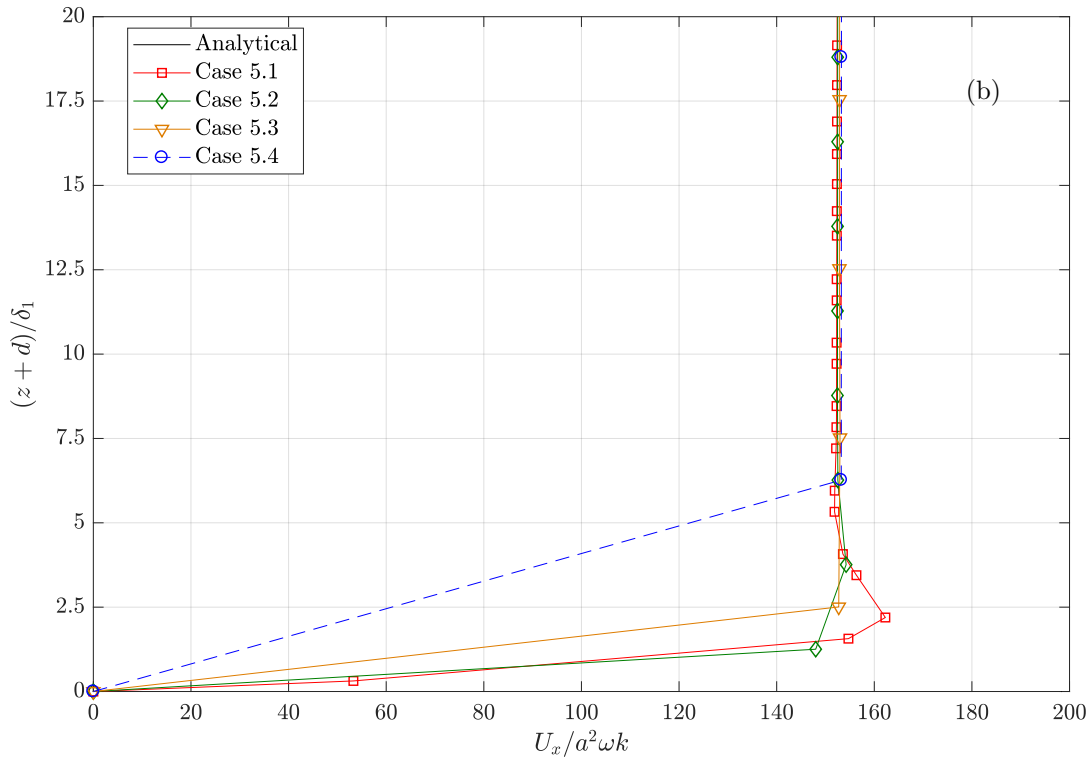
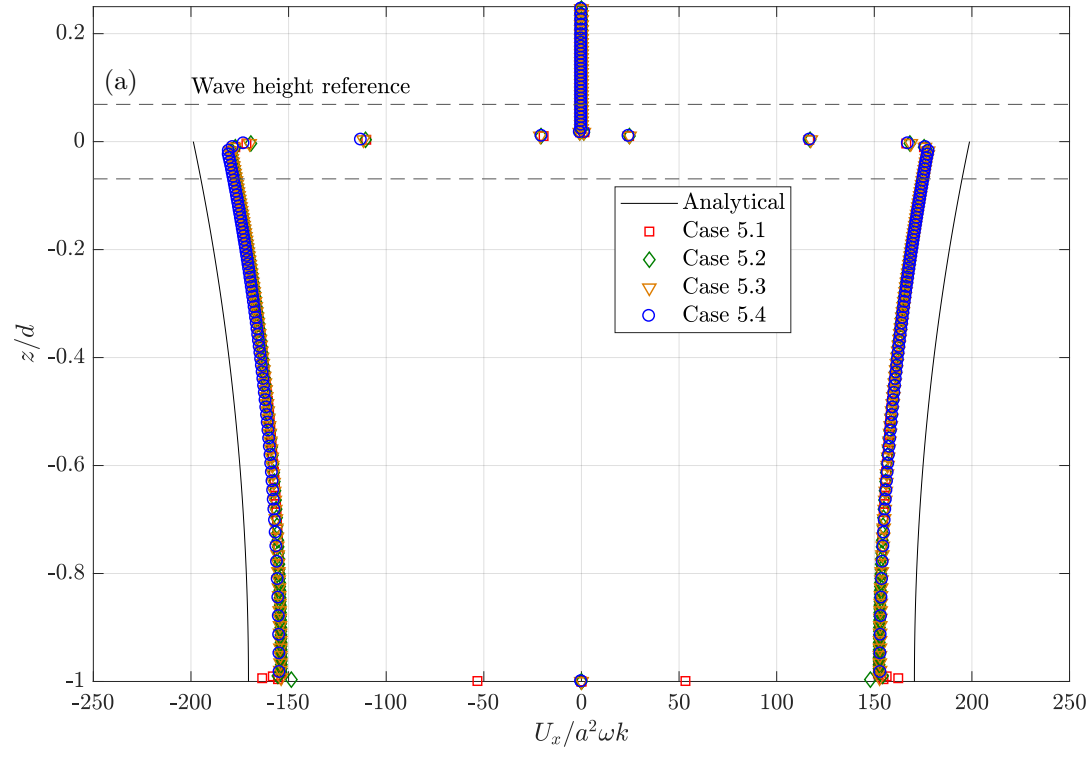


Figure 5.4: (a) Horizontal velocity profile at node for the standing wave case;(b) Near bed maximum horizontal velocity normalize with boundary layer thickness, δ_1

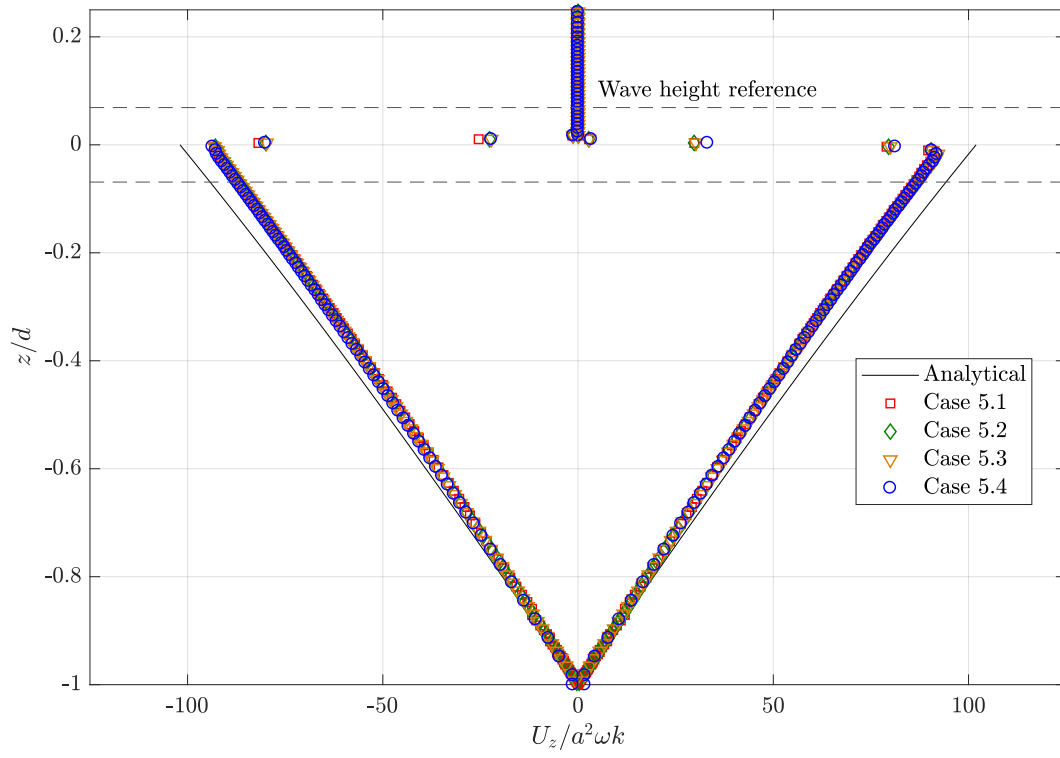


Figure 5.5: Vertical velocity profile at anti node for the standing wave case

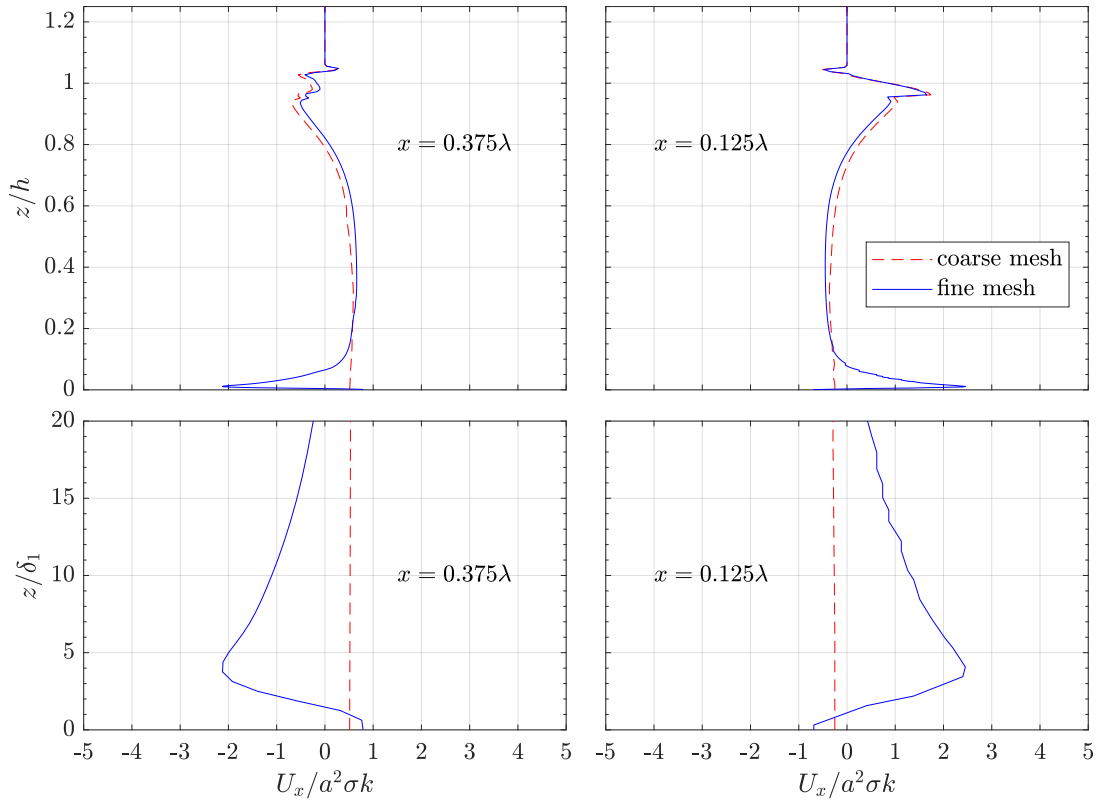


Figure 5.6: Horizontal streaming velocity profile at $x = 0.125\lambda$ and $x = 0.375\lambda$

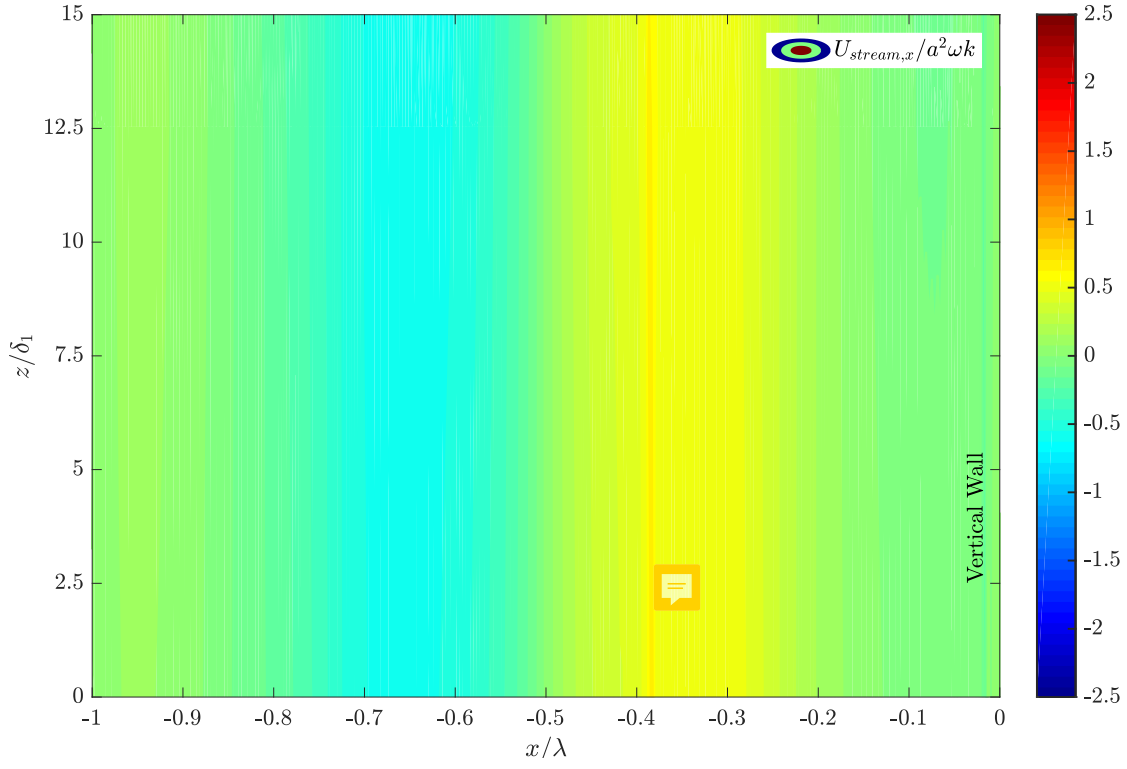


Figure 5.7: Horizontal streaming velocity for coarse mesh configuration

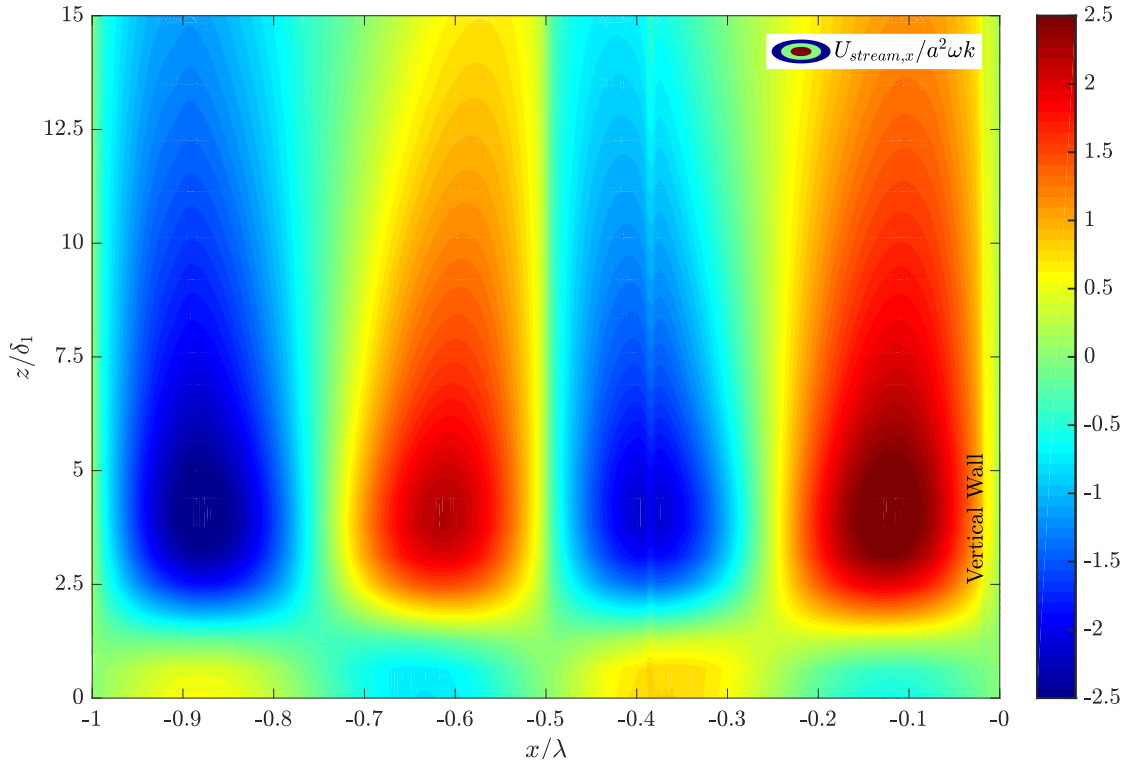


Figure 5.8: Horizontal streaming velocity for fine mesh configuration

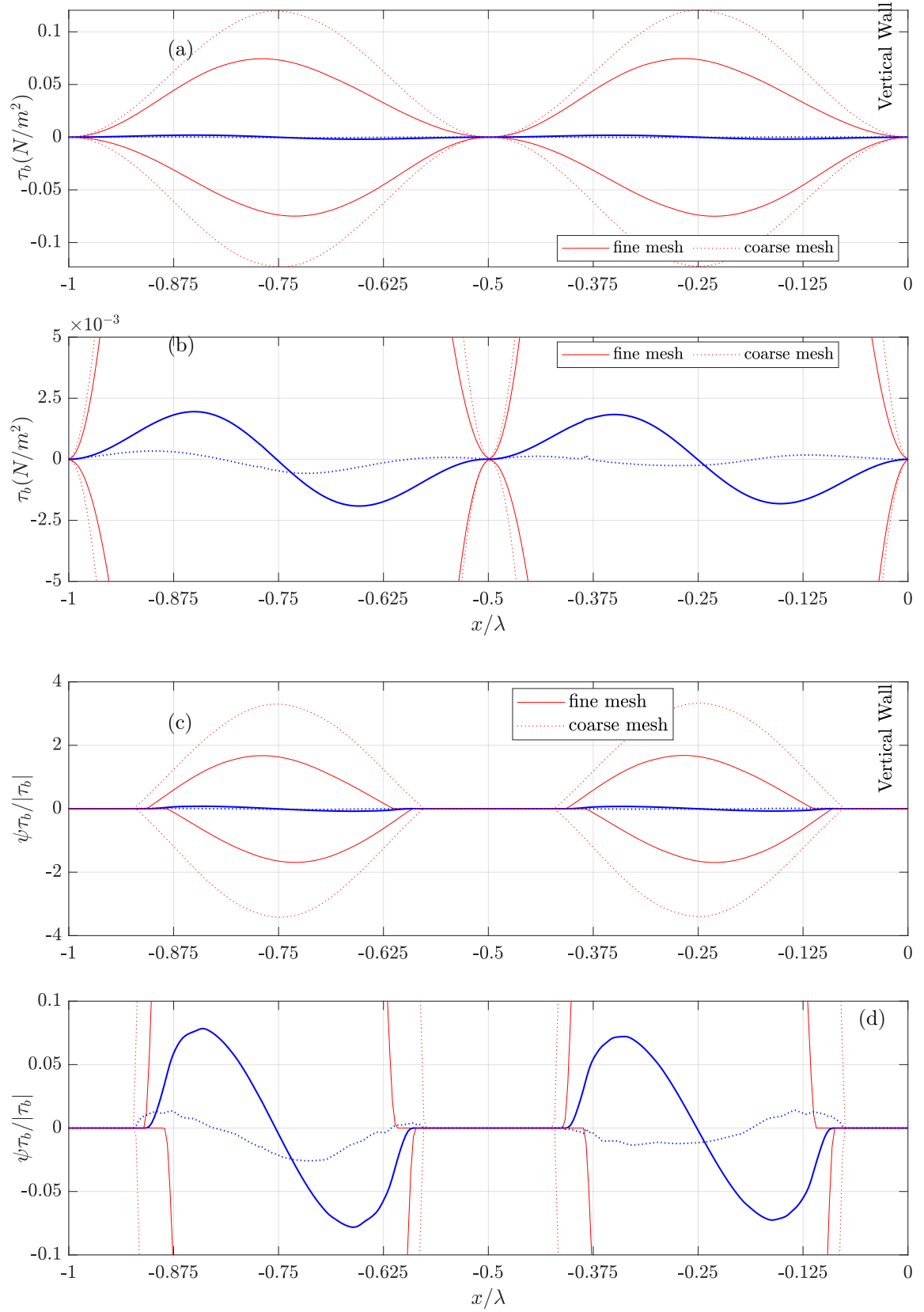


Figure 5.9: Bed shear stress (a,b) and transport stage number (c,d) for the standing wave case; solid line is for the fine mesh; dot is for the coarse mesh; thin red line is the envelope over 20 periods; thick blue line is the value integrated over 5 period

which was a limit imposed by the development of an instability in the morphological model (this is discussed in detail later). The paper by Gislason et al (2009) does not give the duration of the experiment, but it was substantially longer than 200s since the accompanying numerical simulations required of the order of 3 weeks computational time for each case. Their numerical results, however, show that the scour profile develops in a way that is related to the duration of the simulation (Figure 5 of Gislason et al (2009)) so we have scaled the experimental measurements of Gislason et al (2009), which are only provided for the equilibrium bed profile, so as to compare with the numerical simulations, which only correspond to the early stages of bed deformation. The scaling factor has been chosen to match, approximately, the extremes (erosion and deposition) of the computed bed deformation. The first point to note, as shown in Figure 5.10a, and as indicated by Gislason et al (2009), is that although the general elevation in the numerical simulation agrees well with the experiment, for both erosion and deposition, there is a spatial phase shift in the zones of erosion and deposition, so that the compute profile appears shifted towards the breakwater, by a distance (in units of x/λ) of between 0.05 and 0.1. One consequence of this shift is that the numerical simulation appears to predict the development of a large scour hole at the foot of the sea wall, where the experiments suggest an absence of erosion or deposition. This is obviously an important question for the future evaluation of the stability of a sea wall. The results for the coarse resolution are plotted in Figures 5.10b and 5.10c, with the experimental results scaled by 1% for the intermediate results at $50T$ and by 5% for the results at $100T$. There are two main conclusions to be drawn from these results. Firstly, the changes in bed level are very dependent on the time step used in the morphological model, since the results for $\Delta t_m = 0.5T$ are quite different from those for $\Delta t_m = 0.25T$ – the two calculations predict similar extreme values for the bed elevation, but the location of the erosion and deposition are quite different. Secondly, the magnitude of the erosion and deposition is very small, even compared with the reduced scale of the experimental values. This is consistent with the low values of the shear stress obtained in the numerical simulations (Figures 5.9b and d). The results for the simulations with the fine scale numerical simulations are plotted in Figure 5.11 for the two intermediate times $t = 50T$ and $t = 100T$. The first thing to note is that there is almost no influence of the time step for the morphological model – the results are almost identical for the three time steps tested. The second point is that the simulated results agree very well with the scaled experimental results, with only a slight over-prediction of the deposition. Most importantly, there is no evidence of the spatial phase shift which was present in the results of the numerical simulations of Gislason et al (2009), at all intermediate time intervals. The lack of scour at the toe of the seawall was also observed by Xie (1981). These results show another interesting feature, which has lead, ultimately, to the breakdown of the simulation at longer times. The experimental profiles show the development of ripple-like structures on the bed, with relatively short wavelengths, essentially in the regions in which the sediment is mobile. Gislason et al (2009) commented that their numerical simulation could not resolve these structures. In the simulations with the fine resolution, these ripple-like structures have been resolved, and the wavelength is similar to that of the measured structures. However the amplitude of the structures is greatly exaggerated, and these relatively steep bed structures cause problems for the remeshing of the grid, so as to follow the bed. A rough calculation shows that the slope of these features is of the order of 0.1, so the slope is still very much less than the repose angle of the sediments, but the slope is sufficient to require large

vertical adjustments of the grid, leading to instabilities. One solution would be to reduce the remeshing timestep, so as to limit the vertical adjustments that need to be made, but the comparisons with the experimental data suggest that there is another instability mechanism which is causing the ripples to grow too quickly.

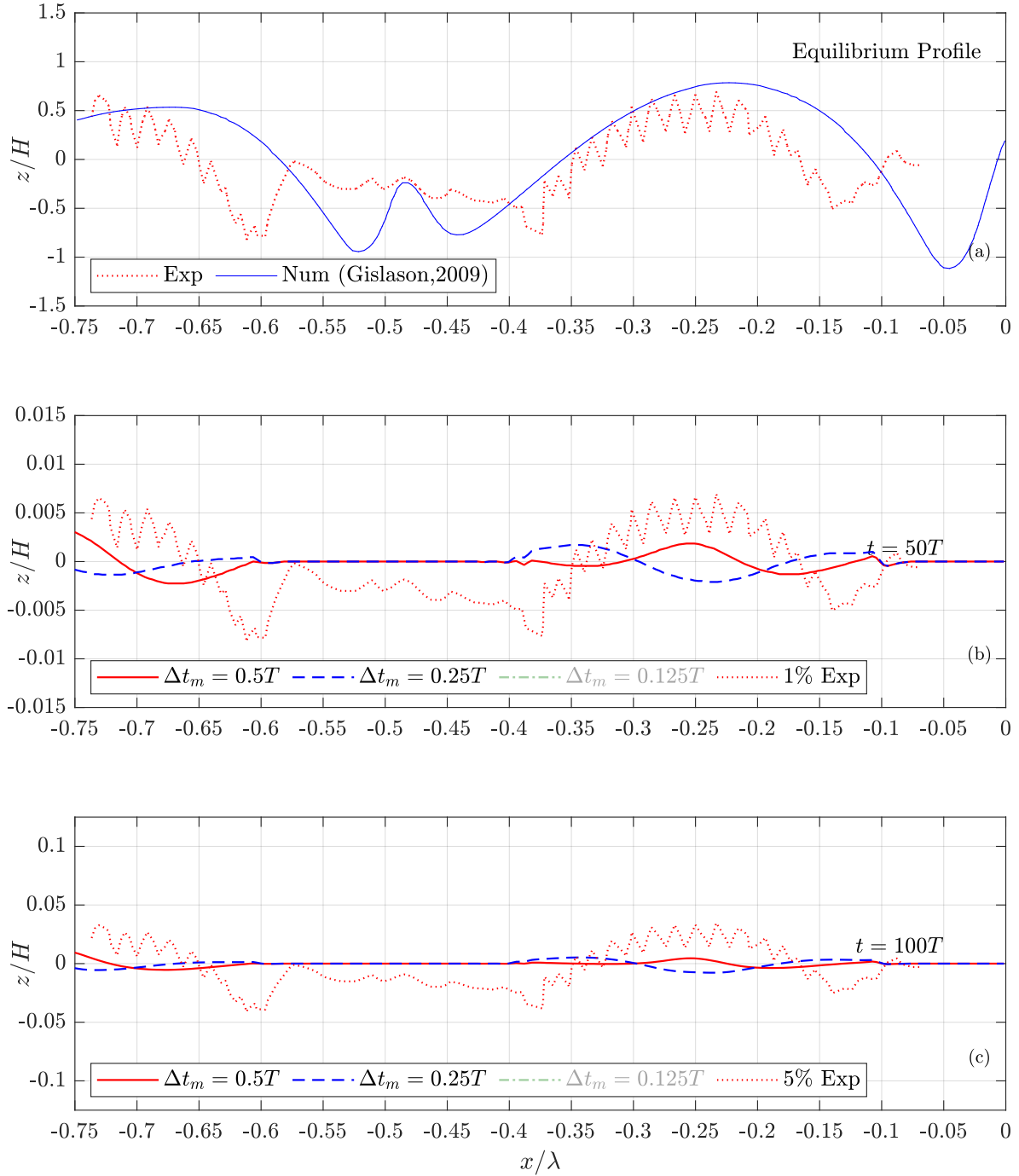


Figure 5.10: Bed deformation for standing wave case with coarse mesh configuration

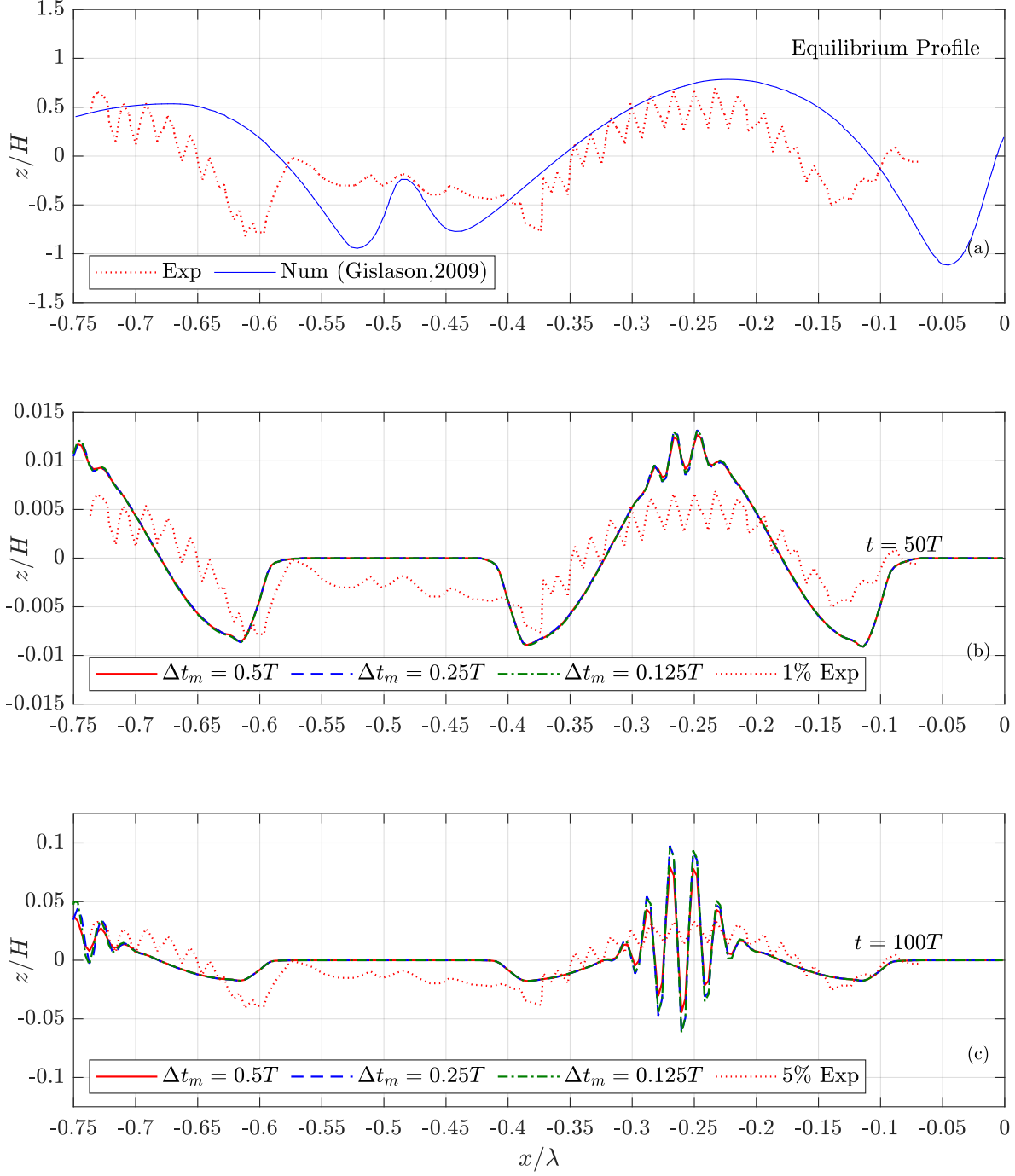


Figure 5.11: Bed deformation for standing wave case with fine mesh configuration

5.1.3 Conclusion

In this section, the scour process under a standing wave has been simulated for the case of a vertical wall on a flat bed. The simulation showed that the wave is not fully reflected with a C_R about 87%. Two mesh sizes were tested to investigate the ability of the numerical model to capture the streaming induced by the standing wave. If the spatial resolution of the computational mesh in the near bed region is refined sufficiently then it is possible to capture the streaming motion in the recirculating cells, and this motion is shown to be important in determining the pattern of sediment erosion and deposition. The amplitude of the time-varying bed shear stress is greater for the coarse resolution simulation, but the time-integrated value is higher for the fine resolution simulation, and the spatial variation of positive and negative bed shear stress also depends strongly on the mesh resolution in the near-bed region. With the fine resolution simulation the results were independent of the time step for the morphological model, suggesting that a morphological time step equal to half the wave period might be sufficient. The scour patterns corresponded well with the measured steady state scour pattern in the experiments, although it was not possible to reach steady state conditions in the numerical model, so it has only been possible to make a qualitative comparison of the pattern. The morphological model showed some evidence of ripple development on the bed, and this feature grows rapidly enough to render the remeshing process unstable.

5.2 Seawall On Sloped Beach

The sloped beach case is based on the experiment of Sutherland et al. (2006) also described in Sutherland et al. (2004). It was carried out in a wave flume 45 m long, 1.2 m wide and 1.7 m high, equipped with a sloping beach (slope 1:30) with its toe 21 m from the wavemaker. The beach therefore rises 0.8 m over its total length. The water depth is set to 1 m in the main channel, giving a water depth of 0.2 m near the toe of the seawall. A test section 5.14 m long, and located immediately in front of the toe, was filled with sand of $d_{50} = 0.111$ mm (figure 5.12).

The numerical simulation domain corresponds to a flume 35 m long and 1.6 m high (figure 5.13). The 2D simulation is performed with a mesh size $\Delta_x = 2$ cm and $\Delta_z = 1.5$ cm for the first 11 m of the domain. The mesh size gradually decreases for the sloped beach with a final size of $\Delta_x = 1.5$ cm and $\Delta_z = 0.75$ cm. The bed is divided into patches, with a fixed bed for the horizontal beach and a mobile bed for the sloped beach. The bed roughness is set to $2.5d_{50} = 0.28$ mm. The wave is generated using a relaxation zone 5.00 m long. Two cases have been studied – the first with regular waves and the second with irregular waves. Even though the experiment was carried out using the irregular wave condition, the regular wave case is investigated first for a better understanding of the system behaviour. The regular wave case uses a Stokes second order wave with a wave height H of 0.20 m and a period T of 1.87 s.

For the computation involving the irregular wave condition, we used the JON-SWAP spectrum with a significant wave height H_s of 0.2 m and a peak period T_p of 1.87 s. Waves with a period of 1.87s, on water of depth 1m will have a wavelength of about 474m. The water surface elevation is monitored at two locations, the first at a distance of 0.5m from the relaxation zone used to generate the waves, and the

second at a distance of 0.5m from the sea wall.

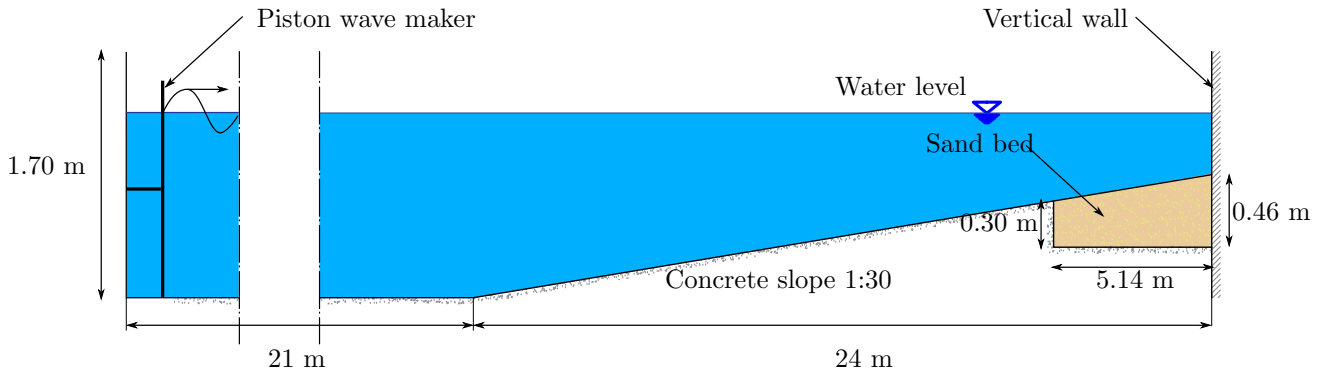


Figure 5.12: Experimental setup for seawall on sloped beach case (Sutherland et al., 2006)

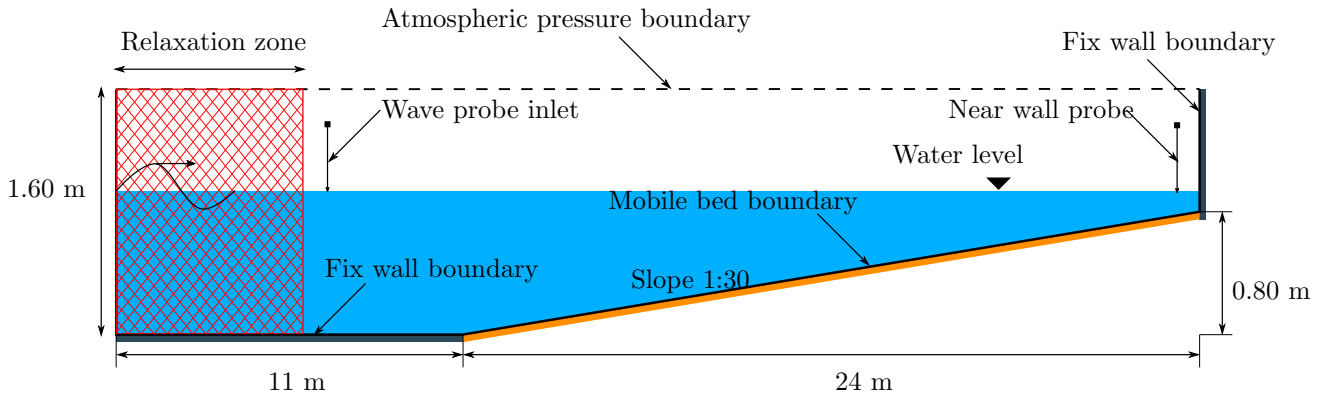


Figure 5.13: Numerical domain of a seawall on a sloped beach

Fixed bed simulation results

To begin with, both cases were simulated using a fixed bed for the bottom boundary, and in both cases for a duration of $100T$. For the regular wave the measured surface elevation has been compared with the surface elevation for a second order Stokes wave, and for the irregular waves the spectrum of surface elevations has been compared with that for the JONSWAP spectrum. The time variation of the surface elevation, measured 0.5m after the wave generation zone, is plotted in Figure 5.14, together with the theoretical profile for a Stokes 2nd order wave. Generally, the two agree well; there is just a small difference at the crests and the troughs, where the numerical simulation produces slightly higher crests and deeper troughs than for the Stokes theory. The Power Spectral Density for the irregular wave case has been plotted in Figure 5.15; as for the regular waves, the surface elevation was measured 0.5m downwave of the wave generation zone. The numerical results agree well with the theoretical profile of the spectrum, except at very low frequencies, where there is some energy in the simulations which is not found in the JONSWAP spectrum.

A visualization of the water surface elevation and the velocity field under regular waves, at 10 successive instants, is shown in Figure 5.16. In the first image in the sequence, a wave crest is incident on the sea wall, and is rising up the face of the wall, with some wave breaking evident. This wave is then reflected from the wall (images b, c and d), before interacting with the incoming wave crest causing it to break some

distance in front of the wall. It is interesting to note that when the wave breaking occurs the high forward fluid velocities are concentrated in the breaking crest of the wave, and the fluid velocities close to the bed are greatly reduced compared with the case of the propagating wave. It is only as the breaking wave slumps back down (images g-i) that the fluid velocities at the bed increase once more. The equivalent sequence for the irregular wave simulation is shown in Figure 5.17. In the first image, the pronounced crest is created by the interaction of an incoming and a reflected wave, since, in the subsequent images, the crest separates into two waves which propagate in opposite directions. In this case the interaction does not lead to any significant breaking, probably because the two interacting waves do not have the same properties – the reflected wave is much less steep than the incoming wave, as can be seen in images c and d. The incoming wave rises up the face of the sea wall (images f and g) in a way similar to that for the regular wave, but the reflected wave (images h-j) is much less steep than the incoming wave.

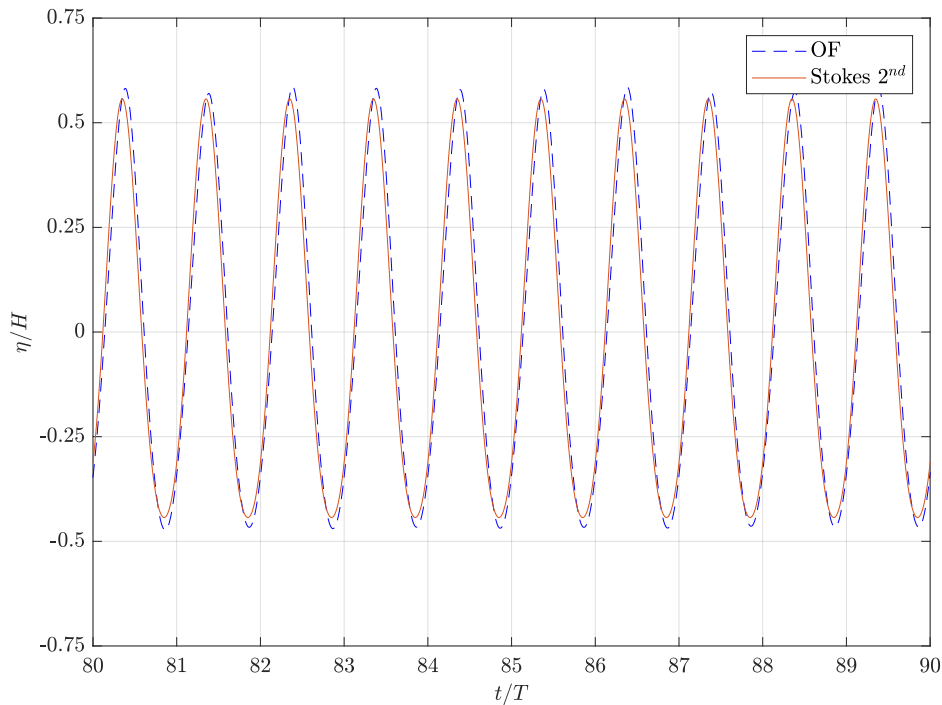


Figure 5.14: Time variation of the surface elevation, for the regular wave case at 0.5 m after relaxation zone

The envelope of surface elevations for the regular waves, computed from a sequence of 10 waves, is plotted in Figure 5.18a, and the corresponding envelope of bed shear stress is shown in Figure 5.18b. The surface elevation shows the characteristic pattern of partial standing waves, with a maximum amplitude of oscillation at the antinodes and minimum amplitude of oscillation at the nodes, but the envelope is far from symmetrical about the undisturbed water level. In fact the elevation of the troughs changes very little with position in front of the wall, and the pattern is quite different from that for reflection from a vertical wall on a flat bed (e.g. Figure 5.3). The only difference between these two cases is the presence of the sloping bed in front of the wall, so this effect must be due to the influence of the sloping bed. The envelope of the bed shear stress shows that maximum amplitude of oscillation occurs at the nodes, and the minimum at the antinodes. It should also be noted

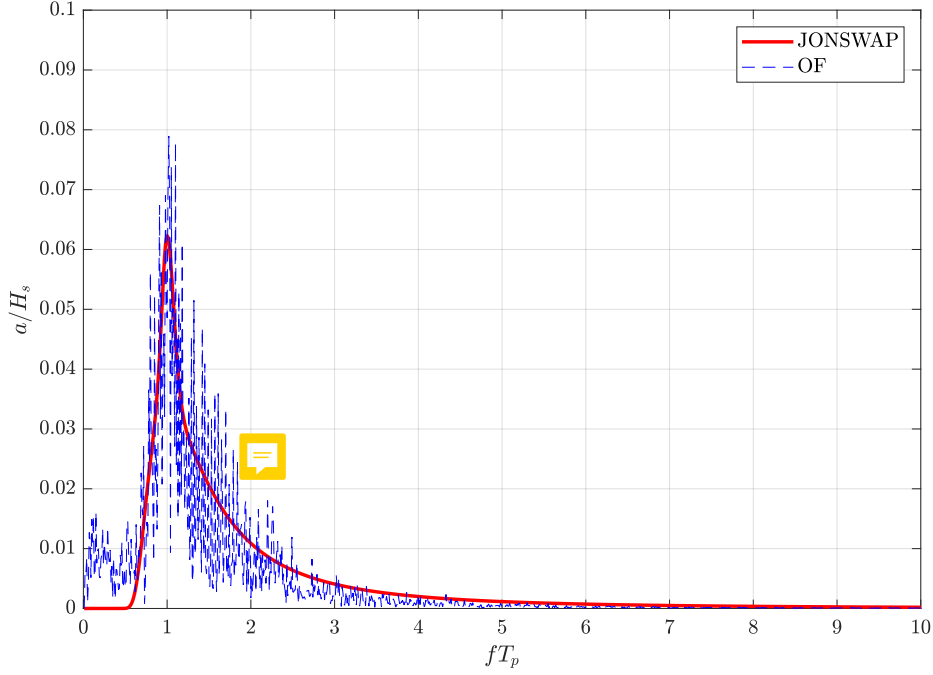


Figure 5.15: Computed Power Spectral Density for the irregular wave case measured 0.5m downwave of the relaxation zone

that the wavelength of the envelope of the wave motion on the sloping bed is about 1.7m (antinode to antinode) which is rather shorter than the value of $\lambda/2$ ($\sim 2.37m$) which would be expected for reflection on a flat bed; this is almost certainly due to the shoaling of the wave and the shortening of the wavelength, as the wave advances over the sloping beach. The variation of wavelength for both the envelope of the surface elevation and the envelope of the bed shear stress has been plotted in Figure 5.21a together with the variation in the wavelength of the surface wave as it undergoes shoaling. This shows that the wavelengths of the two envelopes reduce as the surface wave shoals. To check the relationship between these, Figure 5.21b shows the wavelengths of the envelopes normalised by the local wavelength of the surface wave (λ/λ_s), and in all cases, the envelope wavelength is approximately half the wavelength of the surface wave.

The asymmetry in the oscillation of the surface generates much greater bed shear stress in the direction of wave propagation than in the opposite direction, so we it is more likely that sediment will be moved in the direction of wave propagation than against it (because there is a greater probability of exceeding the threshold shear stress) but when the shear stress is averaged over time, the average bed shear stress is almost zero everywhere.

The corresponding results for the irregular waves are shown in Figure 5.19 and 5.20. Although the surface elevation no longer shows the same regular pattern of nodes and antinodes – because the waves are no longer monochromatic – it is still possible to observe the same difference between the crests and the troughs – there is very little spatial variation in the height of the wave trough, and much greater variation in the height of the wave crests. This is particularly noticeable around $x = -1.5m$.

Although the envelope of surface elevations shows some similarities with that for regular waves, in particular through the asymmetry between crests and troughs, this

is not reflected in the envelope of bed shear stress fluctuations, which is essentially symmetrical about zero, unlike in the case of the regular waves. The integrated shear stress is almost zero everywhere, and it is just as likely that the threshold shear stress will be exceeded in the direction of wave propagation as in the opposite direction. The peak positive and negative values of the shear stress are similar in both cases, suggesting that simulations with regular waves can provide useful information about the scour generated by a sequence of irregular waves.

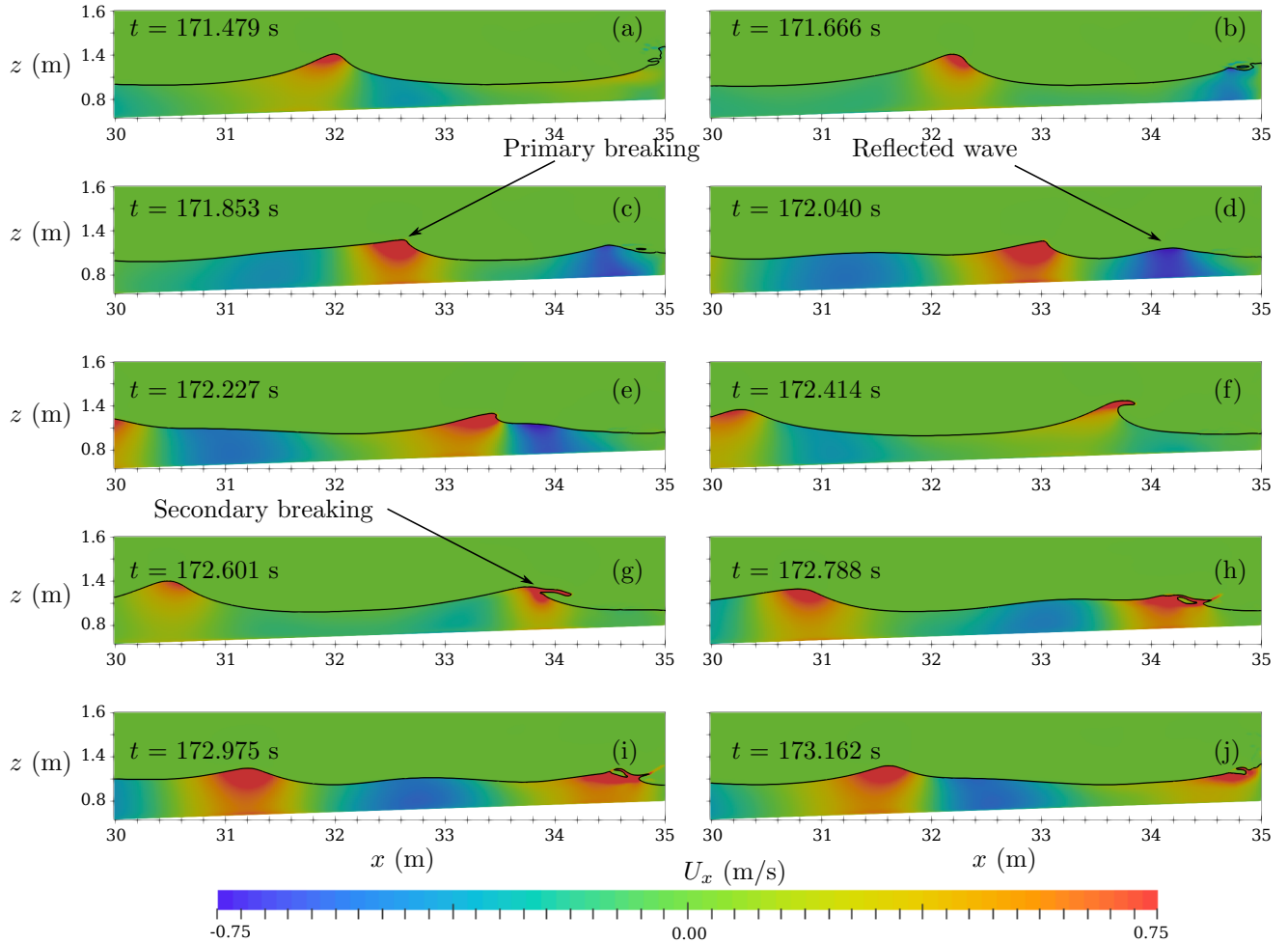


Figure 5.16: Wave breaking snapshot and horizontal velocity pattern for regular wave

Mobile bed simulation results

The numerical model has been used to simulate Case 2 of the experimental measurements of Sutherland et al. (2006). In the experiments, the bed profile in front of the sea wall was measured at $300T$, $1000T$, $2000T$ and $3000T$; because of the computational time required for the simulation, it has only been possible to compare with the results at $300T$. The first problem encountered in comparing the results is that the initial condition for the experiment did not correspond to the theoretical condition, which was defined as a smooth sand bed with a slope of 1:30, and a vertical elevation of 0.8 m at the toe of the sea wall. As can be seen in Figure 5.23, the initial bed profile deviates quite strongly from theoretical value, and the deviation is of the same order as the scour deposition measured at $t = 300T$. There also seems to be

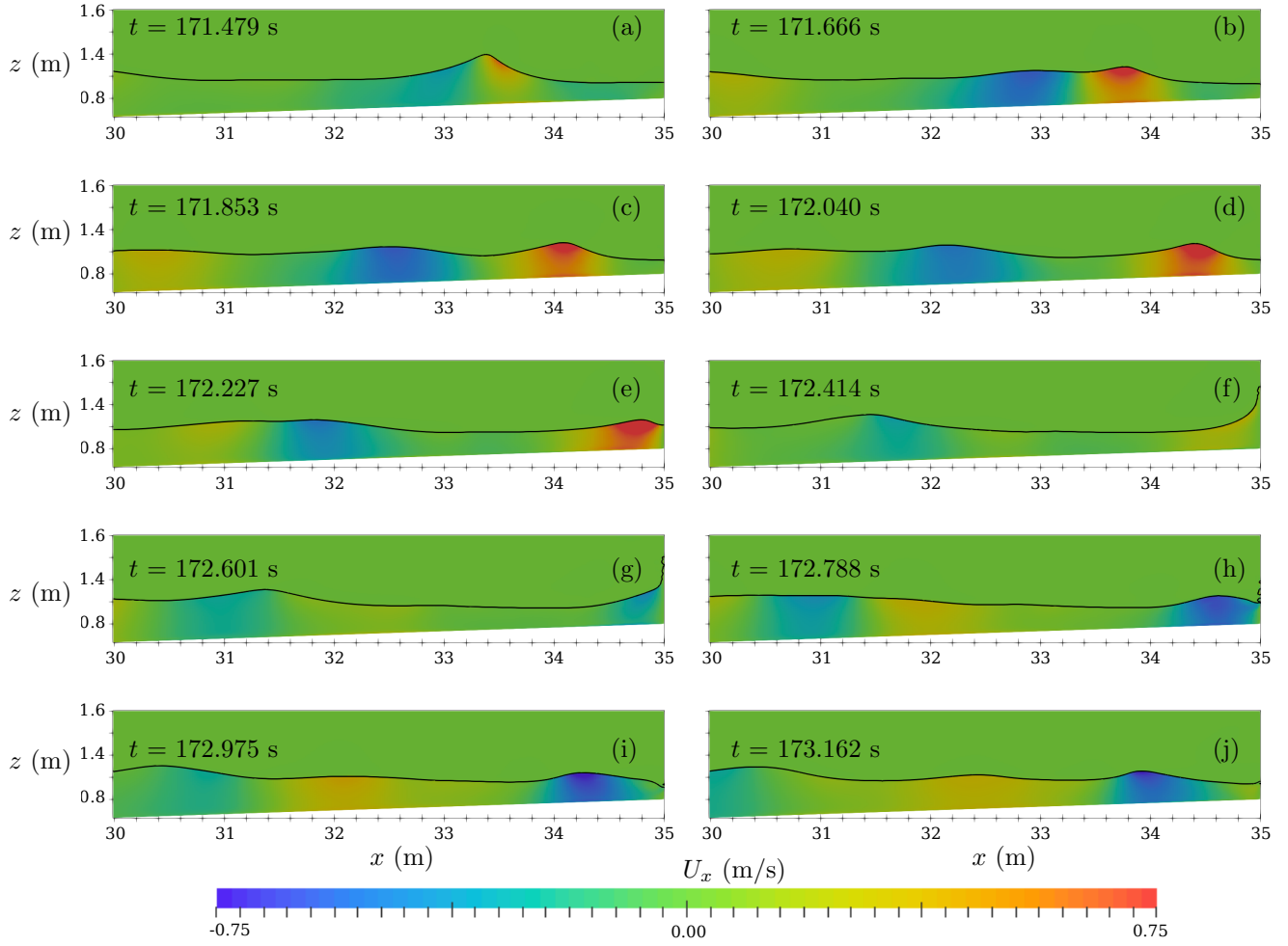


Figure 5.17: Wave breaking snapshot and horizontal velocity pattern for irregular wave

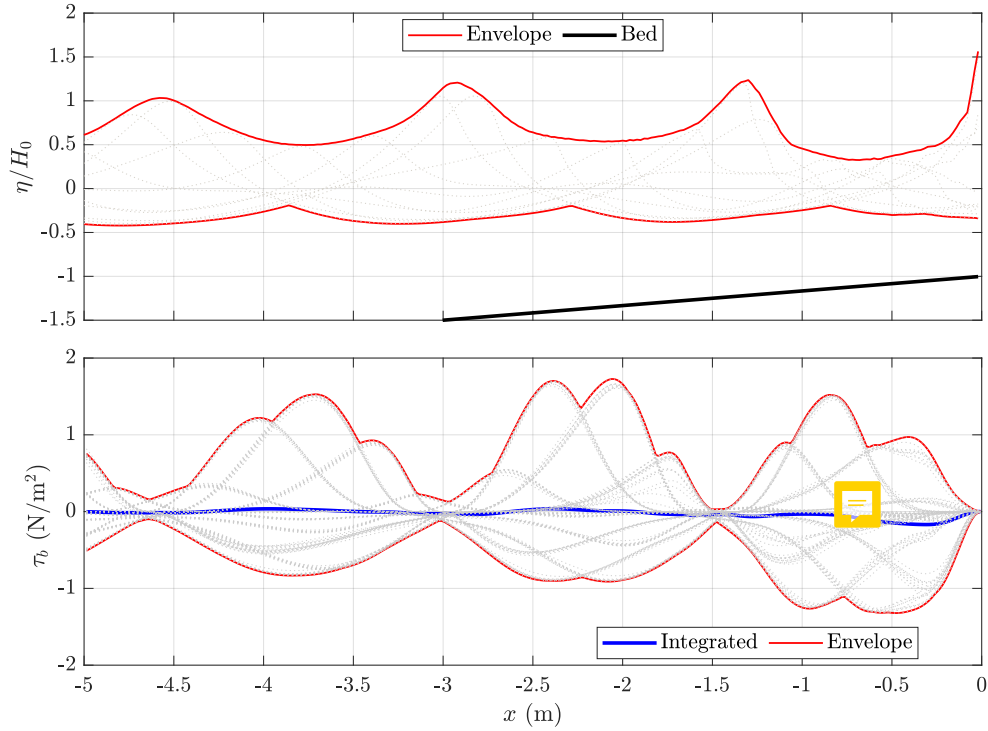


Figure 5.18: Water surface elevation and bed shear stress for regular wave condition; gray dot is the instantaneous value for $10T$

some correlation between the initial bed profile and the profile measured after 300 wave periods, so it is possible that the scour pattern measured in the experiments has been influenced by the initial conditions. In order to obtain general result, and to avoid any possible influence of initial condition, it was therefore decided to initiate the simulation with the theoretical initial profile, and then to compare the change in bed level over 300 wave periods.

The pattern of scour and deposition after 270 wave periods is shown in Figure 5.24 together with the experimental profile measured after 300 wave periods. This shows that it is very difficult to compare the actual profiles in the two cases, since the initial differences are greater than the changes in bed profile. So the change in the bed profile, for the experiment and the simulation, has been plotted in Figure 5.25. This shows that the amount of erosion and deposition measured in the experiments is considerably more than obtained in the simulations, but there are nevertheless some features common to both sets of results. Firstly, both show an alternating pattern of erosion and deposition, with apparently similar wavelengths. To test this we have computed the Power Spectral Density of the change in bed level, and this is plotted in Figures 5.26 and 5.27. Only the lowest frequencies have been plotted, since there is little power in spectrum at frequencies above 5 m^{-1} for the experimental measurements, and none at all for the simulation results. In order to compare the peak frequencies better, the spectra have also been plotted in normalized form, in Figure 5.27, where the normalization factor is the maximum power amplitude in the spectrum.

These spectra show that there is more energy in the higher frequency fluctuation for the experiments than for the simulations, but this could already have been inferred just by comparing the two curves. The lack of energy in the higher frequencies in the simulation is probably due to the fact that the grid resolution was

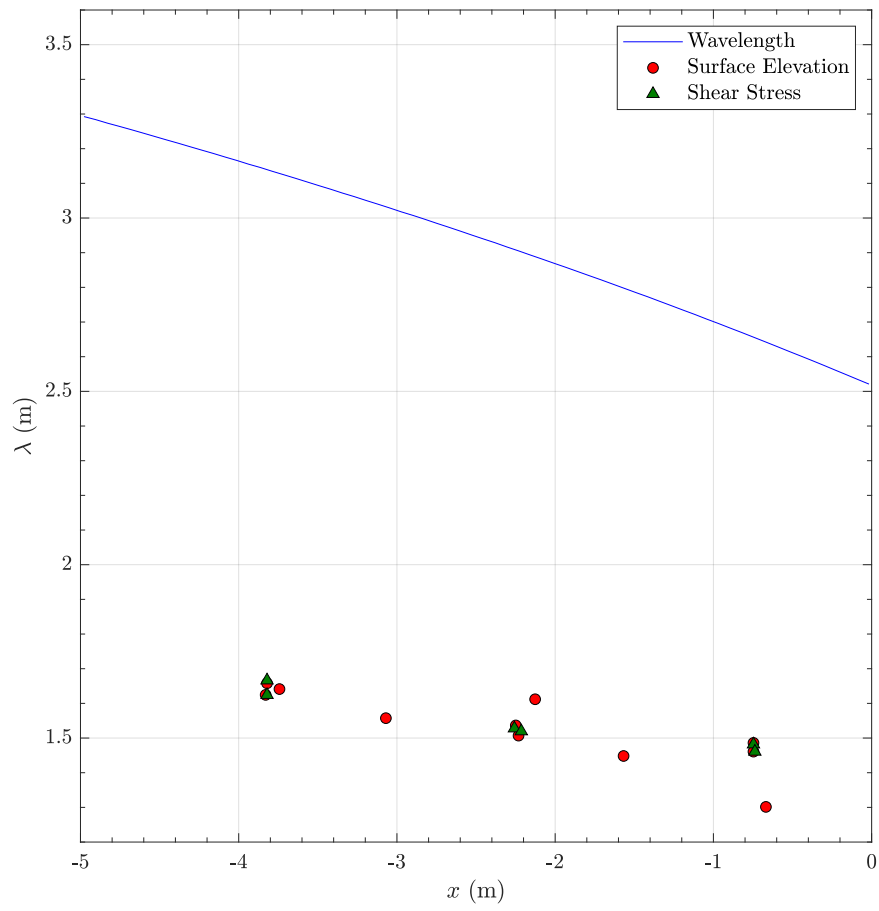


Figure 5.19: Wavelength of the surface wave, the envelope of the partial standing wave and the envelope of the bed shear stress, as functions of the distance from the wall.

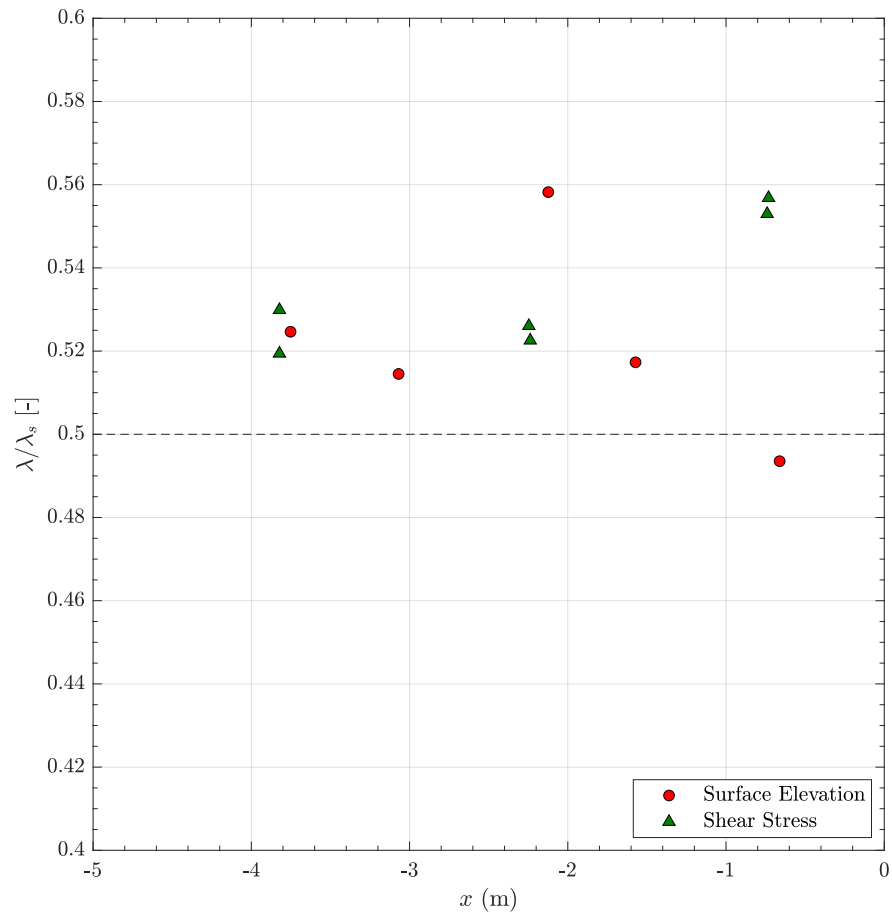


Figure 5.20: Wavelengths of the envelopes normalised by the surface wavelength, as functions of the distance from the wall.

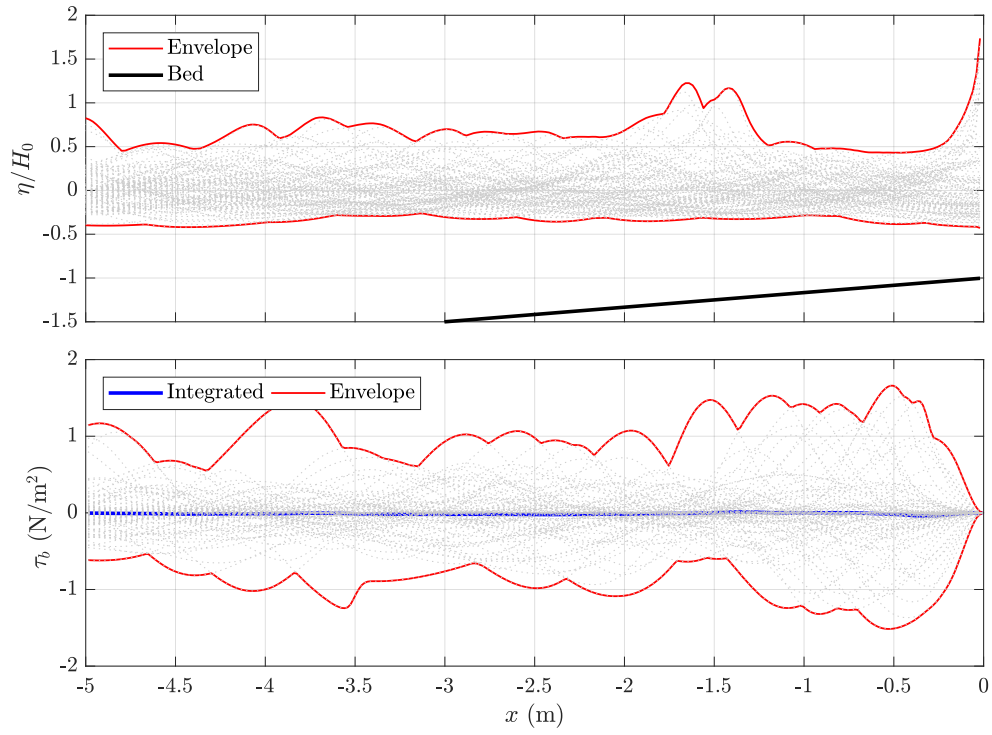


Figure 5.21: Water surface elevation and bed shear stress for irregular wave condition; gray dot is the instantaneous value for $10T$

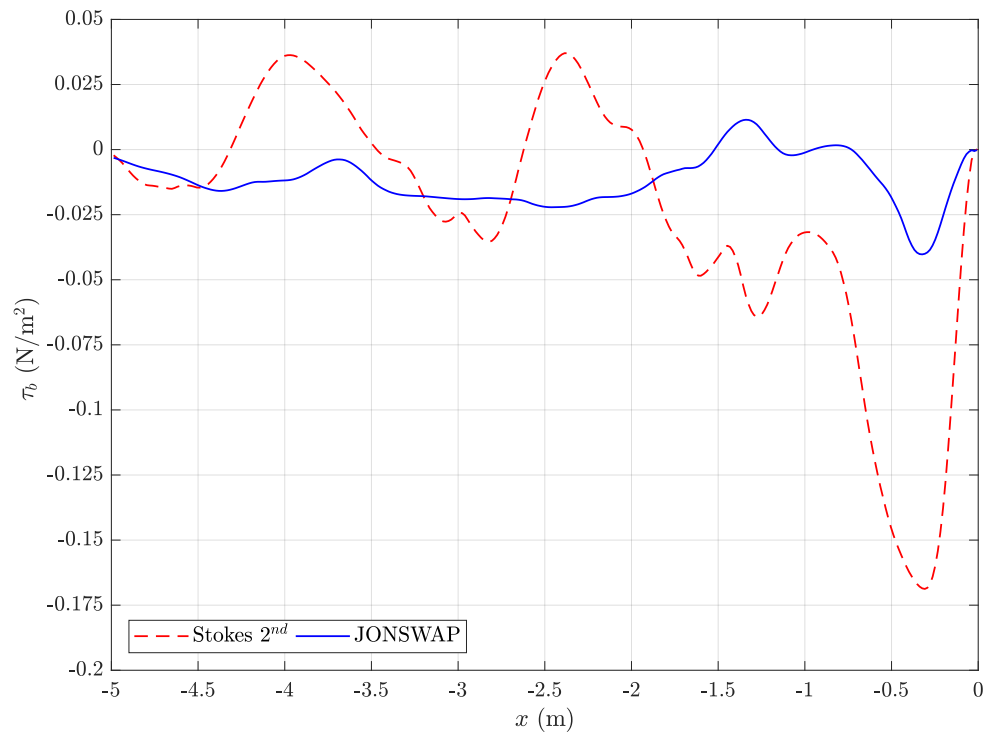


Figure 5.22: Integrated bed shear stress over $5T$ for regular and irregular wave conditions

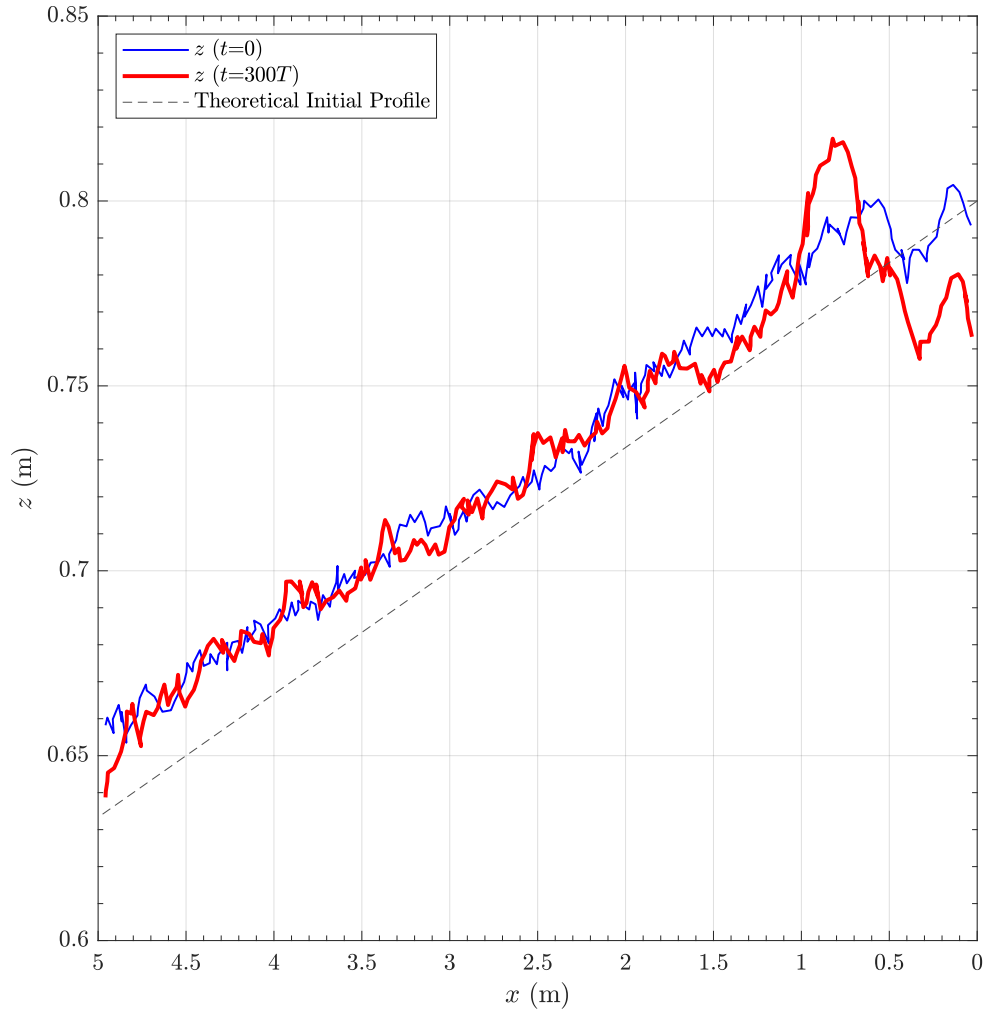


Figure 5.23: Bed profile at $t = 0$ and $t = 300T$ for the experimental study of Sutherland et al. (2006) compared with the theoretical bed profile.

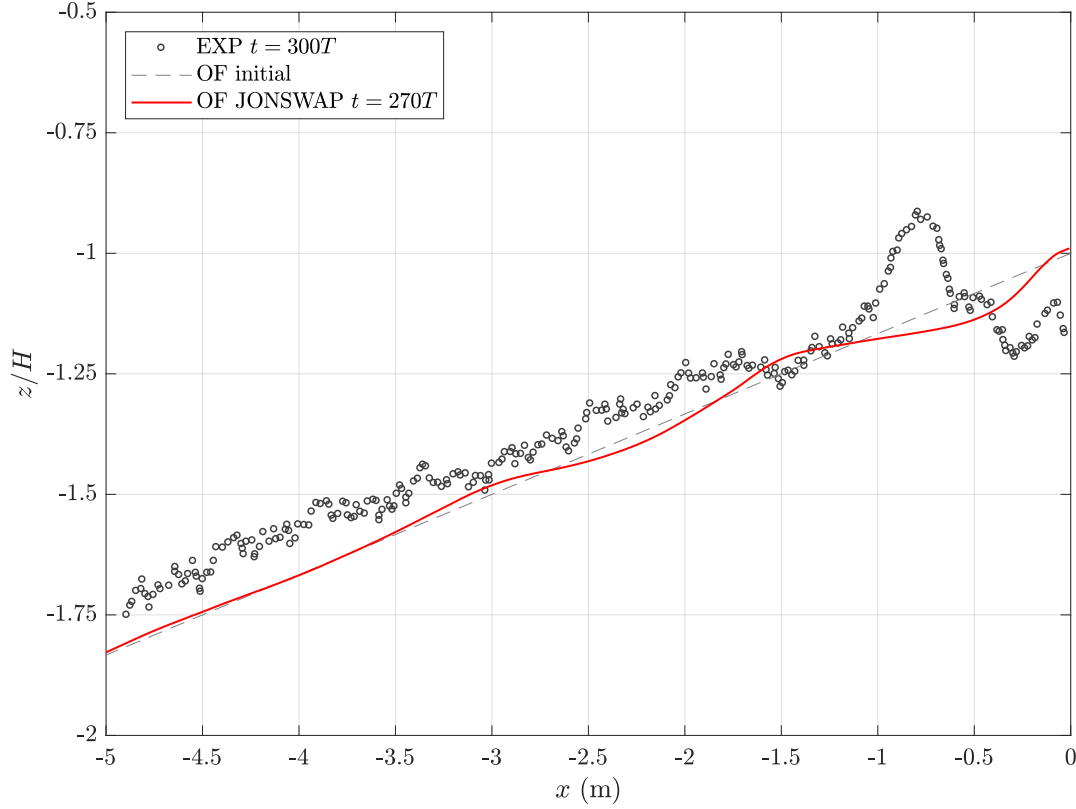


Figure 5.24: Scouring pattern for simulated irregular and regular waves and experiment measurements after 300 wave cycles

still relatively coarse - 2 cm, corresponding to a spatial frequency of 50 m^{-1} - and that the remeshing of the grid also contributes to smoothing the bed. In order to better compare the characteristic frequencies of the spectra, they have been replotted in Figure 5.27 in normalized form (i.e. the value of PSD have been divided by the maximum value so that both spectra are rescaled between 0 and 1). This shows that the major variation in the bed level fluctuations occurs at a spatial frequency of 0.6 m^{-1} , which corresponds to a spatial wavelength of 1.17 m. This is quite close to the separation distance of the antinodes ($\sim 1.17 \text{ m}$) and possibly indicates that the pattern is caused by the recirculating cells that form under the partial standing wave. But the coincidence in the wavelength of the peak variation may also be due partly to the rather coarse resolution of the spatial frequency at low frequencies. The peak in the experimental spectrum is also rather broader than the peak for the numerical results.

The PSD does not contain any information about the phase of the signals, and visual comparison of the two bed change profiles in Figure 5.25 suggests that they are out of phase - erosion in the experiments occurs at locations of deposition in the model. This is difficult to examine from the PSD for the profiles because, in addition, the signal is clearly transient rather than periodic - the amplitude of the oscillations decays with distance from the wall. One way of accounting for this is to represent the bed profile as a decaying sine wave:

$$H = A \exp\{-\beta x\} \sin\{\kappa x + \phi\} \quad (5.1)$$

Where the coefficient A , β , κ and ϕ have to be obtained by a least squares fit between the model function and the data. This has been done and the results are

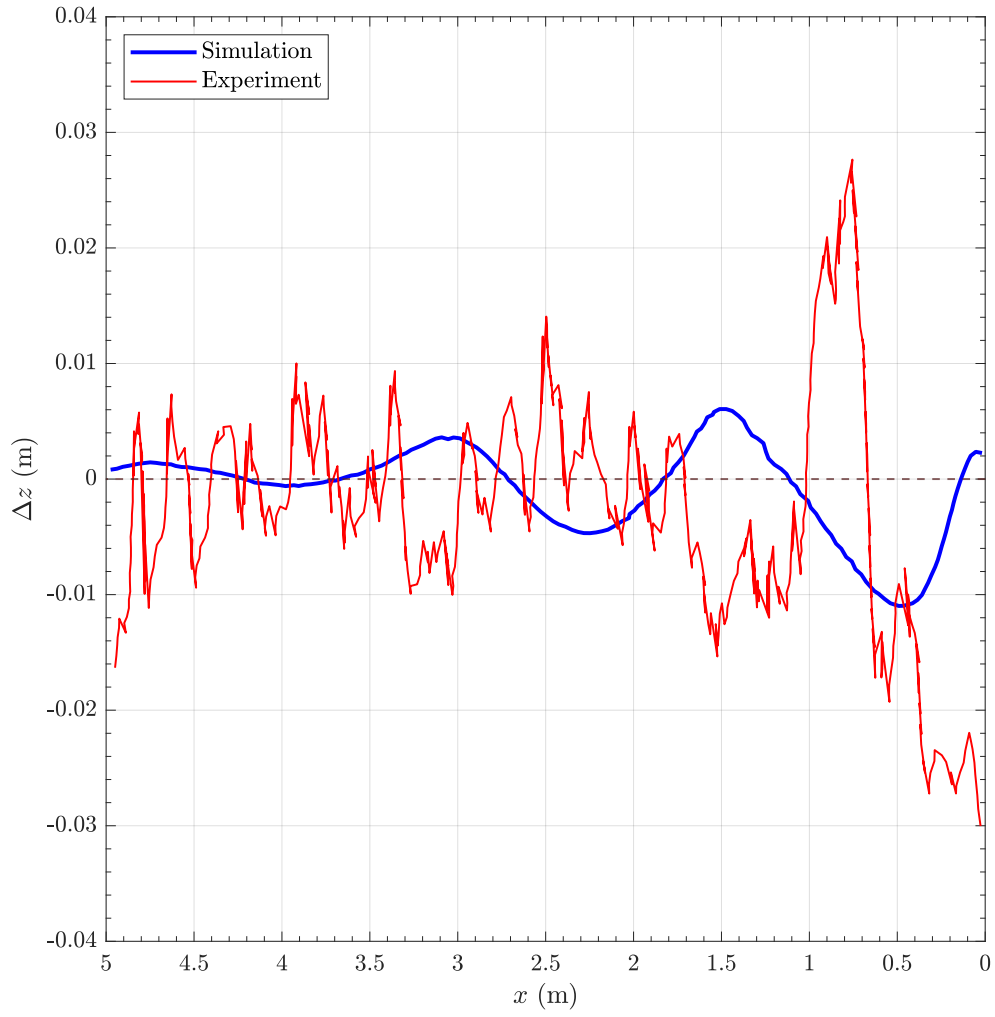


Figure 5.25: Erosion (negative) and deposition (positive) after 300 wave periods, as a function of distance from the sea wall, for the experiments of Sutherland et al (2006) and the simulation with OpenFOAM®

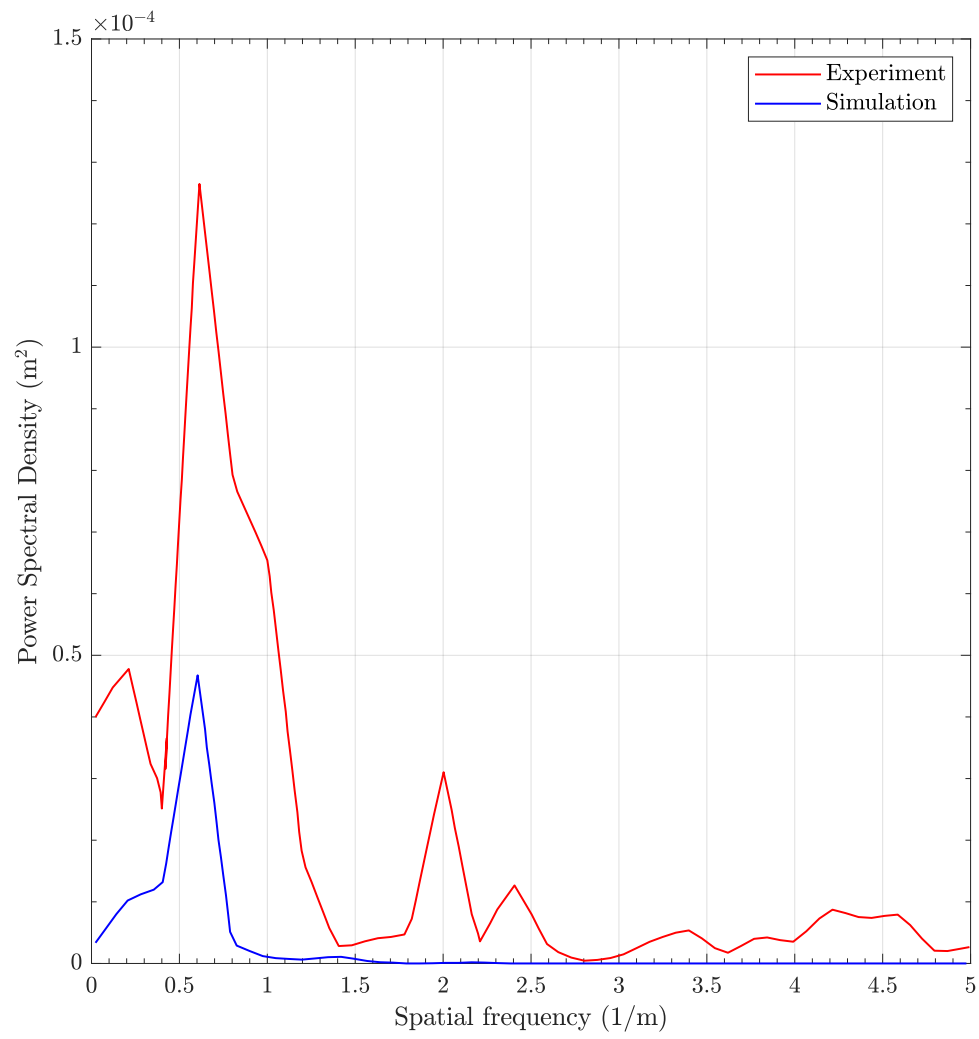


Figure 5.26: Power Spectral Density of bed level change, as a function of spatial frequency

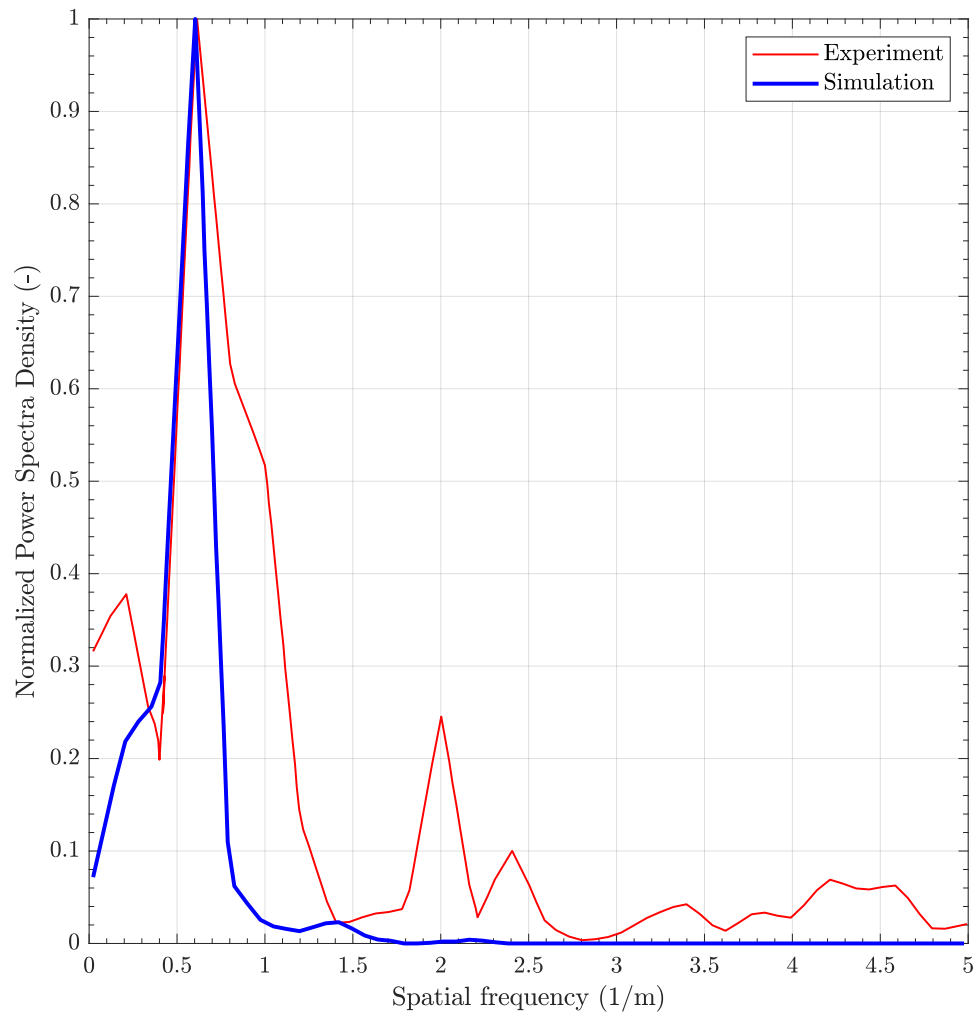


Figure 5.27: Normalised Power Spectral Density of bed level change, as a function of spatial frequency.

shown in Figure 5.28 and 5.29. The values for these coefficients, and derived values, are given in Table 5.2.

Table 5.2: Coefficient for the model function, for the experimental and numerical data

| | A [m] | β [1/m] | κ [1/m] | ϕ | λ [m] |
|------------|---------|---------------|----------------|--------|---------------|
| Experiment | 0.0375 | 1.166 | 4.944 | -2.836 | 1.270 |
| Simulation | 0.0139 | 0.557 | 3.607 | -3.619 | 1.740 |

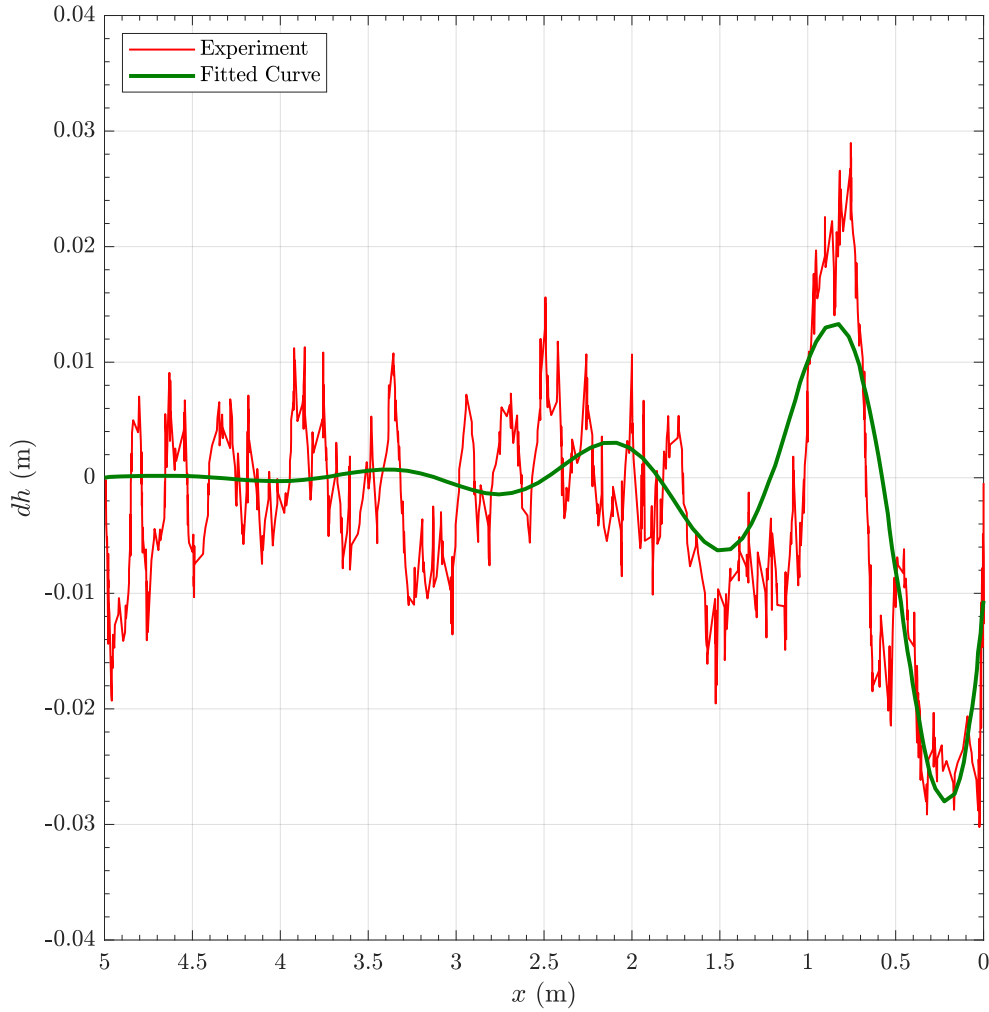


Figure 5.28: The experimental change in bed elevation and the model function

The wavelength of the bed oscillations is computed from $\lambda = 2\pi/\kappa$, and the corresponding spatial frequencies are 0.79 m^{-1} and 0.57 m^{-1} ; since the frequency resolution of the PSD results is 0.2 m^{-1} , this would give peaks at 0.8 m^{-1} and 0.6 m^{-1} respectively. This suggest that the coincidence in the peaks of the two PSD measurements is partly related to the low frequency resolution, and partly to the fact that the signal is transient rather than properly periodic. The wavelength of erosion pattern in the numerical model ($\lambda = 1.74 \text{ m}$) is very close to the value observed from

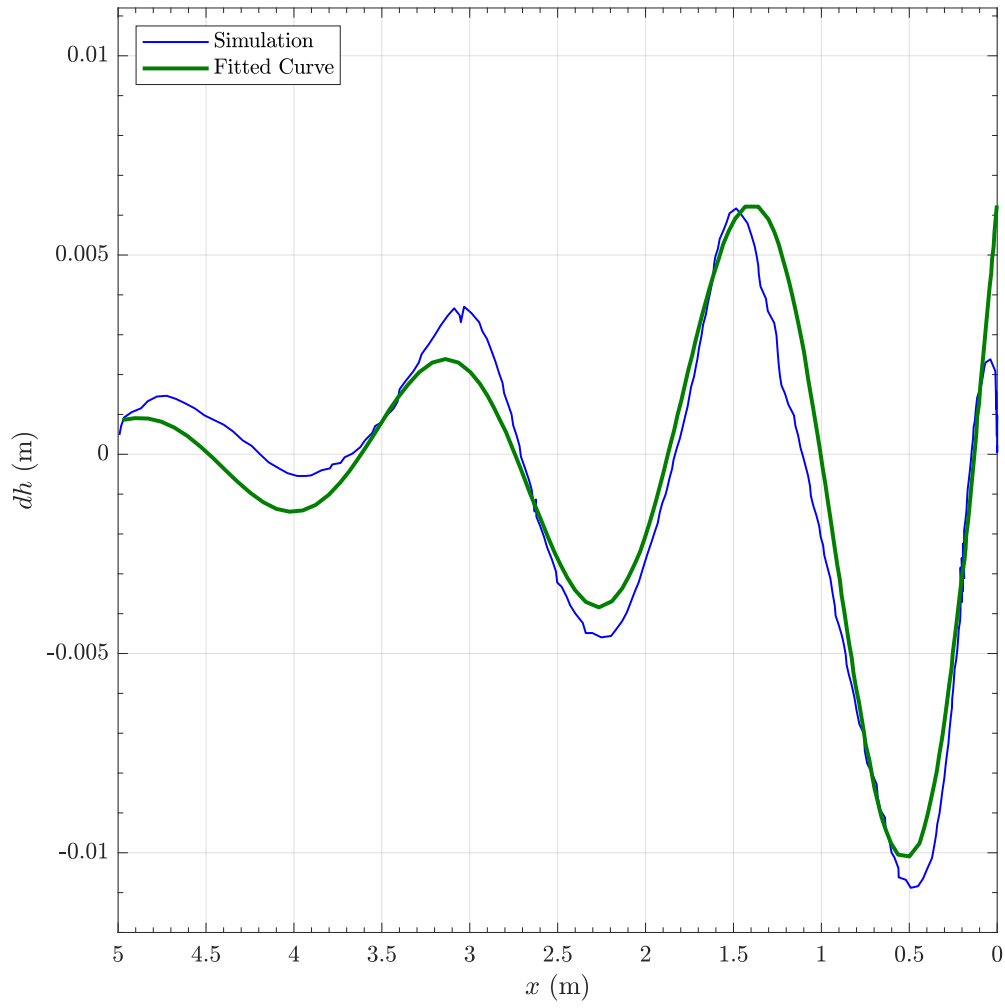


Figure 5.29: Normalised Power Spectral Density of bed level change, as a function of spatial frequency.

the envelope of the reflected waves, suggesting that the erosion and deposition is being driven by the recirculating cells that form under partial standing wave.

The difference in phase between the two model functions gives the relative phase shift:

$$\Delta\phi = 3.619 - 2.836 = 0.783 \sim \pi/4 \quad (5.2)$$

This shows that the two signals are not in antiphase (for which the phase shift would have been π); since each of recirculating cells under partial standing wave have a length of $\lambda/4$ (see Figure 5.2), this phase shift of $\pi/4$ corresponds to changing the sign of the transport at the bed, and could explain why the zones of erosion and deposition do not occur in the same places in the experiment and the simulation.

5.2.1 Conclusion

A 2D simulation of waves impacting a seawall on a sloped beach was carried out for comparison with experimental results of Sutherland et al. (2006). The simulation was able to correctly capture the wave breaking caused by wave reflection. The simulation captured the same pattern of erosion and deposition as observed in the experiments, although with a phase shift of $\lambda/4$. Analysis of the envelope of the partial standing wave suggests that the form of this pattern is closely related to the formation of recirculating cells under the wave, and the phase shift in the simulated pattern may be due to insufficient resolution of these cells close to the bed. The volume of material displaced in the experiment is significantly greater than that displaced in the simulations, and it is possible that conditions at the very toe of the sea wall might be an important factor in determining the total volume of displaced material.

Chapter 6

Conclusions and Perspectives

6.1 Conclusions

In this work, a numerical simulation of scour at foot of seawalls was proposed. The model was developed in the code OpenFOAM[®], based on a previous work of Zhou (2016) that involves three modules including a hydrodynamic, a sediment transport and morphological module. The hydrodynamic module uses the Reynold Averaged Navier-Stokes equation combined with the Volume of Fluid (VOF) method to solve the free surface dynamics. Two types of VOF model are tested: a first model is based on the conditionally averaged method of interFoam solver and the second one is based on the ghost fluid method of gfmFoam by vukcevic (Vukčević, 2016; Vukčević et al., 2017). The turbulent contribution to the flow is solved using the two equations $k - \omega$ SST model. In a multiphase flow simulation, the original $k - \omega$ SST model was found to generate a high turbulence in the free surface area which is not realistic. Hence, a correction involving a buoyancy term was used (Devolder et al., 2017).

The wave was generated on the basis of the relaxation zone method (Jacobsen and Fredsøe, 2011; Jacobsen et al., 2012). Another method based on the body force (Perić and Abdel-Maksoud, 2016) and the dynamic absorption (Higuera et al., 2013) was also tested.

The sediment transport module is based on the bed load and suspended load transport. The bed load transport was calculated based on the formula from Engelund and Fredsøe, 1976 while the suspended load transport was based on the sediment concentration advection-diffusion equation with the entrainment of sediment calculated using the empirical formulation from Van Rijn (1984b). The bed deformation was calculated using the sediment continuity equation. The calculated bed deformation was used to update the mesh using the dynamic mesh library available in OpenFOAM[®].

Based on the wave propagation simulation, it was found that the interFoam solver dissipate the waves more than the gfmFoam. It was also necessary to use a second order time derivative scheme to reduce the dissipation and a limiter for the gradient scheme in order to stabilize the simulation. However, gfmFoam was not found stable in presence of wave breaking. The wave induced mass transport velocity was overestimated in the free surface area, which induced a high return flow.

Moreover, we found that the relaxation zone was not able to satisfy the conservation of the mass, and no equal mass transport return flow was observed. However, the relaxation zone was found to give the least reflection compared to the other tested methods.

The bed shear stress calculation method was tested using the oscillatory boundary layer case based on the experiment of Mujal-Colilles et al. (2014). The bed shear stress calculation was found to be dependent on the mesh resolution. The logarithmic law method for the bed shear stress calculation required the use of a sufficient fine mesh size in order not to underestimate the phenomena. An approach using the friction factor from Rijn (2007) was also tested. It was found more adapted to the case of a coarse mesh.

The whole model modules were implemented for the simulation of a mobile dam break based on the experiment of Spinewine et al. (2005). The bottom boundary for the suspended load was modified by introducing a source term related to the sediment entrainment which allowed a reasonable sediment mass conservation to be achieved. However, the simulation gave a different bed deformation pattern compared to the experiment. The difference may arise from that, in the experiment, the bed location was defined on the basis of the position of the immobile grains while in the model it was derived from the sediment continuity equation which implicitly impose that the bed grain cannot be static. Then, a modified suspended load transport model where the particle diffusion is computed on the basis of the kinetic theory of granular flow (Ding and Gidaspow, 1990) was used. It gave a promising result since the suspended load interface was found close to results found in the experiment.

Finally, the simulation of the scouring process on a toe seawall due to the wave was carried out. A first simulation involved a wave approaching the vertical wall on a horizontal bed based on the experiment of Gislason et al. (2009). The use of a fine mesh allowed us to observe the typical second circulation streaming which cannot be found using a coarse mesh.

The integrated transport stage number over the wave period was found to be in the opposite direction for coarse mesh compared with the fine mesh. The bed deformation obtained with a coarse mesh was found too irregular to derive any conclusion in relation with scour. The simulation result using fine mesh gives sediment deposition at the anti-node which predicted from steady streaming direction. However, no scour was observed at the node because the Shields number was less than the critical Shields number.

The second simulated case was based on the experiment of Sutherland et al. (2006) for seawalls on sloped beach. The model was able to capture the wave breaking influenced by the wave reflecting from the wall. However, the toe scour was greatly underestimated and a small bed shear stress was found as the toe also, acting as a node. Then, another approach for the bed shear stress calculation is required.

6.2 Perspectives

Based on the results found in this work, OpenFOAM® seems on the overall a suitable tool to carry out water wave simulations.

Firstly, the Volume of Fluid model implementation in OpenFOAM® is found to give a dissipation to the waves. It may come from the diffusion term in the free surface area. Even though the gfmFoam already solved the pressure jump condition which improved the model performance greatly, it still not resolve the tangential stress on the free surface (Vukčević, 2016). It is also found not stable under wave breaking, especially when the air compressibility is significant. In the future, it will be necessary to involve a term related to the air compressibility.

Secondly, there is still a need of extensive research on the sediment transport model in waves flow problems. All of the sediment transport empirical formula used in this work are based on a steady flow condition. The sediment transport calculation for waves type problem was also found to be greatly dependent on the mesh size. Further research is required in order to give a practical guidance to build a model suitable to scour prediction project. More sophisticated formulations must be studied in order to evaluate their impact on the quality of the results.

Finally, the dynamic mesh in OpenFOAM® library is found to be robust and stable. However, several limitations were found in this work. In an extreme and sudden deformation case, the dynamic mesh tends to be unstable. A high mesh distortion will also affect the hydrodynamic simulation. An approach based on the immersed boundary method will be interesting to test. With the immersed boundary method, the mesh quality will be conserved. Recent work by Peng et al. (2018) using a partial cell technique in finite difference frame work seems to be promising in this respect.

Appendices

Appendix A

OpenFOAM[®] An Open Source CFD Toolbox

A.1 Introduction

OpenFOAM[®] is an open source computational fluid dynamics (CFD) toolbox based on the finite volume method for solving the Navier-Stokes equation. It stands for Open Source Field Operation and Manipulation, and is not specifically used only for solving fluid dynamics problems. OpenFOAM[®] is developed as C++ library to solve the differential equations using the finite volume method with a user friendly syntax. One of the main advantages of using OpenFOAM[®] is that since it is open source, solver development is relatively simple by using the available finite volume library. This work uses a particular branch of OpenFOAM[®] – foam-extend version 4.0.

A.2 Finite volume discretization

This chapter will describe the numerical schemes and discretization that are used in OpenFOAM[®]. Not all the available methods will be described in this chapter, which is limited to the methods mentioned in chapter 4. Most of the explanation for the numerical scheme and discretization can be found in the OpenFOAM[®] programmer guide (OpenCFD, 2011) and are described in Jasak (1996).

The finite volume method (FVM) in OpenFOAM[®] solves equation 2.65 using the Gauss divergence theorem. The computational domain is divided into discrete control volumes (CV). Each CV is non-overlapping and the set of CVs fills the computational domain entirely. There is no limitation on the number of faces, so it is possible to use a polyhedral shape, and generate an unstructured mesh (figure A.1). If we denote any property evaluated at the centre of the Control Volume by the subscript P , then the centre of the Control Volume \mathbf{x}_P is defined by:

$$\int_{V_P} (\mathbf{x} - \mathbf{x}_P) dV = 0 \quad (\text{A.1})$$

where V is the volume. Then if we define S_f as the total face area of the control volume, and \mathbf{S} is the face area vector with the normal direction pointing outwards from the face. In what follows, we will use f to denote the faces of the Control Volume and also to denote the centre point of a face. From the Gauss divergence theorem, for a control volume P the volume integral for the divergence term for an arbitrary variable \mathbf{a} is denoted in surface integral form as:

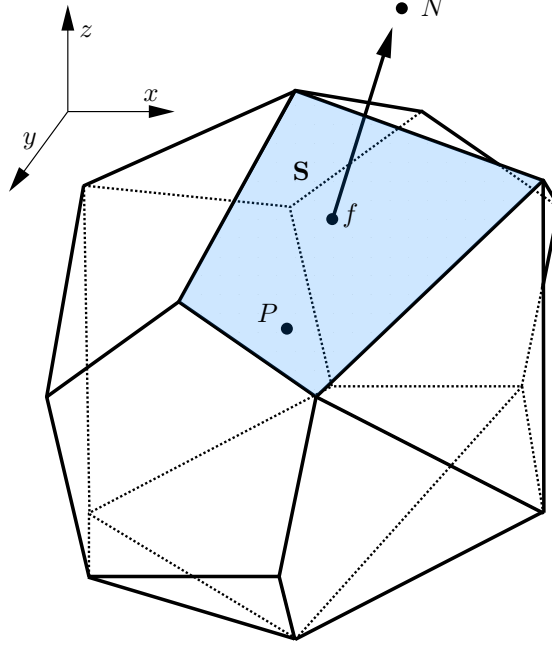


Figure A.1: Arbitrary polyhedral control volume in OpenFOAM[®](Jasak, 1996)

$$\begin{aligned}
 \int_{V_P} \nabla \cdot \mathbf{a} dV &= \oint_{\partial V_P} d\mathbf{S} \cdot \mathbf{a} \\
 &= \sum_{N_f} \left(\int_f d\mathbf{S} \cdot \mathbf{a} \right)
 \end{aligned} \tag{A.2}$$

Variables are assumed to vary linearly in space over the Control Volume, so for an arbitrary variable ϕ :

$$\phi(\mathbf{x}) = \phi(\mathbf{x}_P) + (\mathbf{x} - \mathbf{x}_P) \cdot (\nabla \phi)_P \tag{A.3}$$

which is second-order accurate (Jasak, 1996). $\phi(\mathbf{x}_P)$ is the value at the center point, described as ϕ_P . Equation A.2 can then be rewritten as, for left hand side of the equation:

$$\begin{aligned}
 \int_{V_P} \nabla \cdot \mathbf{a}(\mathbf{x}) dV &= \int_{V_P} [\nabla \cdot \mathbf{a}_P + (\mathbf{x} - \mathbf{x}_P) \cdot (\nabla(\nabla \cdot \mathbf{a}))_P] dV \\
 &= \nabla \cdot \mathbf{a}_P \int_{V_P} dV + \left[\int_{V_P} (\mathbf{x} - \mathbf{x}_P) dV \right] \cdot (\nabla(\nabla \cdot \mathbf{a}))_P \\
 &= \nabla \cdot \mathbf{a}_P V_P
 \end{aligned} \tag{A.4}$$

similarly the right hand side of equation A.2 give:

$$\sum_f \left(\int_f d\mathbf{S} \cdot \mathbf{a}_f \right) = \sum_f \mathbf{S} \cdot \mathbf{a}_f \tag{A.5}$$

Combining equations A.2, A.4 and A.5, the discretized form of divergence term for one control volume is obtained:

$$\nabla \cdot \mathbf{a} = \frac{\sum_f \mathbf{S} \cdot \mathbf{a}_f}{V_P} \quad (\text{A.6})$$

A.2.1 Time derivative dicretization

The time derivative integration over a control volume for variable ϕ is described as:

$$\frac{\partial}{\partial t} \int_V \phi dV \quad (\text{A.7})$$

To simplify the discussion of the different time discretization schemes, the following notation is introduced, to signify the value of a variable (ϕ) at different time steps:

- $\phi^n \equiv \phi(t + \Delta t)$ where n indicates the value of the variable ϕ to be computed at the time step currently being solved
- $\phi^0 \equiv \phi(t)$ where 0 indicates the (known) value of the variable ϕ from the previous timestep
- $\phi^{00} \equiv \phi(t - \Delta t)$ where 00 indicates the (known) value of the variable ϕ from the penultimate timestep

OpenFOAM[®] automatically stores the values of all variables from the preceding two time steps. Several numerical integration schemes are available, and will be described in the following section.

Euler scheme

For the solution of transient problems, the time integration includes the integration of the spatial derivatives. Following the OpenFOAM programming guide (OpenCFD, 2011) we denote the spatial operator on any variable ϕ as $\mathcal{A}\phi$, so that the general time integral form of the equation to be integrated can be written as:

$$\int_t^{t+\Delta t} \left[\frac{\partial}{\partial t} \int_V \phi dV + \int_V \mathcal{A}\phi dV \right] dt = 0 \quad (\text{A.8})$$

The first term of left hand side of equation(A.8) can be discretized using the Euler implicit method as:

$$\frac{\partial}{\partial t} \int_V \phi dV = \frac{(\phi_P V)^n - (\phi_P V)^o}{\Delta t} \quad (\text{A.9})$$

The second term of left hand side of equation (A.8) can be written as:

$$\int_t^{t+\Delta t} \left[\int_V \mathcal{A}\phi dV \right] dt = \int_t^{t+\Delta t} \mathcal{A}^* \phi dt \quad (\text{A.10})$$

where \mathcal{A}^* represents the spatial integration of \mathcal{A} . The time integration for spatial term could be described using either an explicit or an implicit expression. The explicit formulation uses the preceding value of ϕ^o as follows:

$$\int_t^{t+\Delta t} \mathcal{A}^* \phi dt \approx \mathcal{A}^* \phi^o \Delta t \quad (\text{A.11})$$

whereas the implicit formulation uses the current value of ϕ^n in the discretization:

$$\int_t^{t+\Delta t} \mathcal{A}^* \phi dt \approx \mathcal{A}^* \phi^n \Delta t \quad (\text{A.12})$$

Both of these expressions are first order accurate in time. The implicit discretization guarantees boundedness in the solution and is unconditionally stable. The explicit discretization on the other hand is limited by the Courant number (Co) and is unstable if Co is greater than 1. The Courant number is defined as:

$$Co = \frac{\mathbf{U}_f \cdot \mathbf{d}}{|\mathbf{d}|^2 \Delta t} \quad (\text{A.13})$$

where \mathbf{U}_f is the velocity vector and \mathbf{d} is the distance vector from point P to its neighbours N (see Figure A.1).

Backward scheme

The backward scheme uses the two previous time step values and is second order accurate in time. It is defined as follows:

$$\frac{\partial}{\partial t} \int_V \phi dV \approx \frac{3(\phi_P V)^n - 4(\phi_P V)^o + (\phi_P V)^{oo}}{2\Delta t} \quad (\text{A.14})$$

The solution from this scheme is not guaranteed to be bounded.

Crank Nicholson scheme

The Crank-Nicholson scheme uses the mean value of the variable ϕ over the time interval Δt , so that the second term on the left hand side of equation (A.8) can be written:

$$\int_t^{t+\Delta t} \mathcal{A}^* \phi dt \approx \mathcal{A}^* \left(\frac{\phi^n + \phi^o}{2} \right) \Delta t \quad (\text{A.15})$$

This is second order accurate in time, and is unconditionally stable. However, the Crank Nicholson scheme is not bounded, and usually a blending with the Euler implicit method is used to improve the boundedness. The blending is done by introducing the off-centering coefficient, ψ , where:

$$\psi = \begin{cases} 1 & \text{pure Crank-Nicholson method} \\ 0 & \text{pure Euler method} \end{cases} \quad (\text{A.16})$$

$\psi = 0.9$ is usually recommended to retain accuracy and improve stability.

A.2.2 Gradient discretization

Gauss scheme

The Gauss integration scheme for the gradient terms use Gauss's theorem to convert a volume integral of the derivative of a function into a surface integral of the function. For an arbitrary variable ϕ , the Gauss integration scheme is defined as:

$$\int_V \nabla \phi dV = \int_S d\mathbf{S} \phi = \sum_f \mathbf{S}_f \phi_f \quad (\text{A.17})$$

Least squares scheme

The least squares method evaluates the gradient at a point using the sum of the weighted errors with respect to the gradient, at all the neighbouring points P . The tensor \mathbf{G} is calculated at every point P :

$$\mathbf{G} = \sum_N w_N^2 \mathbf{d} \mathbf{d} \quad (\text{A.18})$$

where w_N is the weighting factor which is taken as $1/|\mathbf{d}|$. The gradient of ϕ is then calculated as:

$$(\nabla \phi)_P = \sum_N w_N^2 \cdot \mathbf{d} (\phi_N - \phi_P) \quad (\text{A.19})$$

Gradient limiter

The gradient limiter is used to ensure the boundedness of the solution by its neighbouring cell values. There are two type of scheme: cell limited and face limited. The cell limited gradient scheme evaluates the limit based on the values in the neighbouring cells. Figure A.1 show a typical hexahedral control volume configuration where ϕ_P is the owner cell value and ϕ_N are the values at the neighbouring cells.

The gradient is evaluated on the face f . The maximum and minimum values for every owner and neighbour cells are evaluated:

$$\begin{aligned} \phi_{P,max} &= \max(\phi_P, \phi_N) \\ \phi_{P,min} &= \min(\phi_P, \phi_N) \\ \phi_{N,max} &= \max(\phi_P, \phi_N) \\ \phi_{N,min} &= \min(\phi_P, \phi_N) \end{aligned} \quad (\text{A.20})$$

The limiting values, denoted as $\Delta\phi_{max}$ and $\Delta\phi_{min}$ are evaluated in every owner and neighbour cells, so the subscripts P and N vanish. For every cell:

$$\begin{aligned} \Delta\phi_{max} &= \phi_{max} - \phi + \left(\frac{1}{k} - 1\right) (\phi_{max} - \phi_{min}) \\ \Delta\phi_{in} &= \phi_{min} - \phi - \left(\frac{1}{k} - 1\right) (\phi_{max} - \phi_{min}) \end{aligned} \quad (\text{A.21})$$

where k is a limiter coefficient where for $k = 1$ for fully limited scheme. As $k \rightarrow 0$, $1/k \rightarrow \infty$ and the limit will be so large that, effectively, no limit will be applied. The limiting values are then calculated for the faces of every control volume, and they are used whenever the extrapolated value exceeds these limiting values. The extrapolated value ϕ_{ext} is calculated from the original gradient as:

$$\phi_{ext} = \mathbf{r} \cdot \nabla \phi \quad (\text{A.22})$$

And the limiter is calculated as:

$$\begin{aligned} \psi &= \frac{\Delta\phi_{max}}{\mathbf{r} \cdot \nabla \phi}, \text{ for } \phi_{ext} > \phi_{max} \\ \psi &= \frac{\Delta\phi_{min}}{\mathbf{r} \cdot \nabla \phi}, \text{ for } \phi_{ext} < \phi_{min} \end{aligned} \quad (\text{A.23})$$

where ψ is the limiter coefficient for the gradient. The new gradient value is then calculated as:

$$\nabla\phi_{lim} = \psi\nabla\phi \quad (\text{A.24})$$

In the face-limited gradient scheme, the maximum values of ϕ_{max} and ϕ_{min} are evaluated on the face f , not in the owner and neighbour cells, hence $\phi_{f,max}$ and $\phi_{f,min}$ are calculated as:

$$\begin{aligned} \phi_{f,max} &= \max(\phi_P, \phi_N) \\ \phi_{f,min} &= \min(\phi_P, \phi_N) \end{aligned} \quad (\text{A.25})$$

A multi-directional version is available for both limiters. In the multi-directional version, the evaluation of extrapolated values is done for each face (hence multi-directional– the opposite of using one value of ψ as limiter). The new gradient value for the multi-directional version is calculated as follows:

$$\begin{aligned} \nabla\phi_{lim} &= \frac{\Delta\phi_{max}}{\mathbf{r}}, \text{ for } \nabla\phi > \Delta\phi_{max}/\mathbf{r} \\ \nabla\phi_{lim} &= \frac{\Delta\phi_{min}}{\mathbf{r}}, \text{ for } \nabla\phi < \Delta\phi_{min}/\mathbf{r} \end{aligned} \quad (\text{A.26})$$

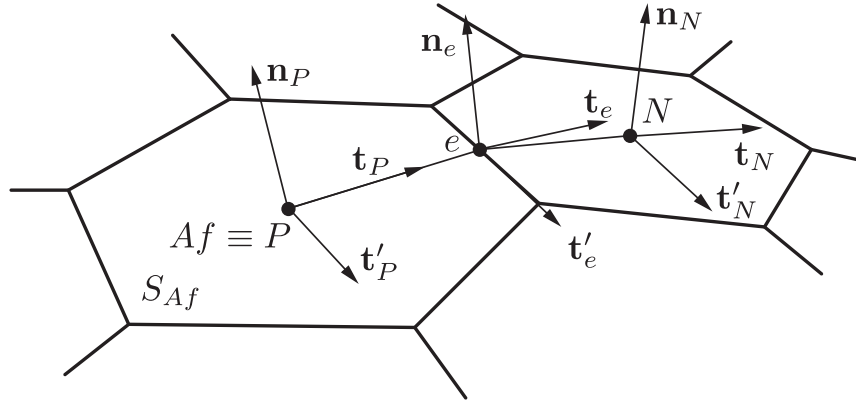
A.3 Finite area method

The Finite Area Method (FAM) is similar to the Finite Volume Method (FVM) but applied to a two dimensional curved surface in three dimension. As in the FVM, the computational domain is discretized into control areas with straight edge boundaries (in the FVM the computational domain is discretized into control volumes bounded by plane surface). The details of the Finite Area Method in OpenFOAM[®] are provided by Tukovic and Jasak (2008). This section will briefly describe the method using notation similar to that of Tukovic and Jasak (2008). Figure A.2 shows a control area with centroid P and a neighbouring control area with centroid N ; they share an edge e with length L_e . The distance vector between the two centroids is d_e . \mathbf{n}_P , \mathbf{n}_N , and \mathbf{n}_e are the normal vectors for the control areas and the edge respectively. \mathbf{m}_e is the vector perpendicular to \mathbf{e} and \mathbf{n}_e . As with the Finite Volume Method, the surface integration is discretized as an edge-based flux using the divergence theorem. In order to take account of the curvature effect, the edge value is calculated using a linear transformation and an edge-based local coordinate is used. Figure A.2 shows the edge-based local coordinate system where t_e is the unit vector tangential to the geodetic line \overline{PeN} at point e . Take $\mathbf{u}_{t,e}$ as edge-center tangential velocity at e , $\mathbf{u}_{t,e}$ is calculated as:

$$\mathbf{u}_{t,e} = \mathbf{T}_e^T \cdot [e_x \mathbf{T}_P \cdot \mathbf{u}_{t,P} + (1 - e_x) \mathbf{T}_N \cdot \mathbf{u}_{t,N}] \quad (\text{A.27})$$

where $\mathbf{T}_{P,N,e}$ is the transformation tensor from global Cartesian coordinates to the edge-based local coordinate system and e_x is the interpolation factor which is calculated as the ratio of geodetic distance \overline{eN} and \overline{PeN} :

$$e_x = \frac{\overline{eN}}{\overline{PeN} + \overline{eN}} \quad (\text{A.28})$$



$$\phi_{n+1}^* = \phi_n + \alpha (\phi_{n+1} - \phi_n) \quad (\text{A.32})$$

where ϕ_{n+1}^* is the new value to be used in the next iteration and a combination of the value from the previous iteration ϕ_n and the current iteration ϕ_{n+1} . Using the relaxation factor, it is possible to obtain stability using $Co > 1.0$. The PIMPLE algorithm uses a combination of both PISO and SIMPLE schemes. The system uses the SIMPLE algorithm for n iterations and then uses the PISO algorithm for the last iteration. The number of iteration is set using the **nOuterCorrector**, which for **nOuterCorrector** of 1 means the pure PISO algorithm will be used.

A.5 Boundary conditions

Several boundary condition is available in OpenFOAM[®]. In this section, several types of boundary condition that can be used in the simulation will be described.

Fixed value boundary condition

The fixed value boundary condition is a Dirichlet type boundary condition which prescribes the value of dependent variables at the boundary face. For a value at the boundary ϕ_{bc} , the evaluation of value at boundary face can be accomplished simply by substituting the value at the boundary face ϕ_f as ϕ_{bc} . The face gradient $(\nabla\phi)_f$ is evaluated as:

$$\mathbf{S}_f \cdot (\nabla\phi)_f = |\mathbf{S}_f| \frac{\phi_{bc} - \phi_P}{|\mathbf{d}|} \quad (\text{A.33})$$

Zero-gradient boundary condition

Zero gradient boundary condition is a Neumann type boundary condition where the prescribed surface normal gradient of g_{bc} is used:

$$g_{bc} = \left(\frac{\mathbf{S}}{|\mathbf{S}|} \cdot \nabla\phi \right)_f \quad (\text{A.34})$$

For the zero gradient boundary condition, g_{bc} is set as zero. The value on the boundary face is interpolated from the cell center value:

$$\begin{aligned} \phi_f &= \phi_P + \mathbf{d} \cdot (\nabla\phi)_f \\ &= \phi_P + |\mathbf{d}| g_{bc} \\ \phi_f &= \phi_P \end{aligned} \quad (\text{A.35})$$

The face gradient set directly as zero:

$$\mathbf{S}_f \cdot (\nabla\phi)_f = 0 \quad (\text{A.36})$$

Inlet-outlet boundary condition

The inlet-outlet boundary condition is a combination of a fixed value bc. and a zero-gradient bc. It works by switching the boundary condition so that it is a fixed-value bc if the flow direction directed to the interior of the domain, and a zero-gradient bc if the flow direction is directed towards the exterior of the domain (Figure A.3). The flow direction is evaluated the flux at each of the boundary faces.

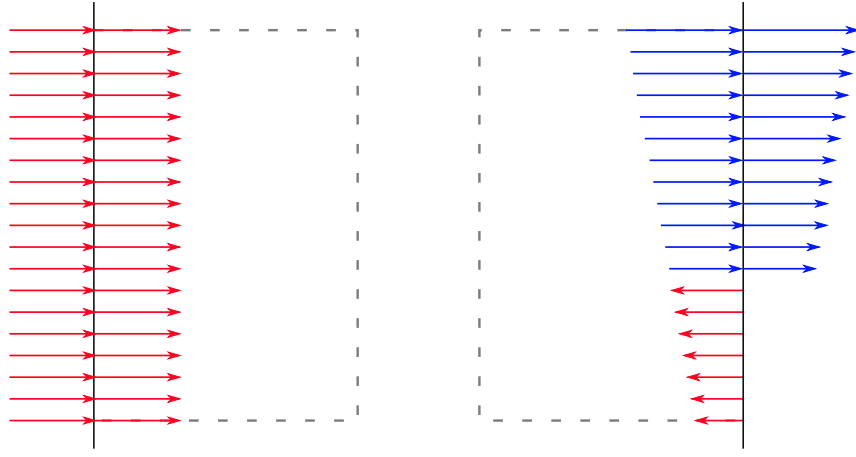


Figure A.3: Implementation of inlet-outlet boundary condition at OpenFOAM®

Total pressure boundary condition

The total pressure boundary condition is based on the fixed-value bc. where the pressure definition is based on the total pressure, p_0 . For an incompressible flow, the pressure value at the patch p_p is calculated by subtracting the dynamic pressure component:

$$p_p = p_0 - 0.5|\mathbf{U}|^2 \quad (\text{A.37})$$

Appendix B

Ghost Fluid Method Discretization

In section 2.4.2 we described how the conditional averaging used in the Volume Of Fluid method overestimates the accelerations in the cells that are not completely full, because the average fluid density is less than the density of the heavier phase. Vukčević (2016) proposed a correction by introducing a pressure discontinuity at the free surface, and he called this the Ghost Fluid Method (GFM). This section will give a brief introduction to the discretization procedure for implementing GFM in OpenFOAM® based on the work by Vukčević (2016).

In the VOF method, the free surface is not explicitly defined. It is described as the transition between the water and air phase. In this work, the free surface is assumed to be located where the phase fraction $\alpha = 0.5$. In order to locate the free surface, wet and dry cells are defined as follows (Vukčević et al., 2017):

- Wet cells are defined as cells where the phase fraction of $\alpha_P > 0.5$ and dry cells are defined as cells for which $\alpha_P < 0.5$.
- The cell faces that constitute the interface are those for which $(\alpha_P - 0.5)(\alpha_N - 0.5) < 0$ as shown in figure B.1. The other faces are treated normally.
- A specific treatment is applied to the interface faces to account for the pressure jump condition.

Figure B.2 shows an example of the computational domain for an interface face. The free surface location vector \mathbf{x}_Γ is calculated as follows:

$$\mathbf{x}_\Gamma = \mathbf{x}_P + \lambda \mathbf{d}_f \quad (\text{B.1})$$

where \mathbf{x}_P is the location vector for the owner cell P and \mathbf{d}_f is the distance vector from P to the neighbour cell N . λ is the dimensionless distance from P to the free surface, calculated based on the phase fraction:

$$\lambda = \frac{\alpha_P - 0.5}{\alpha_P - \alpha_N} \quad (\text{B.2})$$

The pressure jump condition is discretized as follows:

$$[p_d] = (\rho^+ - \rho^-) \mathbf{g} \cdot \mathbf{x}_\Gamma = \mathcal{H} \quad (\text{B.3})$$

The modified pressure p_d extrapolated using jump conditions is calculated as:

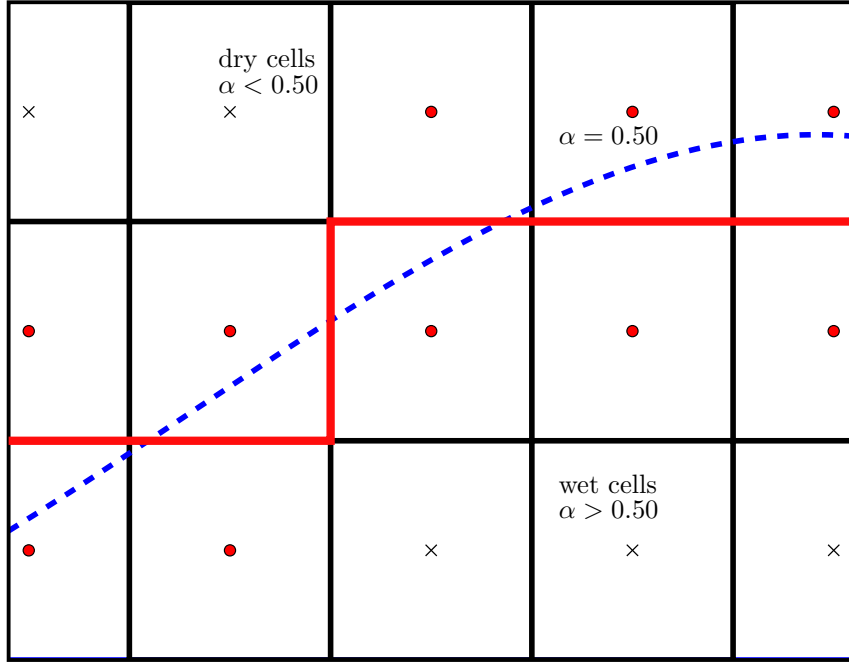


Figure B.1: Wet and dry cells in discretization domain for ghost fluid method (Vukčević et al., 2017)

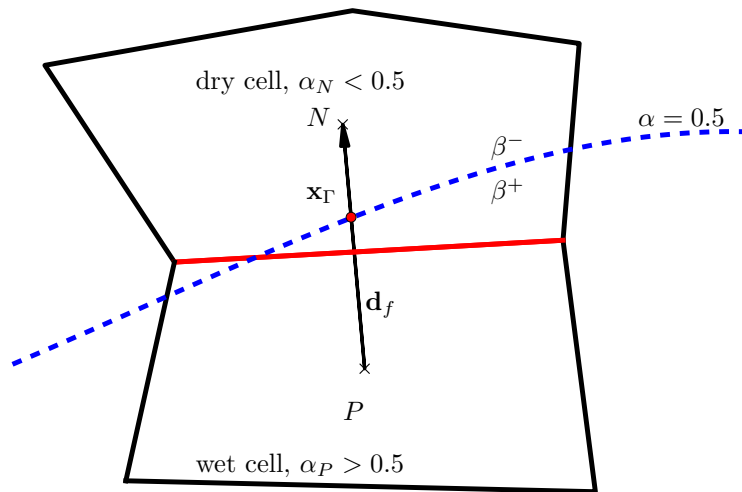


Figure B.2: Free surface distance \mathbf{x}_Γ for one interface face (Vukčević et al., 2017)

- For wet cell P and dry cell N

$$p_{dN\Gamma}^+ = \frac{\beta^-}{\overline{\beta}_w} + \left(1 - \frac{\beta^-}{\overline{\beta}_w}\right) p_{dP} - \frac{\beta^-}{\overline{\beta}_w} \mathcal{H} \quad (\text{B.4})$$

$$p_{dP\Gamma}^- = \frac{\beta^+}{\overline{\beta}_w} + \left(1 - \frac{\beta^+}{\overline{\beta}_w}\right) p_{dN} - \frac{\beta^+}{\overline{\beta}_w} \mathcal{H} \quad (\text{B.5})$$

- For dry cell P and wet cell N

$$p_{dN\Gamma}^- = \frac{\beta^+}{\overline{\beta}_d} + \left(1 - \frac{\beta^+}{\overline{\beta}_d}\right) p_{dP} - \frac{\beta^+}{\overline{\beta}_d} \mathcal{H} \quad (\text{B.6})$$

$$p_{dP\Gamma}^+ = \frac{\beta^-}{\overline{\beta}_d} + \left(1 - \frac{\beta^-}{\overline{\beta}_d}\right) p_{dN} - \frac{\beta^-}{\overline{\beta}_d} \mathcal{H} \quad (\text{B.7})$$

where $\overline{\beta}_w$ and $\overline{\beta}_d$ are the weighted inverse densities evaluated from the wet and dry cells respectively. These values depend on the distance to the free surface λ , hence:

$$\overline{\beta}_w = \lambda\beta^- + (1 - \lambda)\beta^+ \quad (\text{B.8})$$

and

$$\overline{\beta}_d = \lambda\beta^+ + (1 - \lambda)\beta^- \quad (\text{B.9})$$

It can be shown that $\overline{\beta}_w \neq \overline{\beta}_d$.

B.1 Pressure jump implementation in discretized governing equation

B.1.1 Pressure jump implementation in pressure gradient term

The interface-corrected gradient scheme is introduced by Vukčević et al. (2017) in order to take account of the pressure jump condition. The Gauss interface-corrected pressure for cell P is wet is given by:

$$\beta_P \nabla p_{dP} = \frac{\beta_P}{V_P} \sum_{f, \mathbb{K}} \mathbf{S}_f (f_x p_{dP} + (1 - f_x) p_{dN}) + \frac{\beta_P}{V_P} \sum_{f, \Gamma} \mathbf{S}_f (f_x p_{dP} + (1 - f_x) p_{dN\Gamma}^+) \quad (\text{B.10})$$

where $\sum_{f, \mathbb{K}}$ is the sum for regular faces and $\sum_{f, \Gamma}$ is the sum for the interface faces. The interface face interpolation uses $p_{dN\Gamma}^+$, where the index $+$ indicates extrapolation from the wet side. Substituting equation (B.4) into the interface face interpolation on (equation B.10) give:

$$\begin{aligned} \frac{\beta_P}{V_P} \sum_{f, \Gamma} \mathbf{S}_f (f_x p_{dP} + (1 - f_x) p_{dN\Gamma}^+) = \\ \frac{1}{V_P} \sum_{f, \Gamma} \mathbf{S}_f \beta^+ p_{dP} + \frac{1}{V_P} \sum_{f, \Gamma} \mathbf{S}_f \frac{\beta^+ \beta^-}{\overline{\beta}_w} (1 - f_x) (p_{dN} - p_{dP} - \mathcal{H}) \end{aligned} \quad (\text{B.11})$$

A similar expression can be derived for the dry P cell using $p_{dN\Gamma}^-$. Using a similar approach, the least squares gradient scheme can be written as a split sum:

$$\beta_P \nabla p_{dP} = \frac{\beta_P}{V_P} \sum_{f,\mathbb{K}} \mathbf{I}_f (p_{dN} - p_{dP}) + \frac{\beta_P}{V_P} \sum_{f,\Gamma} \mathbf{I}_f (p_{dN\Gamma}^+ - p_{dP}) \quad (\text{B.12})$$

where \mathbf{I}_f is the least squares vector.

B.1.2 Pressure jump implementation in pressure Laplacian term

The implicit part of the pressure equation is written as the split sum of regular faces and interface faces:

$$\begin{aligned} \sum_f \left(\frac{1}{a_P} \right)_f (\beta)_{f\Gamma} |\mathbf{S}_f| \frac{(p_{dN} - p_{dP})_\Gamma}{|\mathbf{d}_f|} &= \sum_{f,\mathbb{K}} \left(\frac{1}{a_P} \right)_f (\beta)_f |\mathbf{S}_f| \frac{p_{dN} - p_{dP}}{|\mathbf{d}_f|} \\ &+ \sum_{f,\Gamma} \left(\frac{1}{a_P} \right)_f (\beta)_{f\Gamma} |\mathbf{S}_f| \frac{p_{dN\Gamma} - p_{dP}}{|\mathbf{d}_f|} \end{aligned} \quad (\text{B.13})$$

For a single wet cell P , the interface face contribution can be written as:

$$\begin{aligned} \left(\frac{1}{a_P} \right)_f (\beta)_{f\Gamma} |\mathbf{S}_f| \frac{p_{dN\Gamma}^+ - p_{dP}}{|\mathbf{d}_f|} &= \left(\frac{1}{a_P} \right)_f \frac{|\mathbf{S}_f|}{|\mathbf{d}_f|} \frac{\beta^+ \beta^-}{\beta_w} (p_{dN} - p_{dP} - \mathcal{H}) \\ &= \left(\frac{1}{a_P} \right)_f \frac{|\mathbf{S}_f|}{|\mathbf{d}_f|} \frac{\beta^+ \beta^-}{\beta_w} (p_{dN} - p_{dP}) \\ &\quad - \left(\frac{1}{a_P} \right)_f \frac{|\mathbf{S}_f|}{|\mathbf{d}_f|} \frac{\beta^+ \beta^-}{\beta_w} \mathcal{H} \end{aligned} \quad (\text{B.14})$$

where $\beta_{f\Gamma} = \beta^+$ and $p_{dN\Gamma}^+$ is given by equation (B.4) for wet cell P . The last term of equation (B.14) is the additional source term due to the introduction of the jump condition, and it reads:

$$S_P = \left(\frac{1}{a_P} \right)_f \frac{|\mathbf{S}_f|}{|\mathbf{d}_f|} \frac{\beta^+ \beta^-}{\beta_w} \mathcal{H} \quad (\text{B.15})$$

The adjacent neighbour cells N for a wet cell P are considered as dry cells. Hence, the jump contribution for a dry cell N is given as:

$$\left(\frac{1}{a_P} \right)_f (\beta)_{f\Gamma} |\mathbf{S}_f| \frac{p_{dP\Gamma}^- - p_{dP}}{|\mathbf{d}_f|} = \left(\frac{1}{a_P} \right)_f \frac{|\mathbf{S}_f|}{|\mathbf{d}_f|} \frac{\beta^+ \beta^-}{\beta_w} (p_{dP} - p_{dN} + \mathcal{H}) \quad (\text{B.16})$$

where $\beta_{f\Gamma} = \beta^-$ and $p_{dP\Gamma}^-$ is given by equation (B.5) for dry cell N . The additional source term contribution from the jump condition for the dry cell N then reads:

$$S_N = - \left(\frac{1}{a_P} \right)_f \frac{|\mathbf{S}_f|}{|\mathbf{d}_f|} \frac{\beta^+ \beta^-}{\beta_w} \mathcal{H} \quad (\text{B.17})$$

Vukčević et al. (2017) found that the additional source terms from the pressure jump condition are anti-symmetric. Hence they are added as an additional flux through the interface faces.

Appendix C

Suspended Load Entrainment Limiter

The suspended model in chapter 3, needs an empirical equation to define the sediment entrainment. In this work a model from Van Rijn (1984b) is used. Equation 3.17 is rewritten in simpler form as:

$$C_s = A\psi^{1.5} \quad (\text{C.1})$$

where A is the constant part of equation:

$$A = \frac{0.015d_{50}}{\Delta d_*^{0.3}} \quad (\text{C.2})$$

However, equation C.1 is unbounded and increases exponentially at high values of the stage discharge number, resulting in physically impossible values of the concentration. Hence, in this work a limiter is applied so that the maximum possible concentration is that given by a close-packing arrangement of the sediment grains:

$$C_{max} = \frac{(1 - n)}{(1 + K_b)} \quad (\text{C.3})$$

where n is the sediment porosity and K_b is the bulk coefficient; this equation implies that the concentration of the suspended sediment cannot exceed that of the sediment that has settled on the bed. One possible approach would be simply to limit the concentration to the value C_{max} , but in reality the concentration is likely to approach this maximum value rather slowly, so instead we have used an interpolation function to provide a smooth transition. The general approximation for the relationship between concentration and stage discharge number is to divide the stage discharge number into three parts, as shown in figure C.1.

The three regions are described as follows:

$$\begin{aligned} \psi \leq \psi_1 & : C_s = A\psi^{1.5} \\ \psi_1 < \psi < \psi_2 & : C_s = f(\psi) \\ \psi_2 \leq \psi & : C_s = C_{max} \end{aligned} \quad (\text{C.4})$$

where a Bézier curve is used to interpolate in the middle region. Bézier curves are curves in parametric form – they are written in terms of an auxiliary parameter, s , which varies between 0 and 1 as the curve moves between the support points. Thus to compute C_s for any given value of ψ , for example, the auxiliary parameter s that corresponds to the value of ψ needs to be computed first. For this reason,

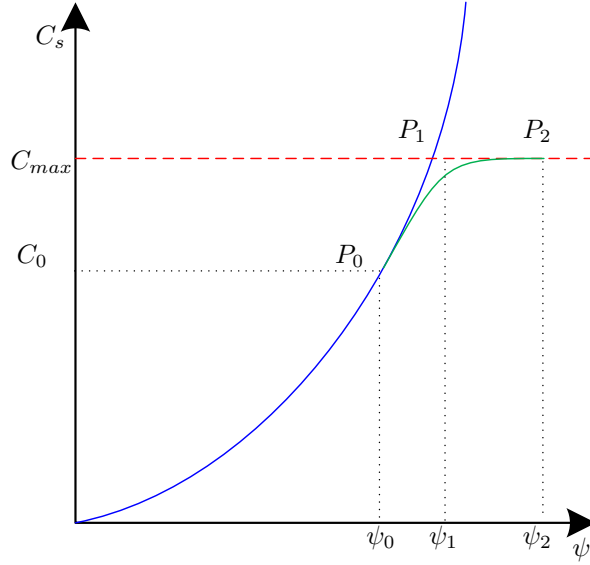


Figure C.1: Concentration as a function of stage discharge number

this application is limited to quadratic Bézier curves – the use of a cubic Bézier curve would require the solution of a cubic polynomial for s . The basic form of the quadratic Bézier curve is shown in Figure C.2, where the point P_1 is the intersection of the tangents to the curve at P_0 and P_2 . Then the equation of the curve between P_0 and P_2 is:

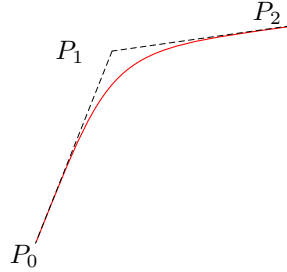


Figure C.2: Quadratic Bézier curve

$$P(s) = (1 - s)^2 P_0 + 2s(1 - s)P_1 + s^2 P_2, \quad 0 < s < 1 \quad (\text{C.5})$$

For this problem, three values need to be decided:

- ψ_0 : the value of ψ at which the interpolated function will diverge from the theoretical function
- C_{max} : the value of the maximum concentration from equation C.3
- ψ_2 : the value of ψ at which C reaches the maximum value.

Using the three points (ψ_0, C_0) , (ψ_1, C_1) and (ψ_2, C_2) as defined in Figure C.1, we obtain:

$$\begin{aligned}
C_0 &= A\psi_0^{1.5} \\
\psi_1 &= \psi_0 + \frac{C_{max} - C_0}{1.5A\psi_0^{0.5}} \\
C_1 &= C_{max} \\
C_2 &= C_{max}
\end{aligned} \tag{C.6}$$

In order to calculate the value of C_s for any value of ψ in the region $\psi_0 < \psi < \psi_2$, it is necessary to solve the following quadratic equation in s :

$$\psi = (1 - s)^2\psi_0 + 2s(1 - s)\psi_1 + s^2\psi_2 \tag{C.7}$$

The concentration then calculated as:

$$C_s = (1 - s)^2C_0 + s(2 - s)C_{max} \tag{C.8}$$

Bibliography

- Ahmad, Nadeem et al. (2015). “Three-dimensional CFD modeling of wave scour around side-by-side and triangular arrangement of piles with REEF3D”. *Procedia Engineering* 116, pp. 683–690.
- Allsop, William (Aug. 2014). *Failures of seawalls: What do we learn from Dawlish? London*. URL: <https://www.ice.org.uk/eventarchive/failure-of-seawalls-dawlish> (visited on 10/26/2017).
- Asano, Toshiyuki (1991). “Two-phase flow model on oscillatory sheet-flow”. *Coastal Engineering* 1990, pp. 2372–2384.
- Bagnold, Ralph A (1954). “Experiments on a gravity-free dispersion of large solid spheres in a Newtonian fluid under shear”. *Proceedings of the Royal Society of London A: Mathematical, Physical and Engineering Sciences*. Vol. 225. 1160. The Royal Society, pp. 49–63.
- Bakhtyar, Roham et al. (2010). “Numerical simulation of two-phase flow for sediment transport in the inner-surf and swash zones”. *Advances in water resources* 33.3, pp. 277–290.
- Barnett, Michael R and Hsiang Wang (1988). “Effects of a vertical seawall on profile response”. *Coastal Engineering Proceedings* 1.21.
- Battjes, JA (1974). “Surf similarity”. *Coastal Engineering Proceedings* 1.14.
- BBC (Nov. 2014). *Smashed sea wall damaged again*. en-GB. URL: <http://www.bbc.com/news/uk-england-devon-30026151> (visited on 10/26/2017).
- Boussinesq, Joseph (1871). “Théorie de l’intumescence liquide appelée onde solitaire ou de translation se propageant dans un canal rectangulaire”. *Comptes Rendus Acad. Sci (Paris)* 72, pp. 755–759.
- Bradbury, A, J Rogers, and D Thomas (2012). “The Toe Structures Management Manual”. *Environment Agency, Bristol, UK*.
- Bruun, Per (1962). “Sea-level rise as a cause of shore erosion”. *Journal of the Waterways and Harbors division* 88.1, pp. 117–132.
- Carstensen, Stefan and B Mutlu Sumer (2015). “Scour At Breakwaters Under Combined Waves And Current”. *Proceedings of the 36th Iahr World Congress*.
- Carter, Trevor G (1972). *Mass Transport in Water Waves. Part II. Experiments*. Tech. rep. Massachusetts Inst Of Tech Cambridge Ralph M Parsons Lab For Water Resources and Hydrodynamics.
- Chappelear, J. E. (1962). “Shallow-water waves”. *Journal of Geophysical Research* 67.12. ISSN: 2156-2202.
- Chauchat, J. et al. (2017). “SedFoam-2.0: a 3-D two-phase flow numerical model for sediment transport”. *Geoscientific Model Development* 10.12, pp. 4367–4392.
- Choi, Junwoo and Sung Bum Yoon (2009). “Numerical simulations using momentum source wave-maker applied to RANS equation model”. *Coastal Engineering* 56.10, pp. 1043–1060.

- Dawlishnewspapers (2014). *Battered*. URL: <http://www.dawlishnewspapers.co.uk/article.cfm?id=31&headline=Battered§ionIs=news&searchyear=2014> (visited on 10/26/2017).
- Dean, Robert G (1970). "Relative validities of water wave theories". *Journal of the Waterways, Harbors and Coastal Engineering Division* 96.1, pp. 105–119.
- (1987). "Coastal armoring: effects, principles and mitigation". *Coastal Engineering* 1986, pp. 1843–1857.
- Dean, Robert G and Chul-Hee Yoo (1994). "Beach nourishment in presence of seawall". *Journal of waterway, port, coastal, and ocean engineering* 120.3, pp. 302–316.
- Delta Flume (2017). URL: <https://www.deltares.nl/en/facilities/delta-flume> (visited on 10/26/2017).
- Devolder, Brecht, Pieter Rauwoens, and Peter Troch (2017). "Application of a buoyancy-modified $k-\omega$ SST turbulence model to simulate wave run-up around a monopile subjected to regular waves using OpenFOAM®". *Coastal Engineering* 125, pp. 81–94.
- Ding, Jianmin and Dimitri Gidaspo (1990). "A bubbling fluidization model using kinetic theory of granular flow". *AIChE journal* 36.4, pp. 523–538.
- Dyke, PPG and SF Barstow (1981). "Wave induced mass transport: theory and experiment". *Journal of Hydraulic Research* 19.2, pp. 89–106.
- Einstein, Hans Albert (1950). *The bed-load function for sediment transportation in open channel flows*. 1026. US Department of Agriculture.
- Engelund, Frank and Jørgen Fredsøe (1976). "A sediment transport model for straight alluvial channels". *Hydrology Research* 7.5, pp. 293–306.
- Fernandez Luque, R and R Van Beek (1976). "Erosion and transport of bed-load sediment". *Journal of Hydraulic Research* 14.2, pp. 127–144.
- Fredsøe, Jørgen and Rolf Deigaard (1992). *Mechanics of coastal sediment transport*. Vol. 3. World scientific.
- Galvin, Cyril J (1968). "Breaker type classification on three laboratory beaches". *Journal of geophysical research* 73.12, pp. 3651–3659.
- Gingold, Robert A and Joseph J Monaghan (1977). "Smoothed particle hydrodynamics: theory and application to non-spherical stars". *Monthly notices of the royal astronomical society* 181.3, pp. 375–389.
- Gislason, Kjartan, Jørgen Fredsøe, and B Mutlu Sumer (2009). "Flow under standing waves: Part 2. Scour and deposition in front of breakwaters". *Coastal engineering* 56.3, pp. 363–370.
- Griggs, Gary B et al. (1991). "The interaction of seawalls and beaches: Four years of field monitoring, Monterey Bay, California". *Coastal Sediments (1991)*. ASCE, pp. 1871–1885.
- Grimshaw, R. (1971). "The solitary wave in water of variable depth. Part 2". *Journal of Fluid Mechanics* 46.3, pp. 611–622. DOI: 10.1017/S0022112071000739.
- Guignard, Stephan et al. (2001). "Solitary wave breaking on sloping beaches: 2-D two phase flow numerical simulation by SL-VOF method". *European Journal of Mechanics-B/Fluids* 20.1, pp. 57–74.
- Guy, Harold P, Daryl B Simons, and Everett V Richardson (1966). *Summary of alluvial channel data from flume experiments, 1956-61*. Tech. rep.
- Hajivalie, Fatemeh et al. (2012). "Euler–Lagrange model for scour in front of vertical breakwater". *Applied Ocean Research* 34, pp. 96–106.

- Hanson, Hans and Nicholas C Kraus (1985). “Seawall constraint in shoreline numerical model”. *Journal of Waterway, Port, Coastal, and Ocean Engineering* 111.6, pp. 1079–1083.
- (1986). *Seawall Boundary Condition in Numerical Models of Shoreline Evolution*. Tech. rep. DTIC Document.
- Harlow, Francis H and J Eddie Welch (1965). “Numerical calculation of time-dependent viscous incompressible flow of fluid with free surface”. *The physics of fluids* 8.12, pp. 2182–2189.
- Hasselmann, K et al. (1973). “Measurements of wind-wave growth and swell decay during the Joint North Sea Wave Project (JONSWAP)”. *Ergänzungsheft 8-12*.
- Hieu, Phung Dang, Tanimoto Katsutoshi, and Vu Thanh Ca (2004). “Numerical simulation of breaking waves using a two-phase flow model”. *Applied Mathematical Modelling* 28.11, pp. 983–1005.
- Higuera, Pablo, Javier L Lara, and Inigo J Losada (2013). “Realistic wave generation and active wave absorption for Navier–Stokes models: Application to OpenFOAM®”. *Coastal Engineering* 71, pp. 102–118.
- Hirt, Cyril W and Billy D Nichols (1981). “Volume of fluid (VOF) method for the dynamics of free boundaries”. *Journal of computational physics* 39.1, pp. 201–225.
- Issa, Raad I (1986). “Solution of the implicitly discretised fluid flow equations by operator-splitting”. *Journal of computational physics* 62.1, pp. 40–65.
- Jacobsen, Niels G (2015). “Mass conservation in computational morphodynamics: uniform sediment and infinite availability”. *International Journal for Numerical Methods in Fluids* 78.4, pp. 233–256.
- Jacobsen, Niels G and Jørgen Fredsøe (2014b). “Formation and development of a breaker bar under regular waves. Part 2: Sediment transport and morphology”. *Coastal Engineering* 88, pp. 55–68.
- Jacobsen, Niels G, Jørgen Fredsøe, and Jacob H Jensen (2014a). “Formation and development of a breaker bar under regular waves. Part 1: Model description and hydrodynamics”. *Coastal Engineering* 88, pp. 182–193.
- Jacobsen, Niels G, David R Fuhrman, and Jørgen Fredsøe (2012). “A wave generation toolbox for the open-source CFD library: OpenFoam®”. *International Journal for Numerical Methods in Fluids* 70.9, pp. 1073–1088.
- Jacobsen, Niels Gjøl and Jørgen Fredsøe (June 2011). “A Full Hydro- and Morphodynamic Description of Breaker Bar Development”. PhD thesis. ISBN: 978-87-90416-64-5.
- Jafari-Nodoushan, Ehsan, Ahmad Shakibaeinia, and Khosrow Hosseini (2017). “A multiphase meshfree method for continuum-based modeling of dry and submerged granular flows”. *arXiv preprint arXiv:1708.04521*.
- Jasak, Hrvoje (1996). “Error analysis and estimation for finite volume method with applications to fluid flow”.
- Jasak, Hrvoje and Zeljko Tukovic (2006). “Automatic mesh motion for the unstructured finite volume method”. *Transactions of FAMENA* 30.2, pp. 1–20.
- Jensen, BL, BM Sumer, and J Fredsøe (1989). “Turbulent oscillatory boundary layers at high Reynolds numbers”. *Journal of Fluid Mechanics* 206, pp. 265–297.
- Jonsson, Ivar G and Niels A Carlsen (1976). “Experimental and theoretical investigations in an oscillatory turbulent boundary layer”. *Journal of Hydraulic Research* 14.1, pp. 45–60.
- Kamphuis, J William (1975). “Friction factor under oscillatory waves”. *Journal of the Waterways, Harbors and Coastal Engineering Division* 101.2, pp. 135–144.

- Kamphuis, JW, KA Rakha, and J Jui (1992). "Hydraulic model experiments on seawalls". *Coastal Engineering Proceedings* 1.23.
- Korteweg, Diederik Johannes and Gustav De Vries (1895). "Xli. on the change of form of long waves advancing in a rectangular canal, and on a new type of long stationary waves". *The London, Edinburgh, and Dublin Philosophical Magazine and Journal of Science* 39.240, pp. 422–443.
- Koshizuka, Seiichi and Yoshiaki Oka (1996). "Moving-particle semi-implicit method for fragmentation of incompressible fluid". *Nuclear science and engineering* 123.3, pp. 421–434.
- Kraus, Nicholas C (1988). "The effects of seawalls on the beach: an extended literature review". *Journal of coastal Research*, pp. 1–28.
- Kraus, Nicholas C and William G McDougal (1996). "The effects of seawalls on the beach: Part I, an updated literature review". *Journal of coastal research*, pp. 691–701.
- Kriebel, David L and Robert G Dean (1985). "Beach and dune response to severe storms". *Coastal Engineering* 1984, pp. 1584–1599.
- Larson, Magnus, Li Erikson, and Hans Hanson (2004). "An analytical model to predict dune erosion due to wave impact". *Coastal Engineering* 51.8, pp. 675–696.
- Li, Yaru et al. (2014). "Development of a new 3D Euler-Lagrange model for the prediction of scour around offshore structures". *Coastal Engineering Proceedings* 1.34, p. 31.
- Liang, Dongfang, Liang Cheng, and Fangjun Li (2005). "Numerical modeling of flow and scour below a pipeline in currents: Part II. Scour simulation". *Coastal engineering* 52.1, pp. 43–62.
- Lin, Pengzhi and Philip L-F Liu (1998). "A numerical study of breaking waves in the surf zone". *Journal of fluid mechanics* 359, pp. 239–264.
- Liu, Xiaofeng and Marcelo H Garcia (2008). "Three-dimensional numerical model with free water surface and mesh deformation for local sediment scour". *Journal of waterway, port, coastal, and ocean engineering* 134.4, pp. 203–217.
- Longuet-Higgins, Michael S (1970). "Longshore currents generated by obliquely incident sea waves: 1". *Journal of geophysical research* 75.33, pp. 6778–6789.
- Longuet-Higgins, MS (1952). "On the statistical distribution of the heights of sea waves". *J. Mar. Research* 11.3, pp. 245–266.
- Marieu, Vincent et al. (2008). "Modeling of vortex ripple morphodynamics". *Journal of Geophysical Research: Oceans* 113.C9.
- Marsooli, Reza and Weiming Wu (2014). "Three-dimensional numerical modeling of dam-break flows with sediment transport over movable beds". *Journal of Hydraulic Engineering* 141.1, p. 04014066.
- Mayer, Stefan, Antoine Garapon, Lars Sørensen, et al. (1998). "A fractional step method for unsteady free-surface flow with applications to non-linear wave dynamics". *International Journal for Numerical Methods in Fluids* 28.2, pp. 293–315.
- Mayer, Stefan and Per A Madsen (2001). "Simulation of breaking waves in the surf zone using a navier-stokes solver". *Coastal Engineering* 2000, pp. 928–941.
- McDougal, William G, Nicholas C Kraus, and Harman Ajiwibowo (1994). "Simulation of wave and beach profile change in supertank seawall tests". *Coastal Dynamics '94*. ASCE, pp. 278–295.
- Méhauté, Bernard (1976). "An introduction to hydrodynamics and water waves".

- Mei, Chiang C and Philip LF Liu (1972). *Mass Transport in Water Waves. Part I. Theory. Part II. Experiments*. Tech. rep. DTIC Document.
- Menter, Florian R (1994). “Two-equation eddy-viscosity turbulence models for engineering applications”. *AIAA journal* 32.8, pp. 1598–1605.
- Meyer-Peter, Eugen and R Müller (1948). “Formulas for bed-load transport”. IAHR.
- Miles, Jonathon R, Paul E Russell, and David A Huntley (2001). “Field measurements of sediment dynamics in front of a seawall”. *Journal of Coastal Research*, pp. 195–206.
- Monaghan, Joe J (1994). “Simulating free surface flows with SPH”. *Journal of computational physics* 110.2, pp. 399–406.
- Moody, PM (1996). “Laboratory Study of the Effect of Seawalls on Beach Erosion”. PhD thesis. MS Thesis, Department of Civil and Environmental Engineering, Massachusetts Institute of Technology, Cambridge, Massachusetts.
- Mujal-Colilles, Anna et al. (2014). “PIV experiments in rough-wall, laminar-to-turbulent, oscillatory boundary-layer flows”. *Experiments in fluids* 55.1, p. 1633.
- Nwogu, Okey G and Zeki Demirbilek (2001). *BOUSS-2D: A Boussinesq wave model for coastal regions and harbors*. Tech. rep. ENGINEER RESEARCH, DEVELOPMENT CENTER VICKSBURG MS COASTAL, and HYDRAULICSLAB.
- OpenCFD (2011). “Openfoam programmer’s guide”. *OpenFOAM Foundation* 2.0.
- Patankar, Suhas V (1980). “Numerical heat transfer and fluid flow, Hemisphere Publ”. *Corp., New York* 58.
- Pedocchi, Francisco and Marcelo H Garcia (2009). “Friction coefficient for oscillatory flow: the rough–smooth turbulent transition”. *Journal of Hydraulic Research* 47.4, pp. 438–444.
- Peng, Zhong, Qing-Ping Zou, and Pengzhi Lin (2018). “A partial cell technique for modeling the morphological change and scour”. *Coastal Engineering* 131, pp. 88–105.
- Penney, WG and A To Price (1952). “Part I. The diffraction theory of sea waves and the shelter afforded by breakwaters”. *Philosophical Transactions of the Royal Society of London A: Mathematical, Physical and Engineering Sciences* 244.882, pp. 236–253.
- Perić, R and Moustafa Abdel-Maksoud (2016). “Reliable damping of free-surface waves in numerical simulations”. *Ship Technology Research* 63.1, pp. 1–13.
- Petersen, Ole Svenstrup and Nicolai F Heilskov (2015). *State-of-the-Art and Implementation of Design Tools for Floating Wave Energy Converters Part 2: Implementation and Results*. Tech. rep. DHI. URL: <http://www.sdved.civil.aau.dk/deliverables/>.
- Pilkey, Orrin H and Howard L Wright III (1988). “Seawalls versus beaches”. *Journal of Coastal Research*, pp. 41–64.
- Powell, KA (1987). “Toe scour at sea walls subject to wave action-a literature review”.
- Raudkivi, Arved J (1998). *Loose boundary hydraulics*. CRC Press.
- Rayleigh, Lord (1876). “On waves”. *Phil. Mag.* 1, pp. 257–259.
- Rijn, Leo C van (2007). “Unified view of sediment transport by currents and waves. II: Suspended transport”. *Journal of Hydraulic Engineering* 133.6, pp. 668–689.
- Rogers, Benedict D and Robert A Dalrymple (2005). “SPH modeling of breaking waves”. *Coastal Engineering 2004: (In 4 Volumes)*. World Scientific, pp. 415–427.
- Roulund, Andreas et al. (2005). “Numerical and experimental investigation of flow and scour around a circular pile”. *Journal of Fluid Mechanics* 534, pp. 351–401.

- Rusche, Henrik (2003). “Computational fluid dynamics of dispersed two-phase flows at high phase fractions”. PhD thesis. Imperial College London (University of London).
- Russell, RCH and JDC Osorio (1957). “An experimental investigation of drift profiles in a closed channel”. *Coastal Engineering Proceedings* 1.6, p. 10.
- Sattar, Ahmed MA, Hrvoje Jasak, and Vanja Skuric (2017). “Three dimensional modeling of free surface flow and sediment transport with bed deformation using automatic mesh motion”. *Environmental Modelling & Software* 97, pp. 303–317.
- Savage, Stuart B and Shawn Mckeown (1983). “Shear stresses developed during rapid shear of concentrated suspensions of large spherical particles between concentric cylinders”. *Journal of Fluid Mechanics* 127, pp. 453–472.
- Schäffer, Hemming A and Gert Klopman (2000). “Review of multidirectional active wave absorption methods”. *Journal of waterway, port, coastal, and ocean engineering* 126.2, pp. 88–97.
- Schiereck, Gerrit J (2003). *Introduction to bed, bank and shore protection*. CRC Press.
- Shakibaeinia, Ahmad and Yee-Chung Jin (2011). “A mesh-free particle model for simulation of mobile-bed dam break”. *Advances in Water Resources* 34.6, pp. 794–807.
- Shields, Albert (1936). *Anwendung der Aehnlichkeitsmechanik und der Turbulenzforschung auf die Geschiebepbewegung*. Tech. rep. Preussischen Versuchsanstalt für Wasserbau.
- Sleath, JFA (1968). “The effect of waves on the pressure in a bed of sand in a water channel and on the velocity distribution above it.” PhD thesis. University of Cambridge.
- Sleath, John FA (1984). *Sea bed mechanics*. John Wiley and Sons Inc., New York, NY.
- Smith, J Dungan and SR McLean (1977). “Spatially averaged flow over a wavy surface”. *Journal of Geophysical research* 82.12, pp. 1735–1746.
- Snider, DM (2001). “An incompressible three-dimensional multiphase particle-in-cell model for dense particle flows”. *Journal of Computational Physics* 170.2, pp. 523–549.
- Snider, DM, PJ ORourke, and MJ Andrews (1997). *An incompressible two-dimensional multiphase particle-in-cell model for dense particle flows*. Tech. rep. Los Alamos National Lab., NM (United States).
- Sorensen, Robert M (2005). *Basic coastal engineering*. Vol. 10. Springer Science & Business Media.
- Soulsby, Richard (1997). *Dynamics of marine sands: a manual for practical applications*. Thomas Telford.
- Spinewine, Benoit et al. (2005). “Two-layer flow behaviour and the effects of granular dilatancy in dam-break induced sheet-flow”. *Hydraulic Structures. University of Catholic the Louvain*.
- Sumer, B Mutlu and Jørgen Fredsøe (2000). “Experimental study of 2D scour and its protection at a rubble-mound breakwater”. *Coastal Engineering* 40.1, pp. 59–87.
- Sumer, B Mutlu, Richard JS Whitehouse, and Alf Tørum (2001). “Scour around coastal structures: a summary of recent research”. *Coastal Engineering* 44.2, pp. 153–190.

- Sutherland, J, B Chapman, and RJS Whitehouse (1999). “SCARCOST Experiments in the UK Coastal Research Facility-Data on scour around a detached rubble mound breakwater”.
- Sutherland, J et al. (2004). *Understanding the Lowering of Beaches in Front of Coastal Defense Structures, Phase 2*.
- Sutherland, J et al. (2006). “Laboratory tests of scour at a seawall”. *Proceedings 3rd International Conference on Scour and Erosion, CURNET, Gouda, The Netherlands*. Technical University of Denmark.
- Toro, Eleuterio F (2013). *Riemann solvers and numerical methods for fluid dynamics: a practical introduction*. Springer Science & Business Media.
- Tuković, Željko (2005). “Metoda kontrolnih volumena na domenama promjenjivog oblika”. PhD thesis. Sveučilište u Zagrebu, Fakultet strojarstva i brodogradnje.
- Tukovic, Zeljko and Hrvoje Jasak (2008). “Simulation of free-rising bubble with soluble surfactant using moving mesh finite volume/area method”. *Proceedings of 6th International Conference on CFD in Oil & Gas, Metallurgical and Process Industries, no. CFD08-072*.
- USACE, CERC (1984). “Shore protection manual”. *US Army Corps of Engineers, Coastal Engineering Research Center, Vicksburg, MS 2*.
- Van Dyke, Milton (1982). “An album of fluid motion”.
- Van Rijn, Leo C (1984a). “Sediment transport, part I: bed load transport”. *Journal of hydraulic engineering* 110.10, pp. 1431–1456.
- (1984b). “Sediment Transport, Part II: Suspend load Transport”. *Journal of hydraulic engineering* 110.11, pp. 1613–1641.
- Vetsch, David Florian (2012). “Numerical simulation of sediment transport with meshfree methods”. PhD thesis. ETH Zurich.
- Vukčević, Vuko (2016). “Numerical Modelling of Coupled Potential and Viscous Flow for Marine Applications”. PhD thesis. University of Zagreb.
- Vukčević, Vuko, Hrvoje Jasak, and Inno Gatin (2017). “Implementation of the Ghost Fluid Method for free surface flows in polyhedral Finite Volume framework”. *Computers & Fluids* 153, pp. 1–19.
- Walker, H Jesse (2012). *Artificial structures and shorelines*. Vol. 10. Springer Science & Business Media.
- Wei, Gengsheng et al. (2014). “The Sedimentation Scour Model in FLOW-3D®”.
- Wu, Nan-Jing, Ting-Kuei Tsay, and Yang-Yih Chen (2014). “Generation of stable solitary waves by a piston-type wave maker”. *Wave Motion* 51.2, pp. 240–255.
- Wu, Weiming, Wolfgang Rodi, and Thomas Wenka (2000). “3D numerical modeling of flow and sediment transport in open channels”. *Journal of Hydraulic Engineering* 126.1, pp. 4–15.
- Wu, Weiming and Sam S Wang (2007). “One-dimensional modeling of dam-break flow over movable beds”. *Journal of hydraulic engineering* 133.1, pp. 48–58.
- Xie, Shi-Leng (1981). “Scouring patterns in front of vertical breakwaters and their influences on the stability of the foundation of the breakwaters”. PhD thesis. TU Delft, Delft University of Technology.
- Yeganeh-Bakhtiary, Abbas et al. (2009). “A three-dimensional distinct element model for bed-load transport”. *Journal of Hydraulic Research* 47.2, pp. 203–212.
- Zhou, Lu (2016). “Numerical Modelling of Scour In Steady Flows”. PhD thesis. Ecole Centrale de Lyon.

AUTORISATION DE SOUTENANCE

Vu les dispositions de l'arrêté du 25 mai 2016,

Vu la demande des directeurs de thèse

Messieurs R. PERKINS et E. VINCENS

et les rapports de

M. L. MING

Senior Lecturer - Department of Civil Engineering and Industrial Design - School of Engineering
- University of Liverpool - Brodie Tower Browlow Street - Liverpool L69 3GQ - Merseyside
Royaume-Uni

et de

M. D. CONLEY

Associate Professor - School of Biological and Marine Sciences - Faculty of Science and
Engineering - Plymouth University - Drake Circus - Plymouth PL4 8AA - Devon - Royaume-Uni

Monsieur SATRIA Anak

est autorisé à soutenir une thèse pour l'obtention du grade de **DOCTEUR**

Ecole doctorale MECANIQUE, ENERGETIQUE, GENIE CIVIL ET ACOUSTIQUE

Fait à Ecully, le 26 mars 2019

P/Le directeur de l'E.C.L.
La directrice des Etudes

